



Experimentelle Physik

**Ice calibration studies for IceCube
Upgrade with multi-PMT optical
modules, and studies of the sensitivity
of future IceCube extensions to
astrophysical neutrinos in the MeV and
GeV range**

Inaugural-Dissertation
zur Erlangung des Doktorgrades Dr. rer. nat.
der Naturwissenschaften im Fachbereich Physik
der Mathematisch-Naturwissenschaftlichen
Fakultät der Westfälischen Wilhelms-Universität Münster

vorgelegt von

Cristian Jesús Lozano Mariscal
aus San Roque (Cádiz), Spanien

—2023—

(leichte überarbeitete Version, May 2023)

Dekan: Prof. Dr. Michael Rohlfing
Erster Gutachter: Prof. Dr. Alexander Kappes
Zweiter Gutachter: Prof. Dr. Christian Weinheimer
Tag der mündlichen Prüfung: 05.05.2023
Tag der Promotion: 05.05.2023

Abstract

The IceCube neutrino observatory is a large-scale particle physics experiment at the South Pole. IceCube consists of a series of sensors embedded in the ice that detect the Cherenkov radiation produced when a neutrino interacts with the ice. Given its great success and reliability, the IceCube detector is being expanded through two extension projects: IceCube Upgrade and IceCube-Gen2. The IceCube Upgrade project aims to install ~ 700 new optical modules in a dense configuration in the existing IceCube volume to detect low-energy neutrinos; construction is planned for the Australian summer of 2025 – 2026. IceCube-Gen2 envisions an expansion of the instrumented volume from 1 to 8 km^3 with new optical modules. Construction is scheduled to begin shortly after the completion of IceCube Upgrade. This expansion will allow IceCube to significantly increase its detection rate of cosmic high-energy neutrinos and further improve our understanding of the universe.

This thesis presents the results of simulation studies that evaluate the potential of future detector extensions for a number of topics. The first study focuses on the detection of low-energy neutrinos released during a core collapse supernova (CCSN) with the new IceCube-Gen2 detector when equipped with multi-PMT digital optical modules (mDOMs). It is shown that CCSNe can be detected up to distances of $\sim 250 \text{ kpc}$ with a false detection rate of less than one per century. The second study examines the calibration of bubble column parameters in IceCube Upgrade. The bubble column, a region of frozen ice in the middle of the strings with poorer optical properties than the bulk ice, is a significant source of systematic uncertainties in the current detector, and determining its properties will benefit not only the future detector but also allow improved re-analyses of existing data. This study shows that its properties can be reconstructed with high precision by lining up two adjacent mDOMs and flashing the LEDs in one of them. The last study investigates the sensitivity of IceCube Upgrade for detecting a GeV neutrino flux from a compact binary merger. The results show that the sensitivity for detecting these sources is improved by a factor of 2.4 compared to current DeepCore capabilities.

Zusammenfassung

Das Neutrino-Observatorium IceCube ist ein groß-skaliges Teilchenphysikexperiment am Südpol. IceCube besteht aus einer Reihe von in das Eis eingebetteten Sensoren, die die Cherenkov-Strahlung aufspüren, die bei der Wechselwirkung eines Neutrinos mit dem Eis entsteht. Angesichts seines großen Erfolgs und seiner Zuverlässigkeit ist geplant, die Fähigkeiten des Detektors durch zwei Upgrade-Projekte zu erweitern: IceCube Upgrade und IceCube-Gen2. Das IceCube-Upgrade-Projekt zielt darauf ab, ~ 700 neue optische Module in einer dichten Konfiguration im bestehenden IceCube-Volumen zu installieren, um niederenergetische Neutrinos nachzuweisen; der Bau ist für den australischen Sommer 2025 – 2026 geplant. IceCube-Gen2 sieht eine Erweiterung des instrumentierten Volumens von 1 auf 8 km^3 mit neuen optischen Modulen vor. Der Baubeginn ist kurz nach der Fertigstellung von IceCube Upgrade geplant. Diese Erweiterung wird es IceCube ermöglichen, seine Nachweisrate von kosmischen Hochenergie-Neutrinos deutlich zu erhöhen und unser Verständnis des Universums weiter zu verbessern.

In dieser Arbeit werden die Ergebnisse von Simulationsstudien vorgestellt, die das Potenzial künftiger Detektorerweiterungen für eine Reihe von Themen bewerten. Die erste Studie konzentriert sich auf den Nachweis von während einer Kernkollaps-Supernova (CCSN) freigesetzten niederenergetischen Neutrinos mit dem neuen IceCube-Gen2-Detektor, wenn dieser mit digitalen optischen Multi-PMT-Modulen (mDOMs) ausgestattet ist. Es wird gezeigt, dass CCSNe bis zu Entfernungen von $\sim 250 \text{ kpc}$ mit einer Falschnachweisrate von weniger als einem pro Jahrhundert nachgewiesen werden können. Die zweite Studie untersucht die Kalibrierung der “Bubble Column” in IceCube Upgrade. Die “Bubble Column”, eine Region aus gefrorenem Eis in der Mitte der Strings mit schlechteren optischen Eigenschaften als das umgebende Eis, ist eine bedeutende Quelle systematischer Unsicherheiten im aktuellen Detektor. Die Bestimmung ihrer Eigenschaften wird nicht nur dem zukünftigen Detektor zugute kommen, sondern auch verbesserte Analysen bestehender Daten ermöglichen. Diese Studie zeigt, dass seine Eigenschaften mit hoher Präzision rekonstruiert werden können, indem zwei benachbarte mDOMs aneinandergereiht und die LEDs in einem der beiden angeschaltet werden. Die letzte Studie untersucht die Empfindlichkeit von IceCube Upgrade für den Nachweis von GeV-Neutrinos aus der Fusion eines kompakten Binärsystem. Die Ergebnisse zeigen, dass die Fähigkeit zum Nachweis dieser Quellen im Vergleich zu den derzeitigen DeepCore-Fähigkeiten um den Faktor 2,4 verbessert wird.

Contents

Glossary	IX
1 Introduction	1
2 The role of neutrinos in astrophysics	3
2.1 Neutrino properties	3
2.1.1 Neutrinos in the Standard Model	3
2.1.2 Neutrino oscillations	4
2.1.3 Neutrino mass ordering	6
2.2 Cosmic rays	7
2.3 Neutrino sources and astrophysics	9
2.3.1 Solar neutrinos	9
2.3.2 Atmospheric neutrinos	10
2.3.3 High energy astrophysical neutrinos	11
2.3.4 Neutrinos from Core Collapse Supernovae	13
2.4 Compact binary mergers and multi-messenger astrophysics	15
3 Neutrino detection at the South Pole	17
3.1 Neutrino interactions	17
3.2 Cherenkov-based detectors	18
3.3 The IceCube Neutrino Observatory	21
3.3.1 IceCube high energy in-ice array	22
3.3.2 DeepCore	23
3.3.3 IceTop	23
3.4 DOM: Digital Optical Module	24
3.5 Calibration devices	26
3.6 IceCube internal background	27
3.7 Detecting neutrinos in IceCube	28
3.7.1 High energy events - IceCube	29
3.7.2 Low energy events - DeepCore	31
3.7.3 Selected results	31
4 Future IceCube extensions	33
4.1 Next generation optical modules	33
4.2 Calibration devices	38
4.3 ICU: IceCube Upgrade	39
4.3.1 Physics motivation	40
4.3.2 Detector geometry	41
4.4 IceCube-Gen2	41
4.4.1 Physics motivation	41
4.4.2 Detector geometry	42
5 mDOM Geant4 simulation	45
5.1 Module simulation	45
5.2 Physics processes	48
5.3 Bulk ice simulation	48

6	Using module segmentation to identify MeV CCSN neutrinos in IceCube-Gen2	53
6.1	Neutrino interactions from CCSNe in ice detectors	54
6.2	Detecting MeV CCSNe in current IceCube	56
6.2.1	Background to CCSN studies in IceCube	57
6.2.2	IceCube’s CCSNe detection capabilities	57
6.3	Effective volume of a detector with mDOMs	58
6.4	MeV CCSN neutrino simulation	60
6.4.1	Description of the CCSN burst models	60
6.4.2	CCSNe simulation	62
6.4.3	Results for galactic CCSNe	65
6.5	Background simulation	67
6.6	Identifying extra-galactic CCSNe	70
6.6.1	Trigger conditions using module’s segmentation	71
6.6.2	False CCSN rate detection	71
6.6.3	Extra-galactic detection range	72
6.6.4	Detection range for known arrival burst time	74
6.6.5	CCSN detection rate	78
6.7	Detected flux analysis	79
6.8	Sensitivity to the CCSN energy spectrum	81
6.9	CCSN detection in IceCube Upgrade	84
6.10	Results using LOM16 modules	87
6.11	Sources of error in the results	90
6.11.1	Estimating the impact of atmospheric muons on the detection range	90
6.11.2	About the simulation, its errors and approximations	94
6.12	Summary and conclusions	96
7	Calibration of the bubble column with mDOM flashers in ICU	101
7.1	The hole ice and the bubble column in IceCube strings	102
7.1.1	Sweden Camera pictures	102
7.1.2	Methods for studying the bubble column in IceCube	103
7.1.3	Current knowledge on the hole ice and the bubble column	103
7.2	LED flashers in mDOMs	104
7.3	Simulation details	105
7.3.1	LED simulation	106
7.3.2	Modules simulation	109
7.3.3	Bubble column simulation	110
7.4	Simulation results	111
7.5	Scanning the bubble column parameters	115
7.6	Statistical uncertainty on column parameters	124
7.7	Systematics	128
7.7.1	Individual influence of each systematic source	129
7.7.2	Combined systematics	139
7.8	Summary and conclusions	144
8	Sensitivity of IceCube Upgrade to GeV-neutrinos from compact binary mergers	147
8.1	Assumed signal and background	148
8.2	Events simulations	149

8.2.1	Geometry	150
8.2.2	Simulation of neutrinos	151
8.2.3	Simulation of atmospheric muons	151
8.2.4	Noise generation	152
8.3	Selection of low energetic neutrino events in Upgrade	152
8.3.1	Triggers and filters	154
8.3.2	Gradient boosting decision trees (GBDTs)	156
8.3.3	GBDT configuration	157
8.3.4	Selection of neutrinos over the noise of the modules	158
8.3.5	First selection of neutrinos over atmospheric muons	163
8.3.6	Second selection of neutrinos over atmospheric muons	166
8.3.7	Background rates after the selections	169
8.4	Expected sensitivity to compact binary mergers	171
8.4.1	Model flux and signal weights	172
8.4.2	Statistical method	172
8.4.3	Time-integrated all flavor fluxes	174
8.4.4	Isotropic energy limit on GW170817	174
8.4.5	Discussion and limits at any distance	176
8.5	Summary and conclusions	178
9	Summary and outlook	181
A	Appendix: detection patterns for different bubble column parameters	185
B	Appendix: variables used to train the GBDT to select neutrinos over noise	195
C	Appendix: variables used to train the GBDT to select neutrinos over muons - 1	197
D	Appendix: variables used to train the GBDT to select neutrinos over muons - 2	201
E	Appendix: alternative selection focused on lower energetic events	205
	Bibliography	209
	Acknowledgements	223

Glossary

- **Bubble column:** name assigned to the central part of the hole ice, where the accumulation of air bubbles negatively impact the optical properties of the refrozen ice.
- **Bulk ice:** term commonly used in IceCube to refer to the glacial ice where the detector is built.
- **CC:** acronym for Charged Current, weak interactions mediated by W^\pm bosons.
- **CoG** acronym for Center of Gravity, average position of hits within the fiducial volume. Used for the analysis in Chapter 8.
- **CP:** used in Chapter 8 as a acronym for Clean Pulses, meaning the use of the pulse dataset that has gone through a noise cleaning algorithm.
- **CCSN/e:** acronym for Core-Collapse SuperNova/e, type of Supernova that occur when the stellar core of a massive star collapses onto itself giving birth to neutron stars and black holes. This includes Supernova types II, Ib, and Ic.
- **D-Egg:** acronym for Dual optical sensor in an Ellipsoid Glass for IceCube-Gen2, a module planned for future IceCube extensions housing 2 PMTs, the corresponding electronics, and some calibration instruments.
- **DOM:** acronym for Digital Optical Module, IceCube devices housing one PMT, the corresponding electronics, and some calibration instruments.
- **ElowEn:** acronym for Extreme low-Energy neutrinos. Used in IceCube to refer to neutrino events with energies around 5 GeV.
- **ENES:** acronym for Electronic-Neutrino Electron elastic Scattering $\nu_e + e^- \rightarrow \nu_e + e^-$.
- **GBDT:** acronym for Gradient Boosting Decision Tree, the machine learning technique used in Chapter 8.
- **GW:** acronym for Gravitational Wave.
- **HLC:** acronym for Hard Local Coincidence, IceCube pulses selected after requiring one or two neighboring DOMs detecting the event within a time window of generally $1 \mu\text{s}$.
- **Hit:** detection of a photon by a PMT.
- **Hole ice:** term used to described the refrozen column of ice after IceCube construction, containing the modules, cables and the region known as bubble column.
- **IBD:** acronym for Inverse Beta Decay $\bar{\nu}_e + p \rightarrow n + e^+$.
- **ICU:** acronym for IceCube Upgrade.
- **LED:** acronym for Light-Emitting Diode. LEDs are installed in the optical modules to calibrate the detector.
- **LOM:** acronym for eLongated Optical Module, devices planned for IceCube-Gen2 housing 16 or 18 PMTs, the corresponding electronics, and some calibration instruments. During the thesis, each LOM type is often referred to as LOM16 or LOM18.
- **MC:** acronym for Monte Carlo methods, algorithms that rely on random sampling to obtain numerical results.

- **mDOM:** acronym for multi-Digital Optical Module, devices planned for future IceCube extensions housing 24 PMTs, the corresponding electronics, and some calibration instruments.
- **Multiplicity:** number of different PMTs within a single module that has detected the event. Definition used in Chapter 6
- **NC:** acronym for Neutral Current, weak interactions mediated by neutral Z bosons.
- **pDOM:** acronym for PINGU-Digital Optical Module, an optical module based on the DOM originally developed for the PINGU detector, a low energy extension planned for IceCube that has been replaced by IceCube Upgrade.
- **PDF:** acronym for probability density function.
- **PMT:** acronym for PhotoMultiplier Tubes, extremely sensitive devices used to detect light.
- **POCAM:** modules with high-precision light sources planned for future IceCube extensions.
- **QE:** acronym for the Quantum Efficiency of a PMT, ratio of generated electrons to incident photons in the photocathode.
- **SLC:** acronym for Soft Local Coincidence, IceCube pulses that do not meet the criteria for HLC but where the PMT signal exceeds certain threshold.
- **SNDQAQ:** SuperNova Data Acquisition System, the search algorithms for galactic supernova in IceCube.
- **UP:** used in Chapter 8 as a acronym for Unclean Pulses, meaning the use of the pulse dataset without undergoing through any cleaning algorithm.
- **WOM:** acronym for Wavelength-shifting Optical Module, a device planned for future IceCube extensions that houses 2 PMTs and a wavelength-shifting coat of paint in the glass, the corresponding electronics, and some calibration instruments.

Introduction

The study of astrophysics has been at the forefront of scientific inquiry for centuries, as scientists have sought to understand the fundamental nature of the universe and the phenomena that occur in it. From the earliest observations of stars and planets to the development of modern telescopes and detectors, the field has undergone tremendous evolution and advancement.

One particularly exciting area of astrophysical research is the detection of neutrinos, subatomic particles that are produced by some of the most energetic and violent processes in the cosmos. Neutrinos have extremely small masses and interact only weakly with matter, making them difficult to detect. However, their unique properties also make them valuable probes of the cosmos, as they can provide information about celestial bodies that is otherwise inaccessible to traditional methods of observation.

The IceCube Neutrino Observatory, located at the South Pole, is a cutting-edge facility focused on searching high-energy neutrinos of astrophysical origin. It consists of an array of digital optical modules (DOMs) embedded in the ice at the South Pole. These DOMs contain a single photomultiplier tube (PMT) that can detect the light generated after a neutrino interaction. The IceCube Collaboration, formed by many universities around the world, has plans to further enhance the capabilities of the current IceCube and expand its range of detection. This process will start with the so-called IceCube Upgrade, which aims to improve the sensitivity and precision of the detector at low energies by building a denser array of optical modules. Then, IceCube-Gen2 will be built, with the objective of significantly increasing the sensitivity of the detector at high energies by instrumenting a much larger volume of ice. In the scope of these extensions, new and more sophisticated optical modules are being designed which combine several PMTs in each module, such as the mDOM, which features 24 PMTs facing in all directions, or the LOM, a smaller concept of the mDOM featuring 16 PMTs.

In this thesis, simulation studies that explore the potential of future detector extensions for IceCube are performed, including the detection of core-collapse supernova (CCSN) neutrinos, the calibration of the ice in the IceCube Upgrade, and the detection of GeV neutrinos from compact binary mergers. These studies try to use the advantages of the new module segmentation when possible.

The work is divided as follows: first, an introduction to neutrinos and astrophysics is given in Chapter 2. Then, IceCube is introduced in Chapter 3, highlighting the most important discoveries made with the detector so far. IceCube Upgrade, IceCube-Gen2 and the new optical modules designed for these extensions are introduced in Chapter 4. Then, Chapter 5 introduces the *Geant4* simulation of the new optical modules that will be used for different analyses later. Chapter 6 shows the studies performed regarding the detection of MeV CCSN neutrinos in the future detector extensions, focusing on an IceCube-Gen2 detector equipped with mDOMs, but also including results for a detector equipped with

LOMs and for IceCube Upgrade. In Chapter 7, studies of the ice calibration in IceCube Upgrade are performed, using the LED system mounted on two consecutive mDOMs within a string to reconstruct the parameters of the *bubble column*, the central region of the refrozen ice. Last, Chapter 8 investigates the capability of IceCube Upgrade to detect a GeV neutrino flux coming from transient sources, applied to the case of compact binary mergers.

The role of neutrinos in astrophysics

Being unique cosmic messengers, the role of neutrinos in astrophysics has grown in importance over the last decades. Neutrinos are characterized by their low interaction probability, allowing them to escape from the inner structure of celestial bodies. As electrically neutral particles, they do not get deflected by magnetic fields in the universe and can be traced back to their source. The detection of high-energy neutrinos is, in fact, evidence of hadronic acceleration, where the majority of cosmic rays come from. Thus, neutrinos can be studied to determine the source of high-energy cosmic rays reaching Earth and ultimately shed light on the extraordinary forces that govern the universe [1]. In this chapter, neutrinos and their relation to astrophysics are introduced, focusing on the physics cases related to the studies performed in this thesis.

2.1 Neutrino properties

Neutrinos are particles that have fascinated physicists for years. They were first introduced as a solution to the apparent energy loss in β -decay by Wolfram Pauli in 1930, who apparently famously said “*I have done a terrible thing; I have postulated a particle that cannot be detected*”. Back then, the neutrino was proposed as a massless particle, and it was not until 1956 that physicists were able to detect them for the first time [2]. Since then, a lot have been learned about such elusive particles, although some questions about their nature remain open.

2.1.1 Neutrinos in the Standard Model

This section references [3, 4] as primary sources for the topic, unless otherwise noted.

Neutrinos are classified as elementary particles by the Standard Model of Particle Physics (SM). Elementary particles are subatomic non-divisible particles, constituting the building blocks of all known matter in the universe. These are divided into fermions, with half-odd-integer spin and following Pauli’s exclusion principle [5] - or bosons, with integer spin number and obeying the Bose-Einstein particle statistics. These categorizations are shown in Figure 2.1. Neutrinos belong to the leptonic family, particles with no color charge that interact through electroweak interactions, while strongly interacting quarks constitute the other fermionic family.

Fermions are subdivided into three different generations. The electron, muon, and tau constitute, respectively, the first, second, and third generation of the charged leptons.

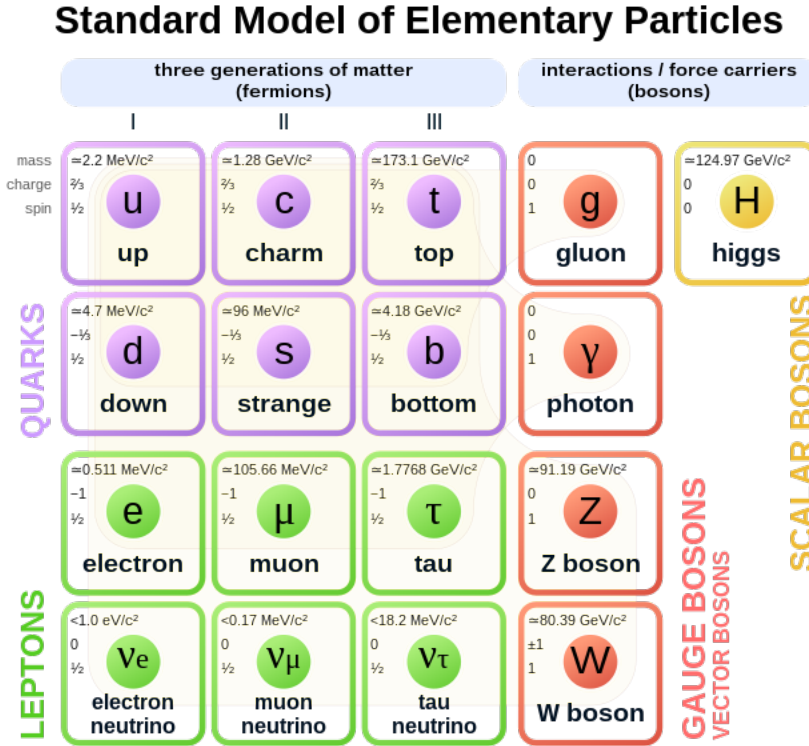


Figure 2.1: Elementary particles of the Standard Model of Particle Physics, classified as fermions (quarks and leptons) and bosons. The figure displays the mass, charge and spin for each particle. Figure from [6].

Each of them has an antiparticle with contrary electric charge. Each lepton generation also has a neutral particle: the neutrino, namely, electron neutrino ν_e , muon neutrino ν_μ , and tau neutrino ν_τ , the so-called neutrino flavors. Neutrinos are distinguished from their antiparticle counterparts by their opposite chirality¹.

The standard model postulates neutrinos as massless particles. Being elementary leptons with no charge, neutrinos would interact only through weak interactions, hence the characteristic elusiveness when trying to detect neutrinos. After many experiments, about 20 years ago, it was finally proven that neutrinos oscillate [8, 9]², for which they need to have non-zero rest mass. Neutrino masses have been measured to be extremely small, with the best current upper limit (90% confidence) on the effective electron antineutrino mass being $m_\nu < 0.8 \text{ eV}/c^2$ [10].

2.1.2 Neutrino oscillations

Neutrino oscillation is the phenomenon by which neutrino flavors change while traveling through space. Neutrino oscillation was first predicted by Bruno Pontecorvo in 1957 [11, 12], and its effects were first detected in the late 1960s with the *solar neutrino problem* [13, 14]. The solar neutrino problem consisted of an apparent deficit of the neutrino flux measured from the Sun with respect to the predictions by a factor of ~ 3 . Later, the puzzle got

¹Some experiments such as SNO+ [7] aim to determine whether neutrinos are Majorana particles by searching for neutrino-less double beta decays, which would imply that neutrinos are their own antiparticles.

²T. Kajita (Super-Kamiokande) and A. McDonald (SNO) were awarded the physics Nobel Prize in 2015 for the discovery of neutrino oscillations.

another component when the relative composition of atmospheric electron and muon neutrinos was again measured to be different from the predictions [15, 16] - named *atmospheric neutrino anomaly*.

Neutrinos interact through flavor eigenstates (ν_e, ν_μ, ν_τ) but propagate through a superposition of mass eigenstates (ν_1, ν_2, ν_3). Thus, the eigenstates of the free-particle Hamiltonian are different from the eigenstates of the weak interaction. The neutrino mass eigenstates ($|\nu_i\rangle, i = 1, 2, 3$) and flavor eigenstates ($|\nu_\alpha\rangle$) are connected as [3]

$$|\nu_\alpha\rangle = \sum_{i=1}^3 U_{\alpha i}^* |\nu_i\rangle, \quad (2.1)$$

where $U_{\alpha i}^*$ is a 3x3 unitary matrix named *Pontecorvo-Maki-Nakagawa-Sakata matrix* (PMNS)¹. The PMNS matrix can be written as the product of three sub-matrices as² [3]

$$U = \begin{pmatrix} 1 & 0 & 0 \\ 0 & c_{23} & s_{23} \\ 0 & -s_{23} & c_{23} \end{pmatrix} \begin{pmatrix} c_{13} & 0 & s_{13}e^{-i\delta_{\text{CP}}} \\ 0 & 1 & 0 \\ -s_{13}e^{i\delta_{\text{CP}}} & 0 & c_{13} \end{pmatrix} \begin{pmatrix} c_{12} & s_{12} & 0 \\ -s_{12} & c_{12} & 0 \\ 0 & 0 & 1 \end{pmatrix}, \quad (2.2)$$

where δ_{CP} is the CP-violation phase (Charge Parity), $c_{ij} = \cos \theta_{ij}$ and $s_{ij} = \sin \theta_{ij}$ with θ_{ij} representing the mixing angles. The division into submatrices is useful to isolate different origins; thus, the first submatrix parameters are sensitive to experiments studying neutrinos originated in the atmosphere, the second one to those measuring reactor neutrinos, and the last submatrix to studies with neutrinos from the Sun.

The flavor eigenstate of a neutrino is defined after its weak interaction and the production of a charged lepton of the corresponding family. The flavor eigenstate can be obtained as a superposition of mass eigenstates, and these propagate following the Schrödinger equation as

$$i \frac{\delta}{\delta t} |\nu_i(t)\rangle = H |\nu_i(t)\rangle, \quad (2.3)$$

with H being the Hamiltonian of the system. The equation can be solved in the form of plane waves as

$$|\nu_i(t)\rangle = e^{-i(E_i t - \vec{p}_i \vec{x}_i)} |\nu_i(0)\rangle, \quad (2.4)$$

with E_i being the energy of the mass eigenstate i and \vec{p}_i, \vec{x}_i the momentum and position vectors. Neutrinos are in all practical cases relativistic, so $p_i \simeq p_j \equiv p \simeq E$, and E_i can be written as [3]

¹A similar connection can be done between quarks eigenstates throughout the Cabibbo-Kobayashi-Maskawa (CKM) matrix.

²This assumes that neutrinos are Dirac particles. If neutrinos are considered Majorana particles, the PMNS matrix contains two additional phase elements. The PMNS would be 4x4 if sterile neutrinos were considered and is sometimes simplified to 2x2 for a two-flavor oscillation scenario.

$$E_i = \sqrt{p_i^2 + m_i^2} \simeq p + \frac{m_i^2}{2E}, \quad (2.5)$$

in natural units. Combining Eq. 2.4 and Eq. 2.5 and considering $L \approx t$ the distance that the neutrino has traveled, it leads to

$$|\nu_i(L)\rangle = e^{-i\frac{m_i^2}{2E}L} |\nu_i(0)\rangle. \quad (2.6)$$

Thus, each neutrino mass eigenstate propagates with a different frequency which depends on m_i . After traveling L , the probability of finding the original neutrino of flavor α with flavor β is [3]

$$P_{\alpha \rightarrow \beta} = |\langle \nu_\beta | \nu_\alpha(L) \rangle|^2 = \sum_{i,j} U_{\alpha i}^* U_{\beta j} |\langle \nu_j | \nu_i(L) \rangle|^2. \quad (2.7)$$

For simplicity, let us consider the situation for only two flavor mixing¹. In this scenario and by introducing Eq. 2.5 into Eq. 2.7, the probability that a neutrino produced with flavor α changes to flavor β after traveling a distance L is [3]

$$P_{\alpha \rightarrow \beta} = \sin^2(2\theta) \sin^2 \frac{\Delta m^2 L}{4E} \text{ for } \alpha \neq \beta. \quad (2.8)$$

Note that the formula depends on the mass-squared difference $\Delta m^2 = m_i^2 - m_j^2$. Experiments usually try to measure a single oscillation channel through the appearance or disappearance of a single neutrino flavor; thus, individual masses cannot be restricted and instead the mass-squared difference is measured². The calculation above represents neutrinos traveling through vacuum. When traveling through matter, one has to take into account the probability of neutrinos interacting with matter, the so-called MSW³ effect. The best measurements to date of the neutrino mass differences yield $\Delta m_{21}^2 \simeq 7.4 \times 10^{-5} \text{ eV}^2$ - known as solar mass splitting - and $|\Delta m_{32}^2| \simeq 2.5 \times 10^{-3} \text{ eV}^2$ - atmospheric mass splitting [18, 19].

2.1.3 Neutrino mass ordering

Since Δm_{21}^2 is known to be positive due to matter effects in the Sun [20] but the sign of Δm_{32}^2 is still unknown [18, 19], the aforementioned measurements of the neutrino mass differences leaves open whether $\Delta m_{31}^2 > 0$ (known as *normal mass ordering* or *normal hierarchy*) $\Delta m_{31}^2 < 0$ (*inverted mass ordering* or *inverted hierarchy*). Conventionally, the mass eigenstates are chosen such as m_1 and m_2 exhibiting the small Δm^2 and m_3 has a

¹This approximation can be useful for $\nu_\mu \leftrightarrow \nu_\tau$ or $\nu_e \leftrightarrow \nu_x$ due to the mixing angle θ_{13} being very small and two of the mass eigenstates being close in mass in comparison with the third one.

²Different methods can also be used to measure the exact value of the effective neutrino masses, as it is done for example in *KATRIN* [17] where a precise measurement in the tail of the energy spectrum of β decays is used to calculate the effective electron antineutrino mass.

³Mikheev-Smirnov-Wolfenstein

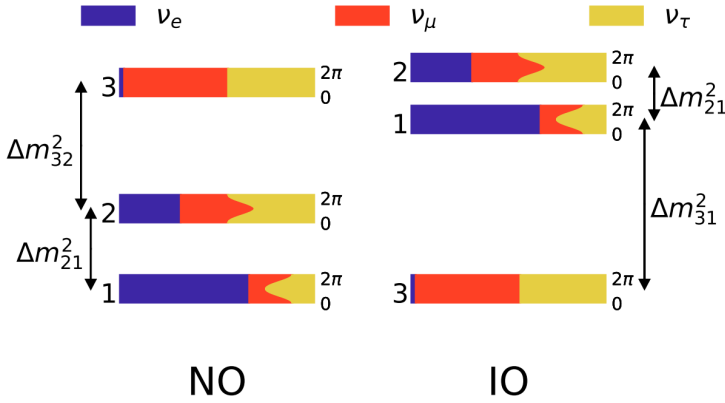


Figure 2.2: Neutrino mass ordering in normal ordering (NO) or inverted ordering (IO). Colors stand for the probability of finding each neutrino flavour in the corresponding mass eigenstate for varied δ_{CP} from 0 to 2π within each bar. Figure from [4].

larger mass in the normal ordering scenario and otherwise in the inverted ordering scenario. Thus, in the first scenario $m_1 < m_2 < m_3$, while the second implies that $m_3 < m_1 < m_2$. These hierarchical scenarios are shown in Figure 2.2. For each, the probability of the neutrino to emerge after a weak interaction with a respective flavor is shown in colors, for all the possible δ_{CP} going from 0 to 2π . The precise value for δ_{CP} is still unknown, however the best estimates are around $3\pi/2$ [3].

Recent efforts to determine the masses of neutrinos experimentally have adopted an approach that involves measuring the oscillation probability of neutrinos as they pass through matter. For this, accurate determination of neutrino energy and direction is essential, yet challenging. Some detectors can explore this possibility using reactor neutrinos, whereas some other detectors would use atmospheric neutrinos. In the near future, detectors like JUNO [21], ORCA [22] or IceCube Upgrade [23] might be able to combine their efforts using this approach and finally solve the neutrino mass ordering riddle.

2.2 Cosmic rays

Cosmic rays and neutrinos are closely related. The interaction of cosmic rays within the atmosphere generates a large number of atmospheric neutrinos that are detected in neutrino experiments. More importantly, the origin of both cosmic neutrinos and cosmic rays is yet not known, and it is believed that they are connected: cosmic ray particles would gain energy in cosmic accelerators and, after their decay, produce high-energy cosmic neutrinos [24].

Cosmic rays consist of ionized nuclei, relativistic particles that reach the Earth's atmosphere at a rate of about $1000 \text{ m}^{-2}\text{s}^{-1}$ [24]. They are mainly composed of protons (90%) and alpha particles (9%), the rest being heavier nuclei. Although some cosmic rays detected at Earth come from the Sun, the higher energetic ones come from outside the Solar System, including distant galaxies. Since they are charged particles, their trajectories to Earth cannot be traced back, as they get deflected in magnetic fields during their propagation. Thus, cosmic rays can be studied in terms of their composition and energy spectrum. Although they do not trace back to their origin, the distribution of the cosmic ray arrival directions can provide important information, such as the confirmation that most of them come from other galaxies [25].

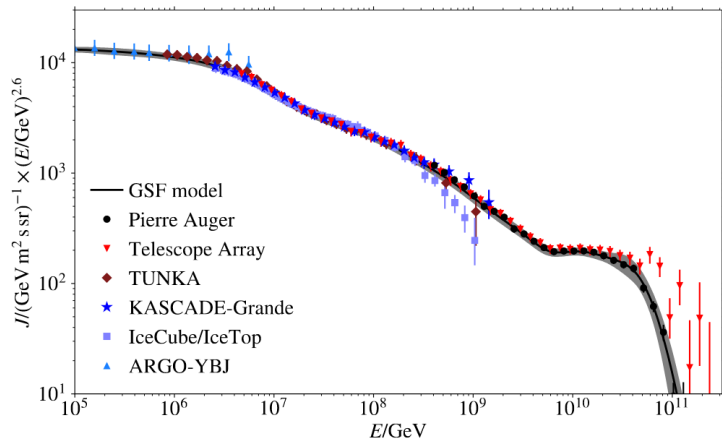
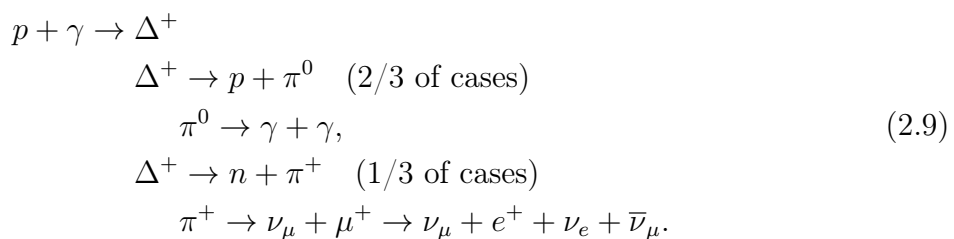


Figure 2.3: Energy spectrum of high energy cosmic rays following the Global Spline Fit (GSF) model [32], together with the observations from different telescopes along the globe. Figure from [26].

The energy spectrum of high energetic cosmic rays is shown in Figure 2.3. The spectrum follows a combination of power laws, and thus is often divided into different parts depending on the index of the power law (named spectral index). The first part covers up to the point sometimes called *knee* at $4 \sim 10^6$ GeV, and shows a spectral index of ~ -2.6 [26]. From there, the spectral index is around -3 , with small differences around a second *knee* at $\sim 10^8$ GeV [26]. Above $5 \sim 10^9$ GeV the spectral index returns to ~ -2.6 in what is called the *ankle* [26]. Different spectral indexes are due to different compositions or source regions, and around the ankle region is generally considered the transition from galactic to extragalactic cosmic rays [27]. Due to the wide energy range of cosmic rays, different types of detectors are necessary to study each part of the spectrum [24].

The spectrum declines rapidly at energies higher than $\sim 5 \times 10^{10}$ GeV, caused by the interaction with intergalactic photons (GZK¹ [28, 29] limit), which increases at higher energies, and/or cutoffs at astrophysical sources in acceleration potential [30, 31]. The interaction of proton cosmic rays with the cosmic microwave background produces Δ^+ resonances and limits the propagation distance to ~ 100 Mpc at these energies. The generated Δ^+ decays after these interactions producing neutrinos and γ as [3]



The neutrinos produced after the interaction of these high-energy cosmic rays with the cosmic microwave background are known as *GZK neutrinos* [33], and are part of the population sometimes called *cosmogenic neutrinos* by neutrino telescopes, with energies from 10^7 to 10^9 GeV.

The acceleration mechanism capable of producing such spectrum is not yet fully understood, although it is believed to be produced by shock acceleration through the *Fermi acceleration mechanism* [34]. The energy of the astronomical object is transmitted to the charged

¹Greisen–Zatsepin–Kuzmin, named after A. Greisen, G. T. Zatsepin and V. A. Kuzmin, who first postulated it

particles ejected from *shock fronts*. The shock fronts are the boundaries between colliding plasma fields. The particles can undergo multiple accelerations because of the magnetic field inhomogeneities on both sides of the front until they finally escape the acceleration region. The cosmic rays can get trapped near the sources and interact, generating π^+ , π^- and π^0 in approximately equal fractions. The decay scheme of π^- is similar to that of π^+ (see Eq. 2.9), with the corresponding particle/antiparticle adjustments and, therefore, also emitting neutrinos.

Due to the interaction of cosmic rays with the atmosphere, these can only be detected directly by detectors in satellites, whose current constraints in size and weight limit the energy of these to $\sim 10^5$ GeV. Higher energetic cosmic rays are measured by detecting the *air showers* produced after their interaction. Air showers are particle cascades generated by the interaction of a single high-energy cosmic ray with the atmosphere. First, the newly created particles further produce more particles in a combination of hadronic, electromagnetic cascades, and weak interactions; enhancing the shower size, until these fall below the threshold for further particle production [24]. Some of these particles would reach the Earth's surface, where they can be detected by sparsely located detector stations¹, with the energy of the original cosmic-ray particle reconstructed from the size of the footprint detected on the Earth's surface [35].

2.3 Neutrino sources and astrophysics

Neutrinos are produced after several different nuclear processes and, as such, have a wide variety of possible sources, some within Earth and others coming from outside the universe. Although neutrinos produced in Earth², such as *reactor neutrinos*, are of great interest for particle physics studies such as neutrino oscillations, within the context of neutrino astrophysics the interest is focused on neutrinos produced in the outer space and reaching Earth or in neutrinos produced after the interaction in Earth and its atmosphere of cosmic rays. This section outlines some sources of neutrinos, excluding less relevant sources for the studies carried out in this thesis.

2.3.1 Solar neutrinos

The center of our planetary system is also a great neutrino source. These neutrinos have typical energies from keV to MeV. The majority of neutrinos produced in the Sun are generated via the interaction [37]

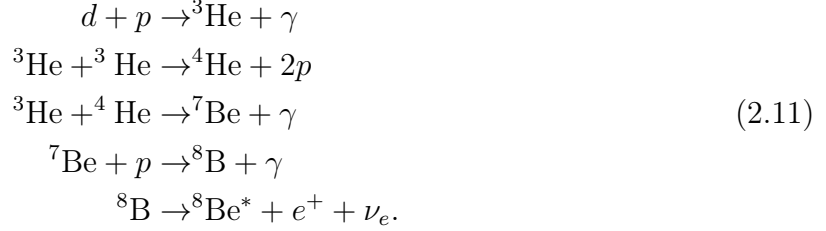


known as *proton-proton chain*, where d is a deuteron particle (${}^2\text{H}$). However, these neutrinos have energies below MeV, which is typically below the threshold of neutrino

¹Antennas are also used to detect the radio emission of the shower.

²Indeed the Earth itself can be considered as a natural reactor, emitting electron antineutrinos after β decays from its mantle and core [36].

experiments based on the Cherenkov effect using water or ice¹. Higher energetic neutrinos are produced in the Sun from a chain reaction after the proton-proton chain, in which the deuteron particle is further merged with another proton and later with heavier particles, following² [38]:



The last β^+ decay of ${}^8\text{B}$ is reached only by 0.02% of all proton-proton reactions; however, this produces neutrinos with energies as large as tens of MeV [39], which are usually detected by neutrino experiments and are often subject to neutrino oscillation studies, while in other cases they form part of the background for other studies. As indicated before, studies with solar neutrinos were the first hint of neutrino oscillation and have been used to determine the oscillation parameters involving the mass eigenstates 1 and 2 [18].

2.3.2 Atmospheric neutrinos

As introduced before, the interactions of cosmic rays in the atmosphere also produce neutrinos. The primary source for neutrino production is the decay of pions and kaons as [3]

$$\begin{aligned}
 \pi^\pm &\rightarrow \nu_\mu(\bar{\nu}_\mu) + \mu^\pm(\sim 100\%), \\
 K^\pm &\rightarrow \nu_\mu(\bar{\nu}_\mu) + \mu^\pm(\sim 63.5\%),
 \end{aligned}
 \tag{2.12}$$

together with the muon decay afterwards [3]

$$\mu^\pm \rightarrow e^\pm + \nu_e(\bar{\nu}_e) + \bar{\nu}_\mu(\nu_\mu),
 \tag{2.13}$$

resulting in a *conventional* atmospheric neutrino spectrum flavor ratio of 1:2:0³.

Some atmospheric neutrinos reaching Earth detectors might come directly from the zenith, but others would have traversed Earth. The composition of the detected atmospheric neutrino ratio depends on their path from generation to its interaction vertex within the detector. Oscillation analysis, such as that performed in DeepCore [40], the low energy subarray of IceCube, often separates the detected atmospheric neutrino spectrum into reconstructed energy and directions. From their direction, their path traversing the Earth can be calculated, and thus the probability that such a neutrino would have oscillated.

¹See Section 3.2 for more information on Cherenkov-based detectors.

²This decay scheme only shows the most important production mode for neutrinos in the context of large neutrino telescope. The entire solar neutrino generation scheme is more complex.

³Indicating the ratio between $\nu_e : \nu_\mu : \nu_\tau$ with no distinction between neutrino and antineutrinos.

This requires a detector capable of reconstructing the initial neutrinos with very good accuracy and the collection of sufficient data. These studies can help determine Δm_{32}^2 and the mixing angle θ_{23} . The energy spectrum of atmospheric neutrinos resembles that of cosmic rays, as they are produced by them. The spectrum features a cutoff for high energies, when muons do not decay in flight and reach the Earth's surface. These surviving muons are often detected in neutrino experiments and can be a source of background noise in such studies.

2.3.3 High energy astrophysical neutrinos

Cosmic neutrinos are those generated by cosmic rays in particle accelerators, featuring energies as high as PeV and beyond [1]. Mesons are produced via proton-proton collisions in cosmic accelerators, as introduced before, or via their interaction with photons generated by synchrotron radiation of electrons, producing Δ^+ resonances (see Eq. 2.9) if their energy is large enough. These mesons, mostly π^\pm, π^0 produced in the same amount, generate neutrinos after decaying with a flavor composition at the source of 1:2:0¹. After flavor mixing, flavor composition should be close to 1:1:1 at Earth [42].

The study of distant sources in the universe using high-energy neutrinos has some advantages over other messengers. Unlike cosmic rays, they do not get deflected by magnetic fields from the source to Earth; thus, they essentially function as a *smoking gun* signature of cosmic ray acceleration [36]. High-energy photons also do not get deflected by magnetic fields, however they are not always a sign of hadronic acceleration and, furthermore, the Universe becomes optically thick for high-energy photons, being attenuated after *short* distances [43]. This is depicted in Figure 2.4, where it can be seen that, using high-energy photons, only as far as the nearest galaxy can be studied. Since these neutrinos are generated after decay of mesons in cosmic accelerators, the identification of high energy neutrino sources can reveal the origin of cosmic rays [1].

Detectors sensitive to these high-energetic neutrinos have been successfully built in recent decades, and their working principles are explained later in Chapter 3. After the first detection of high-energy neutrinos of extraterrestrial origin in 2013 [44], studies try to resolve the high-energy neutrino sky and determine their sources. Fundamental physics is also studied using these neutrinos, such as cross section measurements at high energies or searches for new physics [36]. The most prominent candidates for high-energetic neutrino sources are the following:

- **Active Galactic Nuclei (AGN):** the most steady luminous objects of electromagnetic radiation in the Universe, AGN are massive rotating black holes in the center of galaxies, surrounded by an accretion disc and two highly collimated relativistic jets perpendicular to the disc plane [45, 46]. These jets are believed to accelerate charged particles to extremely high energies [46]. Evidence of high energetic neutrinos has been found from the γ -ray blazar² TXS 0506+056 for the first time in coincidence with a gamma-ray flare from the source [47]. Recently, an excess from the background at the level of 4.2σ

¹This is strictly true only in pion sources, with purely hadronic processes. Other sources are possible that produce neutrinos with different flavor compositions, such as muon-dumped sources or neutron sources [41].

²A blazar is a AGN in which the relativistic jet points toward Earth.

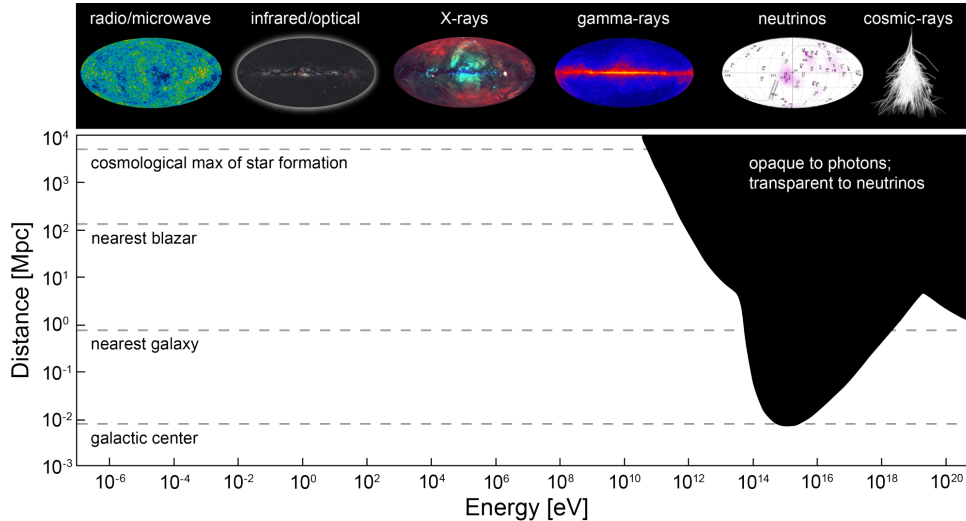


Figure 2.4: Representation of the distance horizon at which the universe becomes non-transparent to photons as a function of its energy. Figure from IceCube public repository.

was found associated with NGC 1068 galaxy, which provided further evidence in favor of AGN as possible neutrino sources [48].

- **Supernova Remnants (SNRs):** diffuse, expanding nebula result of a supernova explosion, with an expanding shock wave of ejected material. The expansion of SNRs can take thousands of years, and they are believed to be the main source of cosmic rays above the *knee* [49]. The collision of the ejecta with the interstellar medium produces a shock front, where particles can be accelerated and high-energy neutrinos can be produced [1].
- **Micro-quasars¹:** miniature analog of quasars [50], active galactic nuclei featuring a binary system of a neutron star or black hole and an ordinary star. The compact object is surrounded by an accretion disk and relativistic jets, where charged particles can be accelerated to high energies [1].
- **Sources of gamma-Ray bursts (GRBs):** GRBs are transient events characterized by an extremely intense emission of gamma rays lasting from milliseconds to several minutes [51]. They are produced by the most cataclysmic phenomena in the universe, such as hypernovae² or binary mergers of compact objects, such as black holes or neutron stars, in which relativistic jets are produced that are the source of GRBs and potentially also neutrinos [1].
- **Starburst galaxies:** galaxies undergoing large-scale star formations, with an ejecta galactic-scale wind produced by the collective combination of supernovae and winds from massive stars, are potential candidates for high-energy cosmic rays and neutrinos [1].

¹Also known as radio emitting X-ray binaries

²Core collapse supernovae with high masses above 40 or more solar masses.

2.3.4 Neutrinos from Core Collapse Supernovae

Core-collapse supernova (CCSN) explosions are among the brightest and most energetic events in the Universe. These explosions are generally the last processes in the evolution of massive stars, and most of the energy released by CCSNe is in the form of neutrinos, which are believed to play a key role in triggering the explosion itself [52]. These powerful events are introduced in this section and are the subject of study in Chapter 6.

Supernova (SN) explosions have historically been classified according to the spectral analysis of their light curve¹, mainly due to the absence (type I) or presence (type II) of hydrogen spectral lines, and each type can be further categorized into groups depending on their light curve [53]. Here, the main focus is on type-II SN - gravitational core-collapse supernovae, since this is what is going to be used for simulations in Chapter 6. Type-II are one of the most interesting phenomena from the point of view of a neutrino telescopes, since $\sim 99\%$ of the released energy is in the form of neutrinos, while $\sim 1\%$ is ejected matter and $\sim 0.01\%$ photons [52]. Not only that, but these neutrinos are produced in the core of the star, thus their study can reveal direct and immediate information about the supernova *engine*. Furthermore, as stated before, it is currently believed that these explosions are not possible without the influence of these neutrinos [52]. But how can such a tiny, weak-interacting particle be a key component triggering such a powerful event?

Neutrinos and CCSNe have been closely related since, in 1987, a CCSN was detected in the form of a neutrino flux prior to the event being visible in the sky. This CCSN, named SN1987A, exploded in the Large Magellanic Cloud, a satellite dwarf galaxy of the Milky Way at about ~ 50 kpc from us. Three different neutrino observatories were successful in detecting a total of 25 neutrinos emitted during the explosion, 12 by the Kamiokande neutrino detector [54], 8 by the IMB detector [55] and 5 by the Baksan scintillation telescope [56], with energies in the range of tens of MeV. 30 years later and with no other detection of a CCSN neutrino burst, these events are still not fully understood. Neutrino detectors around the world are prepared and waiting for the next detectable supernova, whose rate in our galaxy is estimated between 1 and 3 per century [57].

To understand the current theory about the development of CCSNe, it is necessary to first understand the star evolution. Stars are formed after huge clouds of the interstellar medium, mostly hydrogen and helium, gravitationally collapse. The density and pressure in its interior increase, and at a density of $\rho \approx 10^{-13} \text{g cm}^{-3}$ the cloud becomes opaque to photons, the temperature inside the cloud rises, and the so-called *proto-star* is formed, which still attracts matter from the surrounding medium. The density and matter of the proto-star continuously increases due the matter accretion over the next million years. When the temperature in the core of the star exceeds $\sim 3.5 \times 10^7$ K, hydrogen starts to fuse to helium. A new star is born.

The star is constantly getting hotter and denser, and the continuous action of gravity is compensated for by the nuclear fusions in the core establishing hydrostatic equilibrium. The life of stars undergoes a well-defined series of nuclear burnings by which the elements in the core become heavier, whereas energy escapes the star mostly in the form of photons and neutrinos. Heavier nuclei need more energy for further fusion; thus, to maintain the equilibrium, the burning rate also increases. The fusion processes for heavy stars end when the inner core is mostly formed by ^{56}Fe [58], since the production of heavier nuclei

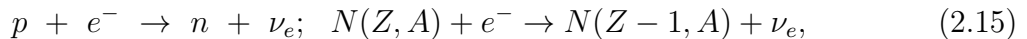
¹Brightness of the SN over time.

by fusion is not energetically favorable¹, triggering the collapse of the core.

Once the collapse of the core starts, the compression rapidly increases the temperature, enabling photons to dissociate iron into α particles and neutrons as



further compressing the core [60]. The high pressure in the core makes electrons form a degenerate electron gas. Due to the Pauli exclusion principle, as more electrons occupy the same volume, their energy level raises [61]. With sufficient compression, electron capture over protons and nuclei occurs:



by which the electron density is reduced in a process known as *deleptonisation* [61]. The core eventually collapses if the Chandrasekhar mass limit is exceeded. The Chandrasekhar mass limit indicates the threshold at which the core cannot stand the gravitational pressure and will collapse into a CCSN. This limit depends on the electron density, but also the reduction of the ratio of electrons to barions simultaneously reduces the Chandrasekhar limit. In cases where the core of the star is not massive enough, the pressure of the degenerate Fermi gas stops the collapse, resulting in a white dwarf, which is the general scenario for stars heavier than ~ 8 solar masses. Otherwise, the star keeps collapsing, further increasing the electron energy and the rate of electron capture [53].

When densities reach as high as $\rho \approx 10^{14} \text{ g cm}^{-3}$ [60], most neutrinos can no longer escape from the core due to their interactions with neutrons and protons. This phase is named *neutrino trapping*, in which neutrinos are pulled toward the core along the matter. The process takes a fraction of a second since the electron-to-neutrino conversion is further accelerated with increasing compression of the core. Finally, at densities near $\rho \approx 6 \cdot 10^{14} \text{ g cm}^{-3}$ [60], nuclear repulsive forces between the nucleons abruptly stop the collapse of the core. The still falling matter bounces back, and, in response, a shock wave colliding with the still falling plasma is created, which is called *core bounce*. The shock loses its energy in only a few milliseconds and is maintained from falling inward by the pressure of the degenerate Fermi gas from the core, resulting in a dense layer of buoyant matter [62, 63].

At this stage is when neutrinos are believed to play an important role in the explosion. Neutrinos are now escaping the core and find the dense buoyant layer on their way, some of them depositing their energy there, interacting mostly by charged-current neutrino-antineutrino capture of free nucleons. The huge flux of neutrinos at this stage is capable of restarting the expansion of the shock front in what is known as the *accretion phase*, eventually resulting in the supernova explosion² [62, 60, 63].

¹This is a generalization. The nucleus with the highest binding energy per particle is ${}^{62}\text{Ni}$, however the competition between fusions and the photodesintegration induced by γ rays produces the isotope ${}^{56}\text{Ni}$ in more abundance than ${}^{62}\text{Ni}$. ${}^{56}\text{Ni}$ then undergoes two β^+ decays that end in ${}^{56}\text{Fe}$ [59]

²The role of neutrinos reviving the stalled shock wave was found by accident by Jim Wilson (Lawrence Livermore National Laboratory). Models back then failed to produce the explosion. On a Friday evening, he forgot to turn off an apparently failed simulation before the weekend. When he returned to his computer on the next Monday, he found that the model had exploded much later than expected.

During this phase, (anti-)neutrinos of all flavors are produced mostly from the annihilation of electrons and positrons as $e^+ + e^- \rightarrow \nu + \bar{\nu}$. Neutrinos escaping from the proto-neutron star cool it down, releasing 99% of the binding energy in approximately 10 s [53], but photons will still need a few hours to escape the star. Thus, a CCSN may potentially be detected first by neutrino telescopes, allowing them to alert other telescopes about it. Furthermore, neutrinos are produced within the inner core of the star and give the final push to the SN explosion; thus, their study can reveal the physics behind these spectacular events.

After the core collapse, the resulting star will be either a neutron star or a black hole, depending on the progenitor mass and metallicity. Generally, progenitors below 30 – 40 solar masses end up in a neutron star, whereas the outcome of heavier CCSN progenitors is generally a black hole [53]. These objects are far from *dead* and are still of great interest in astronomy. They can, for example, interact with other celestial bodies, generating powerful events and interesting physics scenarios, such as the one described in the next section.

2.4 Compact binary mergers and multi-messenger astrophysics

Due to their initial momentum or the action of gravity, heavy massive objects in the Universe may approach each other. When two astronomical bodies are gravitationally bound, the result consisting of both bodies rotating around a barycenter¹ is known as a binary system [64]. Binary systems can be formed by any two celestial bodies, even including galaxies. Here, the focus is set on binary systems of neutron stars (NSNS), black holes (BHBH), or a black hole with a neutron star (BHNS). The collapse of these massive gravitationally bound bodies is known as a compact binary merger. This occurs because, as the two objects in the binary system orbit each other, they lose energy in the form of gravitational waves, causing them to spiral inward. Eventually, the two objects may merge into a single, more massive object [64]. In recent years, the study of these cosmic events has undergone a revolution with the use of gravitational wave (GW) detectors such as LIGO [65], Virgo [66] or Kagra [67].

General relativity predicted the existence of gravitational waves a hundred years ago. The first direct gravitational wave detection did not occur until 2015, when the LIGO-Virgo Collaboration detected a transient gravitational wave signal matching the expectations from a merger of a binary system composed of two black holes into a single, heavier one [68]. Since then, many other detections have been made [69]. GW are the propagations at the speed of light of perturbations in space-time. GW detectors feature a large complex laser Michelson interferometer, in which the length of at least two arms is precisely monitored². The passing of a gravitational wave through the detector causes small changes in the length of one or both arms, which can be measured by the interferometer if the space-time perturbation is strong enough.

¹The baricenter is the center of mass of the system, and in cases where one component of the system is much heavier than the other, it might be located within the heavier object itself.

²Not the only method to detect gravitational waves, but so far the most successful one. Future detectors, such as the Einstein telescope, plan to build arms forming a triangular shape. This enables to fully characterize the position and polarization of detection without the need for two detector facilities [70].

Currently, the LIGO/Virgo Collaboration announces a new GW wave signal detection almost weekly [71]. GWs from all mergers described above have already been confidentially identified by the Ligo/Virgo Collaboration [72]. In 2017, the detection of the gravitational wave event known as GW170817 could be associated with an electromagnetic counterpart, opening a new era of multimessenger astrophysics [73]. Multimessenger astrophysics is the coordination of different detectors measuring the same event or cosmic object using different *messengers*, as it can be the use of photons of different energies, cosmic rays, neutrinos and/or gravitational waves. Each different messenger might carry inherent complementary information of the event, as well as confirmation of, e.g., the event type. For instance, the progenitor masses and distance of the event GW170817 were identified from the GW detection, as well as a constrain on the NS equation of state could be set from these observations. The associated γ and X-ray observations confirmed that it was an off-axis short gamma ray burst, and optical observations identified the merger as a Kilonova [74]. Another example of multi-messenger detection is the neutrino event associated with the gamma-ray flare from the blazar TXS0506+056 at the 3σ level [47].

At the time of writing, no neutrino detection has been observed in association with a reported GW event, nor in the low- or high-energy regime [75, 76]. In Chapter 8, the possibility of the future IceCube Upgrade for detecting a GeV neutrino flux from a compact binary merger is studied.

Neutrino detection at the South Pole

As introduced in the previous chapter, neutrinos are particularly useful for studying the universe because they interact very weakly with matter, which means that they can pass through space undisturbed, providing information about objects and processes that are otherwise difficult to study. However, this also makes their detection challenging. This chapter introduces the working principles of neutrino detectors based on the Cherenkov effect, focusing on IceCube, a neutrino detector located in the South Pole.

3.1 Neutrino interactions

Neutrinos interact only through weak force or gravity. Their tiny mass makes it impossible to detect them gravitationally, so one has to rely on them interacting through the weak force and then measure the secondary particles generated from that interaction. These secondaries then travel through the medium, interacting and generating further particles that can be used to reconstruct the energy and direction of the initial neutrino.

Weak interactions can be divided into Charged Current (CC) or Neutral Current (NC) interactions. In the first, a W^\pm boson is exchanged, which involves the transfer of electric charge. In NC interactions, the exchanged boson is a neutral Z^0 boson. Figure 3.1 shows the CC cross sections of the neutrino and antineutrino interactions as a function of energy for the most important interactions within 0.1 GeV and 500 GeV. At energies $\lesssim 1$ GeV quasi-elastic scattering is the main interaction¹, in which the neutrino scatters with the whole nucleon. Resonance production is the dominant interaction at a few GeV, producing baryonic resonances such as Δ , which further decay [77]. Deep inelastic scattering (DIS),

$$\bar{\nu}_l^{(-)} + N \longrightarrow l^\mp + X(\text{CC}) \quad (3.1)$$

$$\bar{\nu}_l^{(-)} + N \longrightarrow \bar{\nu}_l^{(-)} + X(\text{NC}) \quad (3.2)$$

is the predominant interaction beyond ~ 50 GeV, and as such, high energy neutrino telescopes often focus on the detection of this interaction [1]. Here, l denotes a lepton of any flavor and N represents a nucleon. The resulting X stands for one or more hadronic particles. These cases are represented in Figure 3.2. The outcomes of these interactions are different depending on the neutrino flavor and/or the branch of the weak interaction. The neutral current interaction results in a hadronic shower that can be detected by neutrino

¹In this thesis, the MeV neutrinos from CCSN bursts are the subject of study in Chapter 6. The dominant interaction channels at MeV energies are introduced in Section 6.1.

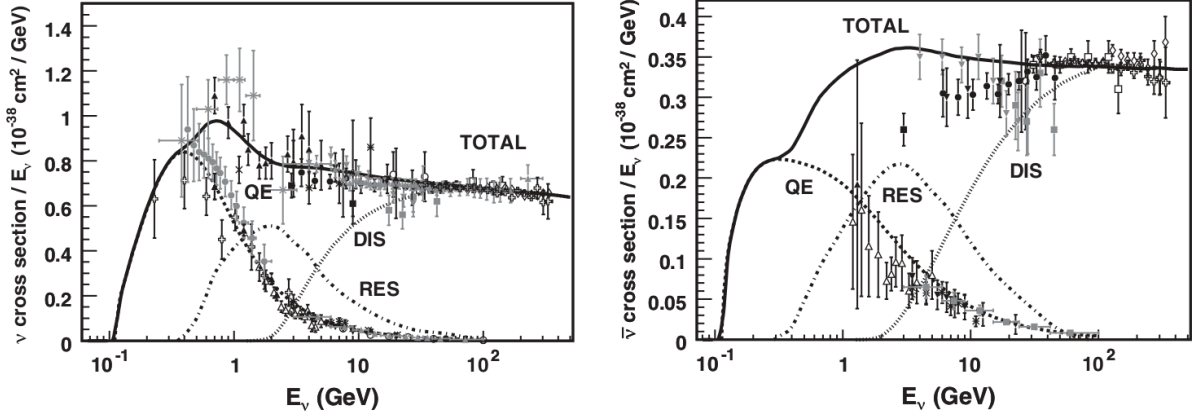


Figure 3.1: Cross section (data and prediction) divided by the neutrino energy of CC interaction of neutrinos (**left**) and antineutrinos (**right**) as a function of energy. The contributions from quasi-elastic scattering (QE, dashed), resonance production (RES, dot-dashed) and deep inelastic scattering (DIS, dotted) are shown. Values for QE scattering are averaged over proton/neutron targets. Figures from [77].

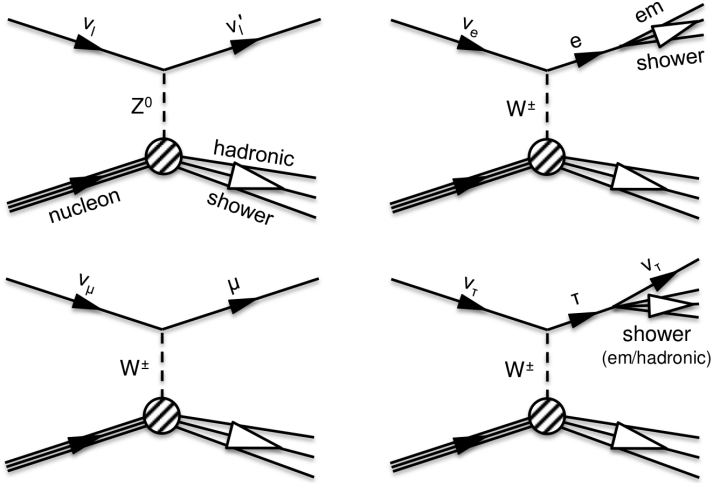


Figure 3.2: Artistic representation of deep inelastic scattering of neutrinos with nucleons in matter. **Top left** figure features the neutral current interaction by any neutrino flavor, while remaining figures show the charged current interactions of each flavor individually. Figures from [78].

telescopes; however, after the neutrino interacts through charged current weak interaction, not only the hadronic shower can be detected, but also the corresponding lepton to the incoming neutrino. Furthermore, these leptons may induce different patterns in detectors, which can be used to identify the flavor of the incoming particle. This is expanded upon later, when IceCube is introduced and the different signatures of each interaction in the detector are showcased. First, the working principles of Cherenkov-based detectors are introduced in the next section.

3.2 Cherenkov-based detectors

Several methods have been used to measure the secondary particles generated after neutrino interactions. Detectors such as MINOS [79] or NO ν A [80] make use of scintillators to detect charged particles produced by neutrino interactions, while other detectors such as GALLEX [81] use Gallium-containing mediums and look for an excess of Germanium

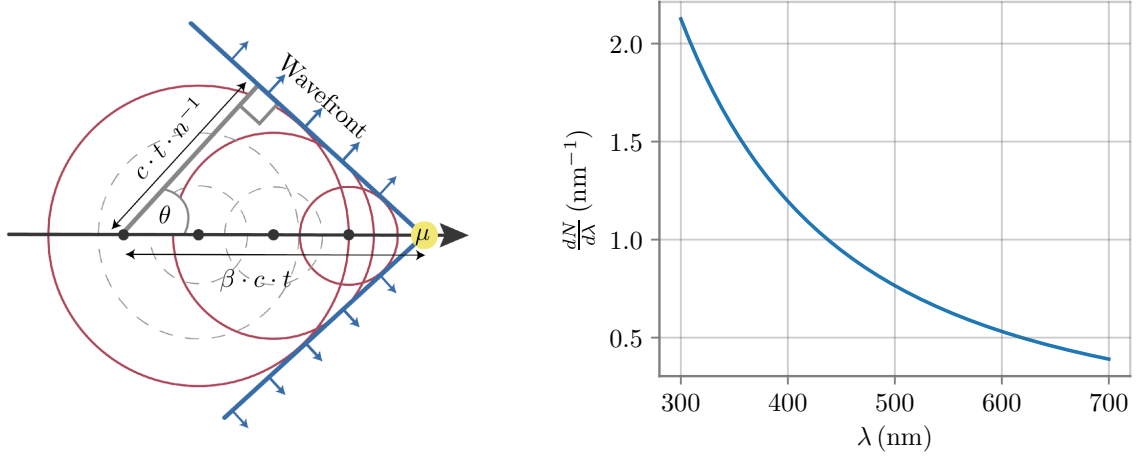


Figure 3.3: **Left:** Sketch of the Cherenkov effect produced by a muon in a dielectric medium of refractive index n . Image from [84]. **Right:** Cherenkov yield induced by a muon travelling $\Delta x = 1$ cm through ice, assuming constant $n = 1.31$ and $v \approx c$.

generated after a neutrino interaction. However, the most common way to detect neutrinos is by using the *Cherenkov effect* or *Cherenkov radiation*, named after its first discoverer¹[82]. The Cherenkov effect occurs in a dielectric medium when a charged particle of sufficient energy travels through it. Generally, it is sought to isolate the medium to identify secondary charged particles produced by the interaction of a neutrino. Due to the very low cross section of weak interactions, a large sensitive volume is an essential feature for neutrino detectors to increase the probability of interactions in it. Detectors based on the Cherenkov effect have the advantage that transparent dielectric mediums are abundant on Earth, and these can be instrumented to form large detectors.

A dielectric medium is defined as an electrical insulator in which electric dipoles can be created under the influence of an external electric field, such as the passage of a charged particle through it [83]. As the particle moves, the polarization region moves along it. The polarization is then spherically symmetric about the particle's position, so at any given distance from the particle there is no resulting field. However, if the particle is moving faster than the speed of light in the medium, the perturbation cannot propagate through the medium fast enough for this symmetry to be maintained. This way, the interference of the dipoles radiation is no longer destructive, and net radiation is emitted in the form of a coherent shock wave. A schematic image of this effect is shown in Figure 3.3 (left). Radiation is emitted, forming a cone around the trajectory of the particles, with an opening angle depending on the velocity of the particles v and the refractive index of the medium n

$$\cos \theta = \frac{1}{n\beta}, \quad (3.3)$$

with $\beta = v/c$, c being the speed of light in vacuum. The energy emitted through Cherenkov effect can be approximated, neglecting quantum mechanic corrections, by the Frank-Tamm formula (in Gaussian units) [3, 85]:

¹Also written as Čerenkov or Cerenkov

$$\frac{dE}{dx} = \frac{q^2}{c^2} \int \left(1 - \frac{1}{\beta^2 n(\omega)^2} \right) \omega d\omega, \quad (3.4)$$

with ω being the angular frequency and q the charge of the passing particle. Hence, the amount of energy induced by Cherenkov effect increases with the energy and charge of the particle traveling through the medium. Equation 3.4 can be alternatively expressed as [3]

$$\frac{d^2N}{dx d\lambda} = \frac{2\pi\alpha z}{\lambda^2} \left(1 - \frac{1}{\beta^2 n^2} \right), \quad (3.5)$$

N being the number of emitted photons, α the fine-structure constant, and z the atomic number of the particle. From equation 3.5, the number of photons emitted by a particle passing through a medium is calculated and shown in Figure 3.3 (right) for the case of a muon traveling a distance $\Delta x = 1$ cm through IceCube with $v \approx c$. Around 370 photons with wavelengths between 300 and 700 nm are produced by a muon at super-relativistic speed traveling through ice, and a similar result is obtained for water since the refractive indexes are similar. Note that the refractive index of the phase velocity depends on the wavelength and, in the case of IceCube, on the depth due to changes in ice structure. For this exemplary case, it has been simplified to a constant value of $n = 1.31$.

Cherenkov-based detectors use photosensor devices to detect this light. If the sensitive volume is large, allowing the charged particle to travel several meters, abundant light is emitted, which can be used to identify the particle. If the light emitted from a single interaction is detected by several photosensitive devices, the interaction vertex and ultimately the information of the incoming neutrino, such as direction, energy, or interaction channel, can be reconstructed. From generation to detection, photon paths can be altered by scattering processes. They can also be absorbed before reaching any photosensitive device and be lost. Thus, the quality of the neutrino reconstruction depends on the quality of the propagation medium, as well as the quality and distribution of the photosensor devices, which usually consist of photomultiplier tubes (PMTs).

Cherenkov-based detectors can be classified into two groups, depending on how the PMTs are distributed and the scientific objective of the detector itself. On the one hand, some detectors place the PMTs side by side, covering almost entirely the walls of the sensitive volume. This arrangement aims to obtain a detection pattern in which the Cherenkov cone is distinguishable. These detectors are usually aimed at detecting neutrinos in energy ranges from hundreds of keV to a few GeV and are focused on oscillation studies, supernova neutrino studies, solar neutrinos, or dark-matter searches, among others. A picture and detection signature display of one of these detectors, Super-Kamiokande [86], is shown in Figure 3.4. On the other hand, some Cherenkov-based detectors distribute the PMTs sparsely to cover a much larger volume. In these detectors, it is not possible to fully observe the Cherenkov cone as in Figure 3.4 (right). Instead, the detection forms a pattern that is distributed along the different photomultipliers, allowing particles traveling through the instrumented volume to be tracked. Therefore, these detectors are optimal for detecting and reconstructing higher energetic neutrinos from tens of GeV to EeV, and are ideal for astrophysical studies using neutrinos as messengers. The IceCube detector falls into this category and is shown in more detail in the following sections.

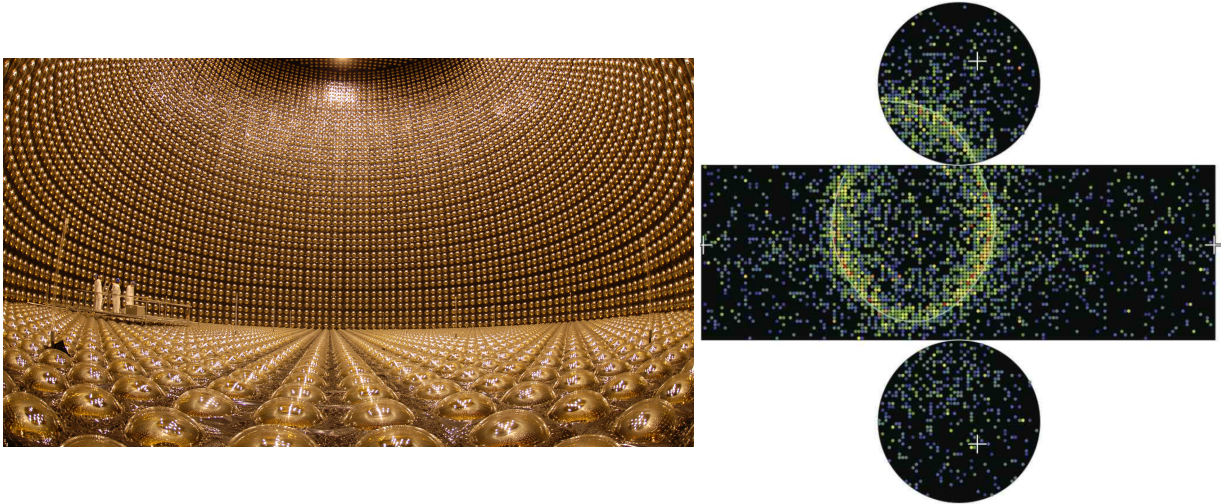


Figure 3.4: Left: Photo of Superkamiokande detector [86] before it was filled with water. Photomultipliers cover the walls of the detector almost entirely. Image from [87]. **Right:** Detection pattern of a typical neutrino interaction in Super-Kamiokande. Each colored bin stands for a photomultiplier detecting light, with the color scaling from blue to red with the charge detected in that PMT. The circular pattern clearly resembles the Cherenkov-like cone light emission. Picture from [88].

3.3 The IceCube Neutrino Observatory

The IceCube Neutrino Observatory [89] is a large-scale particle physics experiment located in Antarctica, at the geographic South Pole, successor of AMANDA¹ [90]. With the main goal of locating the sources of high-energy neutrinos, the detector embeds modules containing photosensor devices and the corresponding read-out electronics in the ice. On the surface, the data measured by these modules are collected and sent to the different institutions that form the IceCube Collaboration for its posterior analysis [89].

IceCube is currently the largest neutrino detector in the world, instrumenting 1 km^3 of glacial ice. It was built over the course of 7 seasons by drilling deep holes in the ice, where optical modules, cables, and calibration systems are deployed before the holes are refrozen again. Due to the extreme climatological conditions at the South Pole, construction work was only possible during the austral summers [91]. The detector consists of a main in-ice array of Digital Optical Modules (DOMs), which contains a more densely instrumented subarray named *DeepCore*, and the surface array *IceTop*. The modules are connected to two cable towers in the IceCube Laboratory (ICL), located on the surface in the central part of the detector. ICL houses the server room, where all data acquisition and online filtering takes place [89]. The detector layout is shown in Figure 3.5. The first ~ 1450 meters of glacial ice are not instrumented and are instead used as an external radiation shield. The detector ends ~ 400 m above the bedrock, where the glacier rests.

¹Antarctic Muon And Neutrino Detector Array

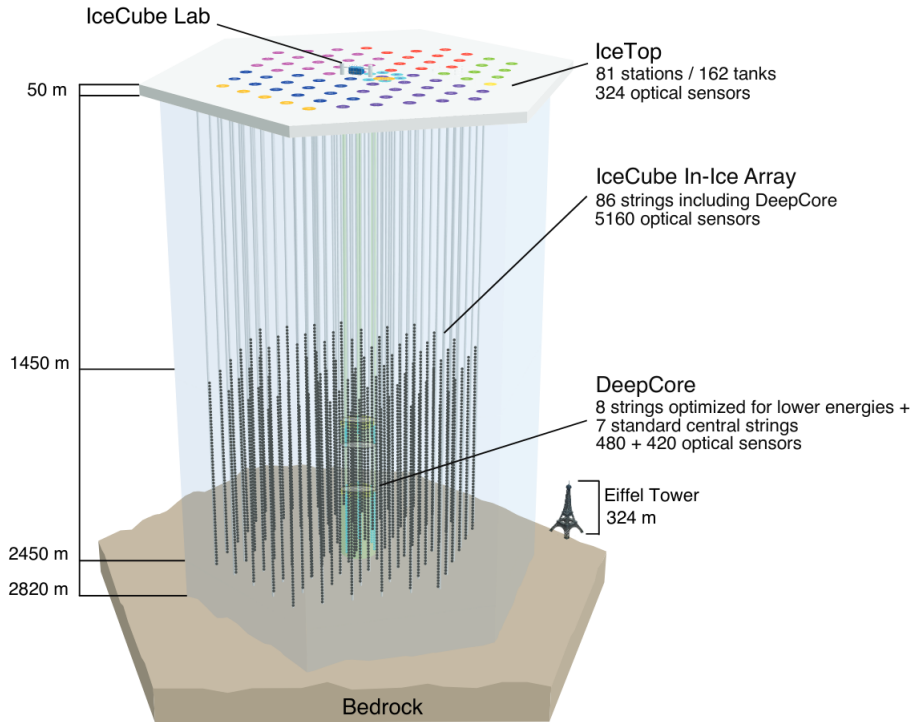


Figure 3.5: IceCube Neutrino Observatory detector layout, showing the in-ice array, the sub-array DeepCore and the cosmic-ray air shower array IceTop. The different string colors represent different deployment seasons. In the side, the Eiffel tower is illustrated for size comparison. Drawing from the IceCube internal repository.

3.3.1 IceCube high energy in-ice array

IceCube’s modules are connected forming vertical columns named strings. The primary in-ice array consists of 78 strings equipped with DOMs deployed between 1450 and 2450 m depth¹, featuring an inter-module spacing of 17 m. The strings draw a hexagonal footprint on a triangular grid on the surface with an inter-string distance of about 125 m. This detector design is optimized for detecting and reconstructing neutrinos in the TeV to PeV range, although it is capable of reconstructing neutrinos from ~ 100 GeV [89]. The distance between modules determines the optimal energy range in which the detector would operate, since events must be detected in several modules to enable reconstruction and subsequent analysis.

The outermost modules can also be used as a veto region in the analyses to determine whether the detected event interacted inside or outside the instrumented volume and be able to reject, for example, atmospheric muons. A schematic view of this veto concept is depicted in Figure 3.6. A muon generated outside the instrumented volume is probably detected first by the outer layer of modules, forming the veto region, and therefore can be rejected in IceCube analyses. In contrast, a neutrino interacting in the sensitive volume is likely detected first by a module of the inner volume.

¹Depth in IceCube is defined as the distance from the floor of the tower used for deployment of string number 21. The center of the detector is then at 1948.07 m deep, which is used as the origin of *IceCube coordinates*.

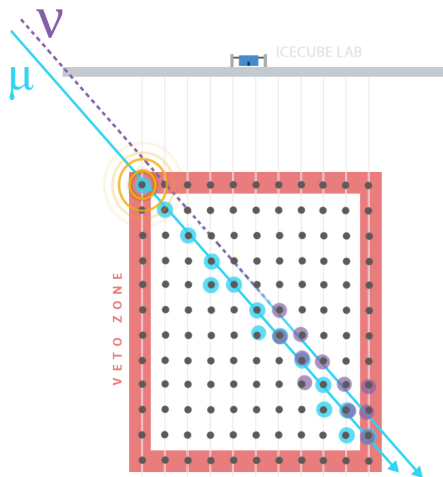


Figure 3.6: Scheme showing the functionality of the high-energy array veto region, indicated in red, representing the detection a muon and a neutrino as examples. Figure from IceCube internal repository.

3.3.2 DeepCore

DeepCore [40] consists of a subset of DOMs that form a denser instrumented region in order to increase the sensitivity to lower energetic neutrinos. This subarray is made up of eight strings located in the center of IceCube, with an interstring spacing that varies from 41 m to 105 m. DeepCore strings have a module distance within a string of 7 meters for the bottom 50 modules, which are deployed at depths between 2100 m and 2450 m, the region with the best optical properties. Additional 10 modules are deployed at depths shallower than 2000 m with a separation of 10 m, which act as a veto to better reject downgoing atmospheric muons. The *dust layer*, located between 2000 and 2100 meters depth, is known for its poor optical properties compared to other parts of the ice, hence it is not equipped with Deepcore modules (see Section 5.3 for more information on IceCube’s glacial ice optical properties). DeepCore analyses typically also use the seven closest strings of the high-energy array, and the rest of the detector as a veto to reject atmospheric muons [40]. A sketch of the DeepCore subarray is shown in Figure 3.7.

The modules in 6 of the 8 DeepCore strings are fully equipped with modules with 40% higher quantum efficiency (QE) than standard IceCube modules, while the remaining 2 strings contain a mixture of standard and higher QE DOMs. QE quantifies the probability that a photon reaching a PMT would be detected, thus these modules detect more light than typical IceCube DOMs. As a direct consequence, they also present higher noise rates. The denser instrumentation optimizes DeepCore for neutrinos with energies from 10 GeV to 100 GeV, which improves IceCube’s ability to identify neutrinos from WIMP dark-matter annihilation and to study atmospheric neutrino oscillations [89, 40].

3.3.3 IceTop

The IceCube surface array, IceTop [93], consists of 162 ice-filled tanks that are instrumented with photomultipliers. They are arranged in 81 stations following approximately the same grid as the in-ice array. It also contains a denser array formed by eight stations that

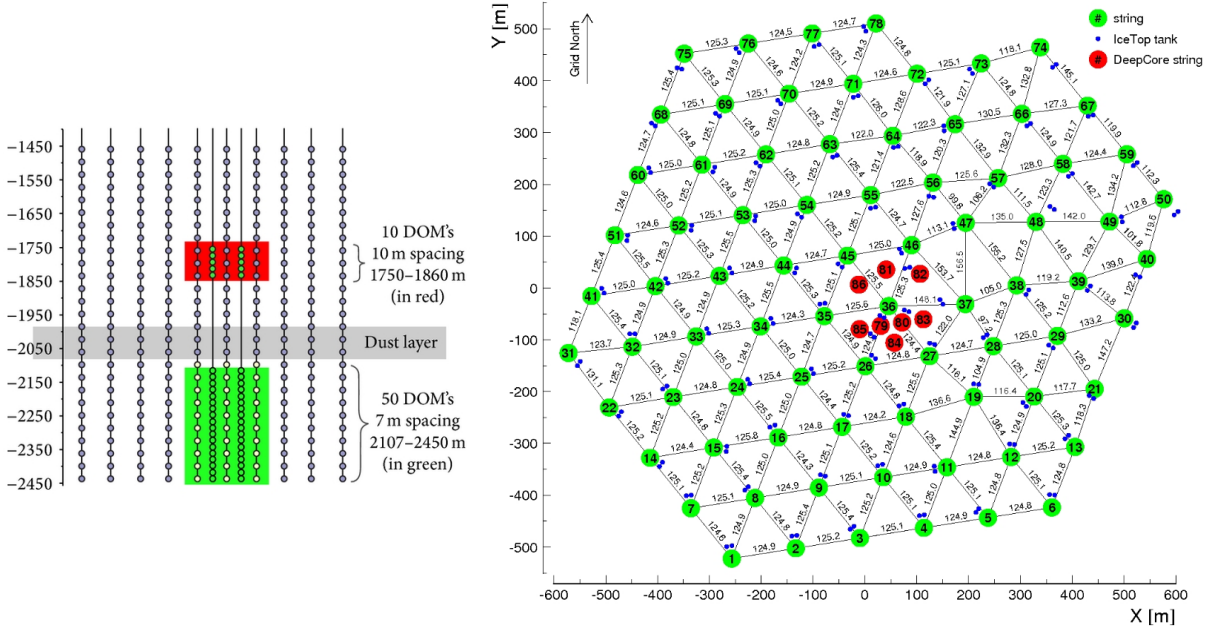


Figure 3.7: **Left:** Artistic side view of DeepCore, where position of the dust layer is marked. Figure from [92]. **Right:** Footprint showing the position of IceCube and DeepCore strings, as well as the position of IceTop tanks. Figure from IceCube internal repository.

correspond to DeepCore. The tanks in each surface station are separated by 10 m, each containing two standard IceCube DOMs, one of them operating at higher gain than the other, in order to increase the dynamic range for air shower detection [89, 93]. A schematic view of the position of the IceTop tanks is shown in Figure 3.7 (right).

IceTop measures cosmic-ray air shower particles (electrons, photons, muons, and hadrons) in the energy range of PeV to EeV with an energy resolution of 25% around 2 PeV, which improves to 12% above 10 PeV [94]. The detector aims to study the mass composition of primary cosmic rays by using the correlation between the shower energy measured in IceTop and the energy deposited by muons in the in-ice detector. The array has also been used to study high- p_t muons¹ and PeV gamma rays, as well as serving as veto for the detection of down-going events for IceCube [89, 93].

3.4 DOM: Digital Optical Module

The Digital Optical Modules, abbreviated as DOMs, are the devices designed for detecting the light produced by neutrino interactions in IceCube. Current IceCube DOMs are designed on the basis of the experience gained with the modules of AMANDA, using updated high-speed electronics design and manufacturing. A drawing and a photo of a DOM are shown in Figure 3.8. DOMs are composed of a single ~ 25 cm (10 inch) photomultiplier tube (PMT) of type Hamamatsu R7081-02 [96], which features low noise,

¹Muons with high transverse momentum produced from cosmic rays very early in the shower, and arrives to the detector separated from the shower core muon bundle [95].

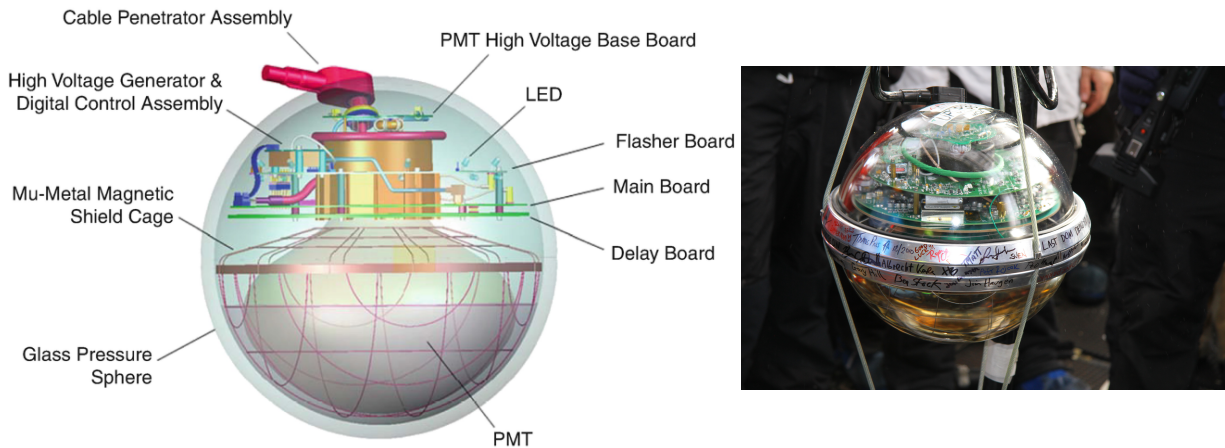


Figure 3.8: **Left:** Rendering of the IceCube DOM, where its main components have been labelled. Figure from [98]. **Right:** Photo of the last deployed DOM. Image from IceCube public gallery.

high gain, and fast timing [97]. The PMT is connected to the main board along with calibration devices and digital read-out electronics, and everything is enclosed in a glass vessel capable of withstanding pressures of 700 bar and temperatures as low as -55° [89]. The photomultiplier is shielded with a magnetic cage to ensure that the electron paths inside the tube are not affected by the external magnetic field.

Photomultiplier tubes (PMTs) are extremely photosensitive light detector devices that usually work in the range of the ultraviolet to visible light spectrum. A PMT consists of a photocathode; which converts photons into electrons, a focusing system which guides the electrons from the photocathode to the first dynode, a dynode system which creates an electron cascade from the initial input, and an anode which collects the final electron cascade. When a photon impacts the photocathode, a bound electron can be released through the photoelectric effect into the tube inner vacuum and guided to the first dynode. Then, the multiplication process increases the intensity by a factor of 10^6 before the cumulative electrons are read out at the anode [99, 100].

However, not every photon that reaches the PMT surface is detected. The final detection probability is a combination of the quantum efficiency (QE) and the collection efficiency. QE measures the probability that an electron is emitted from the photocathode after a photon reaches it, while the collection efficiency measures the probability that such an electron produces a cascade in the dynode system [99]. QE depends on the photon hit position and on its wavelength. In IceCube DOMs, this value peaks at about 25%, while higher QE DeepCore DOMs have values around 40% [101].

The DOM mainboard, located at the interior of the modules, is where the first step of the IceCube data acquisition system (DAQ) is performed, responsible for reading, digitizing, processing and buffering the PMT signals [97]. The flasher board, installed on the main board, controls the LEDs that are intended to perform calibration measurements. The module is connected to other modules in the string and, lastly, to the ICL. The PMT is attached to the glass housing vessel with optical gel, which maximizes the light transmission due to the close refractive index between gel and glass. The borosilicate glass vessel is made up of two half-spheres of diameter 33 cm, sealed under pressure at 0.5 bar [89]. The glass itself is an important source of background in IceCube. Like most materials, this

glass contains a small portion of radioactive nuclei, which can decay and consequently generate particles that can induce light generation through the Cherenkov effect, either in the glass itself (which is also a dielectric material) or in the ice. Furthermore, charged particles that arise from these decays also produce light through scintillation in the glass.

3.5 Calibration devices

IceCube also includes several devices that aim to calibrate the detector. Some of these devices are built into the modules, while others are external. They have not only helped understand the detector and its optical modules, but have also provided crucial information for different studies regarding the glacial ice. Here, some of the most important calibration devices are summarized:

- **LED flashers**

Each DOM contains a total of 12 LEDs connected to a flasher board. The light from these flashers can be detected by DOMs up to 0.5 km away. This system aims to calibrate different aspects of the detector, such as the detector geometry, time offsets, time resolutions, and linearity. They are also used to investigate the optical properties of ice and to test the reconstruction of cascade-like events [102].

The light profile of the LED has a Gaussian component with a standard deviation of $\sim 13^\circ$ in air, while about 10% of the light is emitted outside the Gaussian profile. The length of each pulse can be specified from 5 to 70 ns pulses [103].

- **Sweden cameras¹**

It has been observed that the optical quality of the refrozen ice after the modules had been deployed was not as good as that of the glacial ice, mostly due to the accumulation of air bubbles at the center of the refrozen column. This constitutes one of the largest sources of systematic uncertainties. To have a visual understanding of the ice, some cameras were installed during the construction of IceCube at the bottom of string number 80, one of them facing up and the other facing down with a distance of 6 meters [89].

The cameras are contained in two glass pressure vessels similar to the DOMs. They can move on two independent rotation axes, resulting in near 4π coverage. The pressure vessel also contains 4 white LEDs and 3 lasers [103].

- **Dust loggers**

Dust loggers were deployed in 8 IceCube boreholes to study the stratigraphy of the ice. They consist of a 404 nm laser line source and a small PMT located at the bottom of the logger. The light emitted by the laser can scatter back on the ice or its impurities and be detected by the PMT [104]. The results of these loggers provide the highest resolution stratigraphy in Antarctica to date [103].

- **Standard candles**

These light sources aim to reproduce the cascade-like signal with a more realistic angular emission distribution than LED flashers, improve cascade vertex reconstruction, and investigate the behavior of saturated PMTs [105].

¹Named after being developed in the University of Stockholm, Sweden

3.6 IceCube internal background

IceCube background can be either internal, from the detector itself, or external particles that reach the detector but are not the focus of the concrete study. This section focuses only on the internal background that originates in the detector itself, which is a general background source for any IceCube study. Since the Antarctic ice can be assumed to be radiation-free, the modules themselves are the main background source in IceCube. The background originated within the modules is mostly divided between PMT noise and radioactive decays that can occur in the modules' components, mostly in the glass of the vessel and the PMT.

PMT noise

Even in the complete absence of light, PMTs constantly produce a measurable signal. This is usually named **dark rate** when the PMT operates in pulse mode (as in the case of IceCube PMTs) or **dark current** when PMTs are operated in current mode. PMT noise is due to a combination of different effects, which might be detected randomly or triggered after a detection, therefore, time-correlated in the latter case [100].

The random background originates mainly from thermionic emission, field emission, leakage current, or radioactive decays in the photomultiplier itself [106, 100]:

- Thermionic emission: the main source of the background at room temperature, is caused from the spontaneous emission of electrons from the photocathode due to its thermal energy [106].
- Field emission: the effect by which electrons from the PMT electrodes are emitted by the internal electrostatic field present in the photomultiplier [106].
- Leakage current: current produced by the non-perfectly isolated materials in the tube, which flows into the anode or its pin [100].
- Radioactive decays: radioactive traces, mostly ^{40}K present in the photocathode glass can either directly produce ionizing particles that can hit the photocathode or generate light after their interaction that might be detected. This event, although random in nature, can produce correlated noise signals, such as scintillation effects, or induce further decays that would therefore be correlated with the first [100].

Correlated background is produced in relation to a detected pulse. These are pre-pulses, late pulses and after pulses [106, 99]:

- Pre-pulses: these pulses are produced after a photon crosses through the photocathode without being absorbed, and, instead, it hits the first dynode, where an electron is then produced. Since one dynode stage does not participate in the cascade multiplication, these pulses are usually smaller in amplitude [99]. These pulses are not strictly correlated, since the photon is simply not absorbed in the photocathode, and thus the standard pulse is not generated; however, it appears as a *correlated* peak in pulse-time distribution investigations with respect to the main peak (a few nanoseconds earlier, depending on the distance between the photocathode and the first dynode) [106].
- Late pulses: typically occur several nanoseconds after the initial pulse. These are caused mostly by photoelectrons that backscatter after hitting the first dynode. Then, they can

be redirected again towards the first dynode, therefore inducing a second cascade [99].

- After pulses: these signals, usually high in amplitude, can be measured a few microseconds after the initial pulses. They occur when photoelectrons ionize residual particles inside the tube. The charged ion is then accelerated towards the photocathode, releasing several photoelectrons [99, 106].

Radioactive decays originating in modules

Most of the internally generated background in the modules comes from radioactive decays that occur in the pressure vessel glass. The particles generated after these decays can induce light emission and thus be detected by the photomultiplier. The characterization of this background is therefore of great importance, especially in low-energy studies. These decays, as will be shown later, occur quite often, so it is not uncommon for neighboring modules to measure a signal coming from them at similar times, producing a signal that can resemble those created by low-energy neutrino interactions. This is also the main background affecting the analyses of CCSN neutrinos [107].

Radioactive decays produce light mostly after Cherenkov or scintillation effect. Cherenkov photons are emitted in just a few nanoseconds after decay, however scintillation may produce much delayed photon emission. Scintillation is defined in this context as the process by which light is emitted after a semiconductor (in this case, predominantly the vessel glass) is excited by the passing of high-energetic charged particles, such as alpha particles or electrons [107].

The dominant isotope in IceCube DOM vessel glasses is ^{40}K , which decays with a probability of $\sim 90\%$ by β^- to ^{40}Ca emitting an electron of $E_{\text{max}} = 1.33 \text{ MeV}$ and an antineutrino. The remaining 10% is electron capture, where a gamma of $\sim 1.4 \text{ MeV}$ is emitted after decay of the daughter nucleus. γ particles can interact with the medium generating charged e^-/e^+ , which consequently can induce light production in the medium through Cherenkov or scintillation. The proximity of the decay vertex to the PMT has the consequence that many photons might get detected almost instantaneously, producing a pulse of several photoelectrons in the photomultiplier [107, 84].

The rest of the radioactive contamination is mainly due to decays of the ^{235}U , ^{238}U , and ^{232}Th chains, featuring various isotopes of them. These chains contain decays α , β , and γ decays of different intensities and energies. These α feature a maximum energy of $\sim 5 \text{ MeV}$, below its threshold to induce light through Cherenkov effect in these mediums, however, they induce light emission via scintillation. When an alpha particle is stopped depositing its remaining energy, an electron from an atom might be emitted, known as delta-electron, which can also be detected [84, 107].

3.7 Detecting neutrinos in IceCube

Detected neutrinos in IceCube produce characteristic signatures in the detector, depending on their interaction. This section introduces the characteristics of neutrinos detection in IceCube, DeepCore, and some of the most important results of the detector.

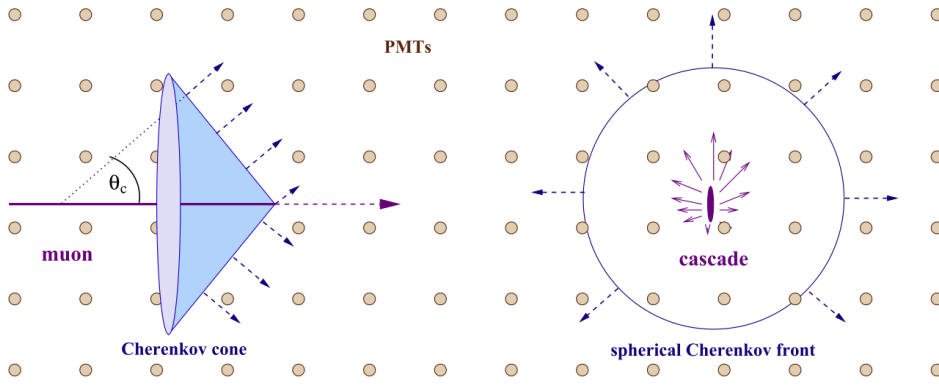


Figure 3.9: Schematic draw representing the detection of a muon track (**left**) or a cascade (**right**) in IceCube, being θ_c the Cherenkov angle. Figure from [1].

3.7.1 High energy events - IceCube

The IceCube high-energy array has a low energy threshold for event reconstruction of approximately 100 GeV, with optimal performance around 1 TeV. As mentioned before, deep inelastic scattering of nucleons in matter is the dominant interaction for neutrinos in this energy range. Depending on the interaction channel, shown in Figure 3.2, the detected signature may be different. This allows IceCube and similar detectors to classify the detected events into three different categories: tracks, cascades, and double-bangs. In all cases, a hadronic shower is produced at the interaction vertex.

Tracks

Tracks are produced by muons generated after a CC interaction $\bar{\nu}_\mu + N \longrightarrow \mu^+ + X$ (Figure 3.2, bottom left). The main characteristic of tracks is that they show an elongated detection pattern in the detector, with an initial cascade if the interaction occurs within the instrumented volume¹. A sketch of a muon track detection is shown on the left-hand side of Figure 3.9. The light front forms a cone with an opening angle equal to the Cherenkov angle. An example of a track detected in IceCube is shown on the left-hand side of Figure 3.10.

The elongated pattern allows for precise directional reconstruction. The direction of the outgoing muon is approximately $\langle\theta\rangle \approx 0.7^\circ/E_\nu[\text{TeV}]$ with respect to the initial neutrino angle. This means that reconstructing the muon direction can be used to trace the neutrino back and study its origin. Ultimately, this serves to study the origin of point sources and the production of such high energy neutrinos and cosmic rays [1]. IceCube has the ability to reconstruct tracks with a typical resolution of $\lesssim 1^\circ$ at 1 TeV [108].

These muons typically travel several kilometers through the ice [109]. Since most tracks are not fully contained in the instrumented volume, their energy reconstruction is less precise than fully contained event signatures. Although the muon deposits energy in the medium along the track, the energy losses are weakly independent of the μ energy above ~ 1 GeV. However, for energies greater than 1 TeV, the muon light emission is produced

¹Detected events whose interaction vertex is inside the instrumented volume are denoted as "starting events".

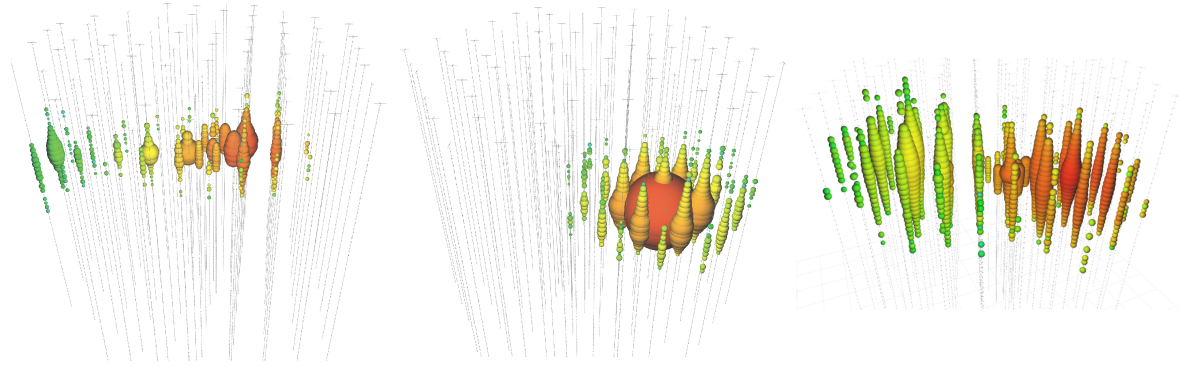


Figure 3.10: Different signatures in IceCube after a high energy neutrino is detected. Each bubble represents a DOM detecting light, and its size is scaled with the detected charged in that DOM. The colors stand for the time of detection, from red to blue transitioning from earlier to later detection. **Left:** Starting track event, corresponding to a high energy muon neutrino. Figure from IceCube public gallery. **Middle:** Cascade event, known as *Ernie*, of reconstructed energy ~ 1.14 PeV [113]. Figure from IceCube public gallery. **Right:** Simulation of a high energy tau neutrino interaction, featuring a double bang signature. Figure from [114].

by stochastic losses and depends on its energy, providing a better estimate of the incoming neutrino energy with a resolution of ~ 0.22 in $\log_{10}(E_\mu)$ for the energy range of 1 TeV to 1 EeV [3, 110].

Cascades

The CC interaction of ν_e and the NC interaction of any neutrino flavor do not produce a track signature but a cascade one (see Figure 3.2). After a ν_e CC interaction, an electron (or positron for the case of $\bar{\nu}_e$) is produced, which only travels short distances in the ice due to its interaction cross section [1]. This translates into an energy deposition in a short range which, at the scale of the detector and after light scattering, effectively looks like a single point source.

The light front of a cascade event is schematically shown in Figure 3.9 right. The event signatures are near-spherical from the interaction vertex. An example of a cascade detected in IceCube is shown in Figure 3.10 (middle). The amount of light produced after a cascade event depends on the initial neutrino energy. In cases where the vertex is contained in the instrumented volume, the neutrino energy can be reconstructed with $\sim 10\%$ accuracy at ~ 100 TeV. The direction of cascade events can be reconstructed using timing asymmetries. However, direction reconstruction for cascades is harder than in the case of tracks, with an angular resolution of about 15° for cascade events at energies ~ 100 TeV [111].

Double-bangs:

The double bang signature is a combination of two cascades and a faint track. It is produced after a tau CC interaction $\bar{\nu}_\tau + N \rightarrow \tau^\mp + X$. As in the other cases, a hadronic cascade is produced at the interaction vertex. Then the tau propagates, producing a weak track signature until it finally decays. Due to its larger mass with respect to the muon, most of the energy losses occur only in its decay, and therefore the τ track does not produce as much light as a μ track [112].

In $\sim 18\%$ of the cases, the tau decay produces a muon (plus the corresponding neutrinos) and, consequently, a new, brighter track. In the remaining cases, the result is an electromagnetic (when decaying into an electron plus the corresponding neutrinos) or hadronic (when decaying into pions in various combinations) cascade [115], producing the double bang signature shown in Figure 3.10. In this simulated case, the two cascades are well separated and easily distinguishable, but this is not always the case. Taus travel a distance around $l \approx 50 \text{ m} \cdot E_\tau [\text{PeV}]$ until they decay; therefore, only highly energetic taus are able to produce the double-bang signature in the detector, since otherwise both cascades, at detector scale, would appear to be a single one. Nevertheless, this case can still be identified as a tau neutrino interaction by looking for a double pulse signature on the detected waveforms [114].

3.7.2 Low energy events - DeepCore

Although high-energy events are generally *easily* distinguishable within the three categories explained above, the situations differ for lower energetic events. Events in the optimal energy range of DeepCore (10 to 100 GeV [40]) are much harder to separate according to their signature and may only be broadly categorized into *cascade-like* or *track-like* statistically. Reconstruction of these low-energy events is also more difficult, even taking into account the higher density of better modules that DeepCore is equipped with. Nevertheless, DeepCore studies have successfully shown the measurement of neutrino oscillation in the disappearance channel $\nu_\mu \rightarrow \nu_\tau$ with competitive precision to dedicated measurements from particle accelerators [116, 117], and excluded the absence of tau neutrino oscillation [118]. DeepCore has also conducted distinguished studies on searches for non-standard neutrino interactions [119, 120], sterile neutrinos [121] and dark matter [122].

3.7.3 Selected results

IceCube has demonstrated to be an extremely successful detector, proving the existence of high-energy extraterrestrial neutrinos [113, 123, 124], measuring the cosmic neutrino flux and spectrum [125, 126, 127] and searching for neutrino sources [128]. The extraordinary success of IceCube in its early years motivated the IceCube real-time alert system, which sends live-time signals when IceCube detects a high energy neutrino to other detectors around the world [129].

Recently and for the first time, a high-energy neutrino event detected by IceCube was associated with the gamma-ray flare from the blazar TXS 0506+056 with a significance level of $3 - 3.5\sigma$ [47]. Posterior archival IceCube data searches specifically focused on the source direction have revealed previous episodes of heightened neutrino emission, constituting 3.5σ evidence for neutrino emission from the source prior to the flaring episode [131, 132]. Later, another neutrino event was detected in coincidence with a radioemitting tidal disturbance event (TDE¹) [134], thus pointing to another potential source producing astrophysical neutrinos. Just a few months prior to the publication of this thesis, IceCube publicly

¹Transient event that occurs when a star get ripped apart by tidal forces after passing sufficiently close to a super-massive black hole [133].

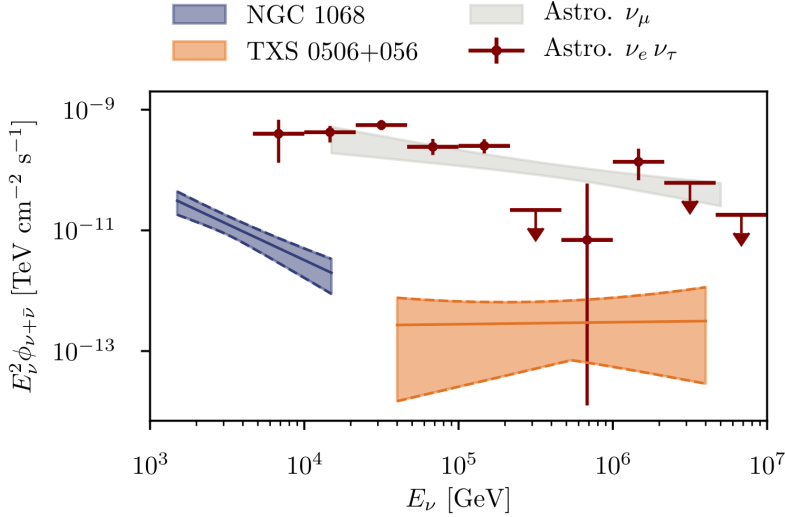


Figure 3.11: Fluxes of the point-sources NGC 1068 and TXS 0506+056 in comparison with the total diffuse neutrino flux detected by IceCube [127, 130]. The fluxes assumed equal flavor ratio. Bands stand for 68% confidence level coverage. Figure from [48].

announced evidence for neutrino emission from NGC 1068, a nearby Seyfert II¹ galaxy, with a significance of 4.2σ [48]. The detected fluxes of TXS 0506+056 and NGC 1068 are shown in Figure 3.11, together with the diffuse flux. The sources differ in terms of density and luminosity by orders of magnitude, and the fluxes of each do not contribute more than $\sim 1\%$ to the observed diffuse flux within their respective energy ranges. The distinct fluxes and source types of TXS 0506+056 and NGC 1068 suggests that there might be more than one population contributing to the diffuse astrophysical neutrino flux detected by IceCube [48].

To-date, IceCube has also successfully identified two τ neutrino candidates [136] and a particle shower consisted with being created at the Glashow resonance² [137, 138].

¹Spiral galaxies whose nuclei are exceptionally bright, with strong and broad emission lines in their spectra [135].

²Resonant formation of a W boson after $\bar{\nu}_e + e^- \rightarrow W^-$.

Future IceCube extensions

In the previous chapter, some of the most important IceCube results were shown. IceCube is not only a very successful detector, but it has also proven to be a very reliable detector, recording an up-time of about 99% in the last years. The low rate of DOM failures in more than 15 years of operation manifests that the South Pole is a suitable location for neutrino experiments [23]. Based on these successes and stable performance, two extensions for the detector are planned to further increase its capabilities, which are introduced in this chapter.

The low energy-focused extension, called *IceCube Upgrade* [23] (ICU), is scheduled to be constructed in the austral summer of 2025 – 2026, and the design process and logistic processes are at an advanced stage at the time of writing this thesis. The high-energy extension, called *IceCube-Gen2* [139], will begin construction after the ICU is fully built, and many details about the detector design are still under discussion. This chapter first showcases various optical module designs for upcoming extensions, then provides an overview and motivation behind each detector extension.

In this thesis, simulation studies are done involving these future detectors. Note that, during the timeline of this thesis, the designs for these detectors have changed on several occasions due to a variety of reasons, and they might still change in the near future. Some of the studies in this thesis were performed prior to recent changes in the geometry of the future detector and, therefore, do not use the most up-to-date design, which indeed might still change. This will be specified later in each analysis chapter if the geometry assumed there differs from the most up-to-date designs explained here.

4.1 Next generation optical modules

The IceCube DOMs were designed more than 15 years ago. Although the modules are reliable and efficient at detecting neutrinos, the new extensions will use new designs with the aim of further enhancing their capabilities [23, 139]. These new modules have been designed and tested by the Collaboration based on what is known about current DOMs and using the latest technological advances. Although the module designs included in ICU have already been decided, for IceCube-Gen2 the decision is less clear, and different prototypes are still being designed and tested. This section shows the most advanced designs that are likely to be deployed in any of the future detectors, exposing the advantages and disadvantages of each.

All module designs share in common that they must endure the harsh conditions beneath the glacial ice of the South Pole, which accounts for a maximum pressure during installation of 70 MPa, while operating at 13 – 30 MPa and between -9°C and -40°C , depending on

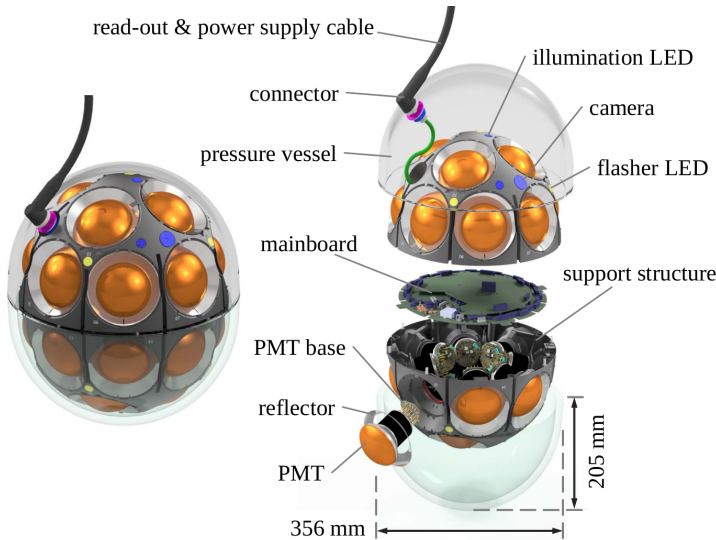


Figure 4.1: Render pictures of the mDOM module, close (**left**) and exploded views (**right**) with its main components labeled. Figure from [143].

the depth of the module. The modules must be tested to survive temperature changes ranging from 20°C , which is the temperature of the liquid water used for drilling, to -40°C [140]. Mechanical tests must also ensure that the modules will survive the long and complex process of transporting them to the South Pole.

To reduce development efforts, the new designs use a modular architecture of common electronic components. Common requirements are low power consumption, low sensitivity to interference signal, high reliability, and the ability to sample semi-complex waveforms from PMTs, assembled in small dimensions [141]. Some new modules will be equipped with calibration devices, which are introduced later in Section 4.2.

mDOM

The multi-PMT Digital Optical Module [141], *mDOM*, is one of the main modules to be deployed in IceCube Upgrade. The mDOM is a module designed to take advantage of a segmented photocathode area, in which the classic DOM with a single PMT is replaced by a module with several smaller PMTs while maintaining a low cost per photocathode area [141]. The concept is based on the KM3NeT module design, adapted to the conditions of the South Pole. KM3NeT optical modules contain 31 PMTs with 80 mm photocathode diameter comprised in a glass sphere of ~ 43 cm diameter. The mDOM, in contrast, contains 24 PMTs of 80 mm photocathode diameter. The reason for having fewer PMTs per module is due to the construction of the detector. As mentioned before, the modules are introduced into the Antarctic glacier after a very deep hole is drilled. The costs of drilling such holes increase significantly with its diameter, which obliges to reduce the diameter of the mDOM in order to keep reasonable costs. This constrains the mDOM to a vessel diameter of 35.6 cm in its widest part, while being 41.1 cm high and not maintaining a spherical shape. Each PMT has an opening angle of 40° and a length of ~ 91 mm [141, 142]. To further increase the sensitivity of the module, reflector cones are mounted around the PMTs, increasing the total effective area by $\sim 20\%$ [141].

A rendering of the mDOM is shown in Figure 4.1, where its main components have been labeled. In the center of the mDOM is the mainboard, which comprises a field-programmable gate array (FPGA) and the Communication, Power and Timing (CPT) module equal to all ICU modules, as well as 24 analog front channels with the corresponding



Figure 4.2: Figure of the D-Egg module, sealed with the waistband harness around the equator. Figure from [144].

read-out system and a microprocessor [141]. Everything is contained in a support structure, a 3D printed plastic part on which PMTs, reflector cones and calibration devices are placed. On top of that, a layer of optical silicon gel couples the components to the glass.

The use of mDOMs has some significant advantages over single PMT modules. The main characteristics are the following:

- Nearly uniform 4π sensitivity.
- Increased sensitive area per module by more than a factor two with respect to the classic IceCube DOM.
- Intrinsic information about the photon direction due to PMT orientations, which is expected to improve event reconstructions.
- Possibility of detecting an event in several PMTs within the same module (local coincidences). This feature can be used to identify neutrino interactions over background and might be of special importance in low-energy studies. Analyses performed later in this thesis try to take advantage of this feature.

D-Egg

D-Eggs, short of Dual optical sensors in an Ellipsoid Glass for IceCube-Gen2 [140], are also one of the main modules that will form the future ICU array. D-Eggs feature two PMTs of ~ 20 cm photocathode diameter, one facing upward and the other downward, with its corresponding electronics and calibration devices, all contained within a glass housing vessel of ~ 30 cm diameter at its widest. The shape of the glass is designed to maximize transparency in PMT areas, reducing its thickness from 12 to 10 mm on the photocathodes, closely following its curvature. Between the glass and the PMTs there is a layer of optical coupling silicon gel. At the center of the module the mainboard is found, similar to the mDOM one but with fewer channels [140, 23]. A figure of the D-Egg is shown in Figure 4.2. The main characteristics of the D-Egg over the other modules are:

- PMT distribution allows one to detect photons from all directions, although not uniformly as in the mDOM case. The sensitivity is higher for photons traveling upward or downward [140].
- Glass with less radioactive contamination than other designs [145].
- Smaller glass diameter, translated into cheaper deployment costs.

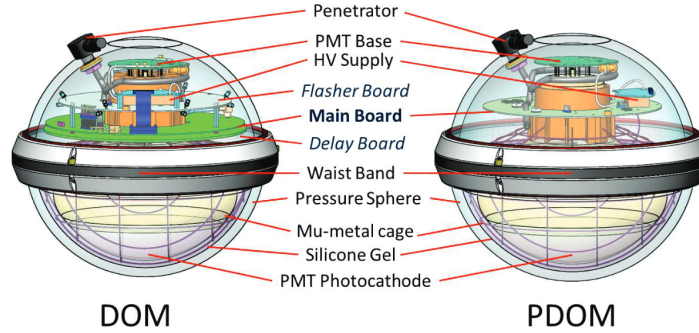


Figure 4.3: IceCube DOM and pDOM, with the different internal components labelled. Figure from [147].

The characteristic of the glass vessel makes the D-Egg the module with the smallest background rates, which is a very important feature for low-energy studies in ICU. Having only two PMTs, however, significantly reduces the ability to use segmentation for specialized studies compared to other segmented modules.

pDOM

Finally, ICU will also be equipped with *pDOMs*¹. The pDOM concept is based on current IceCube DOMs with updated electronics to further improve the module. The module features a single ~ 25 cm diameter PMT facing downward. The mainboard is updated with a high-performance and low-power ADC, which allows continuous digitization of PMT signals in contrast with current DOMs whose waveform window is limited to $64 \mu\text{s}$ at most [147]. A sketch of the pDOM module is shown in Figure 4.2, compared to the classic DOM module.

The main advantage of using pDOMs is its proven design, which is reliable, stable, and efficient. It also has the possibility of using refurbished components from old DOMs to build new modules. Using the same module concept also facilitates the testing phase [146]. However, in contrast to the other new designs, pDOM is not intended to be innovative. In addition to the lack of segmentation, it also has a smaller effective area than the other designs.

WOM

The Wavelength-shifting Optical Module, *WOM*, is a novel optical sensor that uses a wavelength-shifting layer of paint to enhance the photosensitive region of the photomultipliers in the ultraviolet (UV) region. The WOM consists of a hollow quartz cylinder coated with wavelength-shifting paint and two photomultipliers [148]. The idea is that wavelength-shifted photons travel through a photon-capturing tube until they reach the PMTs. Therefore, the shifting area can be larger than that of the photocathode itself, increasing the sensitive area of the module. A sketch of the WOM and its working principle is shown in Figure 4.4. As previously shown in Figure 3.3, the Cherenkov effect produces more photons with lower wavelengths, thus increasing the sensitivity in that regime would significantly enhance the performance of the modules. The glass vessel is 1.3 m long and

¹pDOM arises from PINGU+DOM [146]. PINGU was the previous IceCube plan to extend its low-energy capabilities, for which pDOM was designed.

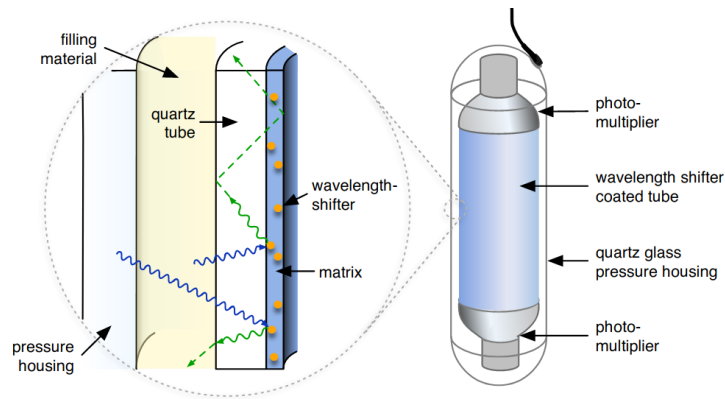


Figure 4.4: The WOM and its working principle. After UV photons are absorbed and shifted, they are guided through the tube to the photocathode. Figure from [148].

has a diameter of 17.3 cm, making the WOM the narrowest module of all designs. PMTs are flat with a diameter of 11.4 mm [148]. WOMs will also be deployed in lower numbers in the next IceCube Upgrade and possibly in IceCube-Gen2.

The WOM advantages over other modules are:

- Increasing the detection range to UV photons considerably increases the detection efficiency due to higher Cherenkov photon production at low wavelengths.
- WOM glass has very low radioactive contamination.
- Narrowest module design, reducing deployment costs if a string is only composed of WOMs.

WOMs enables the detection of light that is invisible to other modules, however, photons being shifted and traveling inside the inner tube produce a wider distribution of arrival times than in cases where photons are directly detected by the PMT, which could potentially affect reconstructions negatively, a matter that is still under investigation.

LOM

The eLongated Optical Module, *LOM* [149], is a module developed for IceCube-Gen2, therefore, its design is still in earlier stages than previously described modules. The idea of the LOM is to compress the concept of the mDOM into a narrower module to adapt to the reduced borehole diameter, which allows to decrease deployment costs. Since IceCube-Gen2 will potentially drill holes for more than 100 strings, a module with smaller diameter can make a significant difference in budget, potentially allowing the inclusion of more modules. A narrower module comes at the cost of fewer PMTs due to the associated space restrictions of the internal volume. Currently, two different LOM designs are under development, which will eventually merge into a single design. One design features 16 PMTs with the pressure vessel glass having similar shape (but narrower) than that of the mDOM. The other design features 18 PMTs with the shape of the vessel glass resembling to the D-Egg module. The two extra PMTs point up and down, as in the D-Egg concept. The LOM will not contain a holding structure like the mDOM¹. Instead, LOMs adapt

¹The LOMs contain a smaller metal sheet that also holds the pieces together. During this thesis, when mentioning that LOMs do not have holding structure, it is referred to a holding structure that completely envelops the inner volume as in the mDOM construction.

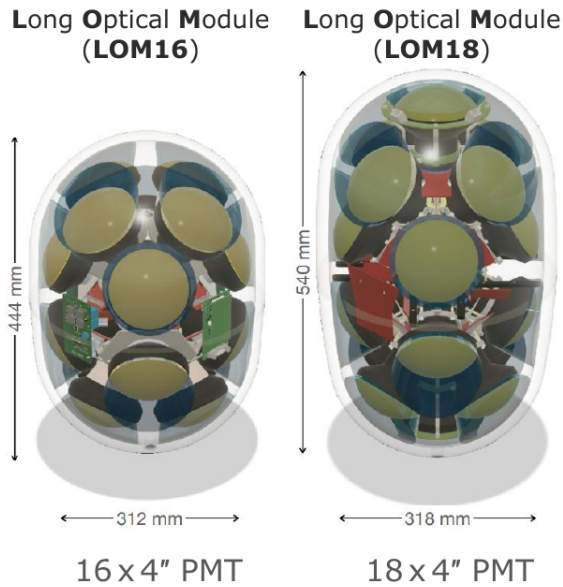


Figure 4.5: Renders of the LOM16 (left) and LOM18 (right) designs. Figures from internal IceCube repository.

conical-shaped silicone gel pads to optically couple the PMTs with the pressure vessel to enhance the photo collection efficiency. These form a conical volume reflecting photons in a way similar to the reflector cones in the mDOM design. The two LOM designs are shown in Figure 4.5.

Although both LOM designs have fewer PMTs than the mDOM, these are compensated for by having PMTs with larger photocathodes, resulting in a slightly larger sensitive area than in the mDOM. However, the smaller number of PMTs would probably negatively affect any study that relies on the module's segmentation in comparison to the mDOM.

4.2 Calibration devices

Calibration devices have also been designed for the future IceCube extensions, aiming to increase the understanding of the detector and its medium. The opportunity to perform calibration studies on ice with new devices is important not only for the future detectors but also for IceCube, as the results can be used to improve the current understanding of the medium, and thus improve IceCube analyses in retrospect.

Some of the new calibration devices are updated versions of those included in IceCube. The new modules will be equipped¹ with cameras and their corresponding illumination devices [150], LEDs, accelerometers, and acoustic, pressure, and magnetic field sensors [23]. Moreover, external devices will be part of the newer detector array, namely POCAM [151], the Pencil Beam [152] and acoustic modules² [153]. Some calibration devices can be utilized to conduct studies similar to those of other calibration devices. While this may sound redundant, it is highly beneficial in minimizing systematic errors in each individual

¹Not all module designs will contain all calibration devices.

²Although it is unclear whether IceCube-Gen2 would include the same calibration devices (both internal and external) than IceCube Upgrade, it is a probable scenario that some of them will be shared. IceCube-Gen2 may deploy newer and more sophisticated versions of similar calibration devices due to the longer development time.

analysis when the results are combined. Some of the most important calibration devices are briefly described below.

Camera system

The camera and illumination system [150] combines transmission and reflection photographic measurements to help determine the optical properties of the glacial ice between strings and in the refrozen drilled hole ice, as well as to determine relative module positions and survey the local ice environment surrounding the modules.

Precision Optical Calibration Module: POCAM

POCAM is a high-precision module [151] with a controlled isotropic light source capable of running multi-wavelength nanosecond short pulses. POCAMs will be embedded in the ice together with the optical modules. Each POCAM module contains two light sources, one per hemisphere. Having a controllable light source helps to measure the properties of the glacial ice and the refrozen ice, the relative DOM efficiencies, or the ice anisotropy [103].

Pencil Beam

Pencil beam devices allow for a laser-like beam that can point to any arbitrary direction, which enables sweeping over different receiver directions. This aims to disentangle the contributions of absorption and birefringence to ice anisotropy [152].

Acoustic modules

Acoustic modules, capable of receiving and transmitting acoustic signals, will be attached to the new strings. These modules aim to calibrate the detector geometry with a precision of ~ 10 cm by trilateration of the arrival times of the acoustic signals [153].

LEDs

mDOMs, pDOMs, and D-Eggs will contain 10-12 LED flashers each [140, 141, 146]. The main goal of the LED system is to calibrate the ice properties, both in the refrozen drill holes and in the glacial ice. It can also be used to time-calibrate PMTs or DOM efficiencies. More details about the LED system can be found in Chapter 7.

4.3 ICU: IceCube Upgrade

IceCube Upgrade [23] (ICU) will be the first extension of the new IceCube era. It focuses on improving the current detector sensitivity to lower energetic neutrinos. Around 700 new optical modules will be deployed within the existing DeepCore volume, increasing the module density at the core of IceCube. The vertical distance between modules in a string will also be shorter, further increasing the density of modules and potentially improving the identification and reconstruction of neutrinos in the GeV range.

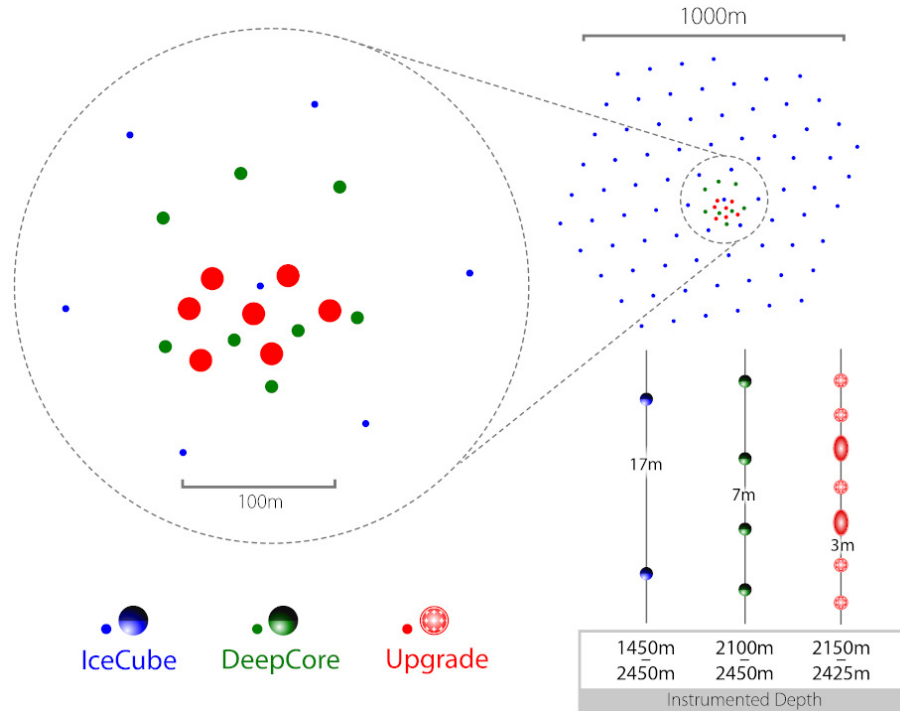


Figure 4.6: Schematic view of ICU geometry arrangement, with a top view of the position of the strings and a side view depicting the modules separation in the physics region. Figure from internal IceCube repository.

4.3.1 Physics motivation

DeepCore is optimized to identify and reconstruct events from 10 to 100 GeV, with a peak performance at about 50 GeV [40]. By increasing the density of photosensors, ICU seeks to increase the performance not only in that region but also in the 1 – 10 GeV range, aiming for a better event identification and reconstruction of low energetic neutrinos. This would enable the detection of tau neutrino appearance with higher precision and the study of the unitarity of the PMNS matrix. Observations of non-unitarity would be an indication for new physics beyond the Standard Model [23]. By improving the efficiency of the detector at lower energies, the capability of the detector to separate signal from background at low energies should also improve, enhancing the sensitivity to dark matter [154], neutrinos from solar flares, or other low-energy searches.

ICU has a secondary but equally important goal, which is to improve the calibration of the IceCube detector [23]. Deploying new modules into the ice is a great opportunity to include new calibration devices, previously described. A better understanding of the detector medium means a reduction of systematic uncertainties. The information acquired from the new calibration devices in the newer ICU can be translated into a better calibration for the existing IceCube detector as well, immediately enhancing IceCube’s sensitivity to high-energy cosmic neutrino fluxes [23]. Finally, ICU will also serve as a test bed for different module prototypes which are developed for the larger IceCube-Gen2 detector.

4.3.2 Detector geometry

The new ICU strings will be located near the center of the current detector, within DeepCore volume. The modules are distributed to maximize the use of the cleanest ice, the so-called physics region, where the modules are spaced only ~ 3 m apart [23]. The strings will also contain modules below and above the physics region, where the module spacing increases to ~ 30 m, but avoiding the depths with the worst optical properties (dust region). These modules here are better suited for calibration purposes or to improve the muon veto, whereas modules in the physics region will primarily collect data for low-energy neutrino analyses. The majority of the modules are mDOMs (~ 400) and D-Eggs (~ 270), followed by pDOMs. In the calibration region, a few LOMs are introduced to test their capabilities for IceCube-Gen2. Below the physics region, WOMs are deployed, and a mixture of modules and calibration devices are placed below them. The positions of the new ICU strings are shown in Figure 4.6. The strings are distributed around the center of IceCube in between the DeepCore strings, making up for a denser region when all sub-detectors are combined.

4.4 IceCube-Gen2

Designed to study the neutrino sky from TeV to EeV energies, IceCube-Gen2 [139] will be the new high-energy extension of IceCube, planned to start construction after the completion of ICU. The newer detector aims to considerably increase the instrumented volume with new sophisticated optical modules that cover close to 8 km^3 , bigger than any other detector currently in the world. The detector aims to detect 10 times more neutrinos than the current IceCube.

4.4.1 Physics motivation

Despite IceCube's extraordinary capabilities and success in finding the first evidence of high-energy neutrino sources, only after more than 10 years of data collection is the detector starting to identify them (see Section 3.7.3). The fluxes from these sources are still only a small part of the total diffuse flux measured by IceCube, showing that the detector is not sensitive enough to identify many other potential sources. Furthermore, the rarity of high-energetic neutrino events has been proven in examples such as the only two tau neutrino candidates identified so far [136] or the only electron antineutrino candidate at the Glashow resonance [138]. The sensitivity of the detector can be improved by increasing its volume, increasing the likelihood of neutrinos interacting within it. IceCube-Gen2 will be able to study sources five times fainter than IceCube. The new modules and new radio arrays will enable improved detection and reconstruction of neutrinos with energies from TeV to EeV, which would enhance the identification and study of neutrino sources and potentially allow for the exploration of fundamental physics through the detection of high-energy neutrinos and cosmic rays, exceeding the capabilities of the current detector [139].

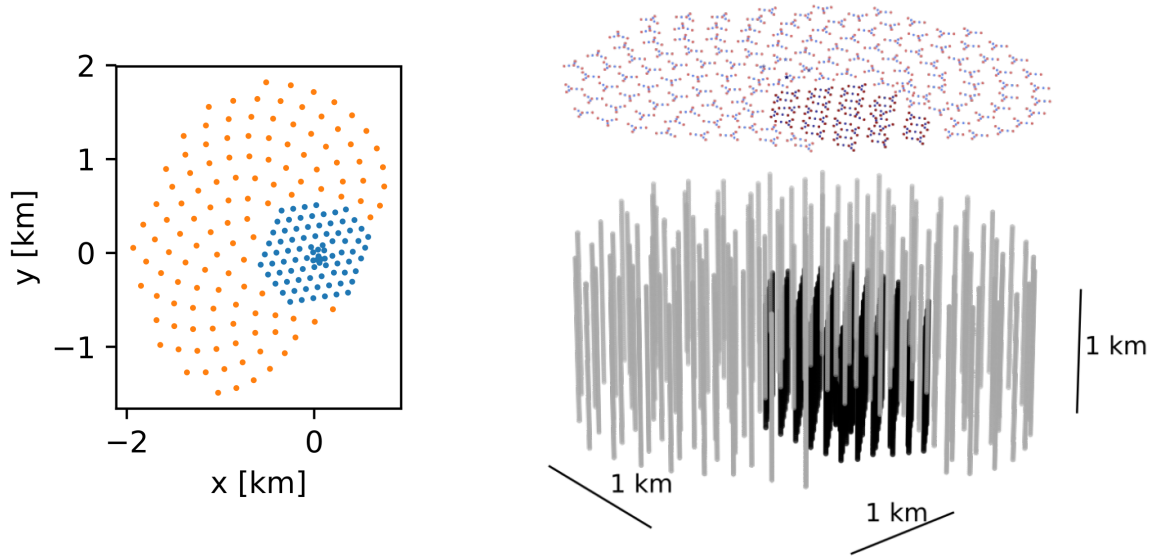


Figure 4.7: **Left:** Top-view of the string positions for IceCube-Gen2 (orange) and IceCube (blue). **Right:** 3D render of the IceCube-Gen2 strings (gray) with IceCube strings (black) and the surface array. Figures from internal IceCube repository.

4.4.2 Detector geometry

Although the final geometry design has not yet been decided, the first plans are already under investigation. The design considers increasing the length of the new strings 125 m above and below the IceCube ones, since measurements have shown that the optical properties are still adequate at those depths [102]. The new strings will feature an inter-string separation of 240 m. Due to the high transparency of South Pole glacier ice, this inter-string distance allows for a high efficiency in reconstructing astrophysical neutrinos while still enabling accurate geometry and timing calibration using the flashers in the modules.

The baseline geometry design is composed of 120 new strings with 80 modules each. With a vertical spacing of 17 m, the modules cover depths between 1344 m and 2689 m below the surface. The total instrumented volume encompasses 7.9 km^3 of glacial ice. The locations of the new strings are depicted on the left side of Figure 4.7, while a sketch of the detector is shown on the right. The IceCube array is embedded within the new geometry, and the new strings are uniformly distributed. For IceCube-Gen2, the surface air shower array will also be extended, which will improve the studies of cosmic-ray air showers and will also act as a veto for IceCube-Gen2 [155]. Furthermore, a radio array is planned for IceCube-Gen2. This array consists of antennas buried up to 200 m below the surface to detect the Askaryan radiation [156]. The Askaryan effect results from the negative charge anisotropy that arises after a hadronic or electromagnetic cascade is created in a dielectric medium, leading to the emission of coherent radiation in the radio or microwave frequency range. The radio array plays an essential role in complementing IceCube-Gen2 to reconstruct the direction of cascade events at EeV energies [139].

Regarding the module composition of IceCube-Gen2, to date, the most favorable choice is one of the LOM designs or a merge of them, due to the segmentation of these modules together with the lower costs than mDOMs would have. However, decisions regarding the

module type and final geometry design are still being evaluated.

mDOM Geant4 simulation

During the completion of this thesis, an existing Geant4¹ [157] simulation containing the mDOM module and surrounding ice has been extensively modified and used, adding new features and updating old ones. This chapter is intended to lay the foundation for the operation of such a simulation for the common elements that are used in different chapters in the thesis. In each chapter where this simulation is used, a description is provided on how the simulation has been adapted to the specific analysis being performed. The Geant4 mDOM simulation was originally written in the framework of two Ph.D. theses [78, 158]. It was first used and modified by the author for his master thesis [159], where the implementation of the ice properties explained in this chapter was first introduced in the code. The current version of the mDOM Geant4 simulation is a combined effort of current and former students of the AG Kappes group in Münster, including the author. Additionally, based on the efforts to recreate the mDOM module, the simulation framework also has the possibility of including other optical modules in different levels of detail, such as pDOMs, LOMs, or D-Eggs.

Geant4 is a powerful, object-oriented C++ toolkit that offers a wide range of tools for simulating the passage of particles through matter and their interactions. The code is freely available under the GPL license, is constantly being updated and has been extensively validated [157]. It was first developed due to requirements at the Large Hadron Collider (LHC) [160] at CERN² and released in 1998. Since then, Geant4 has been used by an ever-growing community that includes multiple disciplines of physics beyond its original intent [161].

Geant4 provides a rich set of physical models to handle particle-matter interactions over a very wide energy range, including physical properties and interactions ranging from electromagnetic processes to complex baryonic interaction processes [157]. Simulating neutrinos with Geant4 would be extremely inefficient due to the tiny interaction probability of such particles; however, simulations in Geant4 can be used to perform studies for IceCube or its future extensions, like calibration studies measuring the impact of optical properties, simulating the background due to radioactive contamination in the modules, or tuning it to simulate the detection of neutrino events in a smart way that avoids the generation of the neutrino itself.

5.1 Module simulation

The simulated mDOM is created by combining basic geometric building blocks and applying boolean operations to create more complex volumes. Each component must be placed

¹GEometry ANd Tracking

²European Organization for Nuclear Research

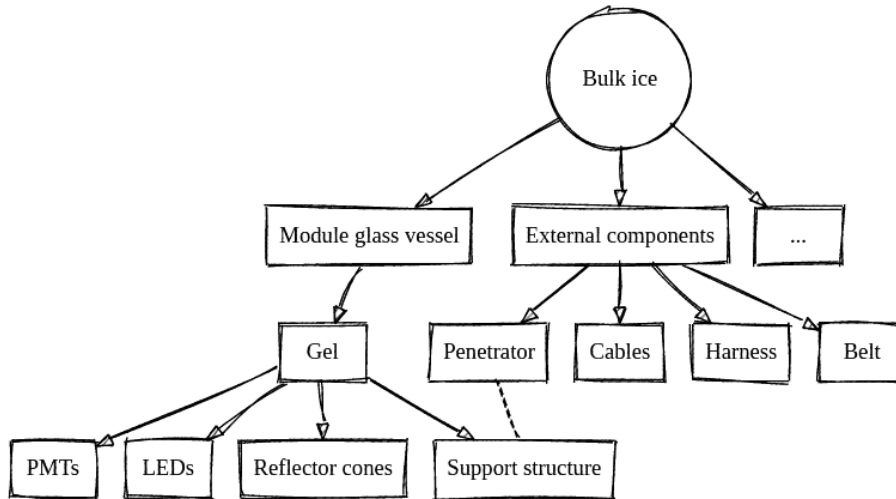


Figure 5.1: Simplified tree diagram showing the geometry hierarchy used in the Geant4 simulation. The bulk ice is the glacial ice where the detector is built. In the simulation, it contains everything other volume. The mDOM is built in layer volumes from outside to inside. External components are created within the bulk ice volume, with the penetrator being the connection between the inner support structure and the external components. Any extra element for a particular simulation study would likely be placed within the bulk ice, like the bubble column in Chapter 7.

in a *mother* volume where it is contained. A graphical representation of the simulation hierarchy tree is shown in Figure 5.1. The figure shows the hierarchy of the most important module components, where each mother volume is connected to its *daughter* volumes with arrows. When two different volumes at the same hierarchy level collide, one must be subtracted from the other.

A brief description of each component is given below. Although the simulation includes several options for each component, such as different PMT or vessel models, only the component used later in this thesis is specified here. In addition, the inclusion or absence of each element in the simulation is optional and chosen by the user using simple input commands. The materials and properties of each element are selected based on manufacturer specifications or measurements.

- The bulk ice is the main mother volume of the simulation and any other volume is contained in it. The optical properties of the bulk ice in the simulation are discussed in Section 5.3.
- The pressure vessel glass is *Vitrovex*¹ glass, with its corresponding absorption lengths and refractive index. The radioactive contamination of such glass was studied in [84, 162] and can also be simulated.
- PMTs are *Hamamatsu*² *R15458-20*. PMT electronics or collection efficiencies are not included in the standard simulation. Instead, when a photon reaches a PMT, the quantum efficiency (QE) of the PMT is checked for the corresponding photon wavelength. A Monte Carlo algorithm is then run to determine whether the photon is detected or not. The simulations can also be done without QE and only account for

¹<https://www.vitrovex.com/>

²<https://www.hamamatsu.com/jp/en.html>

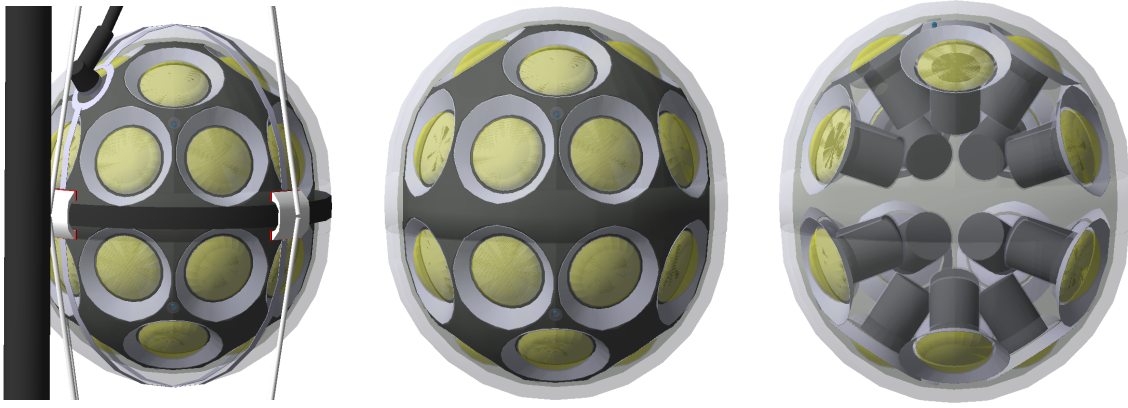


Figure 5.2: Render images of the mDOM in the Geant4 simulation. In the **left** image, the module is shown including all its external components, harness and cables. The **middle** figure shows the mDOM without any of the external components. In the **right** figure, the mDOM is shown without external components and the support structure has been made transparent, together with a few PMTs, reflectors and LEDs.

this later in the analysis. The QE curve of the PMT, as measured and included in the simulation, is shown in Figure 5.2.

- The support structure is simulated as a total absorber body.
- Gel, reflector cones, and all external components are given the corresponding optical properties from the manufacturer, or approximated for the corresponding material. The way LEDs are simulated is explained in detail in Section 7.3.1.

The mDOM geometry simulated in Geant4 is shown in Figure 5.3. The first picture shows the module and the external components that emulate the connection and clamping of the mDOM to the string, including the harness and the penetrator cable. Next to the module, the string cable is placed. The middle picture shows the mDOM as in the simulation without external components. In the last image, the support structure and some PMTs, reflectors, and LEDs have been set to be transparent to show the interior of the module. Although the back of the PMTs is simulated with an absorber coat¹, photons are not able to reach the interior of the module, which is empty. While the mDOM is a self-contained object easily defined in layers, the holding structure and external cables must be built as separated volumes. As such, the simulation stores the local coordinates of each external component in the module and places them accordingly to the mDOM coordinates. The possibility of including several modules in a single simulation run, moving and rotating each one independently, was introduced in the code for the studies performed in Chapter 7.

¹Although not essential, the coat in the mDOM PMTs is due to the introduction of the LOM16 design in the framework, since the PMT class is shared by all optical modules. In the case of the LOM16s, its function is to prevent photons from entering the back of the PMT, which could otherwise be detected.

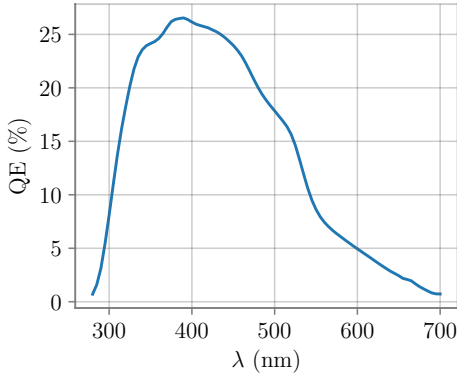


Figure 5.3: Quantum Efficiency of the PMT *Hamamatsu R15458-20*. The data, used as a input in the Geant4 simulation, was measured in [163].

5.2 Physics processes

The physical processes included in the simulation for each particle are described in Table 5.1. Cherenkov effect is given for the corresponding mediums when applicable. Although this table provides a general representation of the physics processes, some studies may not include all processes shown, particularly when the corresponding particle is not expected to be generated in the simulation.

5.3 Bulk ice simulation

The implementation of the ice properties in the Geant4 simulation was first done by the author under the scope of his master thesis [159]. This section explains the modeling and implementation of these properties in the simulation to provide a better understanding of the results presented in subsequent chapters.

The instrumented part of the glacial ice in the South Pole, commonly known in IceCube as bulk ice, shows variations in its properties depending on the depth [102, 164]. This is mainly due to climatological events in the past which resulted in different deposition rates of dust particles over the ancient ice surface and different concentration of air bubbles. The optical properties of the bulk ice have been studied for IceCube [102, 164] and here the results are used to include them in the Geant4 simulation. The refraction index is directly included in the code and does not require additional explanation, however, the absorption and scattering processes are explained in more detail in this section.

Due to the size of dust particles and bubbles in the ice, Mie scattering [165] is the predominant scattering process on the south pole ice [102, 164]. The geometric scattering coefficient b_{coef} is a measure of how often a photon would scatter, and $b = 1/b_{\text{coef}}$, called the scattering length, determines the average distance between successive scatters. Often in this thesis, the effective scattering length is used, defined as

$$b_e = b(1 - \langle \cos\theta \rangle), \quad (5.1)$$

where θ is the deflection angle in each scatter. The scattering coefficients for IceCube have

Table 5.1: Description of the physics list used in the mDOM simulation, with a brief description of each process in the last column.

Particle	Geant4 process	Description
Optical photon	G4OpAbsorption	Optical photons absorption
	G4OpBoundaryProcess	Boundary interactions when photons change medium
	G4OpMieHG	Mie scattering of photons
Gamma	G4LivermoreGammaConversionModel	Gamma conversion into an electron-positron pair
	G4LivermoreComptonModel	Compton effect for gammas
	G4LivermorePhotoElectricModel	Photoelectric effect for gammas
Electron/positron	G4eMultipleScattering	Scattering of e^-/e^+ in medium
	G4eIonisation	Ionisation of the medium by e^-/e^+
	G4eBremsstrahlung	Bremsstrahlung of e^-/e^+
	G4eplusAnnihilation (e^+ only)	Annihilation of positrons with electrons in the medium
Muon (-/+)	G4MuMultipleScattering	Scattering of μ^-/μ^+ in medium
	G4MuIonisation	Ionisation of the medium by μ^-/μ^+
	G4MuBremsstrahlung	Bremsstrahlung of μ^-/μ^+

been measured and parameterized as [164]

$$b_{\text{coef}}(\lambda) = b_{\text{coef}}(400) \left(\frac{\lambda}{400} \right)^{-\alpha}, \quad (5.2)$$

where $b_{\text{coef}}(400)$ is the scattering coefficient for photons with $\lambda = 400$ nm and α is a global parameter whose value was fitted to $\alpha = 0.9 \pm 0.03$ [102]. The Mie scattering profile in Geant4 is calculated using the Henyey-Greenstein approximation and it is fitted to closely match the profile measured in [102]. Within this approximation, the best fit is obtained with $\langle \cos\theta \rangle \approx 0.9$, having then the approximate relation $b_e \sim b/10$. The profile peaks in the forward photon direction, meaning a small change in direction for each scatter in most cases.

Light absorption in the ice depends on both the dust particles and the ice temperature. Defining parameters similar to those before, where a_{coef} is the absorption coefficient and $a = 1/a_{\text{coef}}$ the absorption length, the absorption coefficient at any wavelength has been

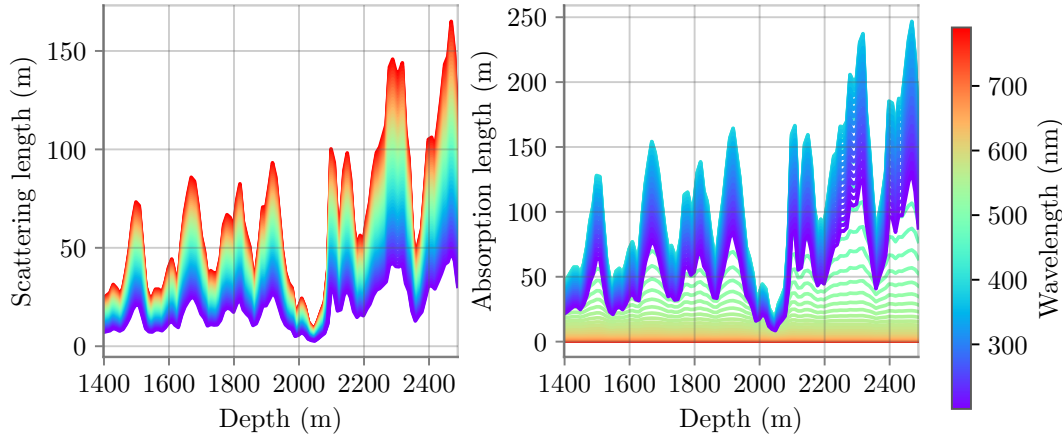


Figure 5.4: Scattering (**left**) and absorption (**right**) lengths of bulk ice as a function of the depth for different photon wavelength.

parameterized as [164]

$$a_{\text{coef}} = a_{\text{dust}}(400) \left(\frac{\lambda}{400} \right)^{-k} + A e^{-B/\lambda} \cdot (1 + 0.01 \cdot \delta\tau), \quad (5.3)$$

being $\delta\tau$ the temperature difference relative to the depth of 1730 m,¹ $\delta\tau(d) = T(d) - T(1730)$ m. The remaining parameters are fitted to $A = (6954 \pm 973) \text{ m}^{-1}$, $B = (6618 \pm 71) \text{ nm}$ and $k = 1.08 \pm 0.01$ [102, 164]. The temperature as a function of depth d has been parameterized in [167, 102] as

$$T(K) = 221.5 - 0.00045319 \cdot d + 5.822 \times 10^{-6} \cdot d^2. \quad (5.4)$$

In the simulations carried out in this thesis, the values of $b_{\text{coef}}(400)$ and $a_{\text{dust}}(400)$ measured in [102] have been used. Then, the scattering and absorption lengths are obtained as functions of the depth for any wavelength, which is shown in Figure 5.4. Various regions in the ice can be observed, where the optical properties vary considerably. Around 2000 m deep is the so-called *dust region* or *dust layer*, where the accumulation of dust particles is greater, producing much shorter effective scattering and absorption lengths. Deeper, one can find the cleaner part where the physical region of IceCube Upgrade will be deployed.

Figure 5.5 shows how the wavelength spectrum changes as the photons travel a certain distance. This has been obtained by simulating a spherical volume of $r = 150$ m of bulk ice in the Geant4 simulation, without modules. In the center of the volume, electrons of 1 MeV are generated. These travel less than 1 cm while inducing photon generation; thus, at the scale of the simulation they can be considered as point source emission of photons following a Cherenkov spectrum. Then, the distance from the center at which the photon is absorbed is saved, substituted by the radius of the simulated volume if the photon reaches the edge. On the left-hand side of the figure, the bulk ice is chosen to have ice properties as the mean value of the depth covered by the physics region of IceCube Upgrade. On the right-hand side of the figure, the bulk ice is given the ice properties of

¹This corresponds to the center of AMANDA detector [166]

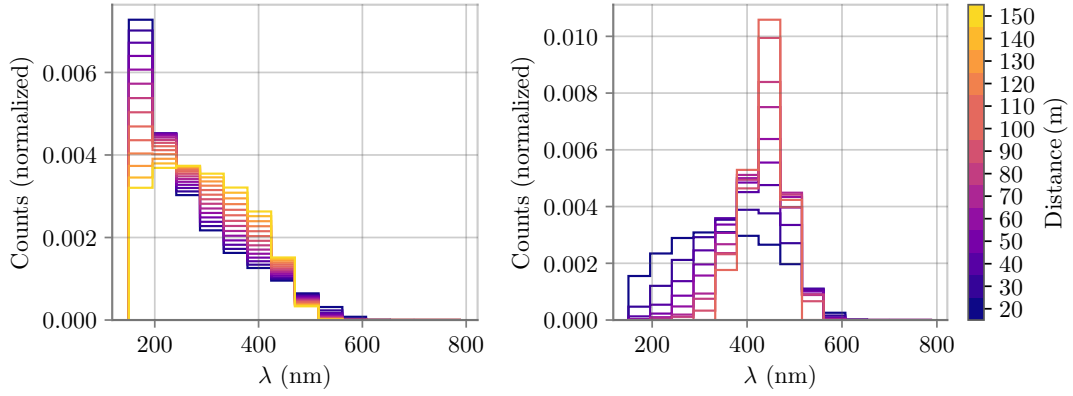


Figure 5.5: Photon spectrum after traveling through the bulk ice, produced after simulating an electron of 1 MeV. **Left:** the bulk ice properties has been chosen as the average of the ICU physics region. **Right:** the bulk ice are given the properties of the dust layer region. For visibility reasons, this figure only shows the result up to a distance of 100 m.

the dust layer. The spectrum differs significantly for both cases even for the first entry at 20 m. It can also be seen that the transmission peaks at ~ 425 nm for the dust layer case, whereas in the cleaner ice the spectrum peaks at lower wavelengths.

The dust layer results in fewer detected photons and increased scattering events, leading to fewer direct *hits*¹, and therefore hindering reconstruction. This is the rationale behind the decision not to deploy modules in the ICU at these depths.

¹The term *hit* is often used in IceCube and refers to the detection of a photon by a PMT.

Using module segmentation to identify MeV CCSN neutrinos in IceCube-Gen2

As introduced in Section 2.3.4, neutrinos are believed to play a major role in CCSN explosions. Neutrinos from CCSNe are generated inside the core of these stars, which makes them suitable for studying these explosions, as they can provide a picture of the physical processes involved in the collapse and subsequent explosion of these stars. CCSN neutrinos are emitted in a short burst of a few seconds and have energies around tens of MeV. This energy range is indeed well below the low energy threshold of DeepCore; however, a neutrino burst from a CCSN explosion can still be detected in IceCube. With no capability for distinguishing these low-energetic events individually, IceCube is able to detect CCSNe explosions as a collective rise on top of the noise rate in all modules within a certain time window.

If future IceCube extensions are equipped with segmented modules, the situation might be different even if the detector is built focusing on a much higher energy range. The proximity of different PMTs within a single module might enable the individual identification of these low-energy events, which is hardly possible in the current detector, because the particle originated from the MeV neutrino interaction only travels a few tens of centimeters in the ice. Using the Geant4 simulation described in the previous Chapter 5, this chapter explores the possibilities of future IceCube extensions for the identification of core collapse supernovae (CCSNe) using coincidences in multi-PMT modules to identify the MeV neutrinos over the background. The results are obtained using models of two type II CCSNe ending up in neutron stars; however, the method introduced here is applicable to any other type of SN from which a MeV neutrino burst is expected. As introduced in Section 2.3.4, these SNe are the most interesting from the point of view of neutrino telescopes, due to the important role that neutrinos are believed to play in the triggering of the explosion. An IceCube-Gen2 detector composed of 10000 mDOMs is assumed for most of the results obtained in this chapter; however, other detector configurations are also explored later in the chapter.

The chapter is divided as follows: first, an introduction of the most important interaction channels for MeV neutrinos in ice and the current capabilities of IceCube for identifying and studying CCSNe is given. Later, the CCSN models used for the simulations in this chapter are introduced. The expected signal and background are then simulated. Trigger conditions based on the multiplicity of the optical modules are introduced to distinguish the signal from background events. Using these trigger conditions, various studies are conducted and compared with IceCube and with IceCube-Gen2 if multiplicity conditions were not used. Some of the results are also calculated for ICU and for an IceCube-Gen2 detector equipped with LOMs. Finally, a discussion of possible error sources for the results shown in this chapter is given.

The technique described in this chapter to identify low MeV events using coincidences in mDOMs was first approached by the author in the scope of his master thesis [159]. Since

then, the Geant4 simulation has undergone a complete overhaul, fixing previous bugs, enhancing the optical module's geometry construction, and improving the flexibility and efficiency of generating CCSN neutrino interactions for adaptability to other studies. The analyses have also been expanded, including the simulation of more background sources. The methods developed for the author's master thesis [159] and used in this chapter are indicated at the beginning of each corresponding section. Some studies carried out during the realization of this thesis and shown in this chapter have been published in [143]. The results shown in this chapter are slightly different from the published ones, due to the use of new simulations with small corrections and changes in the code concerning the geometry of the modules. A discussion about these differences is given in Section 6.11. The results shown in this chapter use the same CCSN models as in [159, 143].

6.1 Neutrino interactions from CCSNe in ice detectors

MeV neutrinos and antineutrinos coming from CCSNe can interact through different channels in the ice of the South Pole. The simulations made in this chapter only consider the two most important interaction channels, which should cover around 95% of the total expected signal from CCSN neutrinos in IceCube [168], which are the inverse beta decay (IBD) and the electron-neutrino electron elastic scattering (ENES). Other less probable interaction channels have not been included for simplicity and time reasons.

Inverse beta decay (IBD)

The inverse beta decay is a CC weak interaction between an electronic antineutrino and a proton by which a neutron and a positron are generated,

$$\bar{\nu}_e + p \rightarrow n + e^+. \quad (6.1)$$

It has the highest cross section of all possible interactions of CCSN neutrinos in ice below ~ 60 MeV [169, 170]. Due to the larger mass of the generated particles, the reaction has an energy threshold of $\epsilon_{\bar{\nu}_e}^{th} \sim 1.8$ MeV assuming that the proton is at rest. Since the positron is much lighter than the neutron, it carries most of the kinetic energy of the incoming $\bar{\nu}_e$. The positron then travels through the medium until it annihilates with an electron of the medium. While traveling through the ice, the positron induces Cherenkov effect while its energy is above the Cherenkov threshold. The generated neutron would eventually undergo neutron capture by some nuclei in the ice, generating γ up to ~ 2.2 MeV [88].

The angular cross section of this interaction is implemented in the Geant4 simulation as [170]

$$\left(\frac{d\sigma}{d\cos\theta} \right)^{(1)} = \frac{\sigma_0}{2} \left[f^2 + 3\alpha^2 + (f^2 - \alpha^2)v_e^{(1)} \cos\theta \right] E_e^{(1)} p_e^{(1)} - \frac{\sigma_0}{2} \left[\frac{\Gamma}{M} \right] E_e^{(0)} p_e^{(0)}, \quad (6.2)$$

expanded in terms of $1/M$ up to the first order (indicated by the superindex), with M the average nucleon mass. The simplified indexes ν and e represent the incoming electronic

antineutrino and generated positron, respectively. σ_0 is given by $\sigma_0 = (2G_F m_e \hbar)^2 / \pi c^2$, with $G_F = 1.166 \cdot 10^{-5} \text{ GeV}^{-2}$ the Fermi constant, and $\alpha \sim 1.26$ the axial-vector coupling constant. $f = 1$ is the vector coupling constant and θ the angle between the incoming $\bar{\nu}_e$ and the emitted e^+ . The parameter Γ depends on the energy of the incident antineutrino (see [170]). The angular distribution of the outgoing positron is approximately isotropic at about 15 MeV, slightly backward at lower energies and slightly forward at higher energies, while the outgoing neutron direction is usually forward peaked [170]. From θ and the incident antineutrino energy, the emitted positron energy is given as [170]:

$$E_e^{(1)} = E_e^{(0)} \left[1 - \frac{E_\nu}{m_p} (1 - v_e^{(0)} \cos \theta) \right] - \frac{(\Delta_{mn}^2 - m_e^2)^2}{4m_p}. \quad (6.3)$$

The total interaction probability of a $\bar{\nu}_e$ inducing IBD is taken into account in the simulation using the total cross section as [171]

$$\sigma = \frac{1}{4} \sigma_0 (1 + 3\alpha^2) (1 + \delta_{WM}) \frac{\epsilon_e p_e c}{(m_e c^2)^2} \delta(\epsilon_\nu - \epsilon_e - \Delta_{np}), \quad (6.4)$$

where $\delta_{WM} \approx -0.0035 \cdot (\epsilon_\nu - \Delta_{mn}/2) \text{ MeV}^{-1}$ is the weak-magnetism correction and Δ_{mn} the mass difference between the neutron and proton masses.

Electron neutrino - electron elastic scattering (ENES)

The elastic scattering of an electronic neutrino with an electron,

$$\nu_e + e^- \rightarrow \nu_e + e^-, \quad (6.5)$$

is the second most important interaction for MeV CCSN neutrinos in ice, however, it only represents around 1.7% of the expected signal in IceCube [168].

The angular cross section of this interaction is implemented in the simulation as [172]:

$$\frac{d\sigma}{d \cos \theta} = \frac{2G_F^2 m_e^2}{\pi} \frac{4E_\nu^2 (m_e + E_\nu)^2 \cos \theta}{[(m_e + E_\nu)^2 - E_\nu^2 \cos^2 \theta]^2} \cdot \left[g_1^2 + g_2^2 + \left(1 - \frac{2m_e E_\nu \cos^2 \theta}{(m_e + E_\nu)^2 - E_\nu^2 \cos^2 \theta} \right)^2 - g_1 g_2 \frac{2m_e \cos^2 \theta}{(m_e + E_\nu)^2 - E_\nu^2 \cos^2 \theta} \right], \quad (6.6)$$

with the constants $g_1 = 0.73$ and $g_2 = 0.23$ and θ being the angle between the incident neutrino and the outgoing electron. In this interaction, the direction of the outgoing electron likely preserves the direction of the incident neutrino. The energy of the outgoing electron can be obtained as [172]:

$$E_e = \frac{2m_e E_\nu^2 \cos^2 \theta}{(m_e + E_\nu)^2 - E_\nu^2 \cos^2 \theta}. \quad (6.7)$$

The total cross section of the interaction can be written as [173]

$$\sigma = \frac{G_F m_e E_\nu}{2\pi} \left[\frac{4}{3} \sin^4 \theta_w + (1 + 2 \sin^2 \theta_w)^2 \right], \quad (6.8)$$

with θ_w as the weak Weinberg mixing angle, $\sin^2 \theta_w = 0.231$ [173].

Interactions not included in this study

In this study, only positrons from IBD and electrons from ENES are generated in the simulations, as they are the largest contributors to the expected signal from MeV CCSN neutrinos in IceCube [168]. This means that the γ produced by the neutron capture after IBD is not included, whose interaction is unlikely to be detected in several PMTs at the same time due to its low energy. Furthermore, other possible interactions, such as elastic scattering of other neutrino flavors with e^- , or $\bar{\nu}_e$ interacting with oxygen nuclei, are not included in this study. This simplification potentially reduces the total event rate by $\sim 5\%$ (see Table 1 in [168]).

6.2 Detecting MeV CCSNe in current IceCube

The optical modules in IceCube are not sufficiently close to each other to enable the identification of MeV supernova neutrinos individually. For such a capability, the detector would need to detect the event in at least two different photosensors, and ideally more. This is very unlikely since the generated particles after a MeV neutrino interaction travel only a few centimeters in the ice in which light is being generated. Although this light can travel even hundreds of meters in the IceCube sensitive volume, chances that the interaction can be traced back are very low. As previously shown, a burst of neutrinos is emitted during the collapse of the star. The intensity of such a burst peaks after ~ 1 s and lasts for ~ 10 s, after which its intensity decreases considerably. If a CCSN occurs close enough, a large number of MeV neutrinos would go through the instrumented volume, and a portion of them would potentially interact within it. Thus, modules along the whole detector can see an increase in their count rates. Since the background rate remains constant over time, with only a small seasonal modulation due to changes in the atmospheric muon flux, a rise on top of the background level can be associated with MeV CCSNe neutrino burst detection [168]. This method is referred to in this chapter as *rate-excess* method.

For this purpose, the photomultiplier rates are continuously monitored, stored, and buffered on each DOM and transferred to the supernova data acquisition system (SNDAQ). The SNDAQ is connected by a low-latency satellite, which is used to transmit alerts [168]. Depending on the level of trigger for SNDAQ, a different action is taken, from an email to experts to an alert sent to the SuperNova Early Warning System (SNEWS) [174, 175]. SNEWS involves an international collaboration of supernova neutrino detectors, IceCube, among them, which aims to send alerts of CCSN detection to its subscribers, including astronomical observatories, neutrino detectors, or even amateur astronomers and citizen scientists. Since the expected SN rate in the Milky Way is about 1.64 ± 0.46 per century [57], the requisite to send a *gold* alert is defined as the signal exceeding a certain threshold high enough to limit the false SN detection rate to ≤ 1 per century, however, the system also

receives and distributes signals with less significance [175]. In IceCube, the delay between the events being detected by the DOMs and the alert signal arriving at SNEWS is about 6 min [168].

6.2.1 Background to CCSN studies in IceCube

IceCube rate-excess method to detect SN can only work if the background rates are stable enough. About 2% of the IceCube DOMs are excluded from SN analyses due to unstable rates. The rest of the modules are monitored for SN detection, both from the high-energy array and DeepCore [176]. The average rate for standard efficiency DOMs is about 540 s^{-1} [168] (a bit higher in DeepCore DOMs), of which it is estimated to be divided into the following:

- 3 – 30 Hz from untriggered atmospheric muons. Although the majority of atmospheric muons are detected by the trigger, a small fraction manages to penetrate into the inner volume and elude association with a muon track by the algorithms, thereby contributing to the background. After losing its energy, μ^\pm decays into e^\pm with energies in the range of tens of MeV, which can also be confused with MeV SN neutrinos. The upper part of the detector is most affected by atmospheric muon-induced noise. The IceCube SN detection system has a dedicated algorithm to identify and therefore reduce the rate of positive false triggers due to statistical agglomerations of cosmic ray muon-induced hits [176].
- ~ 40 Hz due to thermal emission on the PMT photocathode and induced afterpulses [168] (see Section 3.6).
- The remaining background rate comes mainly from radioactive decays in the glass of the pressure vessel (see Section 3.6), with a large fraction of hit bursts that last up to 15 ms coming from scintillation after α or β decays [168]. This is the largest contribution to the total background rate.

The data acquisition system is designed to reduce the noise rate by eliminating correlated hits within a single module, trying to maintain the uncorrelated ones unmodified, and enforcing a dead time after every count. This considerably reduces the correlated component of the background. After an appropriate dead time of $250 \mu\text{s}$, the average noise rate per DOM is reduced to ~ 280 Hz [168].

6.2.2 IceCube’s CCSNe detection capabilities

The significance of IceCube for the detection of CCSNe as a function of distance is shown in Figure 6.1 right for the Lawrence-Livermore model [177] and assuming different oscillation scenarios. The inverted hierarchy oscillation scenario yields the best results due to the energetic $\bar{\nu}_x$ oscillating into $\bar{\nu}_e$, which later interacts by IBD, while the scenario without oscillation leads to the weakest signal. Using this model, IceCube would be able to observe CCSNe throughout the Milky Way, with $\sim 12\sigma$ significance at 30 kpc. The sensitivity to the next closest CCSN population residing in the Large Magellanic Cloud (LMC) is about 5σ , however, this is already below the 0.1 year^{-1} false trigger rate caused by the atmospheric muons. The next CCSN population in the Small Magellanic Cloud (SMC)

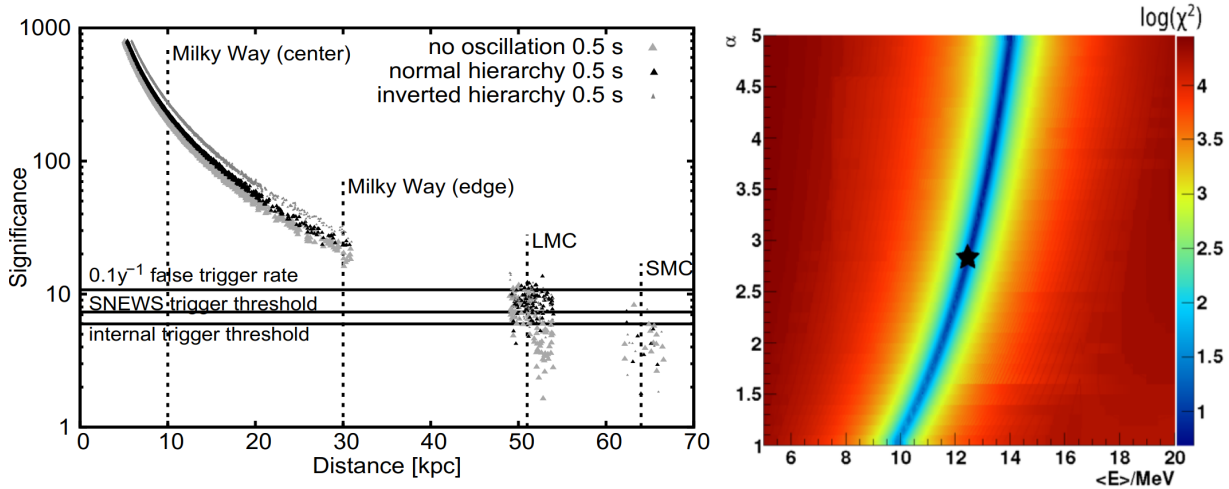


Figure 6.1: **Left:** Significance of IceCube for detecting CCSNe expressed in terms of one sided Gaussian standard deviations, as a function of the distance assuming the Lawrence-Livermore model [177], for the 3 different oscillation scenarios. The density of data points stands for the star distribution. Horizontal lines shows some trigger levels for different false detection rates. The SNEWS trigger rate shown correspond to one false trigger every 10 days on average. Figure from [168]. **Right:** Reconstruction of $(\langle E \rangle, \alpha)$ parameters of CCSN neutrinos energy distribution through a χ^2 method using simulated neutrinos of a $8.8 M_{\odot}$ progenitor star at 10 kpc. Figure from [178].

already lies below one false detection every 10 days, and the significance CCSNe detection here is about $\sim 3\sigma$ [168].

IceCube also has the capability to reconstruct the average neutrino energies using a comparison of single rates with coincident rates between different DOMs in the detector. Although coincidences between different modules are unlike at these energies, if the CCSNe is close enough, this method is still usable. The results of this are shown on Figure 6.1 on the right. Neutrino energies have been modeled using the mean energy of the burst and a shape parameter α . The figure shows that the parameters can be constrained, but the degeneracy between them can not be resolved [178]. The energy model is explained later in detail, as it is also used in this work, in Section 6.4.1.

For a CCSN in the center of our galaxy, IceCube would detect a large number of neutrinos, allowing for a clear distinction between the accretion and cooling phases and an estimation of the progenitor mass. It also has the ability to distinguish between inverted and normal hierarchies for a large fraction of CCSN bursts occurring in our Galaxy [176].

6.3 Effective volume of a detector with mDOMs

Results of this section were first obtained by the author for his master thesis [159], and are summarized here for their later use in weighting the CCSN neutrino events.

The effective volume is a quantification of the capability of the optical module to detect certain type of events, in this case MeV neutrino interactions. It can be seen as the volume around the module in which any interacting event would be detected. Of course, this is

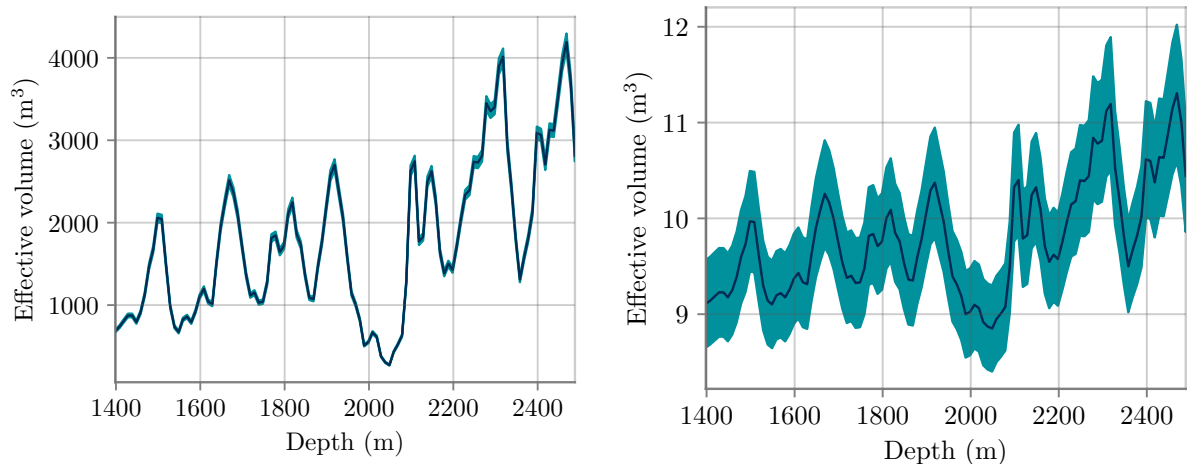


Figure 6.2: Left: Effective volume of a mDOM for CCSN MeV neutrinos as a function of the depth of the module, obtained simulating e^- of 25 MeV. **Right:** Same but only for events detected in 4 different PMTs at least. Shaded region stands for the statistical uncertainties. The results shown in this figure were obtained by the author for the first time for [159] and later published in [143].

a generalization since this would ultimately depend on the direction of the event itself, scattering processes, etc. In this section, the Geant4 mDOM simulation presented in Chapter 5 is used to calculate this quantity and compare it with the IceCube value. This can also be used to check whether the simulation yields a reasonable result. The effective volume is also used later as a measure to scale the detected events depending on the optical properties of any module in the detector. All studies done in this chapter include a single mDOM with no external components.

The effective volume for the detection of MeV neutrinos with mDOMs is calculated as

$$V_{\text{eff}} = \frac{N_{\text{det}}}{N_{\text{gen}}} \cdot V_{\text{gen}}, \quad (6.9)$$

being N_{gen} and N_{det} the number of events generated and detected, respectively, and V_{gen} the generation volume. The generation volume must be large enough to ensure that increasing the generation volume would not further increase the effective volume. To do that, using the Geant4 simulation (see Chapter 5), electrons¹ of 25 MeV are produced in a spherical generation volume of ice with the mDOM in its center at different depths, i.e. different optical properties of the ice, with randomized e^- position and direction. The generation of the electron stands for the ENES interaction of a CCSN neutrino.

The effective volume should approximately scale linearly with the absorption length; thus a linear fit is done, and the values are extrapolated to any depth in the detector. The effective volume of the mDOM depending on the depth is shown on the left side of Figure 6.2. On the right side of the figure, the effective volume is calculated with the condition that the event was detected in at least 4 different PMTs. The effective volume of a single mDOM has a maximum value of about 4000 m³ at depths where the ice is cleaner (see Figure 5.4).

¹Similar result is expected when generating e^+ corresponding to the IBD instead of e^- from ENES.

Table 6.1: Effective volume and effective mass for IceCube and a detector equipped with 10 000 mDOMs for the detection of e^- with an energy of 25 MeV. IceCube data obtained from [168]. mDOM results include only statistical uncertainties, while IceCube results also include systematic ones. The results shown in this table were obtained by the author for the first time for [159] and later published in [143].

	\bar{V}_{eff} per module (m^3)	Total V_{eff} (m^3)	Total M_{eff} (Mton)
IceCube	725 ± 95	$(3.8 \pm 0.5) \times 10^6$	3.5 ± 0.5
10 000 mDOMs	1776 ± 6	$(1.705 \pm 0.005) \times 10^7$	15.71 ± 0.05

When applying the condition of being detected in several PMTs, the effective volume is obviously considerably smaller. It is important to note that, without any condition, the effective volume is much more sensitive to the absorption length, whereas when the event is detected in different PMTs, the effective volume is less dependent on the optical properties of the ice. Most of the events detected in several PMTs are generally generated very close to the modules; therefore, the photons are less affected by changes in the ice properties since they simply travel less distance.

The results are averaged for all depths and compared with IceCube [168] in Table 6.1. The results for mDOM are approximately 2.4 larger than those for IceCube DOMs, in agreement with the larger effective area of the modules. The effective volume is also given assuming an IceCube-Gen2 detector composed of 10000 mDOMs. The equivalent mass of such detector is also calculated, being ~ 4.5 times the equivalent mass of the current IceCube.

6.4 MeV CCSN neutrino simulation

This section describes how the Geant4 simulations for CCSN MeV neutrinos presented in this chapter were made. The simulation of the mDOM and the South Pole ice is as described in Chapter 5. The results are calculated for an IceCube-Gen2 detector composed of 10000 mDOMs equally distributed between 1400 and 2490 m depth. Although IceCube-Gen2 would probably extend towards deeper ice, here the study is limited to the depths whose ice properties were measured in [102].

6.4.1 Description of the CCSN burst models

To simulate the passing of neutrinos from CCSN bursts, two flux models [179] are employed to generate the events in this chapter¹. Both models are based on the *LS220* (Latimer-Swesty) Equation of State (Eos) [180], and involve:

- A CCSN from a progenitor star with mass $27.0 M_{\odot}$, which leads to a neutron star of $1.77 M_{\odot}$ [179].

¹Models were kindly provided to the author by *T. Hanka*.

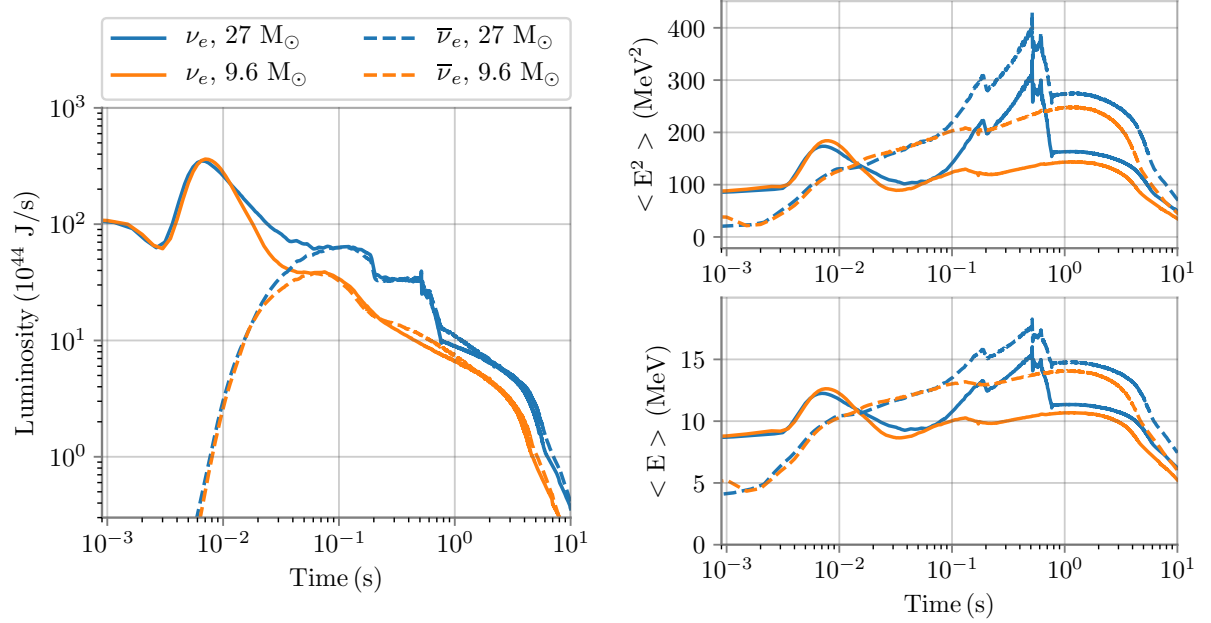


Figure 6.3: Luminosities, mean energies and mean squared energies of electronic neutrinos and antineutrinos for the 2 type II-p CCSN models used in this chapter to simulate a MeV neutrino burst. Models from [179]. Slightly modified version of the figure published by the author in [143].

- A CCSN from a progenitor star with mass $9.6 M_{\odot}$, resulting in a neutron star of $1.36 M_{\odot}$ [179].

Both progenitor masses are close to the low and high limit for these types of events, since lighter progenitors than $\sim 8 M_{\odot}$ would likely result in a white dwarf, while heavier than $\sim 35 M_{\odot}$ would end up creating a black hole. The fluxes are modeled after calculating the iron-core collapse and bounce, neutrino transport, and the propagation of the shock [179]. Calculations are made in one dimension. Although neutrino-powered supernovae cannot be represented in such a way, multidimensional models are computationally very intensive and the community still debates how to perform them properly [179]. One-dimensional simulations are precise enough for the purpose of this study, and it also allows for longer simulations than multidimensional ones, which are usually limited to fluxes of about 1 second or less.

The fluxes contain information on neutrino and antineutrino luminosities, mean energies, and mean squared energies. The fluxes are shown in Figure 6.3 for the first 10 seconds of the burst, for electronic neutrinos and antineutrinos. One can observe the different phases during the flux, with the neutronization peak, where the luminosity for ν_e is at maximum, followed by the accretion phase, where the ν_e and $\bar{\nu}_e$ fluxes present roughly equal intensity, since both are mostly created by pair production. Here is where the neutrinos have larger energies, with a maximum $\langle E \rangle$ of ~ 17.5 MeV for the case of the $27.0 M_{\odot}$ and ~ 14.5 MeV for the $9.6 M_{\odot}$ model, for the case of antineutrinos. Electronic neutrino energies are generally below the antineutrino counterpart, except at the neutronization peak instant. Lastly, during the cooling phase, the intensity and energies of the fluxes rapidly decrease. Both models behave similarly up to the neutronization peak; however, at the accretion phase, the flux and neutrino energies are higher for the heavier model, therefore, it can be

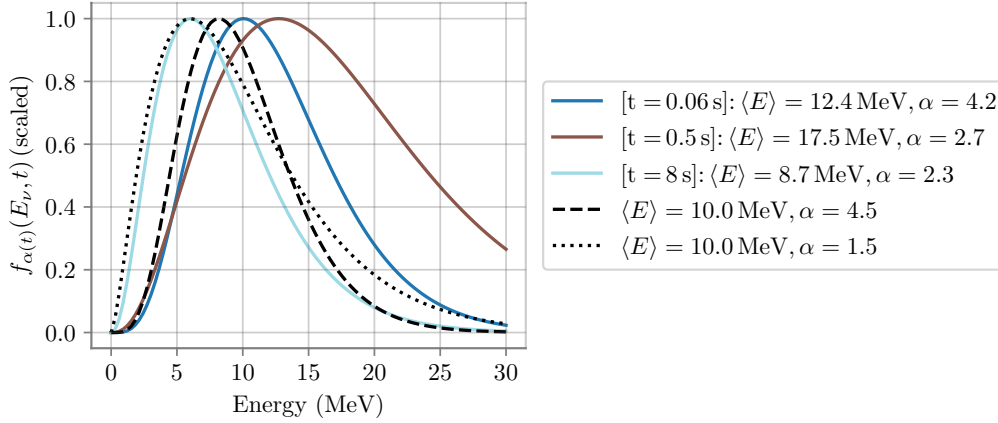


Figure 6.4: Energy spectra at different times of $\bar{\nu}_e$ from the $27.0 M_{\odot}$, together with two reference curves with the same mean energy but different α . Slightly modified version of the figure published by the author in [143].

expected that more events are detected from this one.

From the mean and squared mean energies, the model proposed in [181, 182] is used to obtain the neutrino energy spectra as

$$f_{\alpha(t)}(E_{\nu}, t) \propto E_{\nu}^{\alpha(t)} \cdot \exp \left[- (\alpha(t) + 1) E_{\nu} / \langle E_{\nu} \rangle (t) \right], \quad (6.10)$$

where ν stands for both neutrino and antineutrino and $\alpha(t)$ is a numerical parameter that describes spectral pinching, which can be calculated from as [181]

$$\frac{\langle E_{\nu}^2 \rangle (t)}{\langle E_{\nu} \rangle^2 (t)} = \frac{2 + \alpha(t)}{1 + \alpha(t)}. \quad (6.11)$$

In Figure 6.4 the energy spectra at different phases of the $27.0 M_{\odot}$ model for electronic antineutrinos are shown together with two reference curves. The curve at $t = 0.06$ s corresponds to the neutronization peak, where the energy and flux of the antineutrinos is still small. The next line represents the spectrum during the accretion phase, near the maximum mean energy. It is observed that, while the mean energy is $\langle E \rangle = 17.5$ MeV, the spectrum extends to energies above 30 MeV during this phase. These higher-energy neutrinos are more likely to be detected because of a larger cross section and higher Cherenkov yield. Lastly, during the cooling phase ($t = 8$ s in the figure), the energy spectrum is narrower and peaks at lower energies. Reference curves are added with fixed parameters that share the same $\langle E \rangle$ but different α . This shows that the spectrum peaks at lower energies for smaller values of α , but in this case its tail is also extended towards higher energies.

6.4.2 CCSNe simulation

The algorithm to generate CCSN neutrino interactions within the Geant4 mDOM simulation and the math to weight the events were first developed by the author for his master thesis [159], being updated and expanded during the realization of this Ph.D.

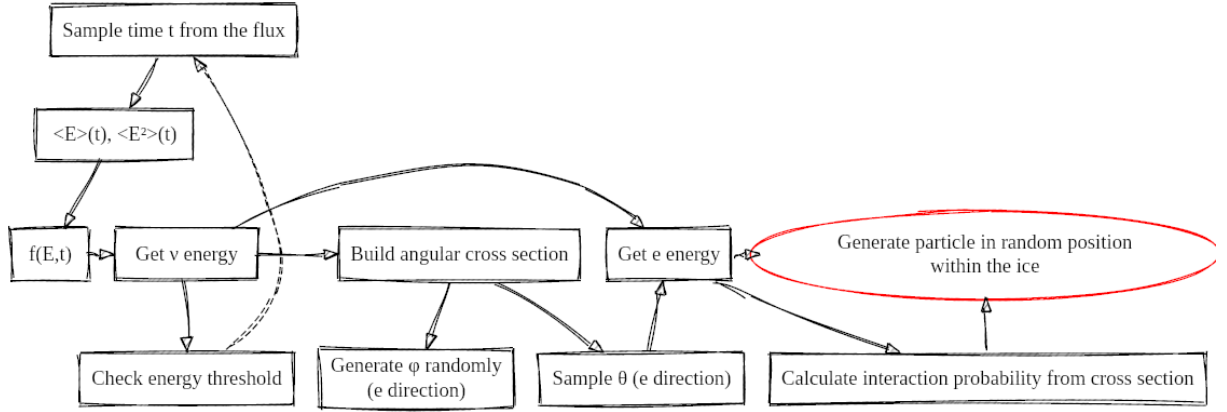


Figure 6.5: Diagram of the steps involved to generate the events for the simulation of CCSN neutrinos. The scheme is valid for both IBD and ENES, except for the threshold check. Here, e stands for both electron from ENES or positron from IBD, and ν for both electronic neutrino from ENES or electronic antineutrino from IBD.

To simulate the passing of MeV CCSN neutrinos through a detector with mDOMs, the previously described Geant4 simulation (see Chapter 5) is used again. The generation volume is simulated as a cylinder of 40 m long and 20 m radius of South Pole ice facing the SN direction with the mDOM in its center. This arrangement simplifies the calculation of the weights that are explained later. The ice properties can be selected at any depth shown in Figure 5.4, but remain constant within the simulated volume. The neutrino burst is simulated as coming from the zenith. A different burst direction should not affect the results, since the effective area of mDOM is approximately isotropic, as well as the direction of the positrons after IBD.

The neutrinos are not directly generated in the simulation, since its low interaction cross section would make the process extremely inefficient. Instead, the resulting particles from the interactions described before are directly produced in the ice with their corresponding energy and direction. The workflow, exemplified by the sketch shown in Figure 6.5, is the following:

1. Using the models described before, the expected flux per area is calculated from the luminosity $L(t)$ and the mean energy $\langle E(t) \rangle$ as

$$\Phi(t) = \frac{1}{4\pi d^2} \cdot \frac{L(t)}{\langle E(t) \rangle}. \quad (6.12)$$

2. Using the distribution of $\Phi(t)$, a time t of the burst is sampled using the inverse CDF (Inverse Cumulative Function) method [183]. All other sampling from distributions done here also employs the inverse CDF method.
3. For the sampled time t , the corresponding mean energy and the mean squared energy are obtained from the models. These parameters are used to construct the energy spectrum $f(E, t)$ from Eq. 6.10.
4. The neutrino/antineutrino energy E_ν is sampled from $f(E, t)$. If the energy is below the threshold for the IBD, the algorithm returns to the second step.

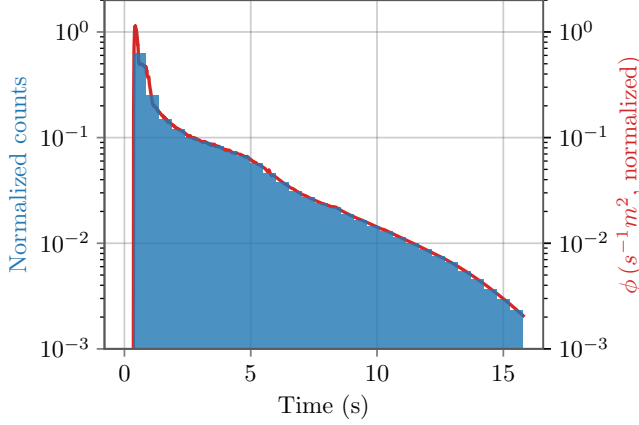


Figure 6.6: Generation test for IBD of the $27.0 M_{\odot}$ progenitor mass CCSN model. The left axis stands for the histogram data, showing the normalized counts after generation in the Geant4 simulation. The right axis shows the flux of the model used to generate the events.

5. From E_{ν} , the angular cross section is constructed using Eq. 6.6 or Eq. 6.2, depending on the interaction. From this, the angle θ between the incoming neutrino and the generated e^{-}/e^{+} is sampled. The ϕ direction is randomly generated between 0 and 2π .
6. The energy of e^{-}/e^{+} is calculated from θ and E_{ν} using Eq. 6.3 or Eq. 6.7, depending on the interaction. The interaction probability is saved using the corresponding total cross section to calculate the interaction weight (described below).
7. The e^{-}/e^{+} is generated at a random position in the ice volume.

A generation test is performed and shown in Figure 6.6 for the case of inverse beta decay from the $27.0 M_{\odot}$ model. The histogram data following the model shows that the simulation is producing the events properly. Similar tests were performed for the angular distribution, for the ENES interaction, and for the $9.6 M_{\odot}$ model to ensure that the whole algorithm works as intended.

After generation, a weight must be assigned to each event. The weight is composed of 3 components, accounting for the interaction probability, the SN flux through the simulated volume, and the different optical properties of the modules at different depths:

$$W = W_{\text{int}}(E) \cdot W_{\text{flux}}(d) \cdot W_{\text{eff}}. \quad (6.13)$$

- The interaction probability weight stands for the probability that such a neutrino or antineutrino event would interact when traveling through the simulated volume:

$$W_{\text{int}}(E_{\nu}) = \sigma(E) \cdot n_{\text{target}} \cdot l, \quad (6.14)$$

being $\sigma(E_{\nu})$ the total cross section for the interaction, n_{target} the number of targets for such interaction per unit of volume, and $l = 40$ m the length of the generation volume within the neutrino direction axis. Due to the generation volume being a cylinder facing the CCSN, this is simply the length of such cylinder.

- The flux weight,

$$W_{\text{flux}} = \frac{4\pi r^2}{N_{\text{gen}}} \cdot \int \phi(t) dt = \frac{1}{N_{\text{gen}}} \cdot \frac{r^2}{d^2} \cdot \int \frac{L(t)}{\langle E(t) \rangle} dt, \quad (6.15)$$

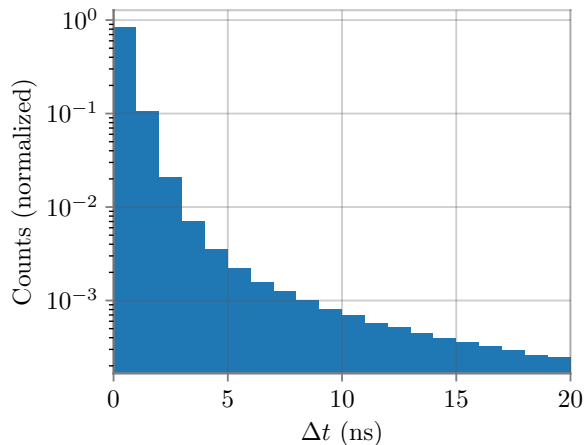


Figure 6.7: For events detected in coincidences, time difference between first and last detected photon in different PMTs within the same mDOM. Updated version of the figure published by the author in [143].

weights the events according to the total flux traveling through the finite simulated volume. Here $r = 20$ m is the radius of the cylindrical generation volume and d stands for the distance from Earth at which the CCSN is assumed to occur.

- The last component W_{eff} takes into account the different optical properties depending on the depth of the module. Since only a single module is being simulated, when extrapolating the results to a detector with more modules, it must be considered that modules are at different places and, as such, the ice surrounding them would have different optical properties. This is calculated using the effective volume obtained before as

$$W_{\text{eff}} = N_{\text{modules}} \cdot \frac{\langle V_{\text{eff}}(m) \rangle}{V_{\text{eff}}(m, z_{\text{sim}})}. \quad (6.16)$$

Here, N_{modules} is the total number of modules included in the simulated detector, $V_{\text{eff}}(m, z_{\text{sim}})$ is the effective volume at the depth at which the simulation is performed, and $\langle V_{\text{eff}}(m) \rangle$ is the mean effective volume for all modules in the simulated detector. m stands for multiplicity, defining multiplicity as the number of different PMTs within a single module that has detected the event. It was shown before that the ice properties have a larger impact when considering events detected in a single PMT than events detected in several PMTs within the same module. Thus, this is taken into account by separating the events at this stage into multiplicities and applying the corresponding weight. Therefore, this factor affects events detected in a single PMT in a more significant way, and its importance decreases with increasing multiplicity.

6.4.3 Results for galactic CCSNe

The simulation is performed as previously described for the two CCSN models, assuming that the event occurs at 10 kpc from Earth, approximately the distance to the center of the Milky Way, and considering only a no-oscillation scenario. This is the most conservative choice, since for both normal and inverted mass ordering scenarios, an increase in the number of detected MeV neutrinos would be expected [168].

The simulation yields a total of 2.7×10^6 detected events for the model with $27.0 M_{\odot}$ progenitor mass, while the quantity decreases to $\sim 1.1 \times 10^6$ for the lighter model with $9.6 M_{\odot}$ progenitor mass. Furthermore, $\sim 13\%$ of events are detected in more than one

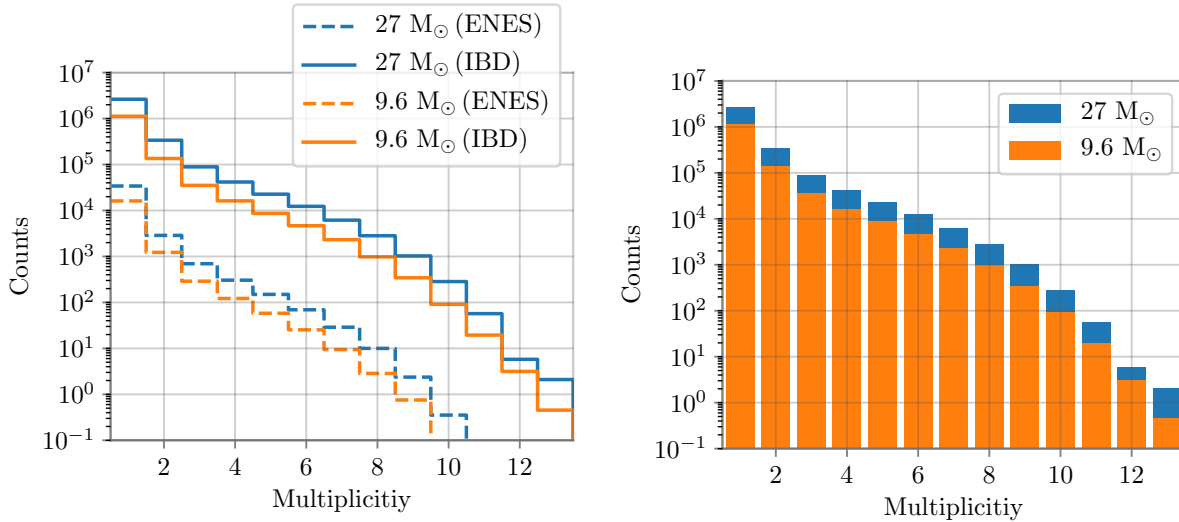


Figure 6.8: Detected events in a detector with 10000 mDOMs for two models of type-II CCSNe with different progenitor masses, as a function of the multiplicity within $\Delta t_{\text{coin}} = 20$ ns, for CCSNe at 10 kpc and considering the first 10 seconds of the neutrino burst. In the **left**, the counts are separated into the different interactions that were simulated, with the overall counts in **right**. Updated version of the figure published by the author in [143].

PMT when simulating the heavier CCSN model, while $\sim 12\%$ for the second one. When multiple PMTs detect the event, the light reached all PMTs in very short times. This is shown in Figure 6.7, where the time difference between the first and last detected photons is plotted in a histogram¹. For $\sim 85\%$ of the events detected in coincidences (i.e. by several PMTs within a single module), these occur within 1 ns. A time window of 20 ns covers 99.5% of all coincidences. This is due to the proximity of the interaction vertex to the modules, while longer coincidence times would indicate indirect photons detected after undergoing scatter a few times. Note that these are the arrival photon times to the photocathode, since the PMT itself is not simulated. The detected photon times by the real module would be smeared as a result of the transit-time spread of the PMTs.

The detected events are plotted in a histogram according to their multiplicity, which is shown in Figure 6.8. A time condition has been applied, requiring that the coincidences occur within a time window of $\Delta t_{\text{coin}} = 20$ ns. The time window is long enough considering the expected PMT time resolution [184], and it can serve to identify events from the background afterwards. On the left side of Figure 6.8, the contribution of each interaction is shown separately. IBD dominates over ENES by roughly 2 orders of magnitude. ENES events are also less likely to produce coincidences, as these drop from $\sim 13\%$ to $\sim 8.5\%$ of all detected events for the $27.0 M_{\odot}$ model, and a similar drop occurs for the $9.6 M_{\odot}$ model. The reason why additional interaction channels are not considered in these simulations is because the second most significant interaction is already nearly negligible. On the right side of Figure 6.8, the number of events detected per multiplicity condition is shown by summing both interactions. It can be seen that both models behave similarly when multiplicity is increased, although the lighter SN model overall has a lower ratio of events in coincidences.

¹The figure is done for the case of the $27.0 M_{\odot}$ progenitor mass model, but it is indistinguishable from the $9.6 M_{\odot}$ one.

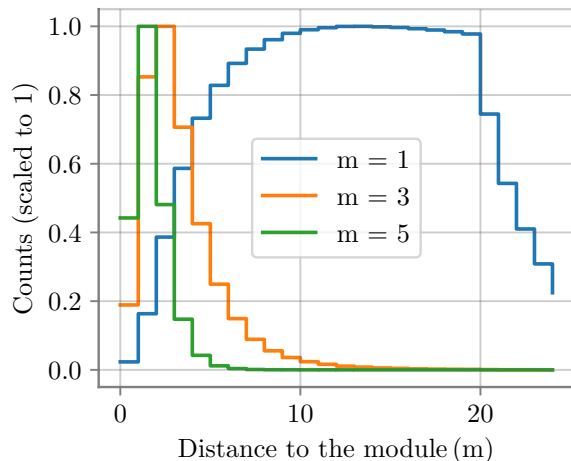


Figure 6.9: Distance from interaction vertex to the center of the module for the detected events applying different multiplicity conditions, y-axis scaled to one. The events are generated in a cylindrical volume of 20 m radius and 40 m long, with the mDOM and its center.

Comparing the results obtained here with the IceCube results, IceCube expects $(0.57 \pm 0.18) \times 10^6$ [168] events from all interaction channels assuming a normal hierarchy scenario from a CCSN of $15 - 20 M_{\odot}$. Using the ratio between the effective volumes, this would translate into $\sim 2.6 \times 10^6$ expected events for the detector simulated here. As a first approximation using the results in [168] for different and non-oscillation scenarios, this can be scaled down to $\sim 2.3 \times 10^6$ events for the no-oscillation scenario, to directly compare with the results here. This lies in between what has been obtained here for both models, as expected due to the mass of each model.

Note that the size of the generation volume, which had to be constrained to the chosen cylinder size for computational reasons, causes an underestimation in the total detected events obtained here. As shown in Figure 6.9, the volume of generation is too small, since many events generated in the edge of the generation volume are still being detected, and it can be expected that events generated farther from the module will also be. This does not affect events detected in coincidences, since these are generally generated much closer to the module. In conclusion, the limited size of the generation volume decreases the total detection rate; however, events in coincidence should not be affected. Note that Figure 6.9 has not been scaled according to the differential volume contained in each bin, thus the density of events detected at a large distance from the module is much smaller than closer to the module.

6.5 Background simulation

In this study, three different sources of background are considered: intrinsic uncorrelated component of the PMT dark rate, radioactive decays within the pressure vessel glass, and solar neutrinos.

Uncorrelated PMT dark rate

The calculation of the uncorrelated noise rates explained in this section was first developed by the author for his master thesis [159], based on a similar approach presented in [169].

As discussed in Section 3.6, there are multiple sources that produce the so-called dark rate

on the photomultipliers. The dark rate of the mDOM PMT has been measured in [184] to be on average 30 s^{-1} at -30° , which is a good average temperature for operating modules in deep ice. However, the dark rate in PMTs varies from unit to unit, with some units with rates as high as 50 s^{-1} at -30° . Here, all PMTs are approximated to have the same rates. To be conservative, the dark rate is assumed to be $f_d = 50\text{ s}^{-1}$ for all PMTs.

To calculate the probability that the dark rate would produce a signal in m PMTs of a mDOM within a time window Δt_{coin} , first the probability that the PMT would produce a dark rate signal is obtained through the complementary probability of not detecting anything at all, as

$$P_d = 1 - P(0, \mu = f_d \Delta t_{\text{coin}}) = 1 - e^{-f_d \Delta t_{\text{coin}}}, \quad (6.17)$$

using the Poisson distribution. Then, once the first photon is detected, the probability that $m - 1$ more PMTs detect dark-rate-induced signal within the time window is given by

$$P_{\text{dark}} = 1 - B_{\text{cum}}(m - 2 | N_{\text{PMT}}, P_d), \quad (6.18)$$

again using the complementary probability, with N_{PMT} the number of PMTs in a module and $B_{\text{cum}}(m | n, p) = \sum_{k=0}^m \binom{n}{k} p^k (1 - p)^{n-k}$ the cumulative binomial distribution for m successes out of n tries when the probability of success is p . Finally, the rate at which this occurs in a detector with N_{tot} mDOMs is given by

$$f_{\text{bg}}^{\text{PMT}} = P_{\text{dark}} \cdot f_d \cdot N_{\text{tot}}. \quad (6.19)$$

Radioactive decays from the module's glass

The contribution of radioactive decays from the module glass to the detection rate was measured and simulated within the scope of a Ph.D. thesis [185] and the results were then provided to the author.

Radioactive decays can be detected by the modules after their generated particles induce light production mainly through Cherenkov or scintillation effect. The radiation levels of the borosilicate mDOM glass (Vitroplex) were measured, detecting mainly elements from the ^{235}U , ^{238}U and ^{232}Th chains, together with a significant contribution of ^{40}K , while radioactive decays from other parts of the module are negligible¹ [185].

The isotopes activities are used to simulate the chains in the Geant4 simulation, assuming secular equilibrium. The number of isotopes that decay within a time window of 20 min is randomly drawn from a Poisson distribution in each simulation run. Each decay chain is simulated separately, with the detected photon times combined later. The temporal correlation between mother and daughter is preserved when the decay time is within the time window. Otherwise, the decay time is decided randomly within the time window, preserving the number of decays. Afterwards, the hits are checked for coincidences, using the same time window as above of 20 ns. The simulation is done only at a fixed depth; however, changing the ice properties does not have a significant impact on the rates.

¹There is a contribution to the correlated radioactive background from the decays in the PMT glass. Although this should be much smaller than the contribution from the vessel, the majority of mDOM PMTs received for ICU shows a much larger radioactive contamination than initially expected. This is discussed and considered in Section 6.9.

Solar neutrinos

As explained in Section 2.3.1, the Sun generates a large neutrino flux that reaches Earth, although most of them have very low energies. Those with energies above the Cherenkov threshold in ice originate mainly after β^+ decays of ${}^8\text{B}$, producing electron neutrinos of energies around ~ 10 MeV [39], thus similar energies of the SN neutrinos on which this study is focusing. These may interact within the vicinity of the modules and be indistinguishable from CCNS MeV neutrinos. Although these events are not a significant source of background for IceCube SN studies, they are simulated here to check whether their influence is more important at high multiplicities. The impact of solar neutrinos is simulated with Geant4 using a total flux of $\Phi_{\nu_e} = 1.7 \times 10^6 \text{ cm}^{-2}\text{s}^{-1}$ and $\Phi_{\nu_{\mu,\tau}} = 3.3 \times 10^6 \text{ cm}^{-2}\text{s}^{-1}$ [186]. Only the elastic scattering of each neutrino flavor with the electrons in the ice is considered, since these interactions dominate by two orders of magnitude [187].

Non-included background sources

The most important background sources that are not included in this chapter are:

- Muons or electromagnetic showers from low-energy atmospheric neutrinos: these neutrinos, with energies between 10 MeV and 1 GeV, might be confused with the MeV CCSN ones, especially the lowest energetic ones. However, this was not included due to its low interaction rate of only $\sim 1 \text{ s}^{-1}$ in a Gton volume of ice [188].
- Cosmic-ray-induced atmospheric muons: being a considerable part of the current detector background in many studies, these muons can penetrate into the instrumented volume. The majority of them can be identified and thus rejected, which would result in a short dead time. However, since they lose energy while traveling through the ice, there is the possibility that they reach the instrumented volume just with enough energy or direction to do not leave a whole signature in the detector and instead just leave a pattern similar to MeV interactions, which would then be part of the background for this analysis. Furthermore, after μ^\pm decay, a e^\pm is generated, which can also be confused with the events studied in this chapter. Due to the simulations here being done with a single module, one can not evaluate how good the muon identification might be, which would depend on the whole geometry. Therefore, it has been decided not to include this source in the calculations as its significance can only be speculated at this point. A brief discussion of muon identification and its potential implications within the current geometry is provided in Section 6.11.1.

Combining the background

The background produced by each source is calculated or simulated as previously described, and the results are shown in Figure 6.10, as a function of the multiplicity of the events within $\Delta t_{\text{coin}} = 20 \text{ ns}$ for the proposed detector of 10000 mDOMs.

It can be seen that the majority of the expected background is coming from the radioactive decays within the glass vessel for any multiplicity condition. The uncorrelated PMT dark rate plays a significant role if no multiplicity condition is required; however, the chances to randomly produce coincidences in different PMTs within such short time window events within the given time window in different PMTs are much lower. Thus, the contribution from the uncorrelated noise rapidly decreases as the multiplicity condition becomes more

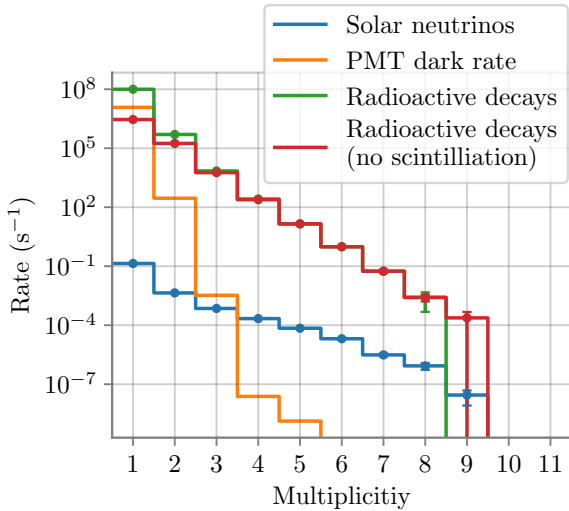


Figure 6.10: Expected background rates for a detector of 10000 mDOMs from radioactive decay, uncorrelated PMT dark rate and MeV solar neutrinos, as a function of the multiplicity within $\Delta t_{\text{coin}} = 20$ ns. The background induced by radioactive decays within the vessel glass is shown for the cases where scintillation effect has been included into the Geant4 simulation or not. Updated version of the figure published by the author in [143].

strict. Solar neutrinos present a flatter spectrum in multiplicity, however, its rate is several orders of magnitude smaller than that produced by the radioactive decays.

Regarding the radioactive decays, two different lines are shown in Figure 6.10. In green, the radioactive decays are simulated in Geant4 and the particles are allowed to produce light through scintillation¹. The data of the red line shows the result of running the radioactive decays simulation with scintillation disabled. Although the scintillation produces most of the light, this is produced at a slower rate than the Cherenkov light. Thus, it is less likely that these events would fulfill the multiplicity condition in such a small time window. The consequence is that for multiplicity 4 or greater, the Cherenkov effect dominates the detection rate, producing roughly all counts. Note that the cut in the histograms at high multiplicity is simply due to these events being very rare, and thus the simulation was incapable of producing them within the time that it was running. However, longer simulations shall produce events with greater multiplicity as well. The simulation of radioactive decays without considering scintillation is faster and enables better statistics at higher coincidence levels.

When using the sum of all the background sources throughout this chapter, it refers to the sum of each noise source presented here, where for the radioactive background the result with scintillation is used up to multiplicity 5. Above that, the results without scintillation, which have smaller statistical uncertainties and similar values, are used.

6.6 Identifying extra-galactic CCSNe

When trying to detect neutrinos from far sources, a logical problem arises: while the signal decreases rapidly with the square of the distance, the detector background rates is obviously maintained at the same level. Thus, rejecting the background as much as possible is necessary for detecting distant events. Here, the possibilities to detect distant CCSNe using the segmentation of the mDOM module are analyzed. As shown in Section 6.4.3, some neutrino events are in coincidences that occur only within a few nanoseconds. This

¹Scintillation properties of the mDOM glass were measured in [162]

is used here to set conditions to identify them over the background.

6.6.1 Trigger conditions using module's segmentation

The method explained in this subsection was first developed by the author for his master thesis [159].

Considering the brief, intense MeV burst from CCSNe lasts only a few seconds before rapidly declining, trigger conditions can be established to detect the signal of these neutrinos. These are defined as follows:

- a) A time window of length Δt_{coin} is opened once a PMT detects a photon. This short time window is aimed at looking for coincidences within the same module. Then, the first condition to be fulfilled would be to detect the event in, at least, $m - 1$ different PMTs within the time window after the first hit has been detected. When met, a *neutrino event* is claimed to be detected;
- b) Once a *neutrino event* is detected, a second longer time window ΔT_{SN} is opened to search for more *neutrino events* in the detector. If $N_\nu - 1$ more neutrino events according to a) are triggered in *any* module in the detector within a time window ΔT_{SN} , a supernova detection is claimed.

Within this work, the longer time window is kept to $\Delta T_{\text{SN}} = 10$ s, which cover fully covers the fluxes up to the most intense part of the cooling phase. This is a conservative choice, since only the first couple of seconds of the flux are the most intense. The shorter one is always fixed to $\Delta t_{\text{coin}} = 20$ ns, since the radioactive background simulation has been done only using this time window. Although it might be interesting to study the shortened Δt_{coin} , this would likely affect in the same way the radioactive noise and the signal, since both are mostly caused by fast Cherenkov photon generation.

6.6.2 False CCSN rate detection

The mathematical analysis of this subsection was first developed by the author for his master thesis [159].

The background can produce a signal satisfying the trigger conditions, which would unavoidably result in a number of false supernova detections N_{fSN} within a certain observation time δt . The number of false CCSN detection fulfilling the conditions can be calculated as

$$N_{\text{fSN}} = f_{\text{bg}}^{\text{tot}} [1 - P_{\text{cdf}}(N_\nu - 2, \mu = f_{\text{bg}}^{\text{tot}} \Delta T_{\text{SN}})] \delta t, \quad (6.20)$$

where P_{cdf} stands for a cumulative Poisson distribution, N_ν and ΔT_{SN} the values for the trigger condition explained before and $f_{\text{bg}}^{\text{tot}}$ is the rate at which the trigger condition a) with parameters $(\Delta t_{\text{coin}}, m)$ is met anywhere in the detector due to background, given as the sum of each individual contribution

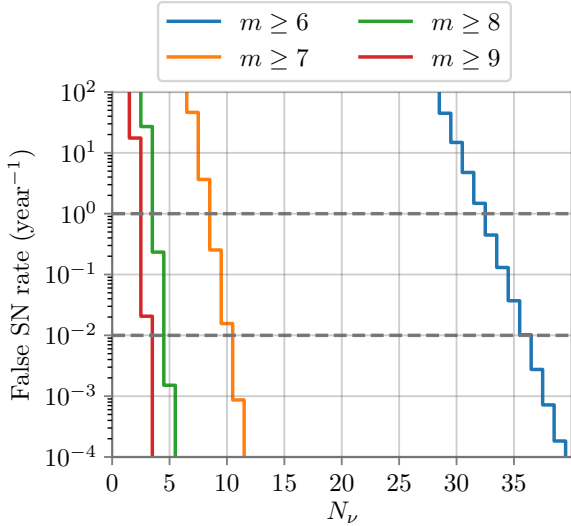


Figure 6.11: Expected false CCSN detection rate cause by background applying the trigger conditions a) and b), for different values of the multiplicity m and the number of required triggered events N_ν , with $\Delta T_{\text{SN}} = 10$ s and $\Delta t_{\text{coin}} = 20$ ns.

$$f_{\text{bg}}^{\text{tot}} = f_{\text{bg}}^{\text{PMT}} + f_{\text{bg}}^{\text{Decays}} + f_{\text{bg}}^{\text{Solar}}. \quad (6.21)$$

The question of which false CCSN detection rate $r_{\text{fSN}} = N_{\text{fSN}}/\delta t$ should be accepted is difficult to answer and would depend on the goals and the expected detection rate. If one can reach as far as Andromeda by having a higher r_{fSN} it might be worthwhile; however, for shorter distances, not many progenitors of CCSNe are expected, so a rather low r_{fSN} seems the most logical choice. Here, results are shown requiring $r_{\text{fSN}} \lesssim 0.01 \text{ year}^{-1}$ and for $r_{\text{fSN}} \lesssim 1 \text{ year}^{-1}$. The first, allowing 1 false CCSN detection per century, is the rate for a *gold alert* by SNEWS. In Figure 6.11 the false detection rate is shown for requiring different trigger conditions, maintaining $t_{\text{coin}} = 20$ ns and $\Delta T_{\text{SN}} = 10$ s. Using high multiplicity conditions, only a few events can drastically decrease the false detection rate, while lowering the multiplicity condition rapidly escalates the required N_ν to keep the false CCSN detection rate low.

6.6.3 Extra-galactic detection range

The mathematical analysis of this subsection was first developed by the author for his master thesis [159].

The probability of satisfying the conditions shown in Figure 6.11 for the CCSN models can be calculated from the simulation results. Taking into account that the simulation was originally weighted for a source at 10 kpc, the probability that N_ν neutrinos are detected from such a supernova at a distance d for a certain m condition is given by

$$P_{\text{SN}} = 1 - P_{\text{cdf}}(N_\nu - 1, \mu(d) = \mu_0(10 \text{ kpc}/d)^2), \quad (6.22)$$

with μ_0 being the expected number of detected neutrino events that pass the trigger condition at 10 kpc. The results are shown for both models in Figure 6.12, showing

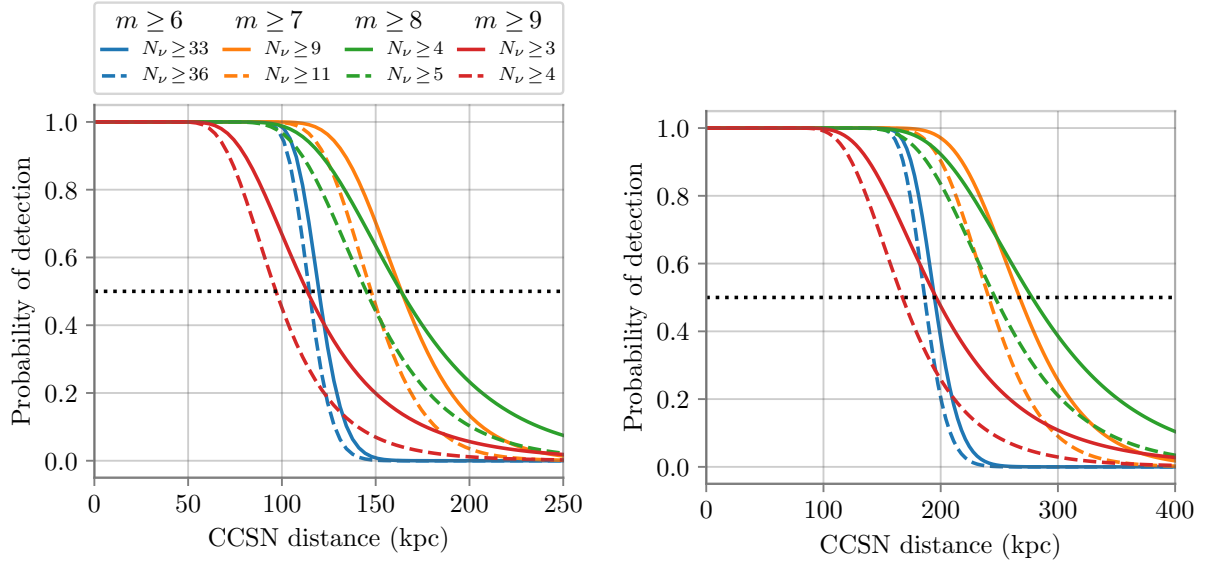


Figure 6.12: Probability of detecting a CCSN based on the $9.6 M_{\odot}$ model (**left**) or the $27.0 M_{\odot}$ model (**right**) as a function of the source distance for a detector equipped with 10000 mDOMs, using trigger conditions with multiplicity $\geq m$, being N_{ν} the number of events required at such multiplicity level. $\Delta t_{\text{coin}} = 20 \text{ ns}$ and $\Delta T_{\text{SN}} = 10 \text{ s}$ are used. A straight-line is show for the best condition resulting in $r_{\text{fSN}} \lesssim 1 \text{ year}^{-1}$, while a dashed line stands for the best conditon keeping $r_{\text{fSN}} \lesssim 0.01 \text{ year}^{-1}$. Updated version of the figure published by the author in [143].

the probability of detection for the less restrictive condition that still maintains a false detection rate of $r_{\text{fSN}} \lesssim 0.01 \text{ year}^{-1}$ or $r_{\text{fSN}} \lesssim 1 \text{ year}^{-1}$. Results for lower multiplicities are not shown since the detection range is considerably shorter in those cases. It can be seen the method would enable CCSN detection much beyond the galactic range. Generally, the ranges increase with increasing m due to less noise, up to a condition where the signal is too weak. The range in which the heavier CCSN is still detectable with 50% probability reaches 246 kpc for the best condition satisfying $r_{\text{fSN}} \lesssim 0.01 \text{ year}^{-1}$, while it reaches 278 kpc for the less restrictive condition of $r_{\text{fSN}} \lesssim 1 \text{ year}^{-1}$. For the case of the lighter CCSN model, the range goes to 147 kpc for the condition satisfying the *gold-alert* criteria, while it reaches 164 kpc for the less restrictive one. In both models $m \geq 7$ and $m \geq 8$ yield close results, but the tail of the curves with $m \geq 8$ is always extended to farther distances.

The ranges at which the CCSN is detected with 50% probability are summarized in Table 6.2 for the best trigger conditions resulting in $r_{\text{fSN}} \lesssim 0.01 \text{ year}^{-1}$ or $r_{\text{fSN}} \lesssim 1 \text{ year}^{-1}$ for different multiplicities. The condition ($m \geq 8, N_{\nu} \geq 5$) could therefore be used to send CCSN *gold-alerts* with much less than one false alert per century, and to identify type-II CCSN up to a distance of 246 kpc. It can also be seen from Table 6.2 and Figure 6.12, that relaxing the conditions as much as increasing the false CCSN rate by a factor 100 does not considerably increase the CCSN detection range, since the false detection rate quickly escalates when decreasing the required N_{ν} . This method suppose a significant improvement in comparison to IceCube, which can detect CCSNe at 50 kpc with a false detection rate of 0.1 year^{-1} [168].

Table 6.2: Summarized results for CCSN detection using the trigger conditions for a detector equipped with 10000 mDOMs for different values of m and N_ν , with fixed $\Delta t_{\text{coin}} = 20$ ns and $\Delta T_{\text{SN}} = 10$ s. The false CCSN detection rate is calculated using the contribution of PMT uncorrelated dark rate, solar neutrinos and radioactive decays within the modules. The range of supernova detection at 50% probability is given for the two CCSN models shown in Section 6.4.1. Updated version of the results published by the author in [143].

Trigger		False CCSN rate (year ⁻¹)	Range (kpc)	
m	N_ν		27 M _⊙	(9.6 M _⊙)
≥ 6	≥ 33	0.45	195	(120)
	≥ 36	0.01	186	(115)
≥ 7	≥ 9	0.25	267	(164)
	≥ 11	< 0.001	241	(147)
≥ 8	≥ 4	0.23	278	(164)
	≥ 5	0.002	246	(145)
≥ 9	≥ 3	0.02	196	(113)
	≥ 4	< 0.001	167	(97)

6.6.4 Detection range for known arrival burst time

It is plausible that the CCSN is detected by other telescopes and thus it is known that some neutrinos might have been detected. If that is the case, the archival data can be searched for a signal. Then, the conditions explained above can be used to identify events rather than as a trigger. It is realistic to assume that, in this scenario, the time at which the neutrinos should have reached the detector can be known with an accuracy of one hour [189]. Using Eq. 6.20, the expected number of false CCSN detections can be calculated for certain conditions within the time window $\delta t = 1$ h. Then, the probability Q that the background did not produce such a signal within the time window can be calculated as

$$Q = P(0, N_{\text{fSN}}(\delta t = 1 \text{ h})). \quad (6.23)$$

The result is shown in Figure 6.13 only for the case of $m \geq 8$, since this condition yields the best results. Q is expressed in terms of one-sided Gaussian standard deviations. It is observed that Q drastically increases if more *neutrino events* have been detected, but obviously the probability of detecting that many events from the CCSN decreases to shorter distances. Under these conditions, detecting $N_\nu = 3$ neutrino events within $m \geq 8$ yields $\sim 3\sigma$ confidence that this signal was not produced by background, while the confidence increases to 5.2σ if $N_\nu = 5$ are detected. The first case would occur with 50% probability for a (27.0 M_⊙, 9.6 M_⊙) CCSN at (327, 190) kpc, while at (246, 145) kpc for the second case.

A different way to calculate the detection sensitivity is through a signal vs. noise ratio. This requires the assumption that the arrival burst time is precisely known. The same method as in IceCube is used here, while instead of using the rate of all events, only events fulfilling certain multiplicity conditions are used. The sensitivity is therefore obtained considering the expected number of detected signal events $s_{\geq m}$ with multiplicity $\geq m$ at a distance d over the expected background for that multiplicity condition $b_{\geq m}$. The

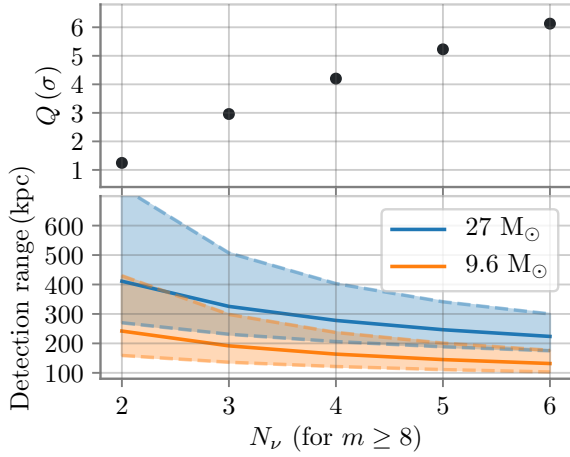


Figure 6.13: Detection prospects for a CCSN assuming that the neutrino burst arrival time is known with a precision of 1 h using the multiplicity conditions with $m \geq 8$, $\Delta t_{\text{coin}} = 20$ ns and $\Delta T_{\text{SN}} = 10$ s, for a detector equipped with 10000 mDOMS, as a function of the number of detected events N_ν fulfilling such condition. **Upper figure:** probability that the signal was not produced by background, in one-sided Gaussian standard deviations. **Lower figure:** distance at which each CCSN model would be detected with 10% (upper dashed line), 50% (middle line) and 90% probability (lower dashed line), when at least N_ν are required. Updated version of the figure published by the author in [143].

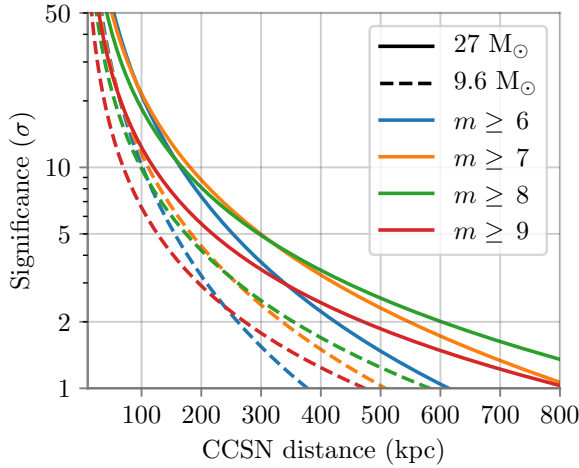


Figure 6.14: Significance of CCSN detection assuming that the arrival burst time is exactly known, for different multiplicity conditions and both CCSN models, using $\Delta t_{\text{coin}} = 20$ ns and $\Delta T_{\text{SN}} = 10$ s. The significance is expressed as one-sided Gaussian standard deviations.

significance of such detection can be expressed as¹ [190]

$$Z_{\geq m}(d) = \sqrt{q_{\geq m}} = \sqrt{2((s_{\geq m}(d) + b_{\geq m}) \ln(1 + s_{\geq m}(d)/b_{\geq m}) - s_{\geq m}(d))}. \quad (6.24)$$

The results are shown in Figure 6.14 for the multiplicity cases that yield the best results. The distance at 5σ is obtained at 300 kpc for the $27.0 M_\odot$ CCSN model, while it reaches 183 kpc for the $9.6 M_\odot$ model. In both cases, the farthest detection range is obtained for $m \geq 7$, although closely followed by the range obtained when using $m \geq 8$. At larger distances, the results for $m \geq 8$ improve. Note that what is shown here is the significance for such a detection, and the result must not be misunderstood as the certainty that a

¹This formula is an approximation valid for sufficiently large b . This is shown in [190], Fig. 7, where one can observe how the formula slightly deviates for decreasing b . To calculate the significance without relying on approximations, one would need to do a toy Monte-Carlo simulation sampling from s, b and calculating a likelihood ratio. However, this is very inefficient in our case due to the very high significance values that result at most distances, requiring a huge sample to obtain the significances through pure MC. Thus, the approximation is used as valid, which induces an error estimated in the worst case to be $\sim \pm 0.5\sigma$ at 5σ .

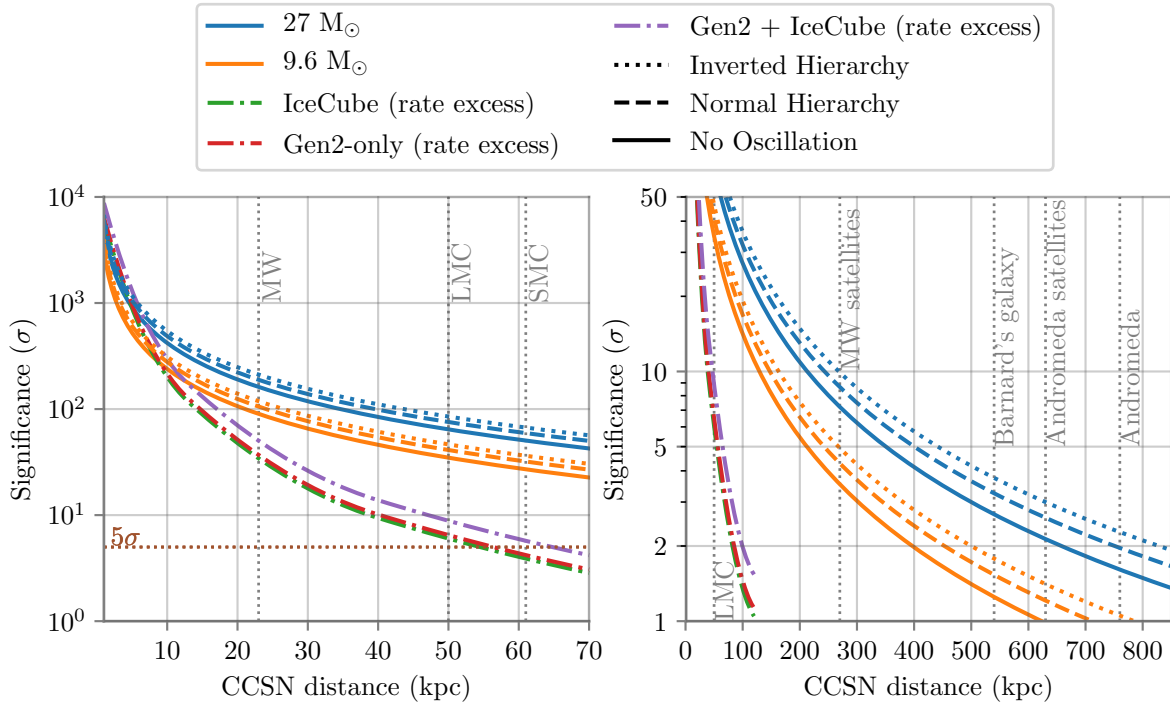


Figure 6.15: Significance of a detection for a CCSN when the arrival burst time is exactly known, combining the individual sensitivities from multiplicity $m = 6$ to $m = 9$ for both CCSN models and $\Delta T_{\text{SN}} = 10$ s. The significance is expressed as one-sided Gaussian standard deviations, calculated for a no oscillation scenario (continuous line) and scaled to a normal hierarchy (dashed line) and inverted hierarchy (dotted line) scenarios. The significance for IceCube [191] and a IceCube-Gen2 detector with 10000 mDOMs using the standard rate excess method, using all hits and a dead time window to reduce correlated noise, is also shown for the case of the $27.0 M_{\odot}$ model and averaged between all oscillation scenarios. Both figures show the same data at different scales. The approximate distance of some galaxies are also shown in the figure, including the Milky-Way (MW) limit, the farthest MK satellite and the closest Andromeda satellite.

CCSN at such distance would be detected, since the expected number of triggered events for such distant CCSNe is quite low, and the high significance is a consequence of the much lower expected background. As an example, the significance 5σ for $m \geq 7$ is obtained with the expectation of 0.56 background events and 6.9 signal events within the 10 s time window.

One could also combine the information of all multiplicities and get an overall significance using the result for each multiplicity condition as an independent bin. Note that to achieve this, only events detected exactly with multiplicity m are taken into account in each bin and not $\geq m$ as before, as otherwise the bins would not be independent of each other. The combined significance is calculated as [192]

$$Z = \frac{\sum Z_m}{\sqrt{N}}, \quad (6.25)$$

with N the length of the summation. In this case, it is summed from $m = 6$, due to smaller values not contributing to the significance at large distances, to $m = 9$, due to the limit on the simulated radioactive noise.

The results are shown in Figure 6.15, where the results for the no-oscillation scenario have been scaled to the normal and inverted hierarchy scenarios. This has been approximated by scaling the expected number of detected events using the ratio of events between each oscillation scenario and the no oscillation scenario from IceCube results [168]. The figure also includes the significance of a detection by IceCube with its *rate excess* method¹, based on the same $27.0 M_{\odot}$ model. This result is obtained by simulating only 1.5 s around the accretion peak, averaging for the different oscillation scenarios and applying the corresponding dead-time window to reduce the correlated noise. In this case, the significance is calculated as

$$Z = \frac{s}{\sqrt{b}}, \quad (6.26)$$

approximation valid since b is sufficiently large [190], which is assumed as $b = 280 \text{ s}^{-1}$ after the dead-time window used in the detector. Similarly, the capacity of an IceCube-Gen2 detector with 10000 mDOMs is calculated if the same method as in IceCube would be used. This allows us to directly compare what is gained due to the separation of detected events within different multiplicities in comparison with what is gained purely by having a larger effective volume. This is obtained using Eq. 6.26, without applying any multiplicity condition. Regarding the background, the application of a dead-time window is considered here, as in the case of IceCube, to reduce the rate due to correlated noise within the same PMT. In Figure 6.10, the sum of all noise components in the first bin is $\sim 540 \text{ s}^{-1}$ per PMT, but the uncorrelated component of the background per PMT in the mDOM was calculated to $f_{\text{Gen2}}^{(\text{unc})} = 120 \text{ s}^{-1}$ [193] after applying a similar dead-time window, thus this value is used for the IceCube-Gen2 case when using all counts as in IceCube.

It can be seen in Figure 6.15 that the significance for IceCube or IceCube-Gen2 are quite similar using the rate-excess method. Although IceCube has fewer modules and each with less effective area, the higher noise of each mDOM plays an important role, and thus, not much is gained by the IceCube-Gen2 detector itself if the same method is used. Combining both, the 5σ horizon is found using the rate excess method at 65 kpc. However, combining the results using multiplicities from $m = 6$ to $m = 9$, the 5σ horizon of such an IceCube-Gen2 detector reaches (350, 212 kpc) for the ($27.0 M_{\odot}$, $9.6 M_{\odot}$) CCSN model for the no-oscillation scenario. The detection horizon at 5σ is obtained at (400, 242 kpc) and (442, 267 kpc) for the normal and inverted hierarchy scenarios, respectively. The significance still remains greater 2σ for the closest Andromeda satellites using the heavier CCSN model, and around 2σ for Andromeda itself. These results clearly show the large improvements obtained when fast multiplicity conditions are used within the same module in contrast with the standard rate-excess method used in IceCube. Nevertheless, the result must be taken with care due to the absence of atmospheric muon background. For IceCube, at 10σ the false SN trigger rate due to atmospheric neutrinos is approximately 0.1 year^{-1} . Determining whether this scenario is similar in our case requires a full detector simulation.

¹Values obtained from internal communication with the SN working group.

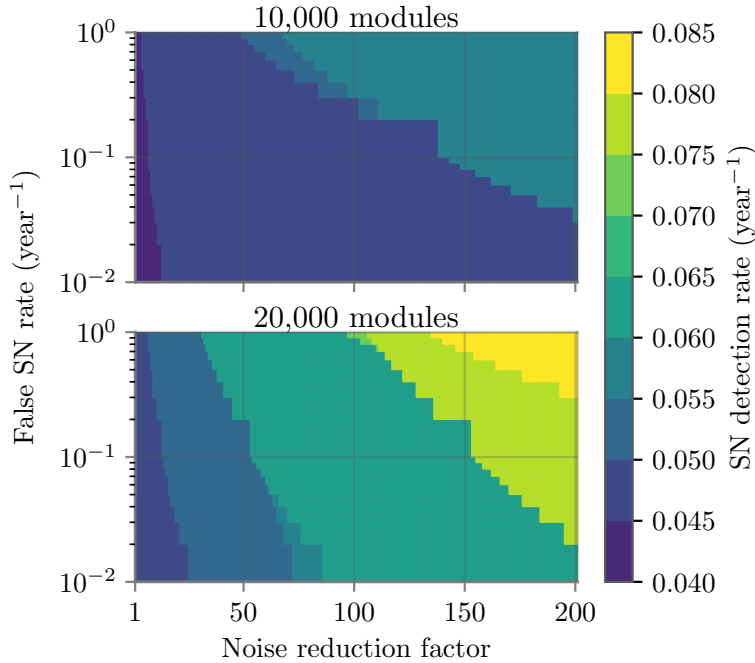


Figure 6.16: Estimation of the CCSN detection rate based on the probability of detecting CCSN using the multiplicity conditions and the estimated CCSN population rate from [169] based on real observations and scaled to match the star formation rate. Results are shown for hypothetical detectors of 10000 (**upper figure**) and 20000 (**lower figure**) mDOMs with reduced radioactive contamination. Updated version of the figure published by the author in [143].

6.6.5 CCSN detection rate

In this work, the detection horizon was used as a value to indicate whether the results are better than the current detector or not. However, in many cases, increasing the detection range does not really add much to the actual physics case. The reason is that, beyond the Milky Way and some small galaxies, the next galaxy that potentially hosts CCSN progenitors is the Andromeda galaxy¹. Although in Figure 6.15, it was shown that the significance according to the $27.0 M_{\odot}$ model for detecting CCSN in Andromeda is around 2σ , this depends on knowing the exact time at which the neutrino burst would arrive, so it is not an independent study with IceCube-Gen2.

Taking as a reference the ranges at which CCSN could be detected shown in Figure 6.12, and using the estimated CCSNe population based on recent observations and scaled to the star formation rate [169], a CCSN detection rate of 0.044 year^{-1} is obtained for the $27.0 M_{\odot}$ model and the condition ($m \geq 8, N_{\nu} \geq 5$).

In this section, it is calculated how much the conditions must soften or how different the detector should be in order to significantly increase the expected detection rate. The results are shown in Figure 6.16. The figures show the results for the detector considered here so far, consisting on 10000 mDOMs, and an alternative hypothetical version with 20000 mDOMs. The plot also speculates about the possibility of mDOMs with much smaller radioactive contamination. Although this might seem unrealistic, the same glass used for D-Eggs might also be used for LOMs, and this has radioactive contamination much smaller than the glass assumed here. Therefore, this would emulate the scenery in which the mDOM has the same glass as these other modules. Each point in the figures represents the detection rate obtained with the multiplicity condition that maximizes it, for the $27.0 M_{\odot}$ model. For the detector with 10000 modules, reducing the radioactive contamination in the glass vessel even by a factor 200 does not considerably increase

¹Also known as M31, Messier 31 or NGC 224.

the expected detection rate. To approximately double the expected detection rate, it would be necessary to double the number of modules, to have a much smaller radioactive contamination in each. The trigger condition shall also be softened, allowing a much higher false detection rate. Thus, despite the improvement, regular CCSN detection is not expected.

6.7 Detected flux analysis

The detected events are now divided into time bins of 50 ms and shown in Figure 6.17, for CCSNe at 10 kpc and at 50 kpc. The total flux ($m \geq 1$) and the flux using a multiplicity condition of $m \geq 4$ are shown. The expected background in such a time-bin for that condition has been added to the signal. The background level is shown with a gray horizontal line, and the region covered by its standard deviation is shown with the gray hatched area. This area represents the region dominated by background fluctuations, considering them only statistical. The shape of the histograms only differs slightly for different multiplicities. At 10 kpc, it can be seen that the flux would be distinguishable from the noise for about 5 seconds. After that, the signal falls into the region dominated by background fluctuations. This is similar if a multiplicity condition is applied. However, in the figures at 50 kpc, it is observed that, without applying the multiplicity condition, the whole signal from the $9.6 M_{\odot}$ model is within the noise-dominated region, and therefore the flux would not be distinguishable in this case. On the contrary, the detected signal from the $27.0 M_{\odot}$ model protrudes out of the noise region for the first ~ 0.7 s. However, applying the condition $m \geq 4$, the signal detected from both models are above the region dominated by background fluctuations for a few seconds. Thus, the first seconds of the cooling phase of the CCSN might be visible even at the Large Magellanic Cloud using multiplicity conditions. Here, only results with 50 ms binning are shown. This binning is a good compromise between good time resolution and a sufficient number of counts. Using smaller time bins of the order of a few milliseconds, the result is found to be more unfavorable since the number of counts in each bin is significantly reduced, especially when multiplicity conditions are applied and the CCSN distance is increased.

In view of the results shown in Figure 6.17, it can be expected that any analysis looking at the flux or shape of the curve will be more convenient to do without applying a multiplicity condition when the CCSN is close enough, since the statistics is better there. However, as the CCSN occurs farther away, it becomes more convenient to use a multiplicity condition. Let us check this by calculating how well both fluxes could be distinguished if multiplicity conditions are used or not. To do this, a χ^2 analysis is done as follows:

$$\chi_{\text{red}}^2 = \frac{\sum_i \chi_i^2}{K}, \quad (6.27)$$

where χ_{red}^2 is the reduced χ^2 , K being the number of degrees of freedom and i each time bin. In this case, K is the number of time bins that are used. The individual χ_i in each bin is obtained simply as

$$\chi_i^2 = \frac{(n_i - \mu_i)^2}{\sigma^2(\mu_i)}, \quad (6.28)$$

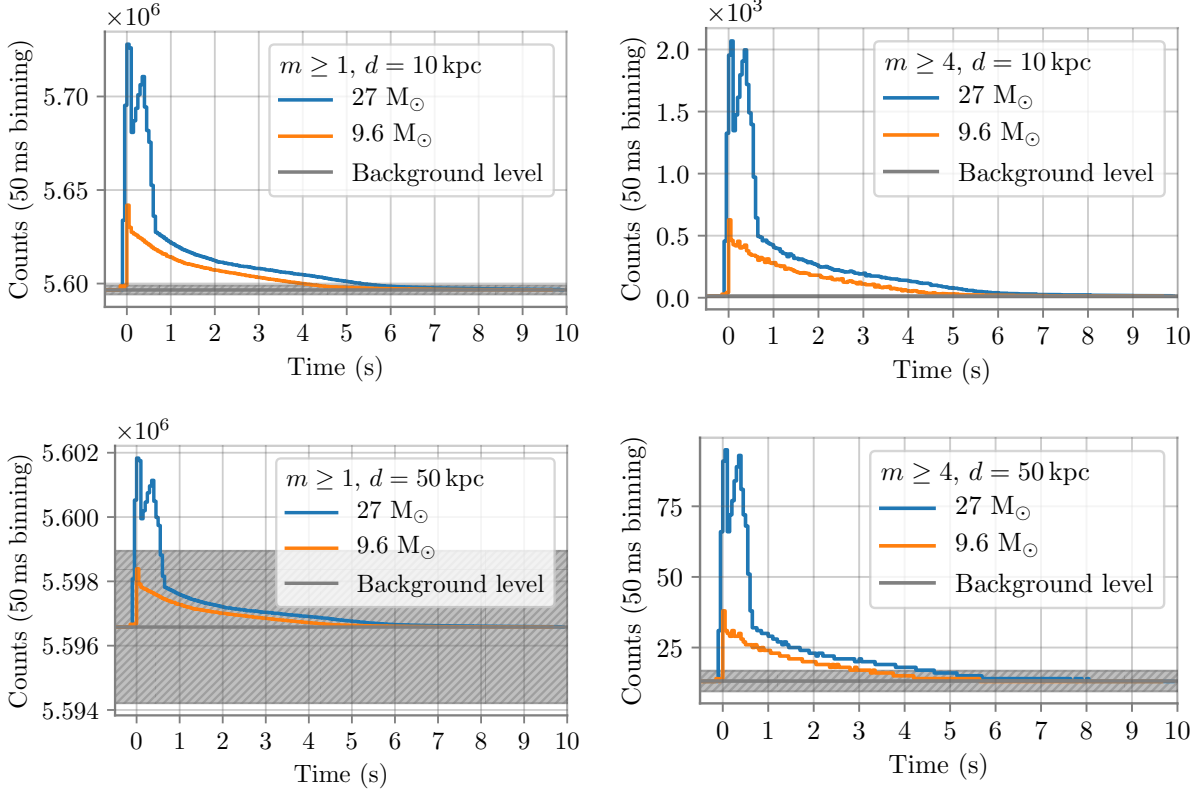


Figure 6.17: Detected flux for each CCSN model in time bins of 50 ms. The dash area stands for the expected background \pm its standard deviation. **Top-left:** Whole detected flux ($m \geq 1$) for CCSNe at 10 kpc. **Top-right:** Flux detected applying the multiplicity condition $m \geq 4$ for CCSNe at 10 kpc. **Bottom-left:** Whole detected flux ($m \geq 1$) for CCSNe at 50 kpc. **Bottom-right:** Flux detected applying the multiplicity condition $m \geq 4$ for CCSNe at 50 kpc.

with μ_i being the counts in each bin obtained for the simulation considered as the model and n_i the same for the other simulation. $\sigma(\mu_i)$ stands for the standard deviation of the model in each bin, assumed as $\sigma(\mu_i) = \sqrt{\mu_i}$. Note that the rate due to the background has been summed to n_i and μ_i , and they have been approximated to the closest integer¹. Thus, this only works under the assumption that one of the models is perfectly known and that all uncertainties are statistical. Since the number of simulated events for the 27.0 M_\odot model is larger than for the 9.6 M_\odot model², the first is used as the model (μ_i). The results for which both models can be distinguished with a confidence of 5σ are shown in Figure 6.18. The result for multiplicity 1, which simply corresponds to using all counts, is found at 27 kpc, covering approximately the entire Milky Way. It can be seen that the 5σ horizon increases in distance for higher multiplicities, up to a maximum of 62 kpc when using $m \geq 4$, covering the LMC.

If a CCSN is detected, a similar analysis can be performed to distinguish between the different oscillation scenarios. This must assume that the expected flux for one of the oscillation scenarios is well known, and thus it can be compared with the other. Although

¹Remember that, due to the weights, the counts are generally float numbers.

²There is no particular good reason for this, simply the 27.0 M_\odot was simulated first and it was found that the number of generated events was unnecessarily high, therefore and to save time, the next model was simulated with fewer events.

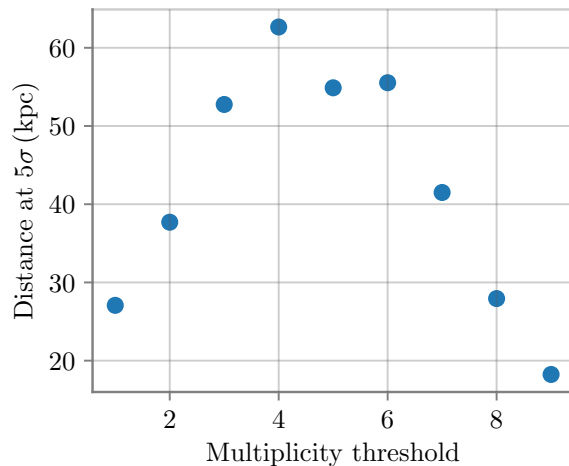


Figure 6.18: 5σ horizon for distinguishing both CCSN models used here as a function of the multiplicity condition. The significances have been obtained through a reduced- χ^2 analysis, assuming the data from the $27.0 M_{\odot}$ simulation as model.

in this work simulations have been done for the conservative choice of the no-oscillation scenario, the results have been scaled to the expectation of normal and inverted hierarchy scenarios, and the 5σ horizon has been calculated as before. Note that this is roughly approximated by scaling the no-oscillation results obtained in this work with IceCube results for each oscillation scenario [168], same as previously done in Figure 6.15. The result must then be taken with care and it is only shown for the purpose of comparing the possibilities of using multiplicity conditions or not. Also, under this approximation, the shape of the detected flux remains the same and only changes in intensity, which is indeed a pessimistic assumption, since the cases are less distinguishable.

The results for each CCSN model are shown in Figure 6.19, using the normal hierarchy oscillation scenario as model (μ_i). It is found that using the multiplicity condition, both cases can be distinguishable at the farthest distances, this time with a maximum for $m \geq 3$ with the 5σ horizon found at ~ 26 kpc for the simulation of $27.0 M_{\odot}$ and at ~ 16 kpc for the simulation of $9.6 M_{\odot}$. The dashed line represents the IceCube result to distinguish both models [168] for a CCSN of progenitor mass $20 M_{\odot}$. Perhaps the result without multiplicity condition seems a bit low judging by the displayed IceCube value and considering the difference between the detector assumed here and IceCube. However, it should be noted that IceCube applies a dead-time window that significantly reduces the noise. Applying a similar dead-time window as before, the results without multiplicity (or with $m \geq 1$, as shown in the plot) would go up to 23 kpc and 14 kpc for each model, still below the result at $m \geq 3$, which does not include dead time.

6.8 Sensitivity to the CCSN energy spectrum

The method described in this section was first developed in the scope of a master thesis [194] co-supervised by the author. Here, the results are summarized with small corrections and updated simulations for both signal and noise.

IceCube performed some studies on the determination of the CCSN energy spectrum, as shown in Figure 6.1 (right), using the ratio of events detected in two modules to the overall events detected in a single module. For segmented modules, this can be substituted by exploring the ratio of events detected at different coincidences, that is, with different

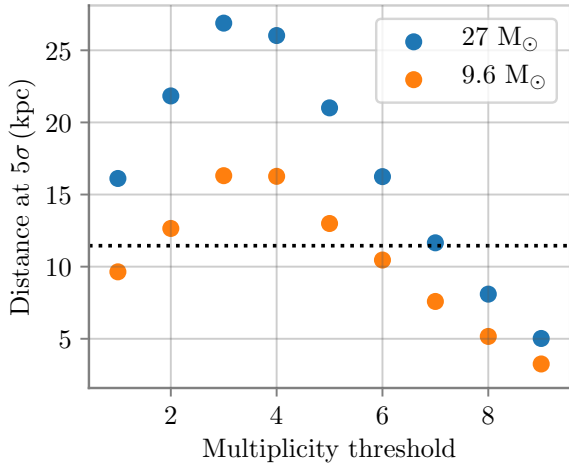


Figure 6.19: 5σ horizon for distinguishing the normal hierarchy oscillation scenario from the inverted hierarchy one. The significances have been obtained through a reduced- χ^2 analysis, and are shown for both models of $27.0 M_{\odot}$ and $9.6 M_{\odot}$ progenitor masses. The signal for each oscillation scenario have been obtained by scaling the results from the no oscillation case, and do not represent a full flux simulation including the corresponding oscillated fluxes. The result for IceCube [168] is shown as a horizontal dashed black line.

multiplicities as has been done throughout this chapter.

Assuming that the energy distribution of CCSN neutrinos can be parameterized in terms of $\langle E \rangle$ and α as shown in Eq. 6.10, simulations have been performed to estimate the sensitivity to these two parameters. For simplicity, only IBD is simulated, where events are generated as explained in Section 6.4.2, but instead of assigning the events to the corresponding $(\langle E \rangle, \alpha)$ from the flux, these values are manually given. Afterward, the antineutrino energy is sampled from the distribution obtained with Eq. 6.10 and the simulation chain continues as usual, where the events are weighted according to the flux from the $27.0 M_{\odot}$ CCSN model. Implicitly, this approximates $(\langle E \rangle, \alpha)$ as constant during burst, since all events are generated from the same energy distribution. The process is repeated for different values of $(\langle E \rangle, \alpha)$ pairs, ultimately forming a grid where each point contains a histogram of detected events sorted in multiplicities as in Figure 6.8. To fine-tune the grid and improve resolution, each point is summed up and averaged to obtain interpolated data between the simulated $(\langle E \rangle, \alpha)$ pairs, reweighting them with the corresponding ratio between the energy spectrum. This also has the effect of smoothing the grid, since all data are used for every point of the interpolated grid with the corresponding reweighting.

Then, the ratio of events detected with a certain multiplicity is compared. Multiplicity ratios are defined as

$$R_{m,i} = \frac{N_m}{N_{\geq i}}, \quad (6.29)$$

being m, i are the multiplicity conditions to calculate the ratio, and N the number of events fulfilling the condition. Thus, $N_{\geq i}$ is all events with multiplicities equal or larger than i , used to normalize the number of events with exact multiplicity m . The use of ratios has the simplicity of not depending on the total number of detected events. Choosing a reference $(\langle E^{\text{ref}} \rangle, \alpha^{\text{ref}})$, one expects that R_m would change for different $(\langle E \rangle, \alpha)$ and thus by comparing the ratios with those of the reference, $(\langle E \rangle, \alpha)$ can be reconstructed. Similarly as before, a χ^2 is constructed to perform the statistical analysis as

$$\chi^2 = \sum_{k=1} \chi_{k,i}^2 = \sum_{k=1} \frac{(R_{k,i} - R_{k,i}^{\text{ref}})^2}{\sigma^2(R_{k,i}^{\text{ref}})}, \quad (6.30)$$

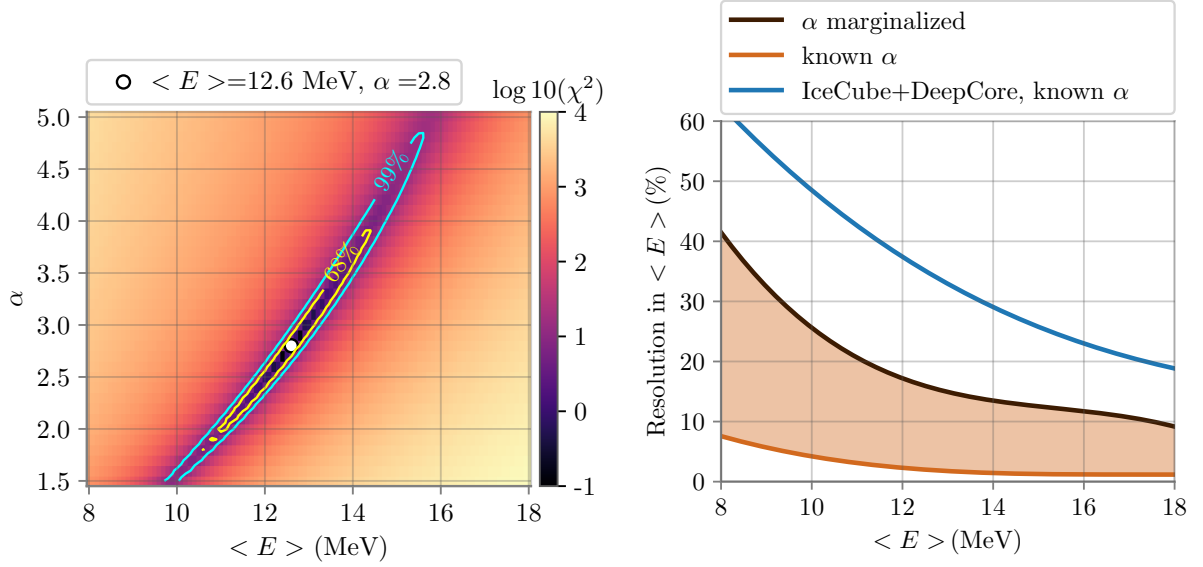


Figure 6.20: Resolution to the energy spectrum of a $27.0 M_{\odot}$ CCSN at 10 kpc with a detector composed of 10000 mDOMs using the combined χ^2 method with multiplicities from 4 to 8, assuming an energy distribution following Eq. 6.10. **Left:** Energy spectrum reconstruction of a CCSN with $(\langle E^{\text{ref}} \rangle = 12.6 \text{ MeV}, \alpha^{\text{ref}} = 2.8)$. The regions for the 68% and the 99% confidence level are also shown. **Right:** Energy resolution assuming that the α parameter is known from another experiment or unknown. The unknown case is obtained by profiling the χ^2 space on the left figure. The results are compared with IceCube [191] for the same CCSN model. For the results here, a time window of 10 s is used, meaning a reference mean α during the flux of $\alpha = 2.8$. Due to higher background rates, IceCube only accounts for the accretion phase, using a time window of 1.5 s with $\alpha = 3.69$. The IceCube result assumes that α is known.

where

$$\sigma^2(R_{k,i}^{\text{ref}}) = \sqrt{\left(\frac{\sigma(N_m^{\text{ref}})}{N_{\geq i}^{\text{ref}}}\right)^2 + \left(R_{k,i}^{\text{ref}} \frac{\sigma(N_{\geq i}^{\text{ref}})}{N_{\geq i}^{\text{ref}}}\right)^2} \quad (6.31)$$

is obtained from Gaussian error propagation, and $\sigma(N_j)$ is the combination of the standard deviation of the signal plus the background as $\sigma(N_j) = \sqrt{N_j + \sigma^2(\text{BG}_j)}$. The whole calculation relies again on the assumption that the background level is well known and uses only statistical errors.

The best resolution for $(\langle E^{\text{ref}} \rangle, \alpha^{\text{ref}})$ is obtained when using $i = 4$ and summing up to $k = 8$: $\chi^2 = \sum_k^8 \chi_{k,i=4}^2$. This is shown in Figure 6.20 (left) for $(\langle E^{\text{ref}} \rangle = 12.6 \text{ MeV}, \alpha^{\text{ref}} = 2.8)$. Note that the 68% and 99% confidence regions have been obtained by taking into account how many χ^2 data are combined by first obtaining the reduced χ^2 form of the sum, as done in the previous section. Contrary to the IceCube result shown in Figure 6.1 (right), the method is able to break the degeneracy between $\langle E \rangle$ and α , which is the result of combining the different χ_k^2 .

On the right side of Figure 6.20, a direct comparison of the results with those of IceCube is made regarding the sensitivity to $\langle E \rangle$. The curves are calculated with the data shown on the left side of the figure. The curve of α marginalized is obtained by taking the minimum of the likelihood for all α in each $\langle E \rangle$, operation known as *profiling*. The results are fitted

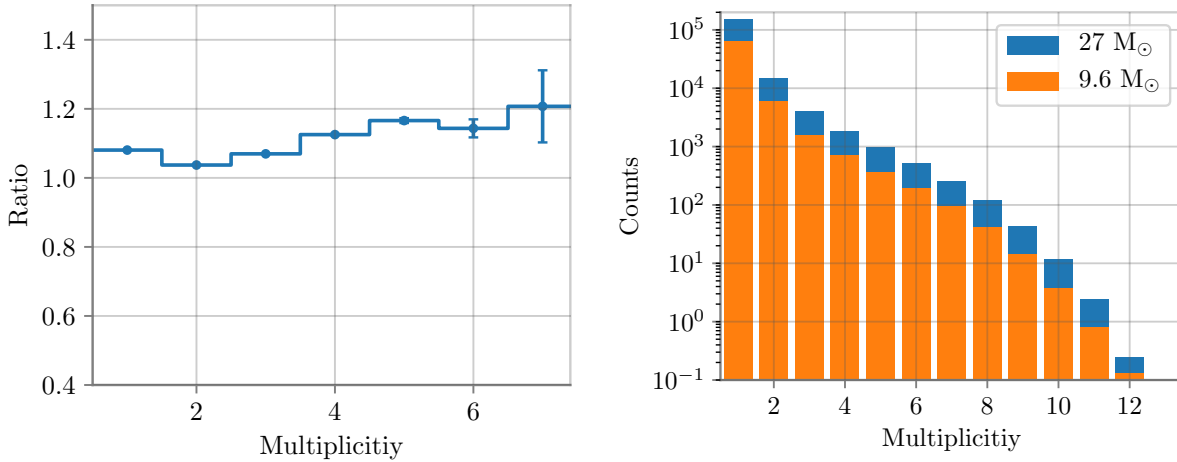


Figure 6.21: Left: Ratio between background due to radioactive processes for each multiplicity condition using $\Delta t_{\text{coin}} = 20$ ns between the simulation including PMTs with larger radioactive contamination and the standard simulation previously used. Here, scintillation is omitted to speed up the computation. **Right:** Events detected after each CCSN simulation has been weighted according to an IceCube Upgrade detector consisting of 400 mDOMs, using $\Delta t_{\text{coin}} = 20$ ns and $\Delta T_{\text{SN}} = 10$ s.

with a 3-degree polynomial function. The curve for known α uses $\alpha = 2.8$ because it is the average α within the first 10 s of the 27.0 M_⊙ model for electronic antineutrinos. IceCube result uses the same 27.0 M_⊙ model, but in this case only accounts for the accretion phase due to the larger background compared to IceCube-Gen2 at high multiplicities, resulting in $\alpha = 3.69$. A considerable improvement of a factor ~ 2 is observed when α is unknown compared to the IceCube result, even if the last assumes α to be known. If α is known for IceCube-Gen2 as well, the improvement is larger than a factor 6 in the whole range considered here.

6.9 CCSN detection in IceCube Upgrade

Although ICU will contain only 400 mDOMs, it is interesting to see if the coincidence method could also be applied to this subdetector and obtain competitive results. Here, the fact that there are other modules in ICU is ignored. Thus, the study is similar to what was done before, but using 400 modules and taking into account that the average ice properties in ICU are cleaner than in the depths assumed for IceCube-Gen2, thus the weight concerning the effective volume has a different value than before.

The first mDOMs for ICU are already being built at the time of writing this thesis, and the Collaboration has already received all the PMTs for the mDOMs. This has allowed the Collaboration to measure a large number of these PMTs, and it was found that their dark rate was higher than previously expected. Even with the higher noise, the Collaboration concluded that the physics goals of the ICU can be met building the mDOMs with this PMT batch. Although, as seen above, the uncorrelated noise of the PMTs contributes very little to the background at high coincidence, it was found that the increased noise in these PMTs is due to a higher than expected radioactive contamination in the PMT glass. Due

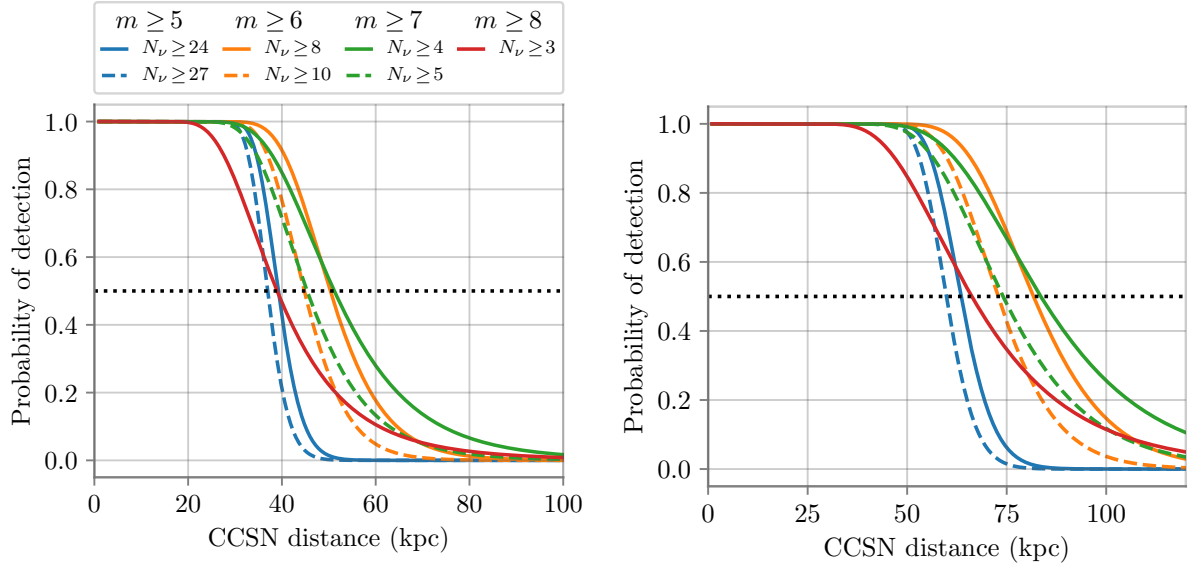


Figure 6.22: Probability of detecting a CCSN based on the $9.6 M_{\odot}$ model (**left**) or the $27.0 M_{\odot}$ model (**right**), using trigger conditions with multiplicity $\geq m$, number of neutrino events N_{ν} , $\Delta t_{\text{coin}} = 20$ ns and $\Delta T_{\text{SN}} = 10$ s, as a function of the CCSN distance for a IceCube Upgrade detector equipped with 400 mDOMs.

to this origin, it can be expected that it might also affect the results at high multiplicity, therefore the simulation of the radioactive decays was repeated, but in this case events were also generated in the PMT glass, following its activity. Since, as seen above, the scintillation is no longer relevant at high multiplicities, the simulations here only include the Cherenkov effect, which is much faster to simulate. The results, compared to previous simulations, are shown on the left side of Figure 6.21. It can be seen that the background increases in all bins up to a maximum of $\sim 20\%$. Therefore, this new simulation has been used for the results of this section. On the right side of Figure 6.21, the histogram in multiplicity of the reweighted results is shown for the ICU simulations. Note that, because of the cleaner ice, the ratio of events in coincidence is smaller. Although there is an increase in all counts due to cleaner ice in all multiplicities, events in $m = 1$ are more affected by the properties of the ice, as shown in Section 6.3, thus the increase at $m = 1$ is larger. Ultimately, this results in a coincidence ratio of 9.7% and 9.1% for the $27.0 M_{\odot}$, $9.6 M_{\odot}$ model, respectively.

With these results, the range at which the CCSN would be detectable using trigger conditions and maintaining a false CCSN detection rate below 1 per year and 1 per century is shown in Figure 6.22, calculated in the same way as explained before for the IceCube-Gen2 case. Now, the trigger conditions are less restrictive than before due to fewer modules, but obviously the detection range has also decreased significantly with respect to the larger detector. The case $m \geq 8$ shows a single line because it is the best condition under both required limits for the false detection rate. The trigger system would be able to detect CCSN up to (74 kpc, 45 kpc) for the ($27.0 M_{\odot}$, $9.6 M_{\odot}$) models, respectively, while keeping a false detection rate below 1 per century. A softer condition that allows for one false CCSN detection per year would increase the range to 84 kpc and 51 kpc, respectively, for each model.

If the burst arrival time is assumed known, the significance of a CCSN detection can be

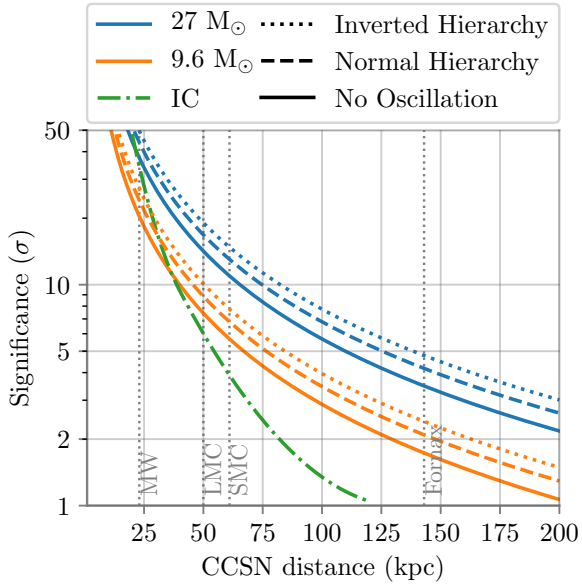


Figure 6.23: Significance of a detection for a CCSN when the arrival burst time is exactly known, combining the individual sensitivities from multiplicities $m = 5$ to $m = 9$ for both CCSN models and $\Delta T_{\text{SN}} = 10$ s, for a IceCube Upgrade detector consisting of 400 mDOMs. The significance is expressed as one-sided Gaussian standard deviations, calculated for a no oscillation scenario (continuous line) and scaled to a normal hierarchy (dashed line) and inverted hierarchy (dotted line) scenarios. The significance for IceCube [191] using the standard rate-excess method is also shown for the case of the $27.0 M_{\odot}$ model and averaged between all oscillation scenarios. The approximate distance of some galaxies are also shown in the figure, including the Milky-Way (MW) limit.

calculated again using Eq. 6.24, combining the significance of each unfolded multiplicity condition as done before. Here, Z_m from $m = 5$ to $m = 9$ (see Eq. 6.24 and 6.25) have been combined, since this case yields the best results. The results are shown in Figure 6.23, where again the values from the non-oscillation simulation have been scaled up to the different oscillation scenarios and compared with IceCube. The ICU detector is not only competitive with the much bigger IceCube detector if using coincidences, but it also surpasses it. Even in the worst case of the $9.6 M_{\odot}$ model with no oscillations, the significance of the detection is still larger than that of IceCube already in the Magellanic Clouds. The 5σ horizon is found at (110 kpc, 67 kpc) for the ($27.0 M_{\odot}$, $9.6 M_{\odot}$) model, respectively, in the no-oscillation scenario. The results increase to (125 kpc, 76 kpc) and (138 kpc, 84 kpc) for the normal and inverted hierarchy scenarios, respectively.

Note that, as before, the contribution of atmospheric muons is not taken into account. In fact, for ICU, it can be expected that most atmospheric muons are triggered in the detector (or even before reaching the ICU region, in DeepCore or IceCube itself), and thus eliminated from the noise contribution. Even then, the signal of some untriggered events might be confused with low neutrino events.

Although not covered in this thesis, it would be interesting to study how the multiplicity method explored here can be combined with coincidences between different modules as well, since the inter-module separation is only 3 m and thus even these low energetic neutrinos might be detected in more than a single module. This would also allow the use of other modules for the study, such as dEgg, and potentially reduce the effects of radioactive decay background.

6.10 Results using LOM16 modules

When this thesis started, mDOM and D-Egg were the main modules designed for IceCube-Gen2. This is the reason this thesis has proposed an IceCube-Gen2 fully equipped with mDOMs. However, although it is still not definitive, currently, the most favorable option for IceCube-Gen2 is the use of one of the LOM designs. In this section, the results of a similar analysis to what was done for mDOMs are shown for a detector equipped with the LOM16 module. The reason for using LOM16 instead of LOM18 is simply that LOM16 is currently implemented more accurately and reliably in the Geant4 simulation. However, one must note that this simulation has undergone much fewer tests and studies than the mDOM one, and small geometry details are still constantly being updated or solved. The implementation of the LOM16 in the Geant4 simulation was initially done in [195, 196], and modified afterwards. The steps to obtain the results shown here are analogous to what was done previously with mDOMs, however, there are some details that shall be noted:

- The detector is assumed again to contain 10000 modules with the same arrangement as before.
- The results are scaled according to the effective volume results of the simulations with mDOMs. This is done because the simulations to perform such study are very time-consuming and probably the final result will not vary much, especially at high multiplicities. The effective volume of LOMs should be approximately 10% higher than for the mDOM, according to the first simulations of the effective area, however, the variation of V_{eff} with the ice properties, which is what is used for the weights, should not differ much from the mDOM case.
- The radioactive background simulations have been performed with two types of LOM16s: one with Vitroex glass (mDOM glass) and one with Okamoto (D-Egg glass). The reason for this is that it is still uncertain which of the two will ultimately be used for IceCube-Gen2, and the results vary considerably for each case. The same signal simulation is used in both models, which approximates the Okamoto glass with the same optical properties as the Vitroex glass.
- Only the background resulting from uncorrelated PMT dark rate and radioactive decays is included, without taking scintillation into account. It can be expected that the absence of scintillation would not influence the background at high multiplicity, as discussed before.
- Only the $27.0 M_{\odot}$ model was simulated and only the inverse beta decay interaction was included.
- The same time windows as before for the CCSN burst and for the multiplicities are used: $\Delta T_{\text{SN}} = 10 \text{ s}$ and $\Delta t_{\text{coin}} = 20 \text{ ns}$.

An image of the LOM16 in the Geant4 simulation is shown in Figure 6.24. The PMTs are directly bonded to the glass by the gel pads. The inside of the module recreates the electronic components, but all of these solids have the same properties, being simply an absorbing material. The simulation works in the same way as done with mDOMs. The photomultipliers have a layer of material behind with the corresponding absorption and reflection parameters following lab measurements, so that photons are not detected when they reach the PMT from behind.

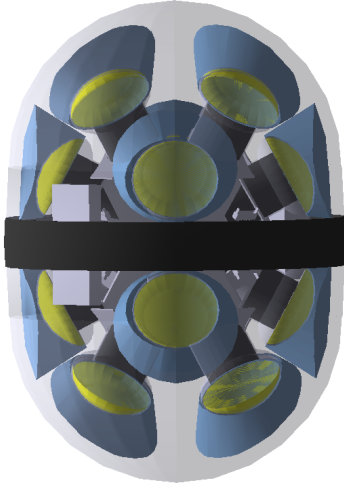


Figure 6.24: Render of the LOM16 module in the Geant4 simulation. The gel-pads are colored in pale blue to make them distinguishable from the glass. The internals are created by importing a CAD file of the module are given the same optical properties as being total absorbers.

The results of the radioactive noise simulation are shown on the left side of Figure 6.24. For comparison purposes, the result obtained previously for mDOMs is also included in the figure. The LOM background is shown from 3 different simulations: once with Okamoto glass, once with Vitrovex, and another one where the LOM geometry has been modified including a support structure similarly as in the mDOM. The last case is an unrealistic case, only studied and shown to comprehend the behavior of the background rates for the other two cases. The support structure was constructed including reflector cones around the area of the gel pads, and a layer of gel is situated between the glass and the structure as in the mDOM case. When comparing the LOM with the mDOM, the cases using the same glass (Vitrovex) show a similar total background rate and in accordance with the effective area scans. However, the rates differ significantly when requiring multiplicity conditions, with the rates for the mDOM case decreasing much faster when increasing the multiplicity. The results for the Okamoto glass are much smaller than those for Vitrovex but behave similarly in multiplicity, which causes the mDOM background at $m \geq 4$ to be already below the LOM one. In contrast, the simulation using Vitrovex glass and support structure decreases much more rapidly with high multiplicity, having smaller background rates than the mDOM. In principle, this is what one might expect: having fewer PMTs makes it less likely to have coincidences in many of them. However, this is not the case when gel pads are used. The reasoning found for this is the following: in modules with a support structure, there is a layer of gel between the glass and the structure itself. Photons that reach the gel, which has a refractive index similar to that of the glass, penetrate it easily so that they can reach the support structure and be absorbed there. However, when gel pads are used, there is nothing between the glass and the low-pressure air inside the module unless there is a gel pad present in that location. The photons are reflected much more often between the glass and the interior; therefore, they keep traveling through the glass until they reach an area with gel pads, then having the possibility of reaching the photocathode and being detected. This has a cumulative effect on the background rates at high coincidences, leading to the results of Figure 6.24 (left).

The simulation of the signal is shown on the right side of Figure 6.25. Note that the case of LOM16s with holding structure is not simulated anymore since it is an unrealistic case only shown before for the purpose of understanding the radioactive background rates. The results of mDOM for IBD are also included for comparison purposes. The overall detection is higher for the case of the LOM and is in proportion to the larger effective area. However, when the multiplicity condition is increased, the rate declines faster in the mDOM case,

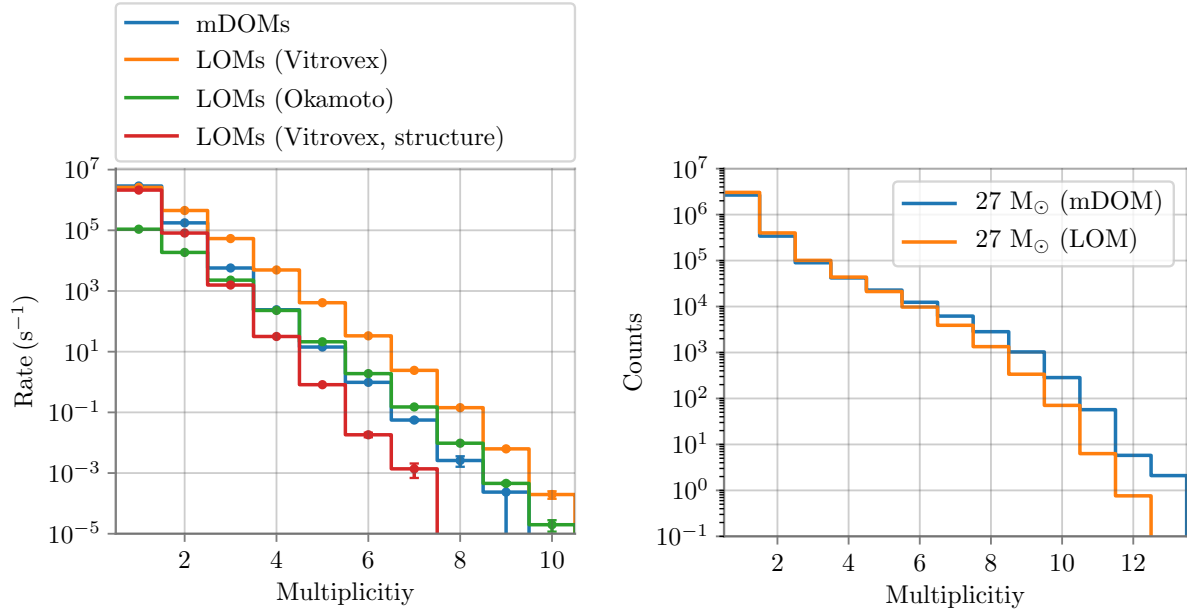


Figure 6.25: Left: Results in multiplicity within $\Delta t_{\text{coin}} = 20$ ns from the radioactive background simulation for the LOM16 and for the mDOM, for a detector with 10000 modules. Results for LOM16 are obtained for Vitrovex glass and Okamoto glass. Furthermore, results for LOM16 with Vitrovex glass are also simulated in a hypothetical case where the geometry of the module has been modified to include a support structure as in the mDOM case. Data from [193]. **Right:** Results in multiplicity within $\Delta t_{\text{coin}} = 20$ ns of the $27.0 M_{\odot}$ model simulated for $\Delta T_{\text{SN}} = 10$ s assuming 10000 modules using LOM16s or mDOMs. The results with LOM16s are only calculated with gel-pads and assume the same transparency for both glasses (Vitrovex and Okamoto).

as expected from a module with fewer PMTs. Thus, the impact of the gel pads on the rates at high multiplicities is much more significant if the events are generated within the module glass.

The efficiency of the method for identifying distant CCSNe with LOMs using trigger conditions is shown in Figure 6.26. Only the detection range for the best multiplicity condition, measured as the condition that produces the farthest distance at probability 50% while maintaining a false CCSN detection rate $\leq 0.01 \text{ year}^{-1}$, is shown for each LOM case. The result obtained previously for the mDOM is also shown for comparison purposes. The detection horizon goes from 246 kpc at 50% probability of the mDOM case to 163 kpc for LOMs with Okamoto glass and 96 kpc for LOMs with Vitrovex glass. In Figure 6.27, the detection significance with known arrival burst time is displayed. In contrast to Figure 6.15, for clarity, only the case without oscillations is shown. The rate-excess curve for the combination of IceCube and IceCube-Gen2 using LOM16s with Okamoto glass was calculated assuming that the noise rate at $m = 1$ is dominated by random noise due to PMTs, assumed at 50 Hz. The corresponding curve with LOM16s using Vitrovex glass is calculated assuming the same total background rate as obtained for the mDOM¹. It can be seen that, using the multiplicity method, the detection significance is extended towards much farther distances. However, the mDOM case covers all Milky Way satellites above 5σ , while the 5σ horizon for LOMs is found at 220 kpc with Okamoto glass and at 129 kpc

¹Note that this is done since scintillation was not included in the LOM16s simulations, effect that probably dominates the rates at $m = 1$.

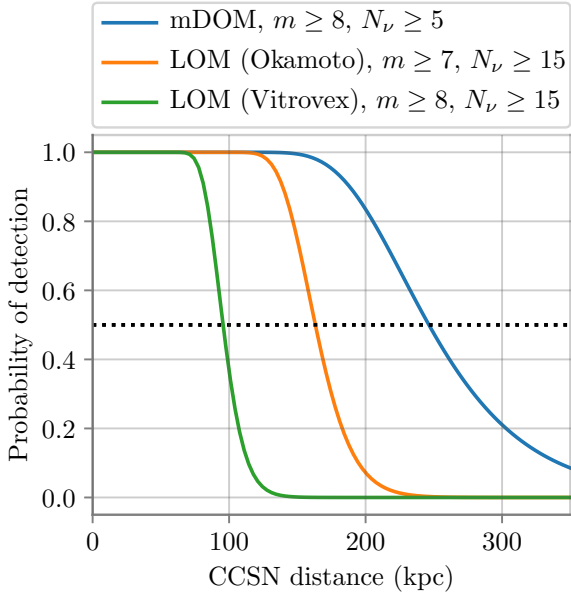


Figure 6.26: Probability of detecting a CCSN based on the $27.0 M_{\odot}$ model using trigger conditions for the case of a IceCube-Gen2 with 10000 mDOMs, LOMs using Okamoto glass and LOMs using Vitrovex glass. Only the result for the condition with the farthest detection range at 50% keeping a false CCSN detection $\leq 0.01 \text{ year}^{-1}$ is shown for each case.

with Vitrovex glass.

The much higher background and lower signal of LOMs with respect to the mDOMs at high multiplicities are translated into a poorer performance for the analyses done here. Still, even in this case, the multiplicity method considerably enhances the ability of the detector to identify distant CCSNe compared to the IceCube method. Note that here only LOM16 has been simulated; however, the higher noise at high multiplicities is due to the gel-pad construction, which is also shared in the LOM18 model. Thus, one might expect the noise in this case to also be higher than in the mDOM case at high multiplicities, and therefore the detection range decreased.

6.11 Sources of error in the results

So far, the possible errors introduced in the final results due to approximations in the simulations or systematic sources have not been considered. Although the models and material properties (for example, the ice) used here might introduce errors in the final results, the largest source of error is probably the simulation itself and the absence of atmospheric muons in the background. This section aims to shed some light on these topics and the possible implications on the results shown throughout the chapter.

6.11.1 Estimating the impact of atmospheric muons on the detection range

The results shown in this chapter are very promising concerning the use of multiplicity conditions to identify CCSN neutrinos. However, the big constraint that a reader might find is the absence of atmospheric muon background. Although it is a very small portion of the total IceCube background, the impact of these events on the rates at high multiplicities is hard to predict without simulating the whole detector, performing dedicated trigger

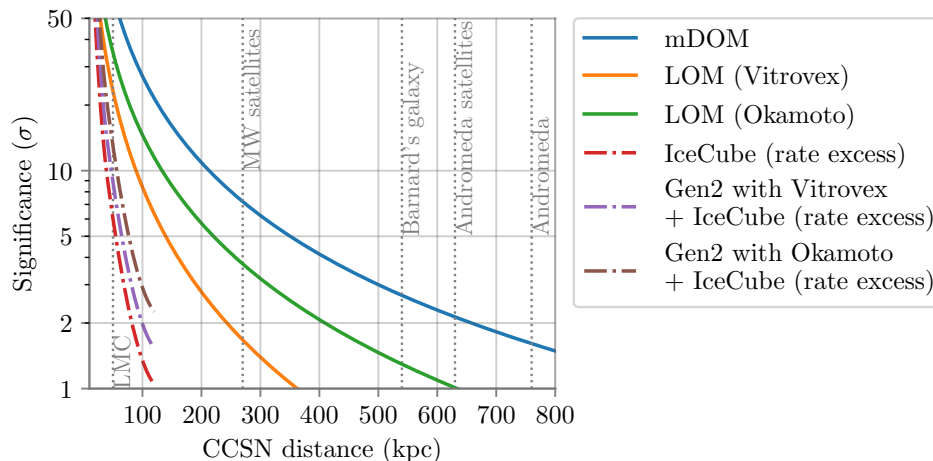


Figure 6.27: Significance of a detection for a CCSN when the arrival burst time is exactly known, combining the individual sensitivities for multiplicities $m = 5$ to $m = 9$ for the mDOM case and from $m = 6$ to $m = 9$ for the LOM cases, using the $27.0 M_{\odot}$ model. Results are obtained for the case of a IceCube-Gen2 detector with 10000 mDOMs, LOMs using Okamoto glass and LOMs using Vitrovex glass. The significance is expressed as one-sided Gaussian standard deviations, calculated for a no oscillation scenario. The significance using the rate-excess method for IceCube [191] and a IceCube+Gen2 detector with LOM16s using Okamoto or Vitrovex glass is also plotted. The approximate distance of some galaxies are also shown in the figure.

studies and studying the background originated by the unidentified muon events. The key feature of this chapter is to use a single-module simulation to perform the studies, and with this arrangement it is not possible to calculate the capability of the detector to identify these events. These simulations and trigger studies will surely be done using the *IceTray*¹ framework [197] once the IceCube-Gen2 is in a more advanced stage, however, at the time of writing this thesis, this is not yet ready.

KM3NeT has conducted a study on CCSN neutrinos also using multiplicities [198]. There, a shortened time window of $\Delta t_{\text{coin}} = 10$ ns is used to separate the events within different multiplicities. The main background source in KM3NeT comes from radioactive decays, where most of them originate from ^{40}K in seawater, some diffuse and localized hit rates due to bioluminescence and, less importantly, atmospheric muons. The average background detection rate of KM3NeT PMTs is approximately 7 kHz per PMT [198], more than 10 times higher than the background rate expected per PMT in deployed mDOMs (or LOMs). However, when analyzing the background in different multiplicities, above a multiplicity of 6, the contribution of atmospheric muons becomes relevant, and this dominates at multiplicities 8 and above [199]. A small test has been performed to estimate whether a similar scenario would occur within IceCube-Gen2 and, therefore, atmospheric muons would dominate the background at high multiplicities. For that purpose, the Geant4 simulation has been used to simulate atmospheric muons within a string of mDOMs. The generation volume consists of a cylinder of 40 m radius and 60 m height. To simulate a simplistic veto, 2 mDOMs are placed within the cylinder axis vertically aligned, at 4 m and 17 m from the bottom, respectively, which would account for the inter-module distance within a string of the 10000 mDOMs distributed along IceCube depths within 125 strings of 80 modules each. Muons are generated coming from the zenith; therefore, the bottom

¹Analysis and simulation framework generally used in IceCube, capable of simulating the full detector.

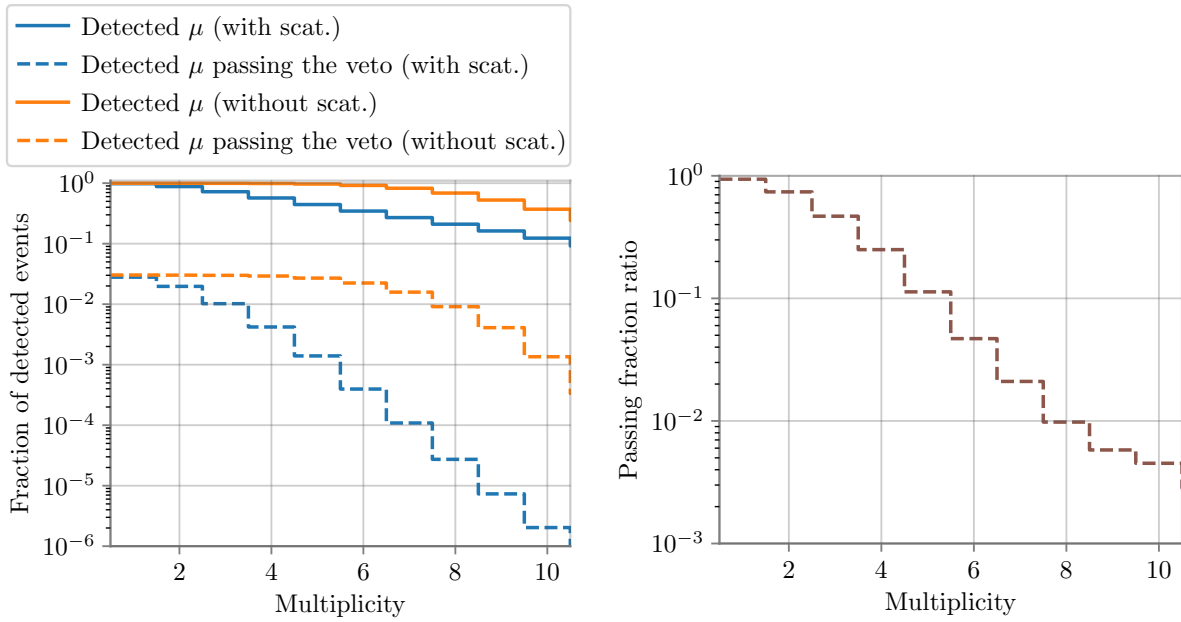


Figure 6.28: **Left:** ratio between detected and generated muon events. The curves are shown for all detected events and for detected events that are not identified by the mDOM that acts as veto module. Both cases are shown when scattering is included in the ice properties or not. **Right:** Ratio of the fraction of events passing the veto in the scenario with scattering divided by the scenario without scattering.

module is used as detector while the upper module would be used as a veto, and the detected events have been separated into different multiplicities using the standard time window of $\Delta t_{\text{coin}} = 20$ ns. The muons have been produced with a flat energy spectrum from 1 to 100 GeV, and then the events have been weighted according to the atmospheric muon spectrum at 2 km depth in the ice from [200].

The simulation was carried out for two different scenarios. In the first scenario, the ice has the effective scattering length corresponding to the mean effective scattering length in IceCube (shown previously in Figure 5.4). In the second scenario, no scattering has been simulated. The results are shown in Figure 6.28. It is observed that the muons are detected up to very high multiplicity, with the detected spectrum in multiplicity being very flat. Using the veto module, a strong rejection of more than 99% is achieved for multiplicities greater than 4, and $> 99.9\%$ above the multiplicity 6. When comparing the scenarios with and without scattering, it is observed that the no-scattering scenario detects more events with higher multiplicity. This is expected because of the spread of the arrival photon times. The short time window of $\Delta t_{\text{coin}} = 20$ ns already has an effect when scattering is present, since photons have the probability of being detected after suffering scattering and therefore these arrive to the module with some delay with respect to direct photons. This time spread would be larger the farther the events are produced from the module. In the figure on the right, the passing fraction in both scenarios is compared. A factor 10 of better rejection is achieved in the scattering scenario for multiplicities greater than 4, and this increases to a factor 100 for multiplicities greater than 8.

The results show that the scattering length can have a significant influence on the detection of atmospheric muons within different PMTs in short time windows. Having KM3NeT a much longer effective scattering length in its medium [201] than IceCube [164], results

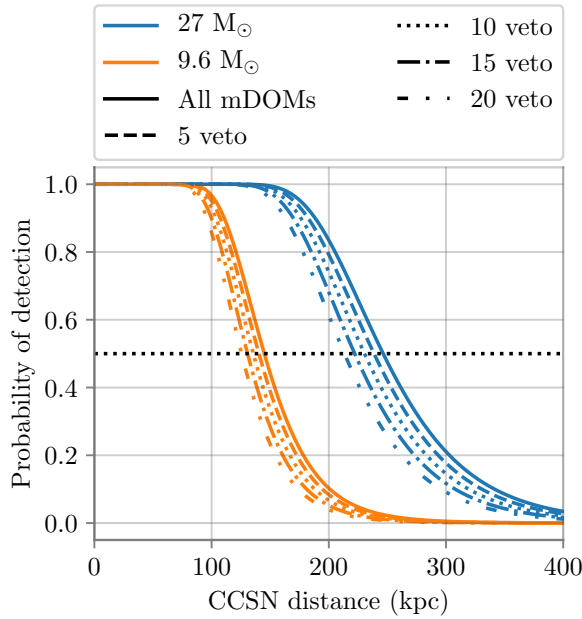


Figure 6.29: Detection range for both CCSN models for the best trigger condition which still maintains less than 1 false CCSN detection per century, for an IceCube-Gen2 detector using the upper modules as atmospheric muon veto. The continuous line correspond to a full detector equipped with 10000 mDOMs distributed along 125 strings of 80 modules each, while the rest uses the first X modules of each string as a veto region. Veto modules are simply considered to not being used for CCSNe detection.

here might indicate that atmospheric muons are less important in IceCube-Gen2 than they are for KM3NeT when using multiplicities. Furthermore, the time window used in this chapter of $\Delta t_{\text{coin}} = 20$ ns could be further constrained without significantly losing sensitivity to CCSN neutrinos (see Figure 6.7) and potentially limiting the number of atmospheric muon events within high coincidences. Furthermore, IceCube-Gen2 would probably be accompanied by an extension of the surface array, which will help in the identification and rejection of atmospheric muons.

However, the discussion here does not pretend to claim that the atmospheric muons would not be relevant for this study, but only to indicate that scattering likely has a positive effect on the veto. The simulations done here are quite limited, since atmospheric muons can come from different directions and the generation volume is likely too small, since atmospheric muons penetrating into the detector from much farther distances could potentially pass close to a single module or two and produce high coincidence uncorrelated signals. As stated before, a full detector simulation and corresponding trigger and veto studies are necessary to estimate the impact that the atmospheric muon background would have on the studies done in this chapter. A safer scenario is to assume that, if the atmospheric muons are a significant background source at high multiplicity, this would be the case for modules closer to the surface, while the rest of the modules would still be dominated by the radioactive background produced within the vessel glass. Thus, a simplistic hard cut on the atmospheric muon background would be to not use the upper modules in the strings when trying to identify the faint signal of a distant CCSN. The detection range to send *gold-alerts* in such a scenario is shown in Figure 6.29 (left) for different number of veto modules in each string, using the trigger conditions as was done in Section 6.6.3. Only the case for the farthest detection range at 50% probability is shown. Decreasing the number of modules obviously scales down both the signal and the background, and the effect is that the detection range decreases when increasing the number of veto modules, however, this is still significantly larger than the IceCube detection range even for the case of using 20 modules in each string as veto, which means a fourth of the whole simulated detector. As the number of veto modules increases, the detection range decreases more rapidly. This can also be understood as: if the detector

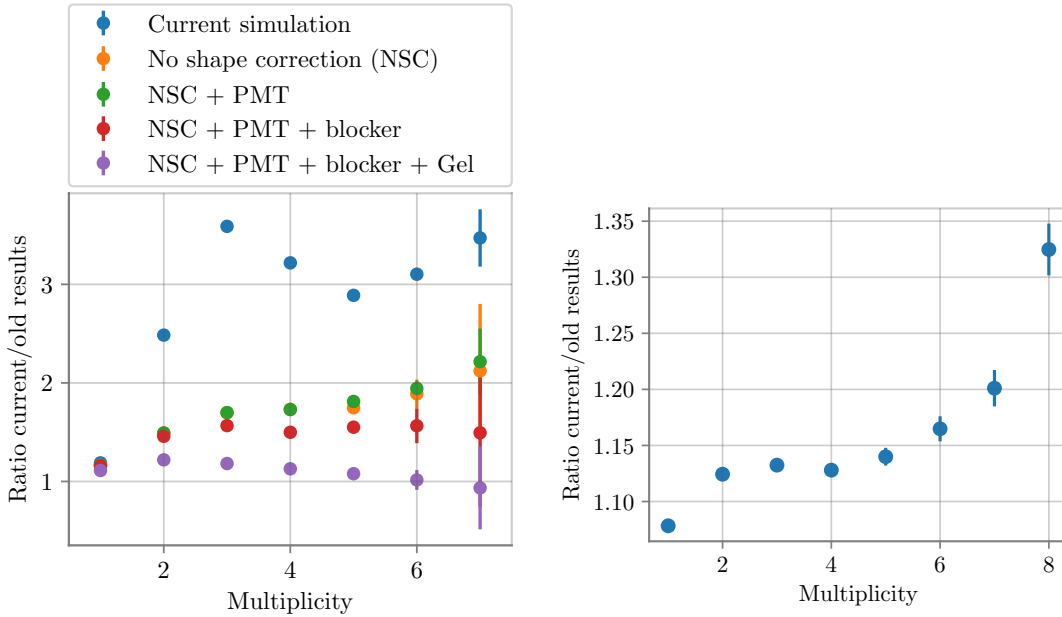


Figure 6.30: Left: Ratio between the radioactive background simulation used here and the one published in [143], where the different geometrical changes to the module are gradually reversed. Data from [185]. **Right:** Ratio between the $27.0 M_{\odot}$ simulation used here and the one published in [143].

were to be constructed with more modules, the detection range would not significantly improve unless the number of modules was significantly higher.

6.11.2 About the simulation, its errors and approximations

During the course of this thesis, the Geant4 mDOM simulation has been continuously updated¹, from just adapting the classes to the newer Geant4 versions to a complete rebuild of the way the modules are coded in order to facilitate the inclusion of different module designs or have more freedom in its location and surroundings. This also included resolving previously unnoticed bugs in the code written to generate the CCSN simulations used in this chapter². The impact of these bugs was never significant, and their correction has influenced the final results only slightly. However, small modifications made to the code aimed at aligning the mDOM geometry more closely with reality had an impact on the results of the study presented in this chapter.

Approximations that were made in the past have gradually been eliminated to make the simulation more realistic. Although small changes like these usually do not significantly affect the outcome of studies, this case turned out to be slightly different. The general approach after making changes concerning the geometry of the modules is, after checking that everything is working properly, to perform some measurements to check whether

¹Again, this has been a collaborative effort of present and former students of the AG Kappes group in Münster, including the author.

²The fact that this part of the code have, to date, only been used by the author, who is also the writer of the code itself, makes it harder to find small bugs than, for example, geometry related ones, which are used by several colleagues.

results change significantly. The results never indicated a change greater than $\sim 5\%$ in most analyses; however, this always excluded the simulation of radioactive decays from modules and their separation in multiplicity conditions, because these simulations are very time-consuming. After several geometry changes, a new radioactive background simulation was performed, where the results were saved in coincidences as before. Although the overall result at a single PMT level was similar, the rates were higher at high coincidences by a factor ~ 3 . To find the reason for this unexpected change, the most important geometry changes were gradually being reversed and the simulation repeated. This is shown in Figure 6.30 (left)¹. Each change referred to in the figure is explained below:

- Gel: older simulations did not have the correct values for the optical properties of the gel that was finally used in the mDOM construction.
- PMTs: previous PMTs had a slightly incorrect size, as well as small details of their construction and positioning in the code that were fixed.
- Photocathode blocker: this item is related to the previous one. Previously, the PMT photocathode was not really simulated. Instead, the entire interior of the PMT was made of a very dense and absorbing material. When a photon hit it, it was removed, and quantum efficiency Monte Carlo was performed to determine whether the photon was detected or not. However, this introduced the problem that other particles reaching the photocathode could generate numerous photons that were directly detected. To avoid this artifact, all particles reaching the photocathode were simply eliminated if they were not photons. In the newer simulations, this was updated, generating the layer concerning the photocathode inside the PMT, so that no further removal of particles reaching the PMT is necessary.
- Shape correction: the most important factor is the small modification made to the shape of the mDOM. In older versions of the simulation, the mDOM was built with the union of 2 semispheres and a cylinder. This, although very close to reality, is not fully precise because the cylindrical area is not really a cylinder, but is a little wider in the center than at the ends. The center of the cylinder with its ends forms an angle of $\sim 177.2^\circ$, instead of the angle of 180° that it had previously in the approximation.

More tests show that the cylinder geometry approximation causes some photons to be constantly reflected by the glass and never enter the gel, which does not happen when the correct geometry is implemented. Although this would in principle impact any study, it is much more noticeable with radioactive background events, since these are produced directly in the glass. In Figure 6.30 (right), the comparison between the older and the newer geometry simulations is shown for the case of the CCSN signal. Although there is also a higher signal in high coincidences, this factor is only 30% at best, while the radioactive noise is changed by a factor 3 in high coincidences. Consequently, this had a negative effect on the results and is the reason the results shown in this chapter differ slightly from the results published in [143]. This discussion serves to establish the basis that probably the major source of error in all the calculations shown here is the simulation itself. It is only recently that the first mDOMs have been built and measurements have begun to be made with them. There is no doubt that the simulation, which still includes approximations, for example, in the photomultipliers, will become increasingly robust and accurate.

¹These simulations do not include scintillation effect in the glass, however the same behavior was observed when this is included at the final level. Note that the last values in purple are not exactly 1 since there are still smaller, more subtle differences in the code between the older and the newer simulations.

6.12 Summary and conclusions

In this chapter, the possibilities of segmented modules to identify and study MeV CCSN neutrinos have been studied. The fact that these neutrinos have such low energy makes it difficult to study them in detectors like IceCube, where the modules are separated by several meters. However, if segmented modules are used, the PMTs are only a few centimeters apart, allowing MeV events to be detected in coincidence. The transient nature of CCSN explosions also allows observation of events in a time window of just a few seconds, which facilitates the study and identification of these events.

The detection capabilities of an IceCube-Gen2 detector composed of 10000 mDOMs was studied by simulating MeV neutrino fluxes from two type-II CCSN models of $27.0 M_{\odot}$ and $9.6 M_{\odot}$ progenitor masses that result in neutron stars. The simulations, done with a single module in Geant4, take into account the optical properties of each module depending on its depth. The masses of each model progenitor are good values for estimating the full detection range of this type of supernovae, since they are close to the upper and lower limits for inducing CCSNe resulting in neutron stars. The total number of detected neutrinos after simulating each model was found to be in agreement with expectations from IceCube scaled by the effective volume of the new modules to these events. A time window of only $\Delta t_{\text{coin}} = 20 \text{ ns}$ was found to be more than enough to group the detected neutrino events in coincidences in different PMTs within the same module, here named multiplicity. This set the foundation for the analyses that followed.

Three different sources of background were included in the analysis: solar neutrinos, PMTs dark rate, and radioactive decays originated within the vessel glass. In agreement with IceCube, the latter was found to be the most significant component of the background. Most of these background events come from scintillation in the glass induced by the particles after decay. However, the short time window of 20 ns eliminates most of them, so that at multiplicities ≥ 4 , the rate generated by scintillation becomes practically zero and only the light generated by Cherenkov effect of these radioactive decays remains.

Trigger conditions were introduced to identify neutrino events by detecting them in at least m PMTs within a module in the $\Delta t_{\text{coin}} = 20 \text{ ns}$ time window proposed above, naming it a triggered event if this condition is met. A longer time window of $\Delta T_{\text{SN}} = 10 \text{ s}$ is then used to search for at least N_{ν} triggered events. With this, depending on the values of m and N_{ν} , the background produces a false SN detection rate. Two cases are proposed, allowing for a maximum false SN rate of 1 per year or 1 per century, respectively. The trigger conditions technique is found to detect CCSNe with a probability of 50% at a distance of 246 kpc for the $27.0 M_{\odot}$ model, and 147 kpc for the $9.6 M_{\odot}$, while keeping a false detection rate below one per century. Relaxing the conditions to allow for a CCSN detection rate of 1 per year increases the detection range to 278 kpc for the $27.0 M_{\odot}$ model and 164 kpc for the $9.6 M_{\odot}$.

It is possible that a supernova occurs and does not pass the trigger condition but is detected by other detectors. If the time at which the neutrino burst should arrive is known, one may look at the detector's stored data for a signal. The sensitivity for such searches is calculated in two different ways. In the first, it is assumed that the arrival time of the neutrinos is known to be within 1 hour. In this case, CCSNe could be detected with a probability of 50% at 317 kpc and 190 kpc, for the $27.0 M_{\odot}$ and $9.6 M_{\odot}$ models,

respectively, with a confidence greater than 3σ ¹ that the noise did not produce such a signal. The range at 5σ is found at 246 and 146 kpc, respectively. The second case assumes that the arrival time of the neutrino burst is known exactly, so that a signal-versus-noise analysis can be performed to obtain the significance of such a detection. This is similar to the analyses performed by IceCube, so the results can be directly compared. The detection significance is calculated for each multiplicity condition individually and then combined. The 5σ horizon is at 350 kpc and 232 kpc for the $27.0 M_{\odot}$ and $9.6 M_{\odot}$ models, respectively. If the events were scaled to an inverted hierarchy oscillation scenario, the result reaches 442 kpc for the $27.0 M_{\odot}$ model and 267 kpc for the $9.6 M_{\odot}$ model. If the events are not separated in different multiplicities, the 5σ horizon is found at 60 kpc even if the IceCube-Gen2 detector is combined with the expected signal detected by IceCube. This result clearly demonstrates the direct improvement of the method proposed in this chapter over the classic method.

Despite the improvement with respect to IceCube for the new detector, the expected rate of CCSNe occurring within these distances is still low. It has been calculated that, using the condition that maintains a false detection per century below 1, approximately 0.44 CCSN detections per decade would be expected, using a predictive model of the cumulative supernova number as a function of distance [169]. It was also calculated that the detection rate is indeed very difficult to increase. To, for example, double the previous expected detection rate, it would be necessary to consider a detector of to 20000 mDOMs with 200 times less background rates than current mDOMs, and allow a false detection rate of about 0.3 detections per year. Thus, even if the method explained in this chapter would considerably increase the capabilities of the newer detector to distant SNe, it cannot be expected that it will deliver regular detection of these events.

Next, the analysis of the detected CCSN flux over the time of the explosion concluded that, without using multiplicities, a very good resolution to the detected flux is achieved if the CCSN is close enough. However, as the CCSN takes place farther away, it becomes beneficial to require a multiplicity condition, since otherwise the signal is below the background fluctuation. Then, it was studied how well the two CCSN models could be distinguished from each other by comparing their detected fluxes. It was found that both models are distinguishable in the newer detector with a confidence of 5σ at a maximum distance of 27 kpc if the multiplicity method is not used, while using a multiplicity condition of $m \geq 4$ this range increases up to 62 kpc. A similar analysis was then performed focused on distinguishing the different oscillation scenarios using the detected flux. Both oscillation scenarios (NO and IO) can be distinguished with 5σ confidence at approximately 16 kpc ($27.0 M_{\odot}$) and 10 kpc ($9.6 M_{\odot}$) without using coincidences, while this range increases to approximately 26 kpc ($27.0 M_{\odot}$) and 16 kpc ($9.6 M_{\odot}$) if a multiplicity condition of $m \geq 3$ is required. IceCube, on the other hand, can distinguish both scenarios with 5σ confidence at a distance of approximately 12 kpc for a model based on a CCSN of a progenitor mass of $20 M_{\odot}$ [168].

Furthermore, it was studied whether the multiplicity conditions could be used to reconstruct the mean energy of the CCSN neutrinos. It was obtained that this can be reconstructed with a resolution of $\sim 17\%$ for a CCSN of $\langle E \rangle = 12$ MeV in the ideal case where it remains constant during the flux. The result is a significant improvement from similar IceCube studies using inter-module coincidences, which was expected since coincidences in different

¹One-sided Gaussian standard deviation. This stands valid for other results of this section given in σ as well.

modules in IceCube for such low-energy events are very rare.

Next, the results concerning the detection range to CCSNe were calculated assuming other detector configurations: ICU using 400 mDOMs and IceCube-Gen2 using 10000 LOM16s. It was found that ICU will be able to detect CCSN farther than current IceCube if multiplicity conditions are used to identify events, considering only the mDOMs that will be deployed within the new detector. A detection range of (74 kpc, 45 kpc) at 50% was obtained for the ($27.0 M_{\odot}$, $9.6 M_{\odot}$) models, respectively, while keeping a false detection rate below 1 per century. If the CCSN time is precisely known, the 5σ horizon is found at (110 kpc, 67 kpc) for the ($27.0 M_{\odot}$, $9.6 M_{\odot}$) model, respectively, in the no-oscillation scenario. For the IceCube-Gen2 detector using LOM16s, a shorter detection range was obtained than that obtained using mDOMs with the same number of modules. This is due to the very different behavior of the detection pattern of the radioactive decays in the glass of the modules. While in the case of mDOM, the rates decrease considerably with increasing multiplicity condition, in the case of LOM they decrease much more smoothly. Concretely, the detection range at 50% probability for the $27.0 M_{\odot}$ model was found to be 163 kpc for LOMs with Okamoto glass and 96 kpc for LOMs with Vitrovex glass. The 5σ detection horizon, assuming that burst time is known, is found to be at 220 kpc if the LOM vessels are constructed with Okamoto glass and at 129 kpc Vitrovex glass is used, for the $27.0 M_{\odot}$ model. Thus, from a point of view only concerning the detection of MeV CCSN neutrinos, equipping the future detector with mDOMs would be much more beneficial than doing so with LOM16s.

Finally, details concerning possible errors in the results were discussed. On the one hand, it was shown how small changes in the simulation regarding the geometry of the modules can have significant effects on the final results. Simulation-induced errors are probably the major source for errors in the results of this chapter, since only recently the first mDOMs became operational, and one would still have to compare actual mDOM measurements with simulations to check that these match, especially those concerning radioactive noise at high multiplicities. The other caveat in these results is the absence of background resulting from atmospheric muons. This is a constraint because of the way the simulations have been performed, using a single module, and without having an estimation of how effectively this background will be removed in the future larger detector. To approximate the loss due to this background, it was assumed that the modules closest to the detector surface would be dominated by it at high coincidences and therefore would not be used to send CCSN alerts. It was found that even when removing up to 20 modules per string, the detection range is still above 200 kpc for the $27.0 M_{\odot}$ and above 120 kpc for the $9.6 M_{\odot}$ for sending gold alerts. In this pessimistic scenario, although the results are worsened, the detector would still be far superior to IceCube or IceCube-Gen2 without exploiting coincidences. Once the actual detector is built, the behavior of the modules should also be monitored beforehand to make sure that they do not suffer from artifacts that could cause signals in different PMTs in a correlated manner, like, for example, sparking due to potential differences, breaking the stability of the background in the modules at high coincidences and thus affecting the method here. Thus, unstable modules must be identified and eliminated beforehand from studies like this one.

Overall, it can be concluded that exploiting coincidences between different PMTs in the same segmented module is expected to significantly improve the study of MeV CCSN neutrinos. Each module of the new detector acts as a tiny detector which, when combined, returns a much cleaner view to these events. It should also be noted that not all MeV CCSN

neutrino interactions were included in this work, and that most results were obtained for a conservative scenario of no oscillations. Although IBD and ENES form $\sim 95\%$ of the expected rate in IceCube [168], this ratio is highly dependent on the neutrino energies. The cross section of the $\nu_e(\bar{\nu}_e) + {}^{16}\text{O} \rightarrow e^-(e^+) + X$ processes, not included in this chapter, increases considerably at energies greater than 20 MeV [202]. Although the contribution to the total rate of these is small, the influence on the high multiplicity counts could be significant, potentially increasing the detection ranges obtained here. The sensitivity of the final detector to study CCSNe will only be precisely calculated once a full simulation of the detector and its background is available; nevertheless, the results shown here are a great motivation to exploit the segmentation of the modules for this and other studies that attempt to focus on such low-energy neutrinos. Note that, although only two models are used here for the results, the method developed in this chapter would be applicable also for other models. This could include O-Ne-Mg core SNe or heavier SNe resulting in a formation of a black hole, among others. The future IceCube-Gen2 will not only improve the detector's capability for very energetic neutrinos, but also the inclusion of new modules will provide a new way of looking at events well below the energy range on which the detector is focused.

Calibration of the bubble column with mDOM flashers in ICU

To ensure accurate reconstructions of neutrino events and physics analyses with IceCube, calibration of the detector is crucial. The calibration encompasses understanding all elements that may affect the results, such as measurement devices, analysis methods, and the detector medium. For this reason, the optical modules and their different components are thoroughly characterized, and specific devices are introduced in the detector to study the properties of the ice. The detector is continuously monitored during operation. For IceCube, the biggest challenge from the calibration side is the characterization of the medium, a naturally formed Antarctic glacier, since there is no control over its properties and it can only be studied by performing dedicated measurements. Indeed, the medium represents the largest IceCube systematic uncertainty source.

The bulk ice is an excellent medium for light propagation because of its high transparency, meaning a long propagation distance for photons, and it is also a stable medium in the sense that its properties do not change over time¹. This is a great advantage over other water-Cherenkov detectors in which the medium must be constantly monitored, like for example the KM3NeT detector, where water flow, currents, sediments, and wildlife constantly influence the detector medium [203]. However, measuring and characterizing the ice properties in IceCube is not straightforward. The detector itself is buried thousands of meters in the glacier and occupies a volume of 1 km³. Furthermore, glaciers are entities formed dynamically and influenced by internal ice drifts and external events, and their optical properties are not homogeneous.

Although the South Pole glacier is of natural origin, the construction of the IceCube detector means an artificial modification of the medium. To install the optical modules during the construction of the detector, holes must be drilled into the ice. The optical modules and cables are then installed, and the water in the hole is allowed to freeze, creating a column of new ice. IceCube has observed that the new ice column, commonly known as hole ice, contains an inner section where impurities and bubbles are pushed during the re-freezing process, commonly referred to as the *bubble column*². The bubble column has optical properties much different from those of the rest of the hole ice and the bulk ice itself and largely influences the light propagation in the region.

In this chapter, detailed simulations are conducted, and a method is developed to determine the sensitivity for characterizing the bubble columns in future ICU using LED flashers installed in the mDOMs. This chapter is organized as follows. First, an overview of the findings on the bubble column in IceCube is given. Later, the mDOM LED flashers are

¹On the scale of the detector lifetime.

²In the literature, sometimes authors refer to the bubble column directly as *hole ice*. In this work, the definition of hole ice is kept to the entire drilled column, while the bubble column remains the central part with significantly different optical properties.

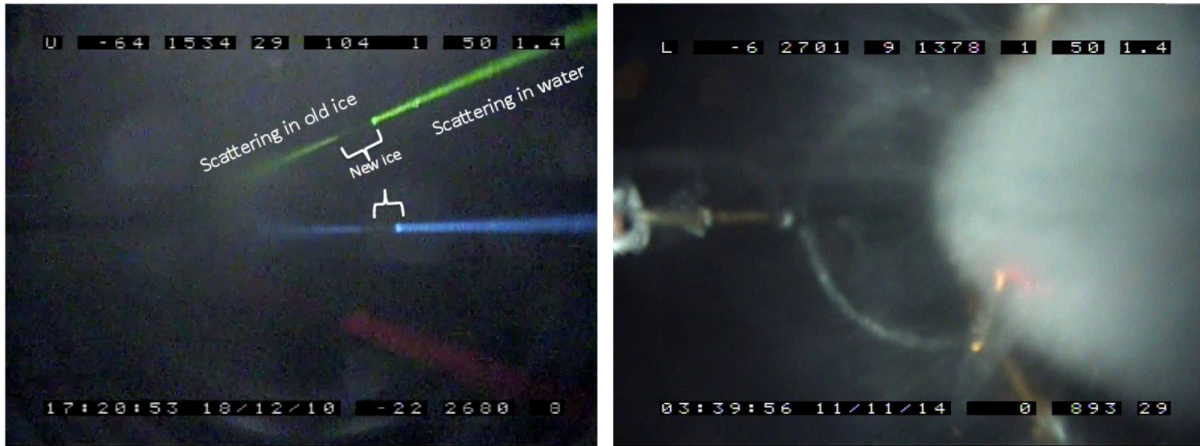


Figure 7.1: Sweden camera pictures. **Left:** Camera facing to one side shortly after deployment. **Right:** Camera facing up the string hole. Here, the bubble column at the right side of the picture is fully develop. Pictures from IceCube’s internal repository.

described, and their inclusion in the simulation is explained. Then, the simulations are performed, scanning the column parameters, and observing the behavior of a defined likelihood space. Finally, the column parameters are reconstructed, first in the ideal case without considering systematics, and finally after introducing the most significant sources of systematic uncertainties for the study, giving the final the precision of the method for the reconstruction of the bubble column parameters.

7.1 The hole ice and the bubble column in IceCube strings

Although several measurements have been performed in IceCube, the optical characteristics of the bubble column are still not known with the required precision [204, 103, 205]. The current proposal for bubble column formation consists of cylindrical freezing. The hole would freeze from the outer to the inner part, pushing the impurities and air bubbles to the center of the cylinder. This creates a substructure inside the hole ice, the bubble column. Initially, the effects of the bubble column were confused with shadowing of the string data cable, but later it was observed and measured in IceCube by different methods, which are summarized here.

7.1.1 Sweden Camera pictures

The refrozen hole ice has been captured in videos and pictures taken by the two so-called *Sweden cameras* that were installed in the IceCube 80 string (see Section 3.5). Two pictures taken with the cameras are shown in Figure 7.1. Each image was taken at different times after deployment. In the picture on the left, the hole is not yet fully refrozen. Laser lights are emitted, which go through the bulk ice, the hole ice, and the water. In the picture on the right, the bubble column is already formed and is clearly visible on the right-hand side. No differences were observed in the refrozen hole ice relative to the bulk ice, except for the bubble column itself.

7.1.2 Methods for studying the bubble column in IceCube

The bubble column has been studied by several methods in addition to visual information obtained from the Sweden cameras. First, a method was developed where the DOMs' angular acceptance curves are adjusted from laboratory measurements to match in-ice detected data. This is achieved by using LED flashers or atmospheric muon data and comparing the results to simulated models [206]. The results provided the first hints to the existence and properties of the bubble column, since the best fits suggest a region of much shorter scattering length centered on the modules.

A more specific method has also been developed that uses the data measured when the LEDs are flashed [103, 204]. In this case, a log-likelihood minimization of the bubble column parameters is performed, trying to fit a detailed ice model. This has been studied using the same module that flashes the LEDs, and also detecting the light in the modules in the vicinity. This approach will be evaluated in this chapter, using the mDOM flashers and 2 modules instead, and trying to improve the results based on the segmentation of the new modules.

7.1.3 Current knowledge on the hole ice and the bubble column

Although the determination of the ice properties within the column is still not conclusive in IceCube, studies have provided insights into the properties of the column. The most important results regarding hole ice properties from the studies described above are summarized in the following¹:

- The outer region of the hole ice has optical properties similar to those of the bulk ice; therefore, it does not impact significantly analyses and reconstructions [205].
- The hole ice contains a central region with a much shorter scattering length, the bubble column. The results indicate an effective scattering length within the bubble column of just a few centimeters, while no significant changes have been found regarding the absorption length. The exact value for the effective scattering length is still uncertain, but the best current fit yields $b_e \approx 3$ cm [204, 205].
- The bubble column has a cylindrical shape with about half-DOM size centered within the holes, with the best fit being a diameter $d \approx 16$ cm [204, 205].

The short scattering length in the bubble column considerably affects the path of the photons that travel through it. This ultimately results in inaccuracy in reconstruction if the parameters are not properly implemented in the models. The influence on the analyses of the bubble column is more significant when focusing on low energetic events, largely influencing the direction reconstruction at GeV energies, where ICU is focused [207]. Thus, the importance of characterizing the bubble column for the future detector is highlighted. Furthermore, ice calibration results obtained with ICU can be brought into IceCube to update ice models and further improve analyses.

¹Note that, at the time of writing this thesis, these studies are still ongoing and results are subject to change.

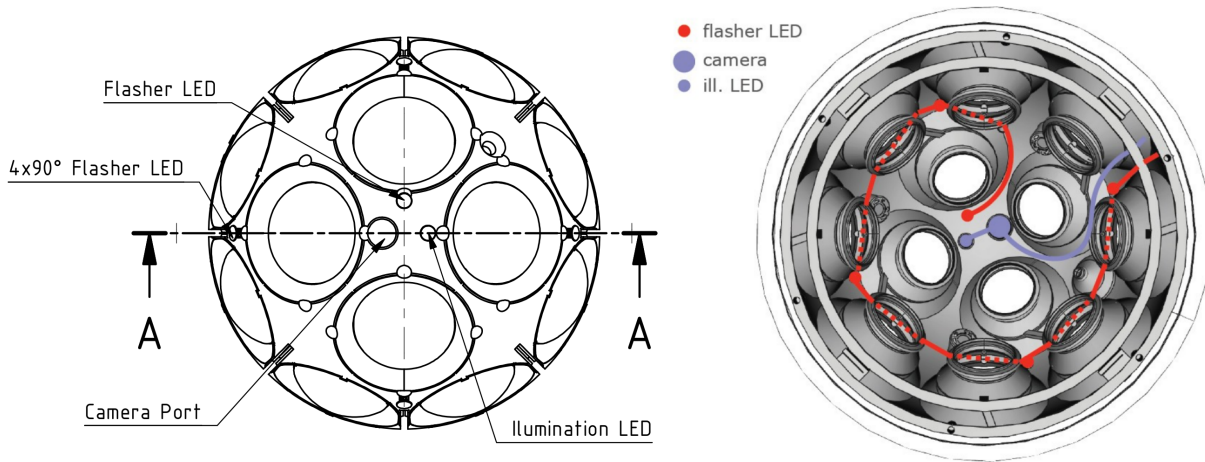


Figure 7.2: **Left:** Sketch of the mDOM support structure looked from above where the position of the calibration devices are labelled. **Right:** Inner view of the mDOM support structure, with the layout for the connection of the calibration devices. Figures from internal communication.

7.2 LED flashers in mDOMs

Among other calibration studies, LED flashers are integrated into the new ICU modules in order to improve the characterization of the bubble column. This chapter focuses on the capability of performing such studies using mDOMs. The segmentation of the mDOM is expected to improve current studies in comparison with the DOMs. In addition, contrary to the DOM case, the mDOM geometry easily allows one to locate one LED centered, and thus likely contained within the bubble column, potentially increasing the sensitivity to the column parameters.

The LEDs that will be mounted on ICU modules must satisfy certain requirements, which include [208]:

- **Placement:** LEDs shall be arranged in rings pointing outward, with at least 4 LEDs spread regularly around the 360-degree azimuth range. Each ring shall point neither more than 45 degrees above nor below the horizontal plane.
- **Brightness range:** dynamic range of $10^5 - 10^9$ photons per flash, programmable to within a factor 1.5 of any target value within the range, and consistent for all pulses throughout a run.
- **Time profile:** ≤ 7 ns FWHM for low-bright pulses, ≤ 10 ns FWHM for bright pulses. The shape must be known within < 1 ns.
- **Emission spectrum:** 405 ± 10 nm, with FWHM of < 30 nm.
- **Angular distribution:** Gaussian-like profile with a standard deviation less than 15° . The emission at large angles should be small and $< 10\%$ beyond 2σ .
- **LED pointing direction:** Once mounted, the LEDs should be oriented within less than 5 degrees from their nominal direction.

The chosen LED model that fulfills these parameters is *Roithner LaserTechnick's XRL-400-*

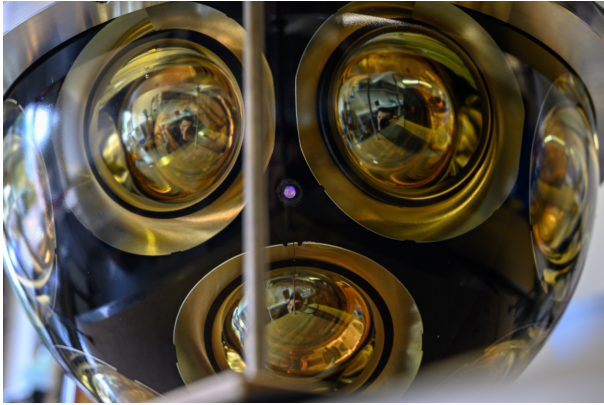


Figure 7.3: One of the first fully working mDOM prototypes flashing one of the LEDs mounted on the triangular spaces. Picture from internal communication.

50¹, which are to be included in all new modules of ICU. Each mDOM will be equipped with 10 LEDs - 5 LEDs per half-sphere. The position of the LEDs can be observed in the sketches shown in Figure 7.2. These LEDs will be located in the triangular spaces between the upper and middle PMT rows in each mDOM hemisphere, whereas two LEDs will be in each pole. These two LEDs are not centered on the mDOM axis, but slightly displaced toward one of the PMTs to leave space for other calibration systems. The LEDs in the triangular spaces are symmetrically distributed along the azimuth angle. The distribution of LEDs along the module has been decided in terms of hardware, construction capabilities and considering the proper performance, using the knowledge acquired from IceCube.

At the time of writing of this thesis, the first mDOM prototypes have already been built and have been subjected to a testing process, including the LEDs. A picture of the mDOM flashing a LED is shown in Fig. 7.3. For simplicity, when referring to the LEDs during the thesis, the LEDs in the equatorial spaces are named *peripheral* LEDs, while the LEDs at the poles are named *centered* LEDs, even though they are not fully centered within the module axis.

7.3 Simulation details

In the following, the simulations performed in this chapter are described. This ultimately aims to use two consecutive mDOMs where the LEDs are flashed to characterize the bubble column properties. In ICU strings, the mDOMs and D-Eggs are mixed, but often two mDOMs are found consecutively [23]. The characterization of the column at some depth can be extrapolated to the whole string², and ultimately, all bubble columns formed in the same way may have similar optical properties, thus the information on different strings and modules can be combined in the real experiment. The validity of this can also be verified by the method proposed in this chapter, once the detector is built and different strings are studied in ICU.

The simulations are written within the *Geant4* [157] simulation framework described in Chapter 5, consisting of two mDOM modules with the surrounding bulk ice and the bubble column in the middle. The LED flashers are simulated in the mDOM geometry, as well as

¹<http://www.roithner-laser.com>

²This is a generalization, since locally each module might be aligned or positioned slightly different, for example.

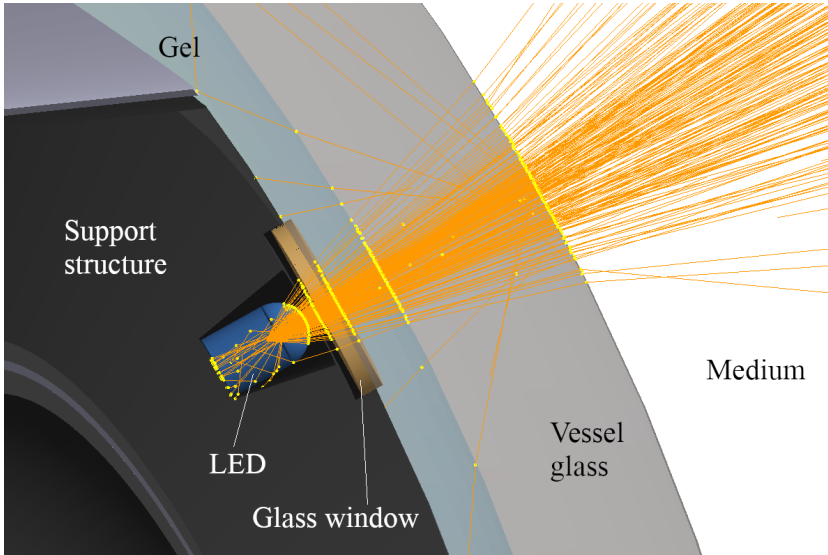


Figure 7.4: Cross section image of the LED shooting photons (orange lines) in the mDOM Geant4 simulation. The LED object, in blue, is embedded in a hole in the support structure and separated from the gel by a flat glass window. The LED volume is constructed as the union of a hollow cylinder and a hollow sphere, with properties corresponding to silicone dioxide glass.

the emission of photons from them. The simulations are performed at a single depth. For simplicity, this depth is chosen where the optical properties of the bulk ice are close to the mean of all ICU modules. This resulted in optical properties for the bulk ice given by a scattering length of $b(400) \sim 50$ m and an absorption length of $a(400) \sim 170$ m, following the models described in Section 5.3 (see Eq. 5.2 and Eq. 5.3). Whether this choice has any influence on the study is explored at the end of the chapter in Section 7.7.1.

It is important to note that many idealizations are introduced when describing the simulations in this section and are carried forward to the analysis, such as perfectly aligned modules, fixed LED light profiles, etc. These assumptions are introduced to obtain initial results of the study. The impact of these assumptions are studied later in Section 7.7.

7.3.1 LED simulation

The construction of the LED geometry in Geant4 and the determination of the transformations for the light profiles were carried out as part of a bachelor thesis, which was co-supervised by the author during the completion of this thesis. A summary of these results is provided here, as they are later utilized in the simulations. For more information, refer to the thesis [209].

The LEDs have been simulated following drawings from the manufacturer. The LEDs are made of silicone dioxide glass, material composition included in Geant4. A representation of the LED in the simulation is shown in Figure 7.4, along with some photons emitted from the LED. Note that the internal components of the LED are not simulated. Photons are simply generated where the light source is located and this is approximated by a point source. Then, the light emission must be calibrated so that the output meets the measured profiles.

The LEDs light profiles have been measured by the IceCube Collaboration since its inclusion in the new optical modules was decided. Measurements were made in air, using a photodiode located at ~ 96 cm of the LEDs [210]. The data of 3 LED samples have been used in this chapter's simulations. These are shown in Figure 7.5. Although the profiles

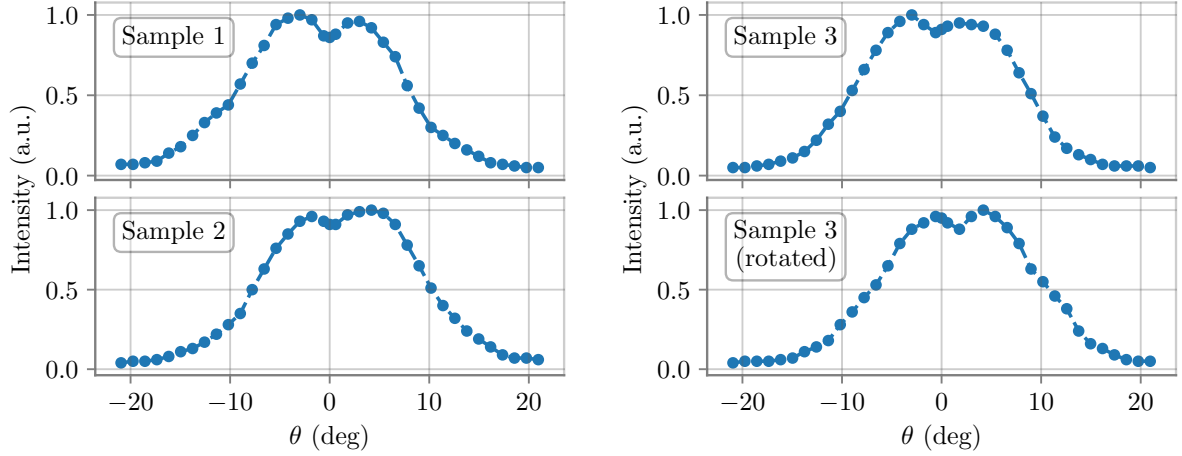


Figure 7.5: Light profiles of 3 LaserTechnick’s XRL-400-5O samples, measured at 96 cm of the LEDs. Sample 3 is measured twice with a rotation of 90° . Each measurement is conducted moving the photodiode in two directions, with $\theta = 0^\circ$ representing the LED pointing directly towards the photodiode. Data from [210].

are similar, the differences between each sample are noticeable. Additionally, the profile is slightly dependent on the orientation of the LED, as can be observed by the asymmetry in θ and confirmed with sample 3, which has been measured twice, rotated 90° each. The maximum light emission is not at $\theta = 0^\circ$ but a few degrees deviated depending on the sample and the orientation of the LED.

In order to incorporate the profiles in the simulation, for simplicity reasons and since there is no 3D scan of the light profiles, these are approximated as being symmetrical around θ . Since each measurement from Figure 7.5 is performed in two directions, assuming this symmetry, there are a total of 8 measurements that are treated as individual light profiles. Whether this approximation affects the results is studied at the end of the chapter in Section 7.7.1.

The profiles must be transformed before incorporating them into the simulations. Since the photons are produced inside the LEDs, if the measured profiles are used directly in the simulations, the light emission after the photons have escaped the LEDs would not match the actual measurements. Three steps are applied to the profiles to correct them in order to produce the right photon emission, which are explained in the following:

- Using the last 3 data points, the profiles are lineally extrapolated to 0 intensity. This is done because the last measured data point in each sample is still at $\sim 5\%$ intensity.
- A transformation on the angle is made that accounts for the combination of the glass curvature and the refraction between the internal air in the LED bulb, the LED glass, and the air outside. The transformation is obtained by simulating photons at different angles θ and measuring the angles at which the photons escaping the LEDs into the medium. The relationship between the generated photon direction θ_{gen} and the photon direction after escape from the LED θ_{em} is shown on Figure 7.6. The ankle at $\theta_{gen} \sim 40^\circ$ is due to the photons starting to pass through the cylindrical part of the LED glass bubble instead of the spherical part.
- The profiles have been measured at different θ at a fixed distance and ϕ . This produces

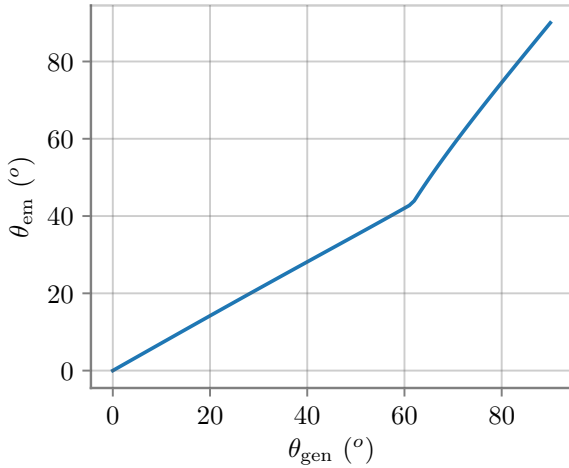


Figure 7.6: Relationship between the direction of the photons at generation inside the LED θ_{gen} and their direction after escaping the LED θ_{em} . Data from [209] and modified.

that, at the measurement point, the solid angle decreases with increasing θ in the $[0, \pi]$ range. To account for this, a $\sin \theta$ factor is included. After this, the final input light profile is obtained.

The application of the steps described above to the measured profiles results in the input profile that must be given to the simulation to generate the photons. For compatibility reasons, the profiles are interpolated and sampled in 1024 data points, which are the inputs for the *Geant4* simulation. To evaluate the validity of the profile transformation described above, the setup used to measure the LED profiles has been emulated with the *Geant4* simulation, by placing the LED and a surface simulating the photodiode at the proper distance in an air environment. Then, photons are generated following the profile obtained with the transformations above in θ , whereas the ϕ component of the photon direction is randomized. The generation of photons is tested and shown in Figure 7.7 on the left, where it is visible that the spectrum is being emitted correctly following the given input profile. Then, if the transformation works as expected, the detected profile in the photodiode should be the measured light profile. The results are shown in Figure 7.7 on the right. The distribution of photons detected in the photodiode precisely follow the measured profile, with $\sim 68\%$ of the normalized residuals¹ within $[-1, 1]$, as expected from a purely statistical deviation.

As previously shown, a total of eight different light profiles are available from the measurements and all have been transformed to use them in the simulations. In the following sections, unless otherwise noted, the mean profile is used to generate the photons, shown in Figure 7.8. The impact of having different profiles on the sensitivity to determine the parameters of the bubble column is studied later in Section 7.7.1.

The LEDs have been incorporated into the mDOM geometry following the arrangement decided by the IceCube Collaboration described above. The position of the LED within the cavity is assumed to be fixed, where the LEDs are perfectly aligned perpendicular to the surface in the spherical part of the module.

For simplification, all photons are generated with a fixed $\lambda = 405$ nm. It was checked that simulating a profile with a Gaussian emission does not influence the results². This is due to

¹Calculated as $\text{res} = (S - M)/E$, with $S \equiv$ Simulation data, $M \equiv$ Measured data and $E \equiv$ Errors.

²This approximation was done because the models were first built as simple as possible. After

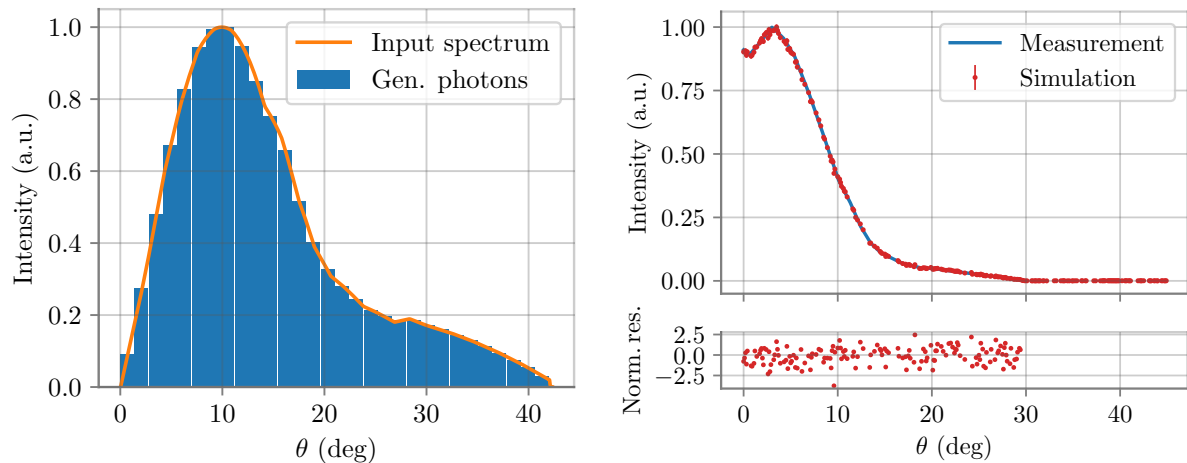


Figure 7.7: Left: Generation test of photons from the LED. In orange, the light profile as given to the simulation is depicted, calculated after the transformations explained in the text. The histogram in blue shows the photons generated in the simulation. **Right:** Result of the simulation of the LED light profiles measurements, showing the measured profile in the lab in comparison with the result of the simulation done here. In the lower subfigure, the normalized residuals between the measurement and the simulation are plotted.

the scattering length not depending on the wavelength inside the column in the simulation, thus having a Gaussian emission only changes slightly the overall detection equally in all PMTs, due to small differences in the quantum efficiency and glass/gel absorption. The properties of the bulk ice do depend on the wavelength, but this does not play any role in the study here (also checked and commented upon in Section 7.7). Also, the quantum efficiency for the PMTs is not directly included in the simulation. Instead, the total number of detected photons is weighted afterwards with the corresponding quantum efficiency value at the simulated wavelength, leading to the same result with fewer simulations.

7.3.2 Modules simulation

The mDOM is constructed in the simulation as explained in Chapter 5. From now on, all simulations consist of two mDOM modules along with all their external components, consisting of the harness, belt, penetrator cables, and the large data cable, which will connect the modules with the surface in the real experiment. Within the standard arrangement, the modules are located in the center of the simulated volume, with 3 m of separation between each other following the latest ICU geometry design. Modules are assumed to be perfectly aligned.

The photons are generated only from one of the mDOMs, which is named *emitter mDOM* (EM), whereas the other is named *receiver mDOM* (RM). Note that this distinction is only made to better refer to each module, since the *emitter* module also detects photons and both modules are used to characterize the column. LEDs from the emitter mDOM

introducing the wavelength spectrum following the requirements, with Gaussian profiles of $\sigma \geq 15$ nm, and verifying that the LLH curves that are shown later in this chapter were identical, the author chose to maintain the simplification and use the existing, more abundant simulations instead of running new ones.

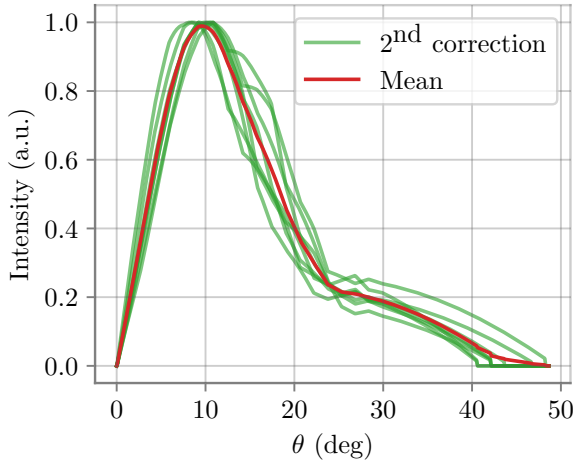


Figure 7.8: Input profiles for the simulation, obtained after transforming all measured profiles as explained in the text. The mean of all profiles, which is used in the simulations as a standardized profile, is also plotted.

are flashed one at a time. In principle, it can be assumed that indistinguishable results would be obtained if the roles of emitter and receiver mDOMs were interchanged. For the emitter mDOM, being in the default arrangement above the receiver one, only the LEDs in its lower hemisphere are flashed, which are those facing the RM. Both modules are assumed to be perfectly aligned and equally oriented. The parameters of the bubble column are then varied and the behavior of the detected signal is studied.

To improve understanding, the LEDs and PMTs will be labeled as shown in Figure 7.9 moving forward. The enumeration of the PMTs is chosen following mDOM electronic sketches, while the enumeration of the LEDs has been simplified since only 5 LEDs are flashed in these studies. The lower LED, named LED = 0, is displaced within the positive x direction in the standard reference frame to the PMT = 20.

7.3.3 Bubble column simulation

Finally, the bubble column is implemented in the simulation. This is approximated as a column of ice with the same refraction index and absorption length as the bulk ice, while the effective scattering length (b_e) can be controlled as an input parameter. The position with respect to the modules (x, y) and the bubble column size (d or r for diameter or radius, respectively) of the bubble column can also be controlled with input parameters, so that all these variables can be properly scanned.

The bubble column is assumed to be perfectly cylindrical and homogeneous, which is a reasonable assumption according to the current knowledge [103, 204]. This way, the transition between the column and the bulk ice is abrupt, without any transition region between the two Geant4 objects¹. Although macroscopically the column and bulk ice are well separated, there should be a narrow transition region between the two. Whether this approximation has any measurable effect on the results is investigated in Section 7.7.

Figure 7.10 shows images of the simulation flashing LEDs from one mDOM for different

¹Note that, within the simulation framework, the volumes of the mDOM and the external components need to be subtracted from the bubble column volume, since all volumes are placed within the same mother volume (bulk ice in this case).

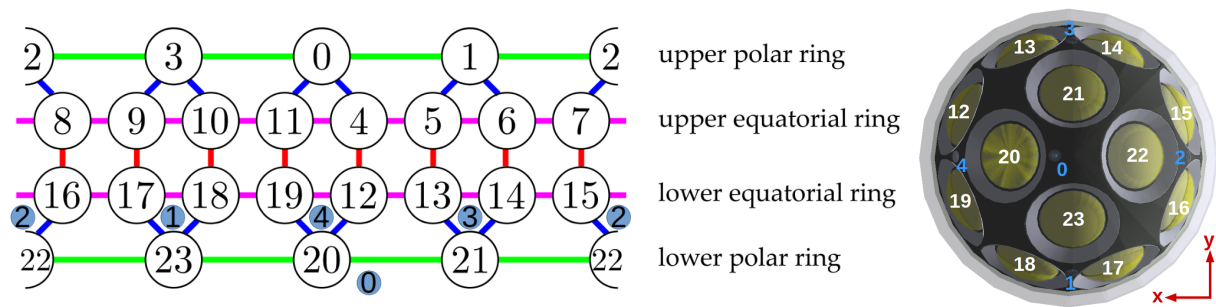


Figure 7.9: **Left:** Enumeration chosen to identify PMTs and LEDs of an mDOM. PMTs are represented by white circles while LEDs by blue ones. The PMTs can be separated in different groups depending on the row they are. As such, the *upper* rows are named being the closer to the ice surface. The enumeration shown here is used in the whole chapter. Figure from [211] and modified. **Right:** The emitter mDOM seen from below in the Geant4 simulation, with the PMT (white) and LED (blue) labels and the reference frame from that view.

bubble column parameters. In the subfigure a), there is an exemplary case of a photon scattering back in the column and being detected in the emitter module. Shortening the scattering length deflects the photons more often, which can be seen comparing the subfigures a) and b). It can be observed that photons emitted by LEDs that are not contained in the bubble column may also scatter and enter the column, which occurs in subfigure c), where the bubble column does not contain any LED. Note that in this chapter, it often will be stated that the LED is contained/not contained in the bubble column. This refers to the LED being in the geometric region that the bubble column occupies when extended towards the module position. Obviously, the LED object is always located within the module.

7.4 Simulation results

The idea of reconstructing the bubble column properties using the LEDs will only work if the position, size, and optical properties of the column have a significant influence on the photons detected in the PMTs. To check this, the detection patterns varying the bubble column parameters are shown in this section. To avoid an excessive number of figures, this is only shown for the case of varying the effective scattering length of light in the column b_e , fixing the column size and diameter, and only the most interesting figures are shown. If the reader is interested in seeing more cases and the figures omitted here, these can be found in Appendix A.

In the real experiment, once the column is refrozen, its properties will remain constant. This means that the results of many LED flasher runs can accumulate during the lifetime of the detector to a limit of infinite statistical resolution. Here, it is chosen that each simulation consists of 10^8 photons emitted per LED, which is a compromise maintaining a reasonable simulation time and getting decent statistics, and, at the same time, it is a realistic value for a single flash. Of course, many simulations can be combined to construct a model, which is done in the next sections.

In Figure 7.11, the pattern of detection in the PMTs of EM and RM is shown when

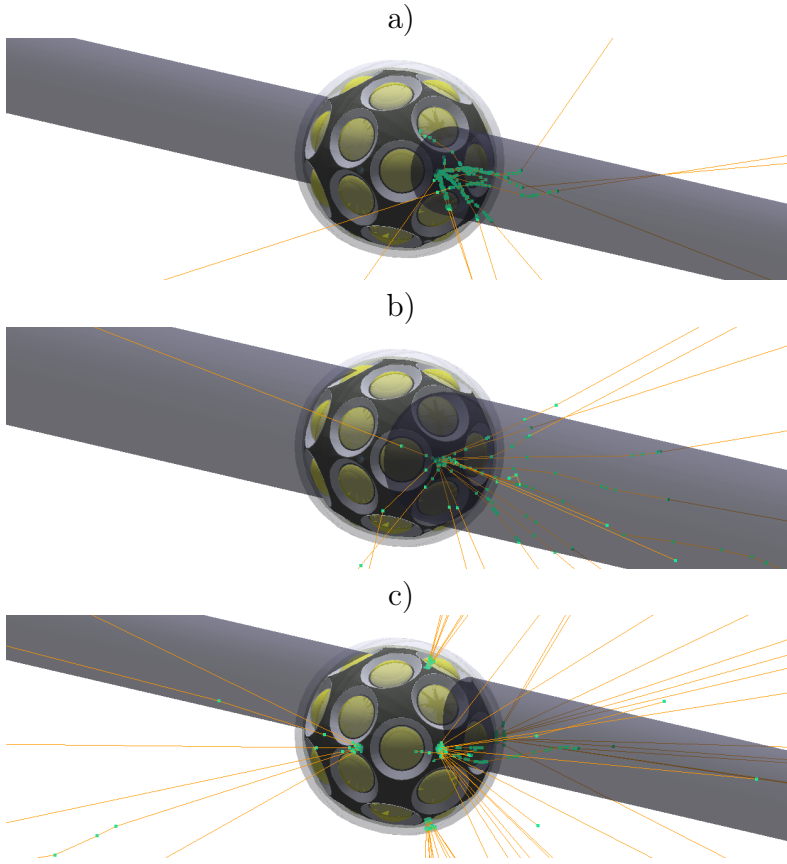


Figure 7.10: Pictures of the Geant4 simulation running the flashers from the LEDs in one mDOM hemisphere for different bubble column parameters. Photons are depicted in orange lines, while the green dots indicate the vertex of an interaction, like scattering, absorption or refraction. The bubble column is shown in gray. For visibility reasons, the external components of the module are not included in these figures, although they are included for obtaining the results later in this chapter. **a)** Bubble column centered at the modules ($x = 0$ cm, $y = 0$ cm) with $b_e = 1$ cm and $r = 8$ cm. The centered LED is flashed. **b)** Centered column at the modules ($x = 0$ cm, $y = 0$ cm) with $b_e = 10$ cm and $r = 12$ cm. The centered LED is flashed. **c)** Non-centered column ($x = -6$ cm, $y = 4$ cm) with $b_e = 3$ cm and $r = 8$ cm. All LEDs from half-hemisphere are flashed, none of them contained within the bubble column.

changing b_e , where the column has a diameter of $d = 16$ cm and is centered at the modules ($x = 0, y = 0$)¹. Only the PMTs that potentially would see more signals are shown, namely, the lower rows of the emitter module and the upper rows of the receiver one. In this case, the LED 0 is contained in the bubble column. The PMTs from the lower polar ring of the EM and from the upper polar ring of the RM are partially contained within the bubble column. When flashing the centered LED (LED=0), the shorter the scattering length, the more photons the PMTs of the emitter module measure. This is a logical expectation, since more photons scatter back at shorter b_e . Therefore, the opposite situation occurs for the RM. The difference between PMTs within the same row is due only to the position of these with respect to the flashing LED. When flashing the LED 1, which is neither contained in the column surface nor pointing to it, the results would not help the reconstruction of b_e , since there is no variation when changing the parameter. From these figures, it can be expected that the reconstruction of b_e is more precise the smaller it is, since at low b_e the counting rates vary more quickly.

¹The position of the bubble column is always given with respect to the center of the modules, even if this is not explicitly mentioned in all cases. The only exception is when one or both modules are moved horizontally, which is only done in Section 7.7. In these cases, the position of the bubble column refers to the center of the modules before they are moved.

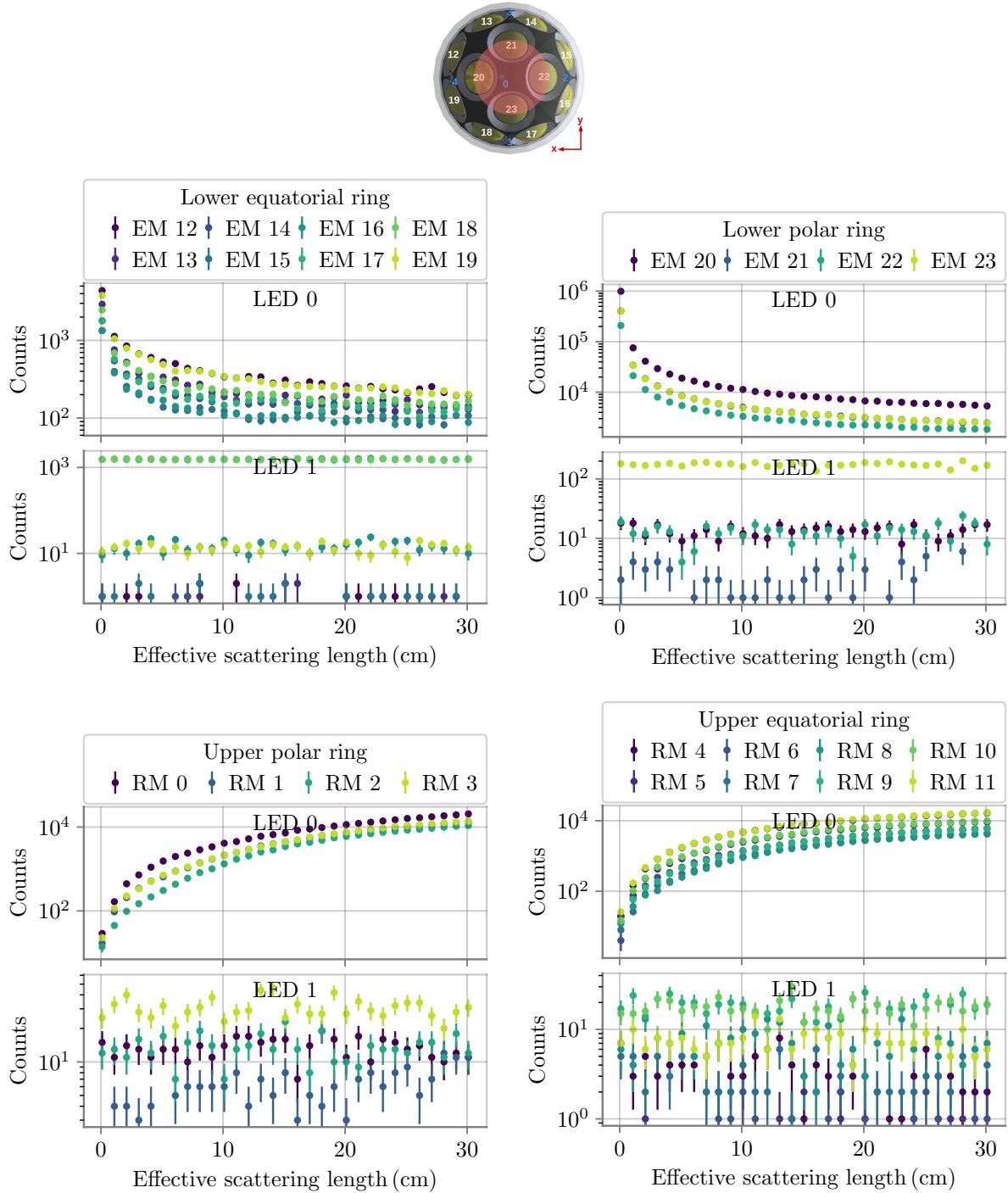


Figure 7.11: Counts on different PMTs of the Emitter Module (EM) and Receiver Module (RC) when flashing the LEDs 0 and 1 varying the scattering length of the bubble column, with a column diameter of $d = 16$ cm centered at the modules ($x = 0$, $y = 0$). The sketch in the upper part of the figure shows the approximate location of the column (red circle) with respect to the emitter module.

The peripheral LEDs are more important when located within the bubble column. As an example, this is shown in Figure 7.12, where the column has the same properties as before, but is located at $x = 0$, $y = -9$ cm with respect to the center axis of the module. LED 1 is contained within the bubble column, but LED 0 in this case is outside it. Nevertheless,

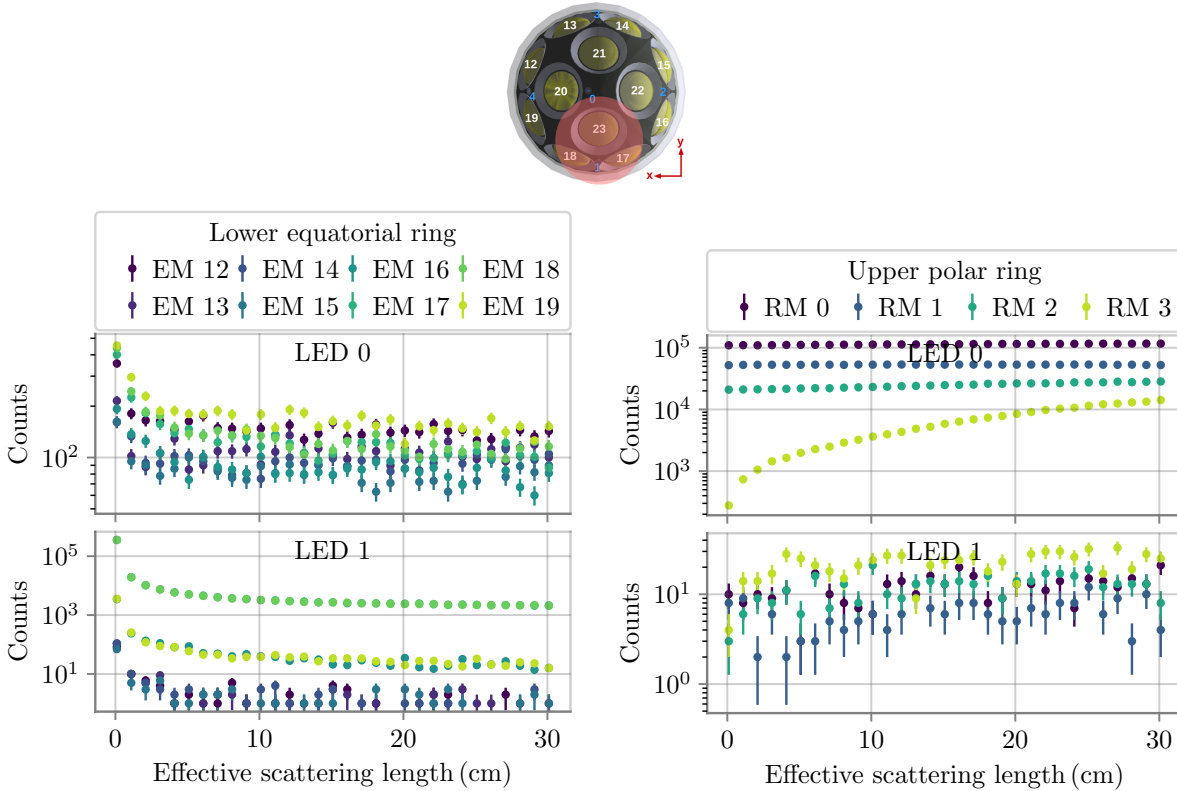


Figure 7.12: Counts on the lower equatorial ring of the Emitter Module (EM) and on the upper polar ring of the Receiver Module (RC) when flashing the LEDs 0 and 1 varying the scattering length of the bubble column, with a column diameter of $d = 16$ cm at $(x = 0, y = -9$ cm). The sketch in the upper part of the figure shows the approximate location of the column (red circle) with respect to the emitter module.

LED 0 still shows dependency in some cases. Moreover, the mDOM does not fully cut the bubble column in this case, thus PMTs in the other hemisphere of the module also detects more photons (see Appendix A) than in the previous case shown in Figure 7.11. The centered LED is therefore the most important one, and provides information even when it is not located within the column. The peripheral LEDs, on the other hand, need to be contained in the column, otherwise it is very unlikely that photons will enter into it. Furthermore, the RM barely detects any photons from the peripheral LEDs due to their orientations.

Another question that arises from the above figures is the capability of the PMT to measure such a high number of photons within a short time. In Figure 7.13, the time distribution of the photons detected by PMT=20 of the EM is shown, which is the PMT that detected the most photons in this simulation¹. Each LED emits 10^8 photons, and the bubble column is centered at the modules with $d = 16$ cm and $b_e = 3$ cm. The photon emission time was smeared using a Gaussian distribution with $\sigma = 7$ ns, following the strictest time resolution requirement for the LEDs. The data shows that the majority of photons are detected within a few nanoseconds, primarily resembling the LED timing profile, with a smaller proportion detected tens of nanoseconds away from the center of the distribution. The PMT dynamic range, once it is calibrated in the mDOM data acquisition system to be sensitive to single photoelectrons, maintains linearity up to a limit of about 200

¹Note that PMT=20 is the closest to LED=0.

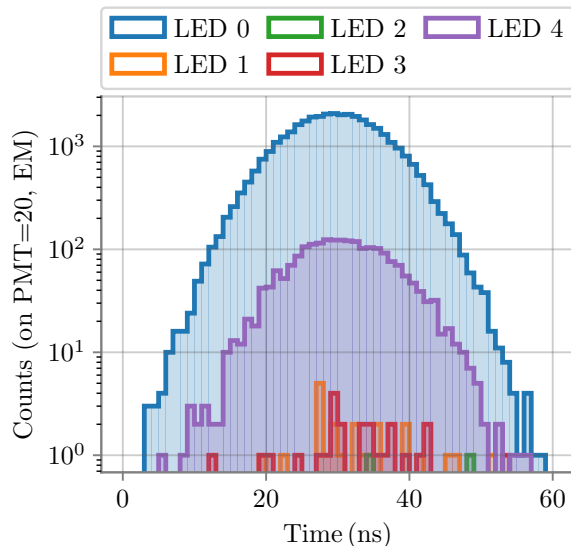


Figure 7.13: Time distribution on the PMT 20 of the Emitter Module (EM) when flashing each LED with 10^8 photons, assuming a time profile with 7 ns FWHM for all LEDs. Times are relative to the first detected photon from that flash in any PMT on any of both modules.

photoelectrons [193]. This means that, above 200 photoelectrons, the output signal does not increase linearly with respect to the number of detected photons anymore. Although photons are not detected instantly but within a few nanoseconds, the most likely scenario is that these PMTs would exhibit nonlinear behavior when flashing 10^8 photons. The results are similar in other PMTs of the EM as well. For the RM, although the photons take around 10 ns to reach the PMTs in the RM, the distribution of the detection times is similar.

Nevertheless, the LEDs are programmable to emit as low as 10^5 photons per flash, 3 orders of magnitude below the value chosen here. For such a smaller flash, the PMT signals are well within the linearity range. In the real experiment, a single flash run usually means running the LEDs many times and accumulating the results. It can be concluded that this study is suitable only if flashers of low intensity are accumulated, thus staying in the linear PMT regime. Thus, this whole chapter is based on the premise that the number of emitted photons is an accumulation of many small flashers and not a single large one, even if this is not explicitly stated in each simulation, in order to avoid the loss of linearity or even PMT saturation.

So far, no effect from the module noise on this method has been mentioned; however, from the intensity of the flashers and the short detection time distribution, the background, estimated at a few hundred counts per second per PMT, would not play any significant role here (see Figure 6.10 for more information about background rates in mDOMs).

7.5 Scanning the bubble column parameters

To reconstruct the parameters of the bubble column, it is necessary to test a hypothesis (or a model) with data. In this case, since there is no experiment, both hypothesis and data are constructed from simulations. This can be seen as a validation of the method that can be tested afterwards once the detector is built and real data is obtained, modifying the model to best fit the detected data. To compare the hypothesis and the data, a test statistic is

performed, where the information of all PMTs and LEDs - or a subsample of them - are combined. This is introduced in this section using a likelihood function. Although this is done only statistically first, systematic effects are studied later in Section 7.7.

Having $n_{i,j}$ the data measured in the PMT i after flashing the LED j , and $\mu_{i,j}(\hat{\theta})$ the model built for certain parameters $\hat{\theta}$ for that (PMT,LED) combination, a log-likelihood (LLH) is built as

$$\mathcal{L}(\hat{\theta}) = - \sum_i^{\text{LED}} \sum_j^{\text{PMT}} \ln P(n_{i,j}, \mu_{i,j}(\hat{\theta})). \quad (7.1)$$

The parameters $\hat{\theta}$ represents all the variables that define the column, in this case the combination of the effective scattering length, size, and position with respect to the modules. $P(n_{i,j}, \mu_{i,j}(\hat{\theta}))$ is the Poisson probability mass function of measuring $n_{i,j}$ events after an expectation of $\mu_{i,j}(\hat{\theta})$

$$P(n, \mu) = \frac{\mu^n e^{-\mu}}{n!}, \quad (7.2)$$

where the notation has been simplified to $n = n_{i,j}$ and $\mu = \mu_{i,j}(\hat{\theta})$ ¹. Therefore, this approach assumes that the distribution of the photons detected after repeating the same measurement (flashing the corresponding LED) in a PMT for fixed $\hat{\theta}$ follows a Poisson distribution. For simplicity, $\mathcal{L}(\hat{\theta})$ will be written simply as \mathcal{L} , since it is generally clear the parameter space that is referring to. Constructed this way, \mathcal{L} becomes smaller the closer each n and μ are. Thus, the best fit value is found at the minimum of the likelihood curve, $\mathcal{L}(\hat{\theta}_{\min})$, with $\hat{\theta}_{\min}$ being the best estimate of the parameters. The difference between the value of $\mathcal{L}(\hat{\theta}_{\min})$ and the value of the LLH at any other $\hat{\theta}$ indicates how well $\hat{\theta}_{\min}$ and $\hat{\theta}$ can be distinguished, therefore, the steeper the curve around the minimum, the better the resolution on the variable space. The use of a negative likelihood is simply to look for the minimum of the function instead of the maximum, which is the general convention. The use of the logarithm also simplifies the calculations, allowing the use of summations instead of multiplications. It also simplifies the computation of the probabilities, since $\ln P(n, \mu)$ can be expressed as $\ln P(n, \mu) = -\mu + n \ln \mu - \ln |\Gamma(n+1)|$ using the logarithm of the gamma function $\Gamma(n+1) = \int_0^\infty t^n e^{-t} dt$, which avoids the factorial that can result in numerical errors if n is too large due to the finite precision of floating values.

The data n are considered in this section under the hypothesis of an Asimov data set², which is defined as a data set in which all statistical fluctuations are suppressed [190]. Thus, each LLH curve shown is obtained by selecting $n = \mu(\hat{\theta}_{\text{ref}})$, with $\hat{\theta}_{\text{ref}}$ being the reference *true* values to be reconstructed. The likelihood curve is then obtained by scanning the rest of the parameter space $\hat{\theta}$ using $\mu(\hat{\theta})$. This is ultimately useful to obtain the best sensitivity that such a measurement can obtain. To have the best possible model while keeping simulation efforts reasonable, the model is built as a normalized combination of

¹For clarity reasons, the simplified notation is kept from now on.

²Named after the notorious science fiction author Isaac Asimov, inspired in its short story *Franchise*, in which elections between the population are substituted by a single vote of a representative individual.

16 flash runs of 10^8 photons each¹.

First, one-dimensional simulations are performed, varying the properties one by one to check whether the method has sensitivity to such variations. The rest of the column parameters are fixed and therefore assumed to be known. Later, the same is done by combining the variables in two-dimensional maps and, lastly, all 4 parameters are scanned simultaneously. In all these figures, a reference value must be chosen at which n is obtained and where the global minimum of the likelihood should be.

LLH on column's scattering length

First, the effective scattering length of the bubble column is varied, fixing the other parameters to the most probable values, this being a centered column in ($x = 0$ cm, $y = 0$ cm) with $d = 16$ cm. The results are shown in Figure 7.14 for reference values of $b_e = 2.6$ cm and $b_e = 22.1$ cm. The LLH curves are shown for 3 cases: using the data measured in both modules, only in the EM and only in the RM. For these and future LLH figures, a vertical dashed gray line shows where the reference value is. Note that, although the data are discrete, a continuous line joining the data points has been plotted for easier data visualization.

When analyzing these kinds of negative LLH curves, the ideal situation is a smooth curve with a single minimum at the reference value. The narrower the curve around the minimum, the better the resolution to the parameter. At this stage, only the LLH curves are shown. The statistical resolution on the reconstructed parameter is only calculated later in Section 7.6, when all column parameters are assumed to be unknown simultaneously, assuming the most probable values (measured by IceCube) as true parameters. This is because, when fixing some of the column parameters, the statistical resolution for reconstructing the rest is extremely small, and the result does not provide meaningful information. However, examining the LLH space is useful for understanding how the final results (including systematics) would change if the column had significantly different values than expected, as scanning a less-dimensional space allows for a larger range for each parameter to be covered.

The absolute value of the LLH is, in this case of using an Asimov sample, not important, but rather how deep this minimum is. In any LLH curve shown in this section, there is obviously going to be a global minimum at the right value because of the use of the Asimov sample instead of data, but ideally the curve will not present other local minimums. The curves in Figure 7.14 are smooth without any other minimum than the absolute minimum, which is several orders of magnitude deep within the scanned range, which means a very accurate resolution of the parameter. This also means that the scanned range is probably too large and that a narrower range around the most probable value can be scanned. In both figures, the curve using both modules is steeper than when using a module alone², as expected when combining more information into a single LLH. When comparing the two curves obtained with a single module, it can be seen that the EM is

¹As a reminder, since the PMT quantum efficiency is not directly included in the simulation but the photons are weighted afterwards, 9.6×10^9 photons (16 times 10^8 per flash) were not directly generated in the simulation but the corresponding number taking into account the quantum efficiency, so less simulations are needed. With the QE being 0.2595, this is approximated by 4 instead of 16 simulations of 10^8 photons.

²Note the logarithmic scale in the y-axis, which might cause an error in perception when comparing how steep the curves are.

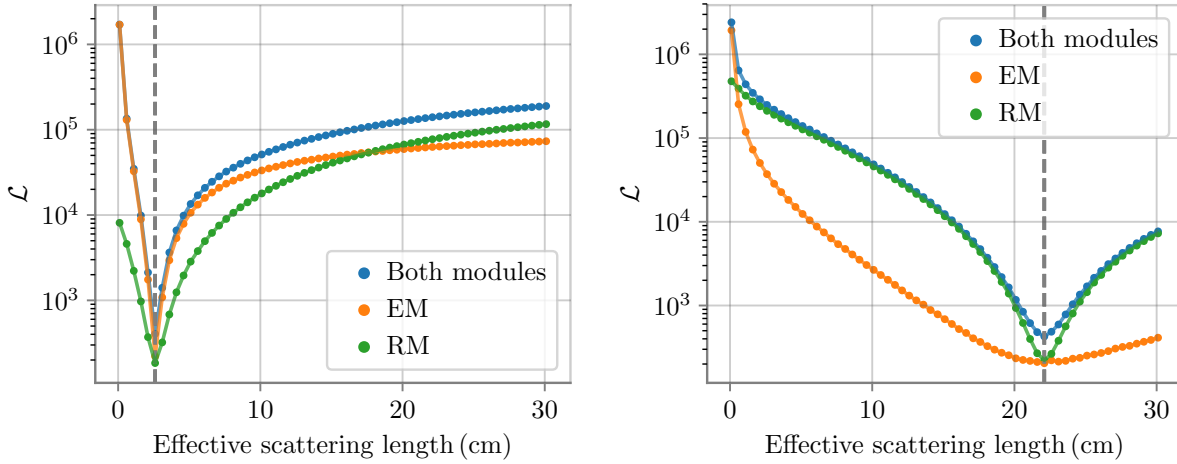


Figure 7.14: LLH curves scanning the effective scattering length of the bubble column at reference values of $b_e = 2.6$ cm (**left**) and $b_e = 22.1$ cm (**right**). The different curves are obtained by calculating the LLH using the measured signal in all PMTs from both modules or using only the PMTs in a single module. The bubble column size and position are fixed to $d = 16$ cm, $x = 0$ and $y = 0$. The reference value for the LLH calculation is shown with a vertical dashed line in each subfigure.

better at reconstructing this parameter for small reference values, and the RM is better for higher ones. The point at which both curves have a similar slope occurs at a reference value of $b_e \sim 6$ cm. This behavior could have been anticipated by looking at the detection patterns in Figure 7.11 and paying attention to the range of b_e , where the counts change more abruptly in both modules.

However, as stated before, the behavior of the LLH curve ultimately depends on all parameters at the same time. In Figure 7.15 (left), similar figures as before are shown for a reference point $b_e = 13.1$ cm, but in this case the bubble column is at 3 different positions, all cases with the same column size of $d = 16$ cm. One of the curves is obtained for the standard position of a perfectly centered column, so $\text{LED}=0$ is contained within the column. Then, in the case where the column is centered at $(x = 9 \text{ cm}, y = 0 \text{ cm})$ the bubble column contains LEDs 0 and 4. Finally, for the case $(x = 0 \text{ cm}, y = -9 \text{ cm})$ the bubble column contains only a single peripheral LED ($\text{LED}=1$) and not the centered one. The LLH curves for the first two cases are similar in appearance, with the case in which the column contains both LEDs exhibiting a steeper, and thus a superior, LLH curve. However, when the column does not include the central module, the curve is much flatter. This indicates that the column parameters are harder to reconstruct if the centered LED is not contained within the bubble column. Note that these cases where the column is moved almost ten centimeters are extreme and highly unlikely. Studies of the IceCube bubble column indicate that displacement of more than a couple of centimeters is rare [204, 205]. Therefore, the scenario where the centered LED is outside the bubble column is highly improbable.

Lastly, the behavior of the LLH is shown in Figure 7.15 (right) for a bubble column of different sizes, always centered at $(x = 0 \text{ cm}, y = 0 \text{ cm})$, for a reference value close to $b_e = 3$ cm. In this case, b_e has been scanned in logarithmic steps to better visualize the curves at low b_e . It can be seen that the LLH curve does not change significantly for different column sizes, although it is steeper the smaller the column width, meaning better

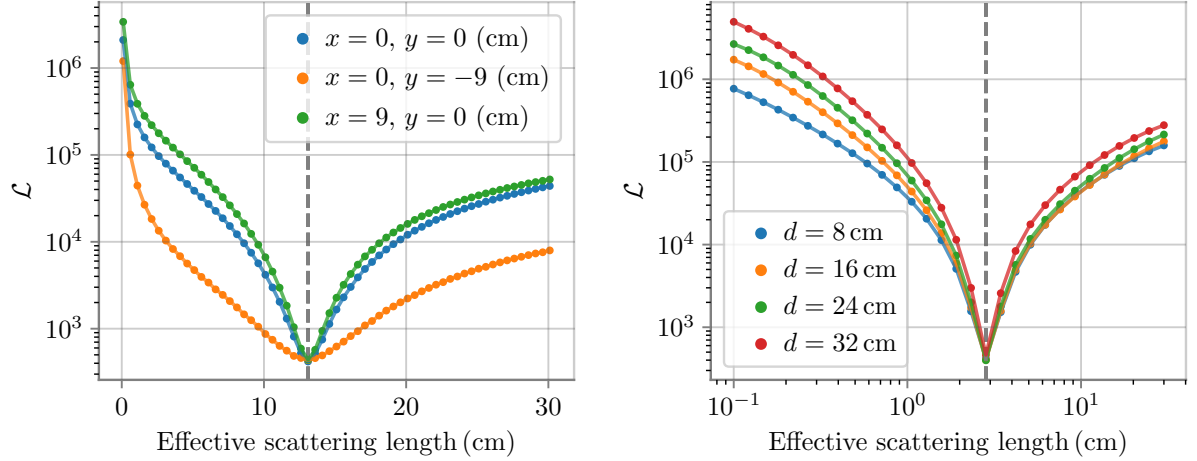


Figure 7.15: Left: LLH curves scanning b_e for a reference value of $b_e = 13.1$ cm. The column has a diameter of $d = 16$ cm and is placed at different positions with respect to the modules, which are perfectly aligned. **Right:** LLH curves scanning b_e for a reference value of $b_e \sim 3$ cm. The bubble column is always centered at the modules at $(x = 0, y = 0)$ but has different diameter in each curve. Here, b_e is scanned in logarithmic steps. The reference value for the LLH calculation is shown with a vertical dashed line in each subfigure.

parameter resolution in these cases. Again, extreme scenarios are shown, since a column of $d = 32$ cm would cover the whole DOM in IceCube. The discussion about how the LLH changes when using different modules or when the bubble column is placed at different places in this subsection is also applicable when scanning the other parameters, therefore it will not be repeated in the next sections.

LLH on column's size

The LLH is now analyzed by scanning the size of the bubble column. The results are shown in Figure 7.16. Note that in these first simulations, a very large range for the column size is scanned, so the LLH space can be observed for extreme cases. The first three figures show the curves assuming different values of the effective scattering length. It can be observed that for low reference values (top-left figure), the LLH curve becomes steeper as b_e decreases. However, this changes at high reference values, where the curve with $b_e = 3$ cm is only steeper on one side. The transition between these two behaviors occurs somewhere near $d = 16$ cm. The behavior of the curves can be explained: if the scattering length is much shorter than the diameter of the column, a small variation of d would not affect the ratio of photons that scatter significantly, since most of them would have scattered anyway. On the other hand, if b_e and d have closer values, the ratio of photons undergoing scattering would be much more dependent on the size of the column as well. Later, when the LLH space is scanned simultaneously in d and b_e , this effect is more noticeable. This hints at a correlation of some degree¹ between d and b_e , a fact that will appear frequently throughout this chapter.

An interesting behavior occurs at $d \approx 30$ cm, caused by the bubble column starting to reach the peripheral LEDs. This is better visible in the last figure (bottom-right) of Figure 7.16,

¹The strength of this correlation is quantified later in Section 7.7.2.

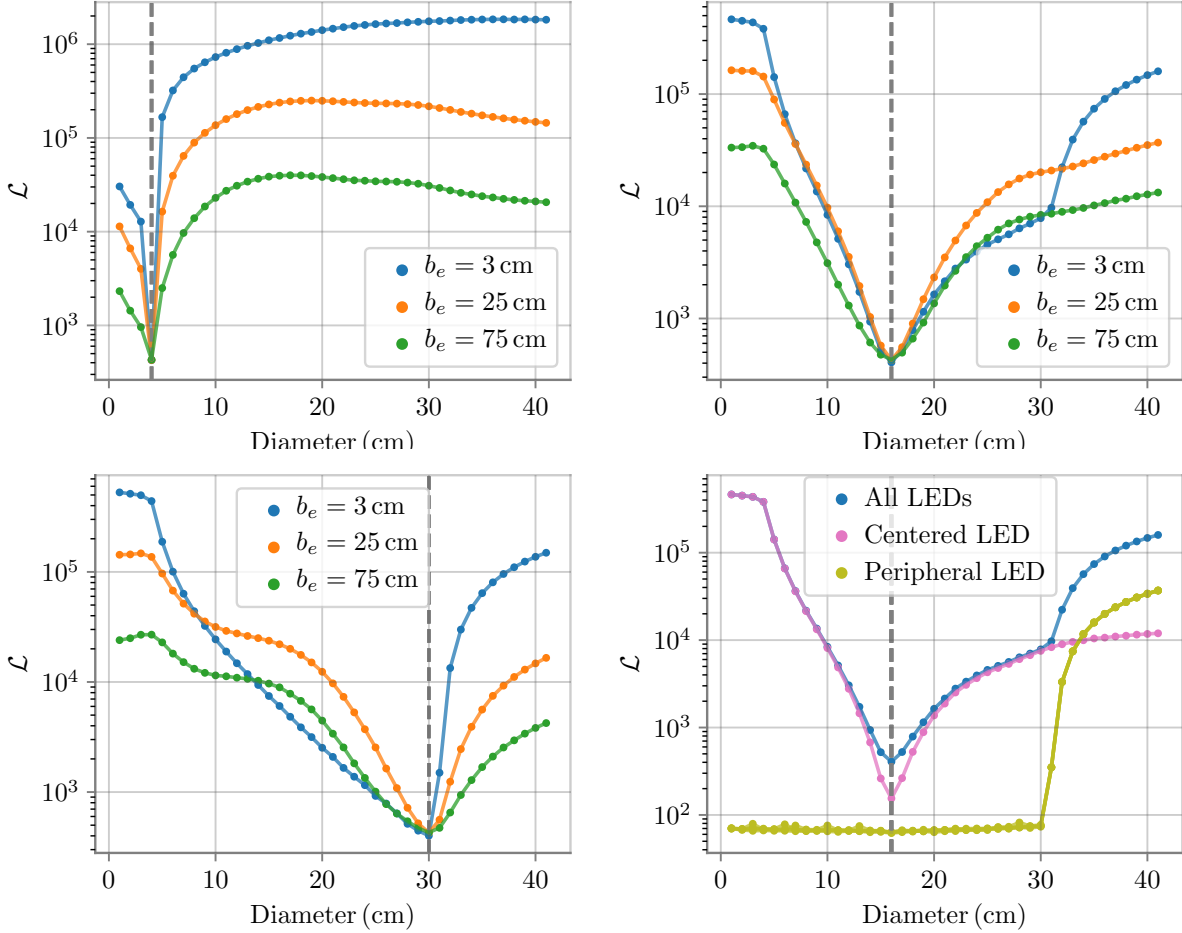


Figure 7.16: LLH curves scanning the diameter of the bubble column, choosing as reference values $d = 4$ cm (**top-left**), $d = 16$ cm (**top-right**) and $d = 30$ cm (**bottom-left**). Different curves are displayed for different effective scattering lengths of the bubble column, always centered at $(x = 0, y = 0)$. In **bottom-right**, the case with $b_e = 3$ cm and a reference value of $d = 16$ cm is shown again. The different curves stands for the LLH calculated using all LEDs simultaneously and each LED individually. A single curve for the peripheral LEDs is visible since they all overlap. The reference value for the LLH calculation is shown with a vertical dashed line in each subfigure.

where the LLH curve is shown for each LED separately as well as for all combined LEDs¹. It can be seen that the peripheral LEDs contribute significantly to the combined LLH curve for $d > 30$ cm, but contribute very little at lower values since the LLH curve there is almost flat. Note also that, if the bubble column is too narrow, the method starts to fail. This is observed in the figures at $d < 5$ cm, where the curve get flat or even the slope is inverted (bottom-left figure with $b_e = 75$ cm). Such a narrow column is, however, not a realistic scenario according to what it has been measured in IceCube [205].

LLH on column's position

Now, the horizontal position of the bubble column with respect to the modules (x, y) is scanned, with fixed $d = 16$ cm and $b_e = 3$ cm. The simulation is performed in steps of

¹Again, the logarithmic scale in the y-axis might give the wrong impression that the curve using only the centered LED is steeper than the curve using all LEDs combined, which is not the case.

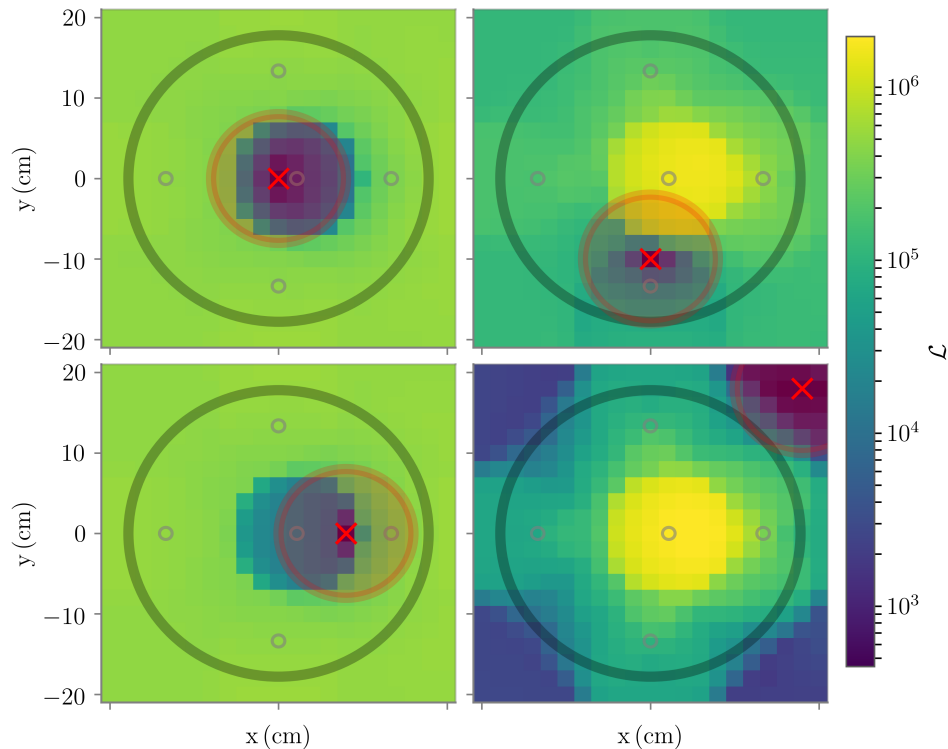


Figure 7.17: Two-dimensional LLH maps when scanning the horizontal position (in x, y) of the bubble column with respect to the center of the modules. In all cases the column has a diameter of $d = 16$ cm diameter and effective scattering length of $b_e = 3$ cm. Each figure correspond to different reference values chosen as the column position to reconstruct: $x = 0, y = 0$ (**top-left**); $x = 0, y = -10$ cm (**top-right**); $x = 8$ cm, $y = 0$ (**bottom-left**) and $x = 18$ cm, $y = 18$ cm (**bottom-right**). The red cross indicates the center of the bubble column, which is also the reference value, while the red circle stands for the bubble column geometrical cross section. The small gray circles are located at the positions where the LEDs are located, while the large gray circle shows the edge of the module glass. In all cases, the minimum of the LLH and the reference values coincide.

2 cm in a range from -20 cm to 20 cm. Again, the range is chosen to include extreme cases. The results are shown in Figure 7.17 for the different reference values. In the upper-left image, the reference values are $(x = 0$ cm, $y = 0$ cm). In this case, the bubble column (at the reference coordinates) only contains the centered LED. In the upper right plot, the reference column is situated over one peripheral LED. In the lower-left plot, the position of the reference column is such that it covers both the centered LED and one of the peripheral LEDs. Finally, in the lower right part of the figure, a very extreme case is shown where the reference column is outside the module. Again, a large difference of several orders of magnitude in the LLH values for the scanned map can be seen in all cases, showing that the statistical resolution is much narrower than the scanned range. In the extreme case of the column being totally outside the module (bottom-right subfigure), the method would only be able to discard the hypothesis of the modules being within the column but not its exact relative position. Still, this last case is very hypothetical and unlikely in the real experiment. In all subfigures except the absolute minimum is found at the right coordinates.

For the cases shown in Figure 7.17, the minimum is most pronounced in the case where

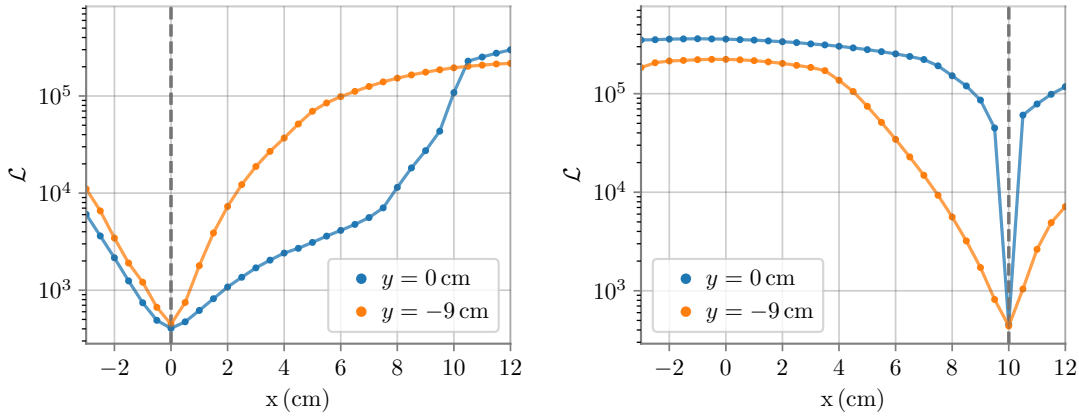


Figure 7.18: LLH curves when scanning the column in x fixing y to $y = 0$ and $y = 9$ cm, for a column with $d = 16$ cm and $b_e = 3$ cm, for a reference value of $x = 0$ (left) and $x = 10$ cm (right). The reference value is shown with a vertical dashed line in each subfigure.

the bubble column contains only the peripheral LED. This is due to a combination of two factors. First, the centered LED strongly rejects the hypothesis that the column is around the center, with very high LLH values in that region. Second, because of the orientation of the peripheral LED with respect to the column, the light emission is more transversal than for the centered LED and thus more sensitive to the horizontal position of the column. The centered LED will contribute significantly to the LLH if it is located at the edge of the column. To better observe this, one-dimensional simulations with shorter steps in x are performed. The coordinate y is fixed to $y = 0$ and $y = 9$ cm. The results are shown in Figure 7.18. In the figure on the left, where the reference value is $x = 0$, the blue curve corresponds to the column containing the centered LED, while in the orange curve, the column contains only a peripheral LED. Like before, it can be seen that the peripheral LED yields more information about the position of the column, with its corresponding LLH curve ($y = 9$ cm) being steeper. In the figure on the right, where the reference value is $x = 10$ cm, the blue curve corresponds to the bubble column containing a peripheral LED and the centered LED. In this case, the centered LED is located near the border of the reference bubble column. The minimum in this curve is more pronounced than in any of the previous cases. Finally, the orange curve on the right Figure 7.18 corresponds to a case where the bubble column does not contain any LED, however two peripheral LEDs and the centered one are near its border. The curve in this case is still similar to that of the column centered at $(x = 0, y = 0)$; therefore, the position of the column can be reconstructed even if this is not located on any of the LEDs.

LLH on column's scattering length and size

The LLH map is now obtained by fixing the column at the center ($x = 0, y = 0$) and scanning at the same time the size of the column and its effective scattering length, in a similar manner as in previous cases. The results are shown in Figure 7.19, for 4 cases choosing a different reference value to reconstruct. The correlation between d and b_e , previously discussed, is clearly visible on all LLH maps, with a darker area of lower LLH value. These areas are of similar size in all subfigures, but the global minimum is more pronounced for shorter scattering lengths, showing a better determination of the parameters in these cases, a fact that was also observable before in the 1-dimensional

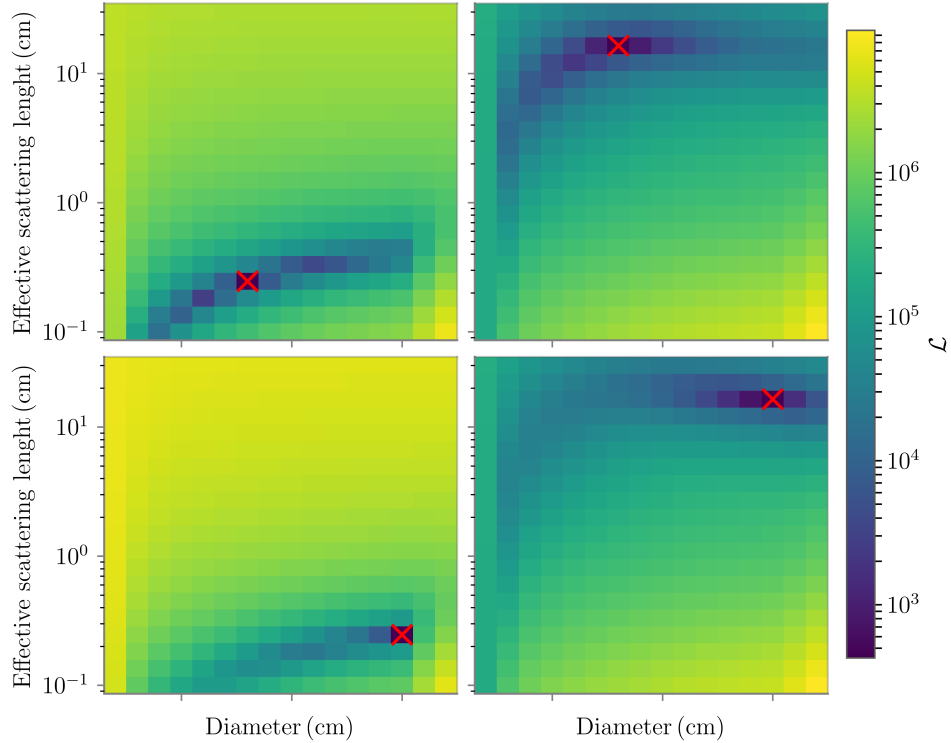


Figure 7.19: Two-dimensional LLH map when scanning the diameter and the effective scattering length of the bubble column, where the column is placed centered at the modules ($x = 0, y = 0$), for different reference values indicated by the red cross: $b_e \sim 0.25$ cm, $d = 16$ cm (**top-left**); $b_e \sim 0.25$ cm, $d = 30$ cm (**top-right**); $b_e \sim 16.5$ cm, $d = 16$ cm (**bottom-left**) and $b_e \sim 16.5$ cm, $d = 30$ cm (**bottom-right**). In all cases, the minimum of the LLH and the reference values coincide.

study. In all figures, the minimum is obviously at the reference values, as expected from the Assimov approach.

LLH on all parameters simultaneously

Finally, the entire variable space is scanned simultaneously. In all previous cases, the value of LLH varied by several orders of magnitude within the whole scanned parameter range; therefore, a smaller range can be scanned for each variable. This is indeed necessary here to maintain a reasonable step size while scanning all 4 dimensions simultaneously. The data is obtained as a grid of 5^4 data points, and the results are presented in Figure 7.20 as the profile LLH for all corresponding two-dimensional combinations and the final one-dimensional figure, for a reference value of $b_e = 3$ cm, $d = 16$ cm, $x = 0$ cm, $y = 0$ cm¹. The profile LLH is equivalent to the scenario in which all other column parameters are assumed unknown, given by

$$\mathcal{L}_p(\theta_1) = \min_{\theta_2 \dots \theta_n} \mathcal{L}(\hat{\theta}), \quad (7.3)$$

being θ_1 the parameter of interest and $\theta_2 \dots \theta_n$ the nuisance parameters². All the resulting

¹This is used, from now on, as the standard values to reconstruct.

²Similarly for the 2D maps, $\mathcal{L}_p(\theta_1, \theta_2) = \min_{\theta_3 \dots \theta_n} \mathcal{L}(\hat{\theta})$.

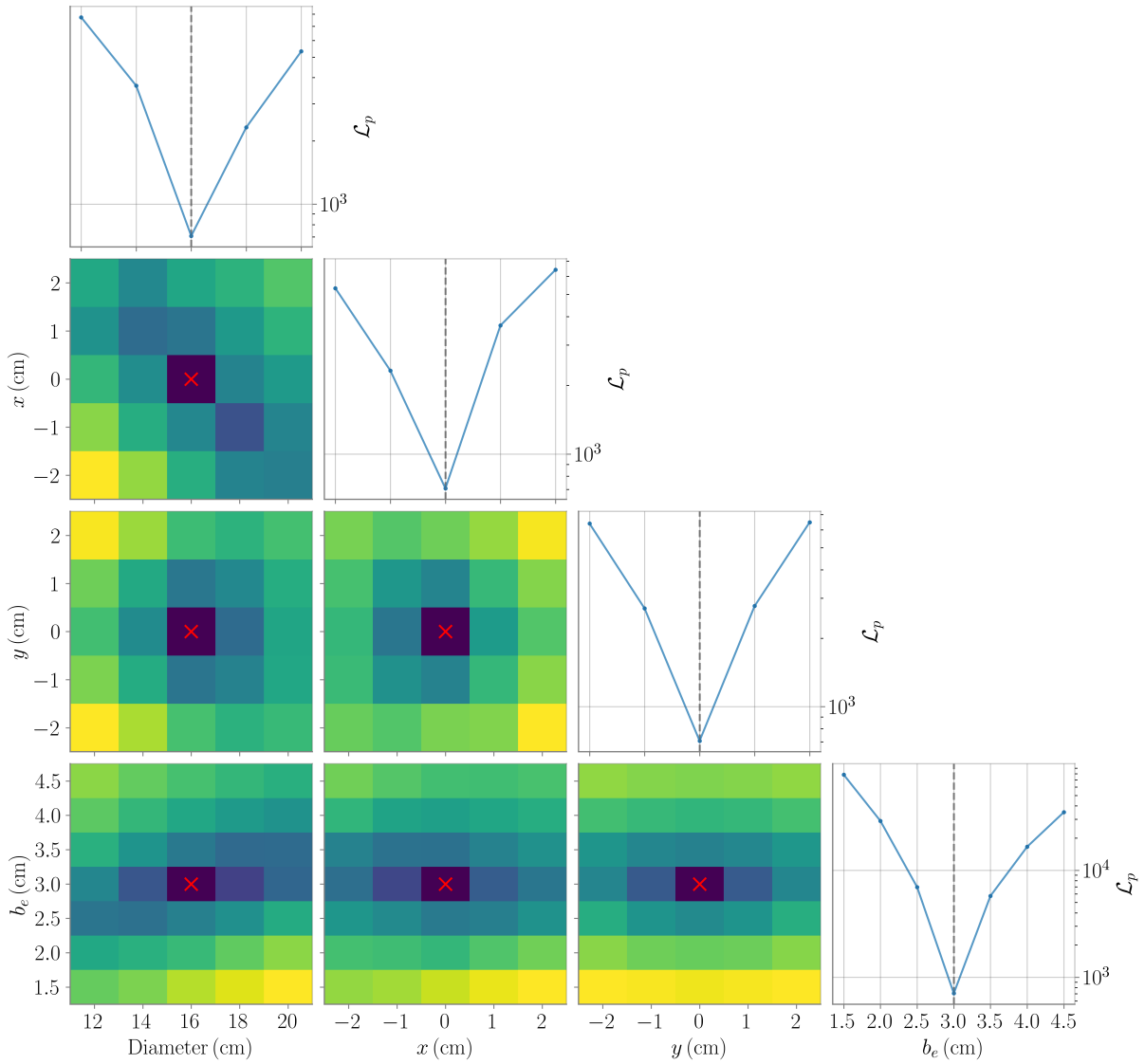


Figure 7.20: LLH maps when all 4 parameters of the bubble column are scanned simultaneously. Each plot is the profile likelihood of the 4 parameter space into 2 or 1 dimension, where the unshown variables have been marginalized, considering them unknown. The reference value to reconstruct is $b_e = 3$ cm, $d = 16$ cm, $x = 0$ cm, $y = 0$ cm, which is indicated by a red cross (2D) or a vertical line (1D).

profile LLH maps show a global minimum at the reference value. More importantly, no local minimums are present in any of the cases. The minimum is also deep enough to indicate that within the scanned variable space the statistical fluctuation should be very small.

7.6 Statistical uncertainty on column parameters

The real experiment has the possibility of accumulating many flasher runs; however, the simulations in this work are limited due to the computational time each one needs. Getting the statistical uncertainty on the column parameters using the data in this study does not

quantify the final precision of the method in the real experiment; however, it is needed to make sure that the statistics are enough to draft conclusions. The statistical uncertainties must be, ideally, smaller than the systematic ones, and thus the impact of the latter can be properly analyzed afterwards. Otherwise, the number of simulations need to be increased.

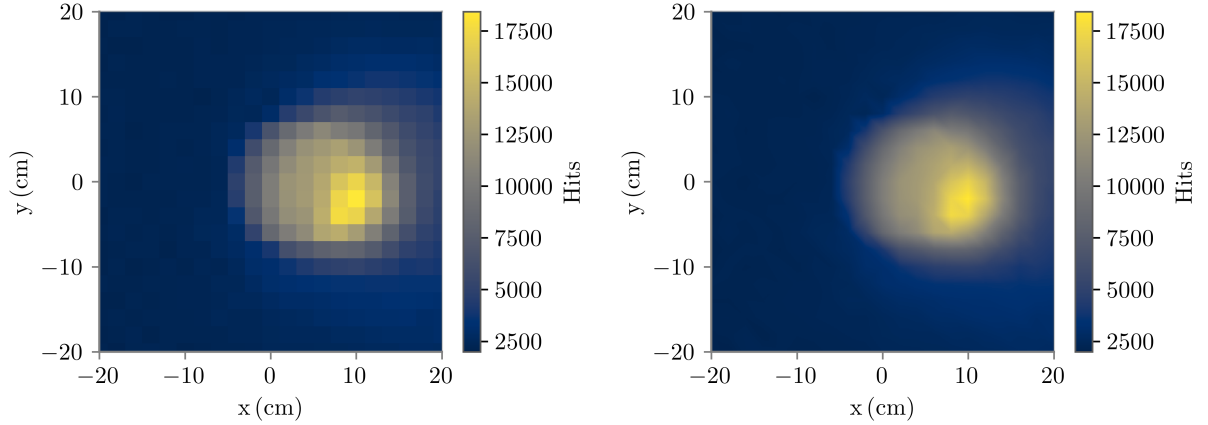


Figure 7.21: Example for the result of the two-dimensional interpolation of $\mu_{i,j}$ for the case studying the column position scanned from -20 to 20 cm in each dimension (x, y) with $b_e = 3$ cm and $d = 16$ cm. The figure shows the detection pattern on the emitter module for the PMT $j = 19$ when flashing the LED $i = 0$. **Left:** data from the simulation. **Right:** interpolated data.

To calculate the statistical uncertainties, the data is first interpolated. Thus, the data for the expected number of detected hits $\mu_{i,j}$ in each PMT j when the LED i is flashed are interpolated. Then, the likelihood is calculated using the interpolated data. The interpolation of the $\mu_{i,j}$ space is performed linearly in each dimension, since it has been checked that this properly reproduces new data. An example of the interpolation is shown in Figure 7.21 for a particular combination of LED, module, and PMT. In this example, the chosen PMT from the emitter module only receives most of the light from the LED when the column is located at a certain position. It can be seen that the interpolation properly transforms the data to a continuous model. For different cases, it has been checked that the interpolation works as expected, replicating the data without introducing artifacts.

When combining each interpolated function¹ the likelihood map can be calculated from the interpolated $\mu_{i,j}$ as before. The results are shown for the four-dimensional case in Figure 7.22, for the standard reference values ($d = 16$ cm, $b_e = 3$ cm, $x = 0$ cm, $y = 0$ cm). The maps retain a smooth behavior, and no artifacts are created from the interpolations. This has also been checked when using different reference values. Note that the interpolation can only be as good as the data used. While for the one- and two-dimensional cases the parameter space is scanned in more numerous and smaller steps, the four-dimensional case was scanned only in a 5^4 grid. The larger complexity of the problem in this case and the smaller grid size make the interpolation less reliable, which is why, when comparing the interpolated LLH maps with the previous one (Figure 7.20), the curves do not match perfectly. This is better visible in Figure 7.23, where the 4-D interpolation has been used to take a 1-dimensional curve in b_e fixing $d = 16$ cm, $x = 0$, $y = 0$ ² and then it is directly compared with the 1-D simulation scanning only b_e and fixing the other parameters to

¹5 LEDs, 2 modules and 24 PMTs, for a total of 240 interpolated curves.

²Note that this is not the same as the 1-dimensional plot on b_e shown in Figure 7.22.

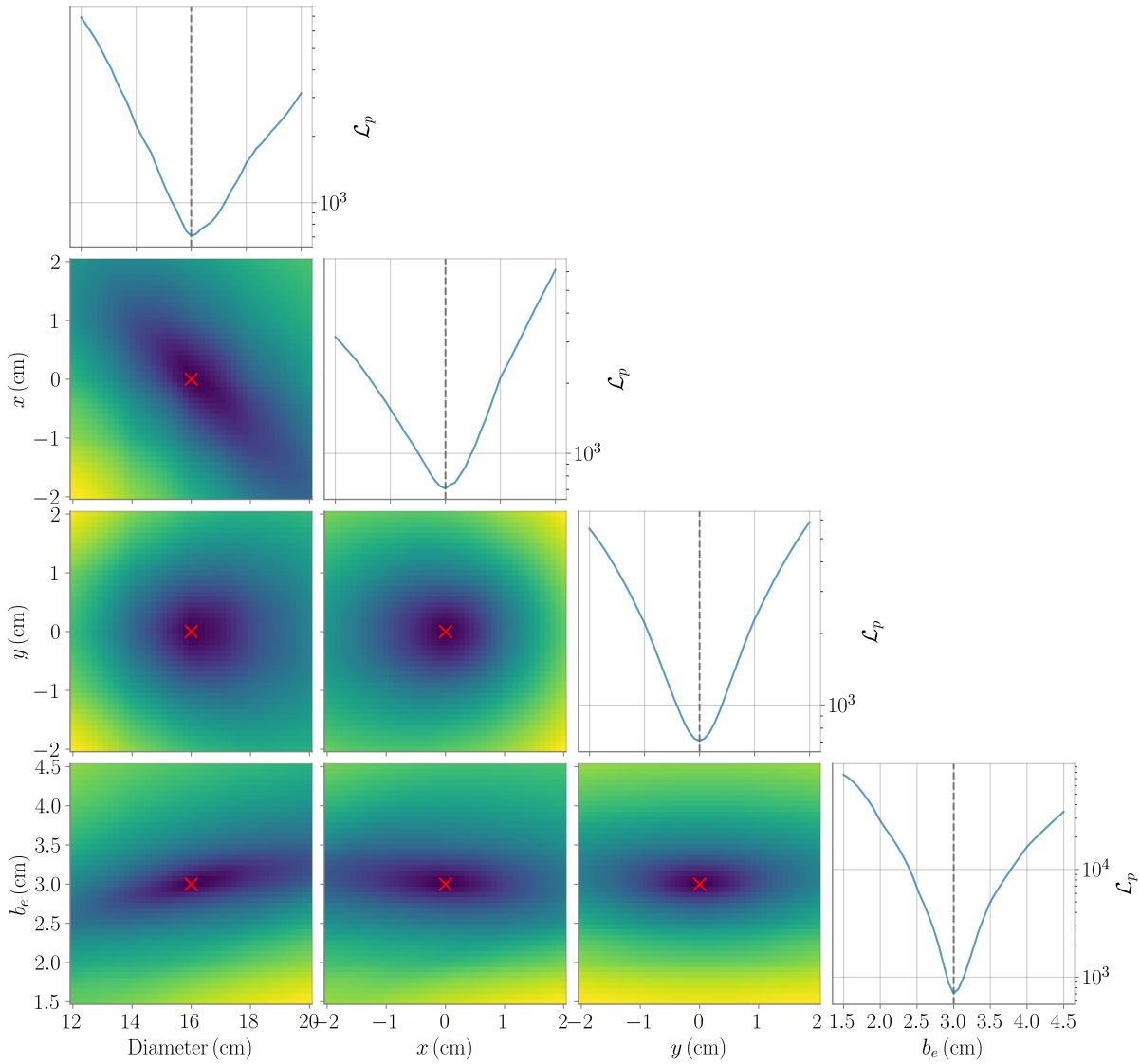


Figure 7.22: LLH maps when all 4 parameters of the bubble column are scanned simultaneously, after interpolations. Each plot is the profile likelihood of the 4-dimensional parameter space into 2 or 1 dimension, where the minimum of the LLH for the unshown variables have been taken, considering them unknown. The red cross or the vertical line stands for the reference point to reconstruct ($d = 16$ cm, $b_e = 3$ cm, $x = 0$ cm, $y = 0$ cm). Note that the discretization of the data in the plots only results from the plotting process.

the same values. Although the curves are similar, they differ slightly, especially near the minimum, where the data from the 4-D interpolation produce a broader LLH curve. A similar result is obtained for the other variables as well. However, this will only be translated into a slightly higher statistical uncertainty when using the 4-D data. This discrepancy needs to be accepted due to the size of the 4-D grid used here, situating the results in a slightly conservative regime in this regard. Still, the interpolating curves are smooth and never contain any other local minimum than the global one at the right coordinates; thus, this data can be given to a minimizer to obtain the minimum.

The statistical uncertainties are now obtained for a column with the default parameters

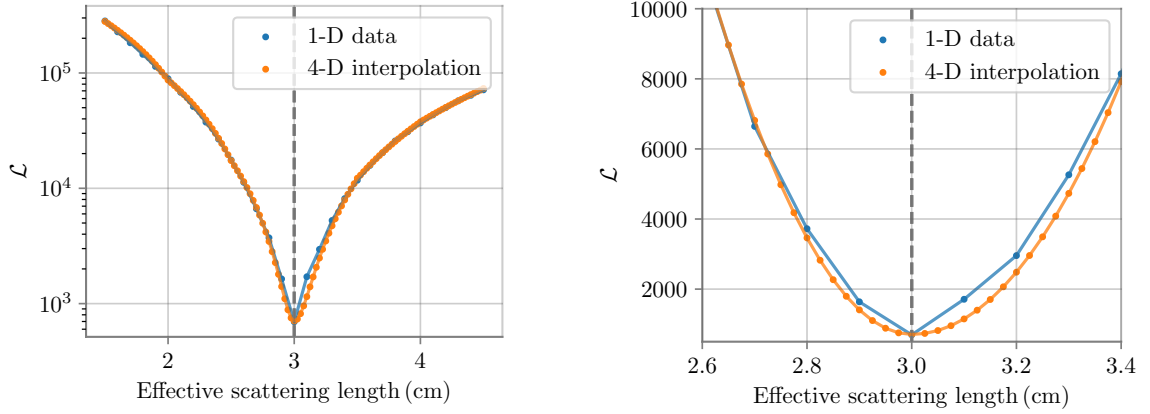


Figure 7.23: **Left:** Comparison when using the 1-D simulation data to obtain the LLH curve with the result from the 4-D simulation when the other parameters have been fixed to $d = 16$ cm, $x = 0$ cm, $y = 0$ cm and reconstructing $b_e = 3$ cm. **Right:** Same but zoomed into the region of interest. The reference value for the LLH calculation is shown with a vertical dashed line in each subfigure.

($d = 16$ cm, $b_e = 3$ cm, $x = 0$ cm, $y = 0$ cm). This is done through a likelihood ratio by counting for an increment on the LLH value of 0.5 from the minimum in the one-dimensional profile LLH curve (after marginalizing all other variables), which accounts for one standard deviation confidence region (σ) [212]. The interval $[-\sigma, \sigma]$ is defined as the interval that would contain 68.27% of results if the experiment is repeated infinitely. Note that by calculating the confidence interval this way, it is assumed that the statistical uncertainties are distributed following a Poisson distribution. This is a simplification that is not necessarily true in all cases, however, it has been checked that it returns the correct coverage here by a sampling Monte-Carlo test. The uncertainty region $\pm\sigma$ when determining each parameter is shown in Figure 7.24 for the 4-dimensional case, assuming that all other parameters are unknown. For each parameter reconstruction, the results have been scaled for flashers of different intensities¹ by weighting each $\mu_{i,j}$ by the corresponding factor, from 10^6 to 1.6×10^9 photons. The last case therefore simply uses all the 16 simulated flash runs that were simulated. When using only 10^6 photons, the uncertainties are on the centimeter level. This rapidly scales down considerably with the total flash intensity. For the best case shown here (1.6×10^9 photons per flash), the parameters would be determined as $d = 16_{-0.02}^{+0.04}$ cm, $x = 0_{-0.02}^{+0.01}$ cm, $y = 0_{-0.01}^{+0.01}$ cm, $b_e = 3_{-0.004}^{+0.005}$ cm. These should be sufficiently small to study the systematic uncertainties. Being much smaller than the grid size used for interpolation, the results are again to be taken with caution; however, it indicates that the statistics are more than enough to get a high resolution of the column parameters even in the worst case of assuming all parameters to be unknown. The results are similar if a different reference point on the grid is reconstructed, since the scanned parameter space is not large.

¹Which can be seen as a combination of smaller flashers.

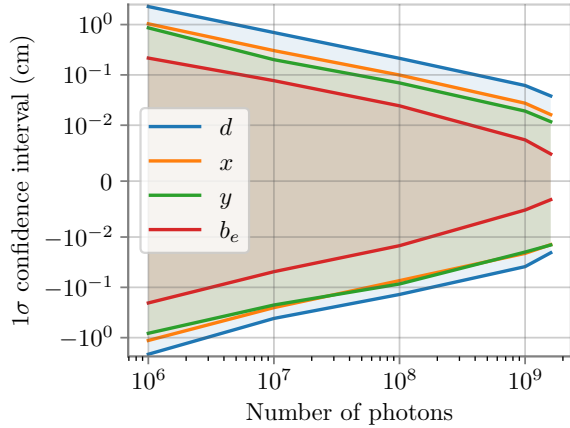


Figure 7.24: Width of the 1σ ($\pm 34.1\%$) confidence region when reconstructing the column parameters for a centered column of $d = 16$ cm and $b_e = 3$ cm, using the interpolation of the 4-dimensional data, for different flash intensities.

7.7 Systematics

So far in this chapter, an ideal scenario has been assumed in which modules face perfectly each other, are completely aligned, PMTs work with 100% accuracy, etc. In the real experiment, the situation will not be that certain and many variables are unknown or known only to some degree, which introduce systematic uncertainties in the final results. The impact of these on this study is investigated in this section. This work, relying only on simulations, cannot contemplate all possible scenarios of systematic sources, and the real experiment, when constructed, might contain unexpected features (as the bubble column itself was for IceCube indeed). With this in mind, those sources of systematics that are expected to be the most important ones have been selected and included in this study.

The procedure for each in an individual systematic study in this section is similar, unless the contrary is specified: simulations varying the corresponding systematic variable are done with the bubble column having the standard reference parameters ($d = 16$ cm, $b_e = 3$ cm, $x = 0$ cm, $y = 0$ cm). Then, the results are compared with the model without systematics. This is done by giving the results from the simulation with systematics to the likelihood calculation algorithm, using the interpolation from the 4-dimensional scan results of the previous section as model, assuming that all column parameters are unknown. From here, the minimum and its statistical confidence interval are directly calculated using a minimizer, thus without calculating the whole parameter space in the 4-dimensional grid. The minimizer used here is *Migrad*, from the *Minuit* package [213, 214] and using the *Minos* approach to obtain the statistical uncertainty of the minimum. Ultimately, the whole process simply means searching for the d, x, y, b_e combination that makes $\mu_{i,j}(d, x, y, b_e)$ more similar to $n_{i,j}$, $\mu_{i,j}(d, x, y, b_e)$ being the number of hits in each PMT j when the LED i is flashed from the interpolated model, and $n_{i,j}$ the simulation data varying the corresponding systematic variable for the same PMT, LED combination. Then, the impact of the corresponding systematic source on the reconstruction of the bubble column can be independently analyzed. In this section, all the simulated statistics (1.6×10^9 photons per flash) is used in each parameter reconstruction.

After considering all systematics as individual cases, the column parameters are reconstructed for simulations that include all of them simultaneously, shown in Section Section 7.7.2. Thus, the first studies give an insight into which systematic might be more relevant for our case studied, while the latter shows the impact of combining all of them

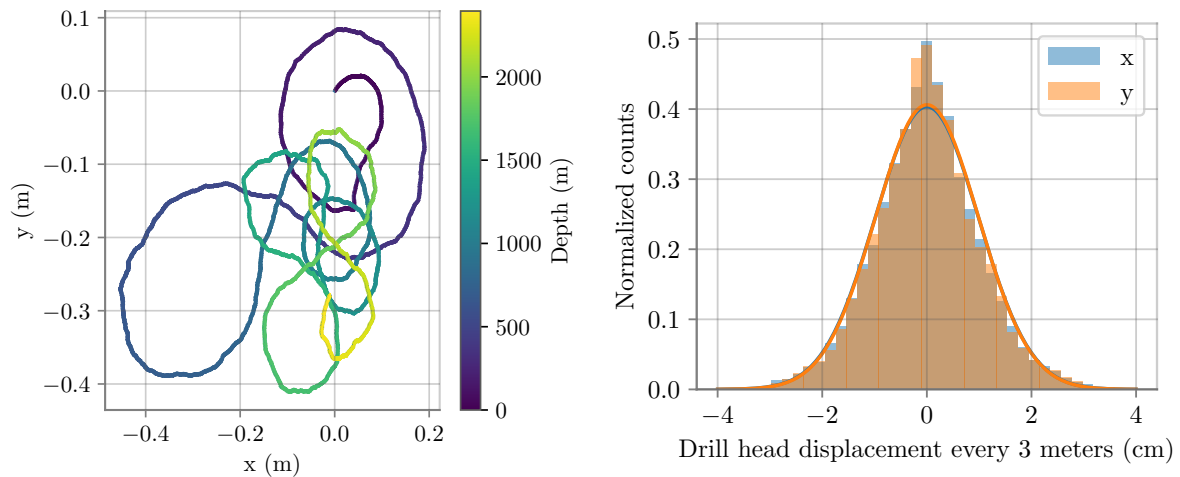


Figure 7.25: **Left:** horizontal position of the drill head during the drilling of hole 80 in IceCube as a function of the depth. **Right:** x-y mean displacement every 3 meters of the head drill head position during IceCube construction, including all available data for all holes.

and ultimately the resolution of the method to the bubble column parameters.

7.7.1 Individual influence of each systematic source

Relative module position

During deployment, modules are suspended from the cables while going deeper into the ice and, as such, they can move within the hole. In addition, the drilling process itself means that the hole does not have a perfectly cylindrical and vertical shape. The outcome is that, after the hole ice has refrozen, modules within the same string are never perfectly aligned. For IceCube, the best information on how large the misalignment of the modules might be is currently obtained from the drilling process itself. Direct data from the drill head indicate that the drill deviates by a few meters over the entire length of the drill hole, and these data are currently used in IceCube for the geometry calibration. As an example, the data is shown for hole 80 in Figure 7.25 left. The position of the drill head during the drilling process does not really mean that the modules' center is at that exact position; however, it is currently the best estimation.

The interest for the study here relies on the uncertainty on the relative positions of two consecutive modules. As of yet, it cannot be known with certainty how much this might be for ICU. An estimation is made here using all available IceCube drill data: assuming a module distance of 3 m, the displacement in x, y is calculated every 3 meters for all strings with available data. The result is shown to the right Figure 7.25. The distributions for both x and y are very similar and are centered at 0, and go as far as ± 4 cm for the worst cases. If the data are to be fitted with a Gaussian distribution, the best result is obtained with $\sigma \simeq 1$ cm. A Gaussian fit to represent this systematic would be a conservative choice, since it does not fit the data precisely, being the data narrower and higher at the center than the fit.

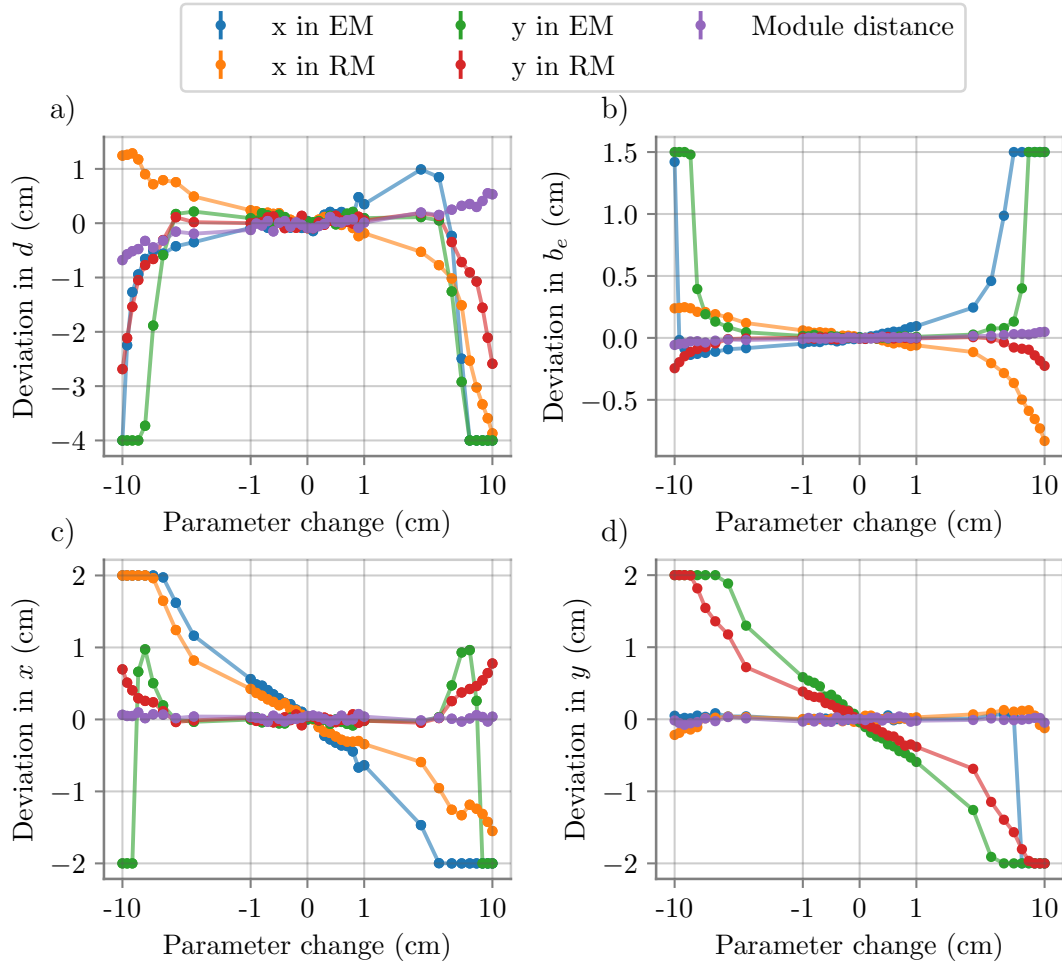


Figure 7.26: Deviations from the true value ($d = 16$ cm, $b_e = 3$ cm, $x = 0$ cm, $y = 0$ cm) of the reconstructed column parameters when the Emitter Module (EM) and Receiver Module (RM) are moved horizontally along their x, y positions and vertically. Each subfigure shows the deviation when reconstructing: **a)** column diameter, **b)** effective scattering length of the column, **c)** column position (x), **d)** column position (y). Note that the deviations of the reconstructed values are limited by the difference between the true and the edges of the scanned parameter space ($d = [12$ cm, 20 cm], $b_e = [1.5$ cm, 4.5 cm], $x = [-2$ cm, 2 cm], $y = [-2$ cm, 2 cm]).

Now, the impact of this systematic on the column's parameter reconstruction is evaluated following the procedure explained above. Both EM and RM have been moved horizontally in the x and y directions up to 10 cm, one module at a time. In addition, the modules were moved vertically to check whether the distance between them also affects the column reconstruction. The results are plotted in Figure 7.26, which shows the deviation of each reconstructed variable from the truth. Note that for all figures presented in this section, the model is the simulation data presented in Section 7.5 and interpolated. Since the center of the scanned grid is used as a reference to reconstruct, there is a limit on the resolution of the figures given by $d = \pm 4$ cm, $b_e = \pm 1.5$ cm and $x, y = \pm 2$ cm (see Figure 7.22). These limits can be observed in the figures when the systematic parameter change is large enough so that the minimum of the LLH space would lie either in the border or outside the scanned range. Note that, when this happens for any variable, the accuracy of determining the other variables may be compromised, as the minimum found may not be a global

minimum, but rather a local minimum within the scanned space.

For the reconstruction of the size of the column, there is little deviation from the true value (less than 0.5 cm) when the modules are moved within ± 1 cm. When the modules are moved ~ 2 cm or farther, considerable deviations larger than 1 cm start to appear. The results are similar for the case of the effective scattering length, but in this case the most significant deviations start later at 5 cm. For the reconstruction of the position of the column in both x and y , the deviation increases when the modules are moved within the same axes, as one would expect. It can also be seen that the deviation when moving the EM position seems to be slightly more significant than when moving the RM. When the modules are separated, no significant deviation in any of the column variable reconstructions is visible within the parameter variation shown here. Assuming that the modules in ICU will be misaligned similarly to what was shown in Figure 7.25, it can be concluded that this will influence more strongly the determination of the column position with the method, and to a smaller degree the determination of d and b_e .

Relative module orientation

Not only the exact position of the modules after deployment might be different from the ideal case, but also the orientation of the modules. For this study, it is important to know the accuracy that can be achieved when calculating the relative orientation of two consecutive mDOMs. At the time of writing, there are no values on this for the new optical modules, however, studies in IceCube using the LED flashers could determine the module's orientation with sub-degree accuracy [205]. It can be expected that, for mDOMs, the method would be even more precise due to the intrinsic segmentation of the modules. Here, the column parameters are reconstructed from simulations in which the orientation of the modules is varied, and the results are shown in Figure 7.27. θ and ϕ are standard spherical coordinates that give the orientation of the modules, where ϕ is the angle from the x to the y axis (see Figure 7.9) and θ is the angle from the z axis, such as $\theta = 0$ means that the module is perfectly aligned with the vertical. Note that θ is shown here only with respect to this reference frame; however, when all systematics are considered together, the θ angle is defined after previously rotating the reference frame in ϕ randomly, so all possible orientations are considered. The results show that when the modules are tilted less than a degree, little deviation is found except for the case of position y when varying θ in the EM. This is also the case where the highest deviation is produced at larger angles. If the whole reference system is rotated in θ by 90 degrees, the same occurs for x . Also, tilting the EM has more impact than the receiver one, since this directly affects the photons at emission and the path that they would follow within the column.

Judging from these results, if the module orientation is known within a degree accuracy as in IceCube, this is not going to cause considerable deviation in the determination of d or b_e . However, it causes a deviation in the reconstruction of x and y , when the module is inclined along that axis.

LEDs light profiles

As previously shown in Figure 7.5 and Figure 7.8, each individual LED might have a slightly different emission curve. So far, all simulations have been performed with the mean of the measured LED profiles (red line at Figure 7.8). Now, the parameters of the column are reconstructed using each of the profiles individually, keeping as model the simulation with the mean profile. The results are shown in Figure 7.28, where each

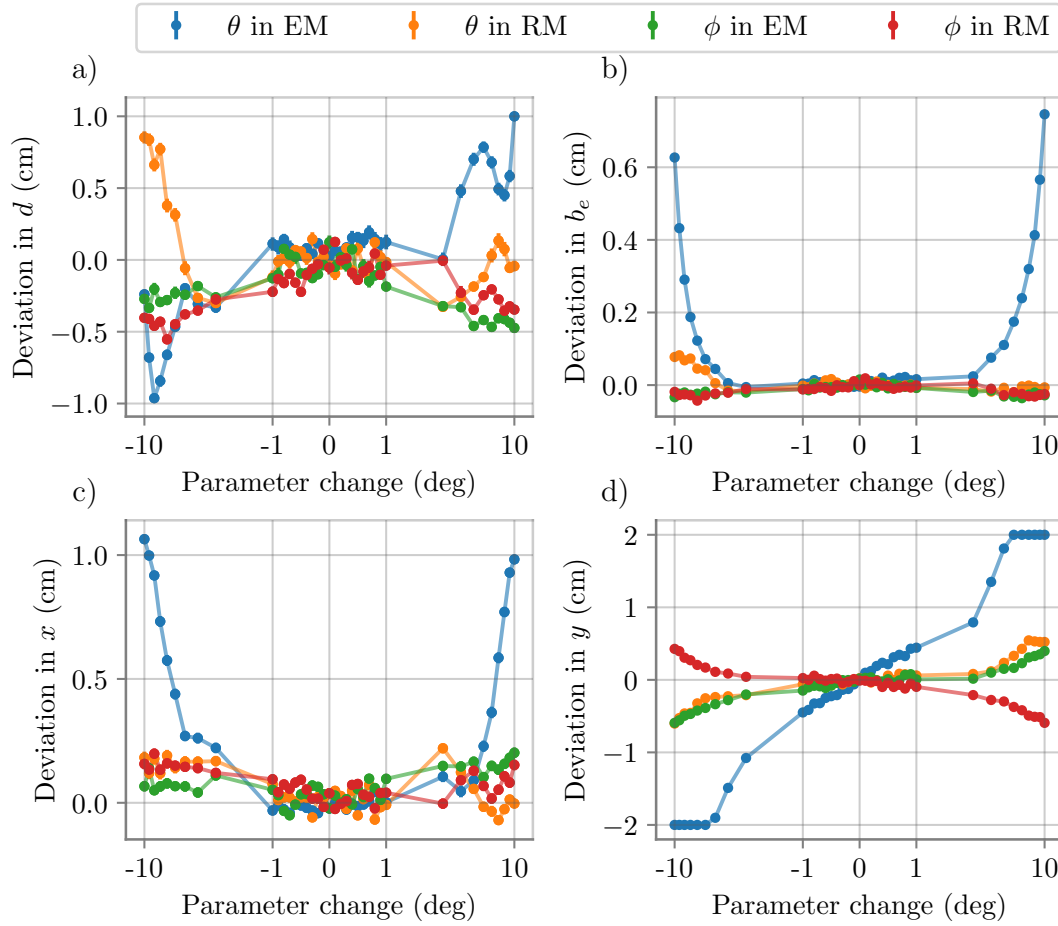


Figure 7.27: Deviations from the true value ($d = 16$ cm, $b_e = 3$ cm, $x = 0$ cm, $y = 0$ cm) of the reconstructed column parameters when one of the mDOMs is tilted along the global θ, ϕ angles. Each subfigure shows the deviation when reconstructing: **a)** column diameter, **b)** effective scattering length of the column, **c)** column position (x), **d)** column position (y). Note that the deviations of the reconstructed values are limited by the difference between the true and the edges of the scanned parameter space ($d = [12$ cm, 20 cm], $b_e = [1.5$ cm, 4.5 cm], $x = [-2$ cm, 2 cm], $y = [-2$ cm, 2 cm]).

measured LED profile has been assigned an integer number. Although the sample 2 shows the largest deviation, this is still small compared to other systematics shown in this section. It can be concluded that, in general terms, the different profiles are similar enough so that reconstruction of the column parameters is mostly unaffected. By definition, this would also apply to the asymmetry observed in each LED light profile.

LEDs light spectrum

Previously, it has been chosen to simulate all photons of the LEDs with the same wavelength of $\lambda = 405$ nm. As mentioned before, it was checked that when a Gaussian profile centered on $\lambda = 405$ nm with $\sigma = 15$ nm (as required in Section 7.2) is simulated, no significant deviations are visible after reconstructing any of the column parameters. However, this is not the case if the center of the distribution is shifted to a different wavelength. This is shown in Figure 7.29, where each simulation is performed, generating all photons with the same λ in each simulation, and performing simulation at different λ . Only the results

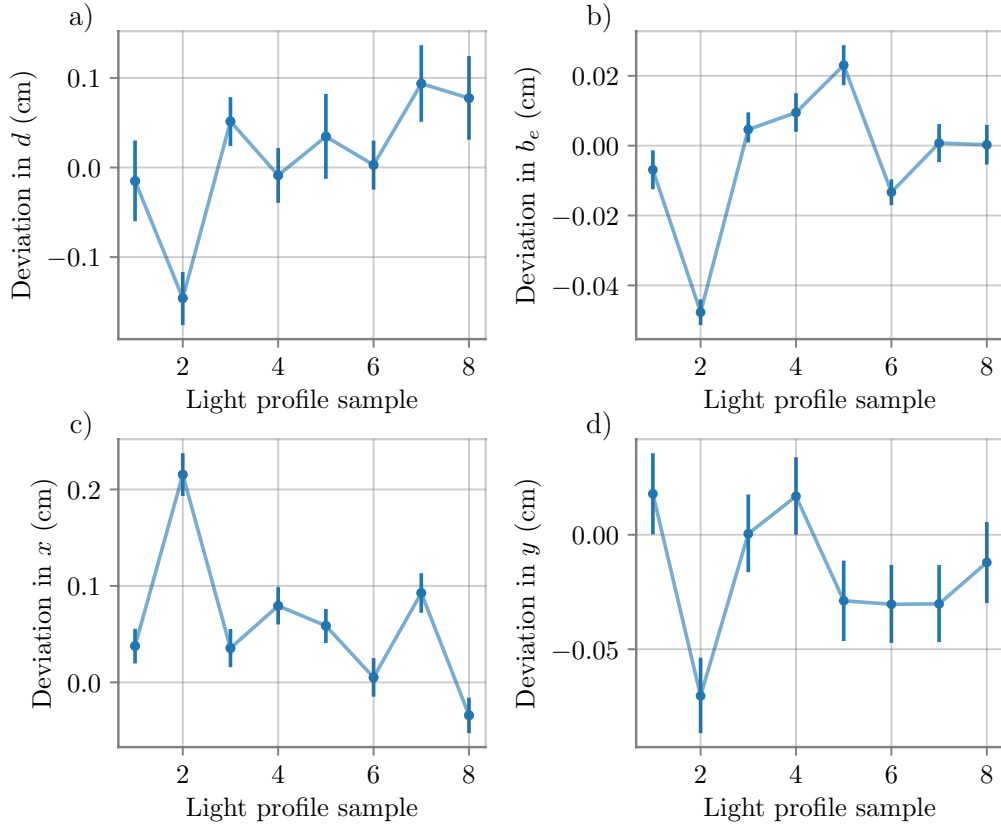


Figure 7.28: Deviations from the true value ($d = 16$ cm, $b_e = 3$ cm, $x = 0$ cm, $y = 0$ cm) of the reconstructed column parameters assuming that the light profile is unknown, chosen from the measured samples previously shown and reconstructed with the mean profile. Each subfigure shows the deviation when reconstructing: **a)** column diameter, **b)** effective scattering length of the column, **c)** column position (x), **d)** column position (y).

for reconstructing the variables d and b_e are shown, since the others do not show any significant deviation. Within the scanned range, the reconstruction of the diameter of the column is deflected by about 1 cm, while the effective scattering length also shows a correlation with λ but on a smaller absolute scale.

LEDs orientation

Another assumption made when writing the simulation code was to place the LEDs perpendicularly to the surface where they are mounted. Although this is the design goal, each LED might have a different small deviation from their nominal orientation. The requirement in Section 7.2 explained that the LEDs should point within 5 degrees from its design direction. The first measurements of LEDs in real mDOMs¹ indicate that this is always the case, with a mean opening angle between the LED and the nominal direction of $\sim 2^\circ$ [208]. Similarly to what was done before, simulations are now performed in which the LEDs are misaligned with respect to the designed direction. The results are shown in Figure 7.30. Note that here θ' and ϕ' are local spherical coordinates relative to the LED object itself. Then, $\theta' = 0$ is the nominal desired orientation of the LED, which is perpendicular to the spherical part of the mDOM surface at the position of the LED. If

¹Done by the Collaboration and shared in an internal call.

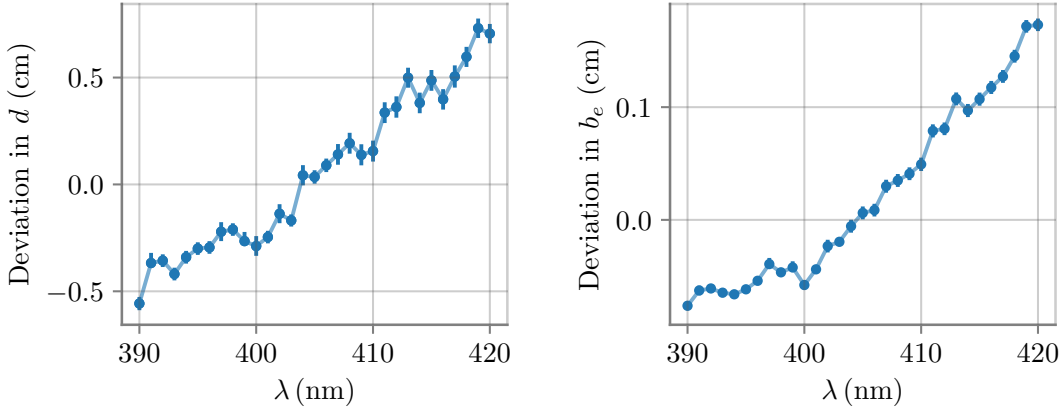


Figure 7.29: Deviations from the true value ($d = 16$ cm, $b_e = 3$ cm) of the reconstructed column parameters when the LEDs emit photons with different wavelength, reconstructed with the model using $\lambda = 405$ nm. Each subfigure shows the deviation when reconstructing: **a)** column diameter, **b)** effective scattering length of the column.

the LED were placed in the center of the spherical part pointing downwards, the locals θ' , ϕ' would coincide with the angles θ , ϕ from the module's reference frame. Note also that each LED has its own z axis, which means its own reference frame. To simplify all the possibilities that could be shown here, the same misalignment is given to all LEDs with respect to their corresponding reference frames. Later, when all systematics are considered simultaneously, each LED is tilted independently with different orientations. Figure 7.30 shows that the effects on the tilting of the LEDs strongly depend on which ϕ' is chosen. Since each LED has a different reference frame, it is probably beyond interest to determine which tilting direction for each LED has the strongest impact for each LED. Maximum deviations are observed in the reconstruction of the column diameter and in the column position.

Bulk ice parameters

The uncertainty in the optical properties of the bulk ice is also responsible for the systematic errors considered in IceCube analyses. There, a conservative value of 10% uncertainty is generally assumed in both the scattering and absorption lengths of the bulk ice. Here, simulations have been performed in which the absorption and scattering lengths of the bulk ice are modified up to $\pm 15\%$ of the values used to construct the model. No deviations are found when reconstructing any of the bubble column parameters using the data with modified bulk ice properties and the model with the original ones. The result is not surprising, since the scattering length of the bubble column is much smaller than either the absorption or scattering length of the bulk ice, so the photons that would be scattered or lost in the bulk ice are negligible in comparison with those that scatter within the bubble column. Furthermore, when building the bubble column in the simulation, the code takes directly the absorption length of the bulk ice, so modifying the latter also modifies the absorption length within the column. Again, scattering processes within the bubble column clearly dominate because of the much shorter scattering length than absorption length; therefore, small changes in the latter do not cause any difference in the detection pattern. This also implies that the method is equally valid at different depths, where the optical properties of the bulk ice are different than those chosen here.

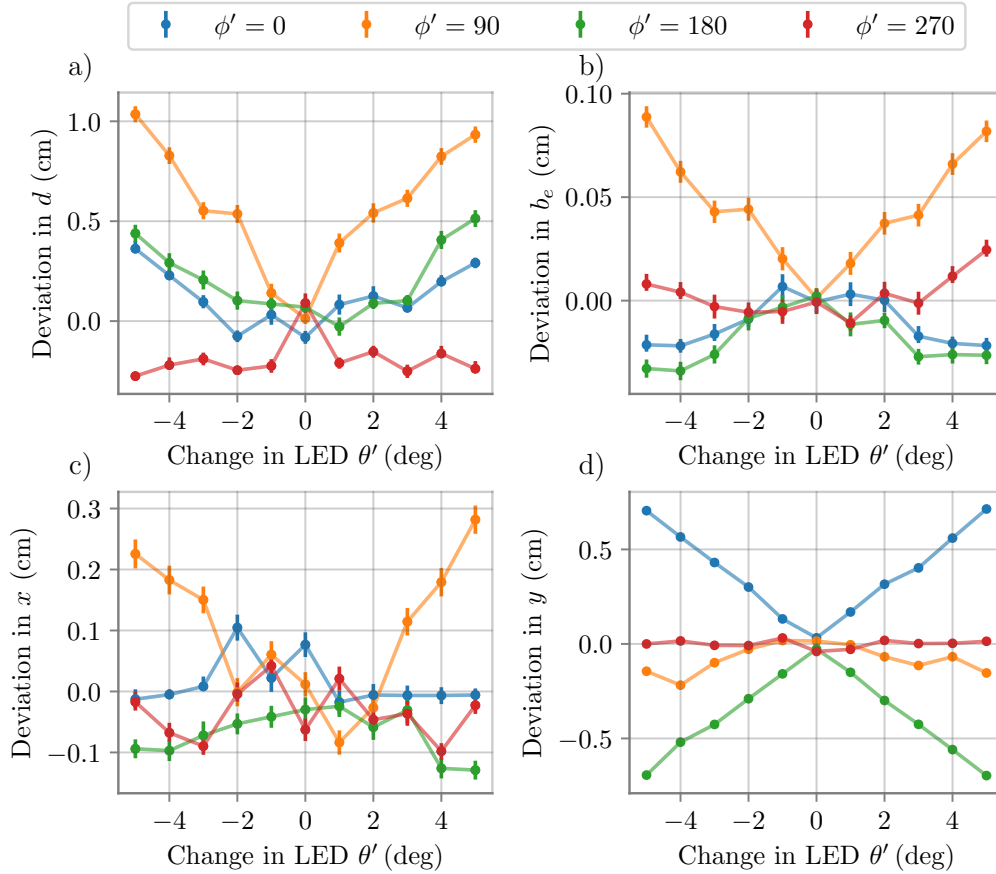


Figure 7.30: Deviations from the true value ($d = 16$ cm, $b_e = 3$ cm, $x = 0$ cm, $y = 0$ cm) of the reconstructed column parameters when the LEDs are tilted with respect to their nominal direction. Each subfigure shows the deviation when reconstructing: **a)** column diameter, **b)** effective scattering length of the column, **c)** column position (x), **d)** column position (y).

PMT response

As of now, all PMTs in both modules have been assumed equal, relying only on the corresponding quantum efficiency obtained from the same curve. The truth is that each PMT usually features a slightly different efficiency and detection probability, including QE. Although the PMTs are being individually characterized, there is a systematic uncertainty when measuring them that cannot be avoided. The impact of this uncertainty in the determination of the bubble column parameters is studied here.

Generally, IceCube uses a conservative value for the uncertainty of PMT efficiency of $\pm 10\%$ that is uniformly distributed. On this basis, in this section the efficiencies of each PMT are sampled using a flat distribution. In this case, the uncertainty of the column parameters is obtained by sampling from the model using a Poisson distribution, and minimizing the LLH space. Before sampling, each PMT is randomly assigned its efficiency within $1 \pm f/100$, where f is the uncertainty in % of the PMT efficiency considered in each case. This procedure is repeated 1000 times for each f , and each time the minimum likelihood is reconstructed. Note that in each iteration, the efficiencies of each PMT are assigned again from the flat distribution, so in each iteration each PMT has a different efficiency. The minimums then form a distribution for each f from which the $\pm\sigma$ limits

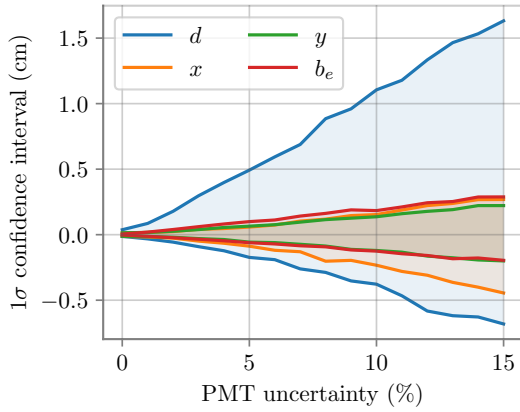


Figure 7.31: Width of the 1σ ($\pm 34.1\%$) confidence region for reconstructing each column variable simultaneously (diameter d , position in x-y and effective scattering length b_e) as a function of the uncertainty on PMT efficiency that is considered and reconstructed using the model with no PMT uncertainty, for a bubble column with true parameters ($d = 16$ cm, $b_e = 3$ cm, $x = 0$ cm, $y = 0$ cm).

Table 7.1: Statistical resolution when simultaneously reconstructing all column parameters with true values ($d = 16$ cm, $b_e = 3$ cm, $x = 0$ cm, $y = 0$ cm) when considering different uncertainties of the efficiency of each PMT individually, given as the width of the $\pm 34.1\%$ confidence range ($\pm\sigma$ in the text).

PMT efficiency uncertainty (%)	Uncertainty ($-\sigma$, $+\sigma$)			
	d (cm)	b_e (cm)	x (cm)	y (cm)
0	-0.02, +0.04	-0.004, +0.005	-0.02, +0.012	-0.01, +0.012
5	-0.17, +0.5	-0.06, +0.013	-0.09, +0.06	-0.06, +0.07
10	-0.4, +1.1	-0.13, +0.18	-0.23, +0.15	-0.12, +0.14
15	-0.7, +1.6	-0.20, +0.29	-0.45, +0.27	-0.20, +0.22

are obtained using the corresponding percentiles. The results are shown in Figure 7.31. At 0 PMT uncertainty, this means directly sampling the model $\mu_{i,j}$, and, as expected, this returns the same result as that obtained in Section 7.6. The σ region gradually increases with the uncertainty on the PMT efficiency, affecting the most, on absolute value, when reconstructing the diameter of the column, with σ greater than a centimeter for a PMT uncertainty of 10%. The relative uncertainties on d and b_e are both $\sim 5\%$ when a PMT efficiency of 10% is assumed. The results are summarized in Table 7.1.

Relative mDOM-cable position

Simulations have also been performed in which the data cable is misplaced within the hole ice with respect to the simulation used as a model, rotating it around the module. No difference in the column parameter reconstruction is found when assuming a wrong cable position. In the simulation, the cable is considered as a black, totally absorber body, an approximation precise enough for the studies made here. The shadow of the cable is noticeable in cases when the light source is positioned outside the hole in the ice. However, in our situation, the cable only absorbs some of the photons that are already traveling through the bulk ice. In any case, these photons would have little chance of being detected and do not influence the determination of the bubble column parameters.

On the bubble column approximation

The simulations performed in this chapter simplify the bubble column as a cylinder with no transition between the bulk ice and the column itself. Although current IceCube studies indicate that the transition between the bubble column and the bulk ice is very sharp,

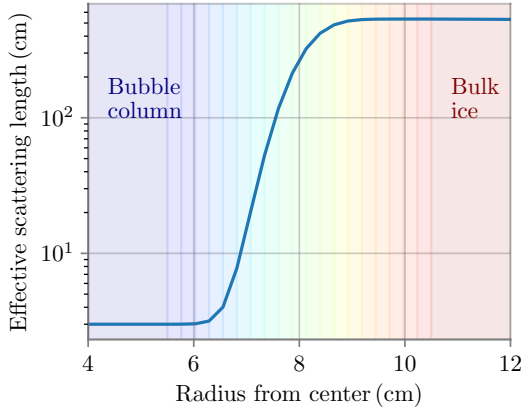


Figure 7.32: Sketch showing how the transition region on the effective scattering length between the bubble column and bulk ice has been modeled. Each colored line indicates the end of each layer, with $N = 20$ layers and $\Delta = 5$ cm ($\sigma = 0.5$ cm) in this example.

there would obviously be a small transition region between the two. In a purely simulation work like this, it cannot be determined whether the transition is there or if it would be noticeable in analyses. However, a small test has been performed to determine whether the transition region between the column and the bulk ice might affect the feasibility of the method developed in this chapter.

The transition region has been simulated using layers, where the effective scattering length gradually increases in each layer¹. This has been done by assuming a model in which the transition in scattering length follows a Gaussian-shaped curve of standard deviation σ . The code takes as input parameters the number of layers N and the width of the transition region Δ and computes the scattering length of each layer symmetrically around the original column radius of $R = 8$ cm. Δ and σ are related as $\sigma = \Delta/10$, so the transition region contains the entire curve. Then, the effective scattering length of the k layer $b_e^{(k)}$ is obtained using the cumulative Gaussian distribution as

$$b_e^{(k)} = b_e^{\text{column}} + \frac{b_e^{\text{bulk}}}{2} \left[1 + \operatorname{erf} \left(\frac{r_k - R}{\sigma\sqrt{2}} \right) \right], \quad (7.4)$$

where erf is the error function, b_e^{column} , b_e^{bulk} the effective scattering length in the inner bubble column or in the bulk ice, respectively, and

$$r_k = r_i + \frac{r_f - r_i}{N - 1} k, \quad (7.5)$$

the radius of the k layer, with $r_i = R - \Delta/2$ and $r_f = R + \Delta/2$ being the radius of the first and last layers, respectively. A sketch of the transition is shown in Figure 7.32 for a standard deviation of $\sigma = 0.5$ cm. To keep simulation times reasonable², $N = 20$ layers have been chosen and simulations are performed varying Δ .

Then, the column parameters are reconstructed as usual using the 4-dimensional model with no transition region. The results are shown in Figure 7.33. For small σ , significant deviations are present only in the reconstruction of the column size. This is no surprise;

¹A different b_e curve for each wavelength, due to this dependency on the bulk ice properties. However, this is not relevant in this case since photons with a single wavelength are being emitted.

²The simulation time considerably increases when a high number of layers is used.

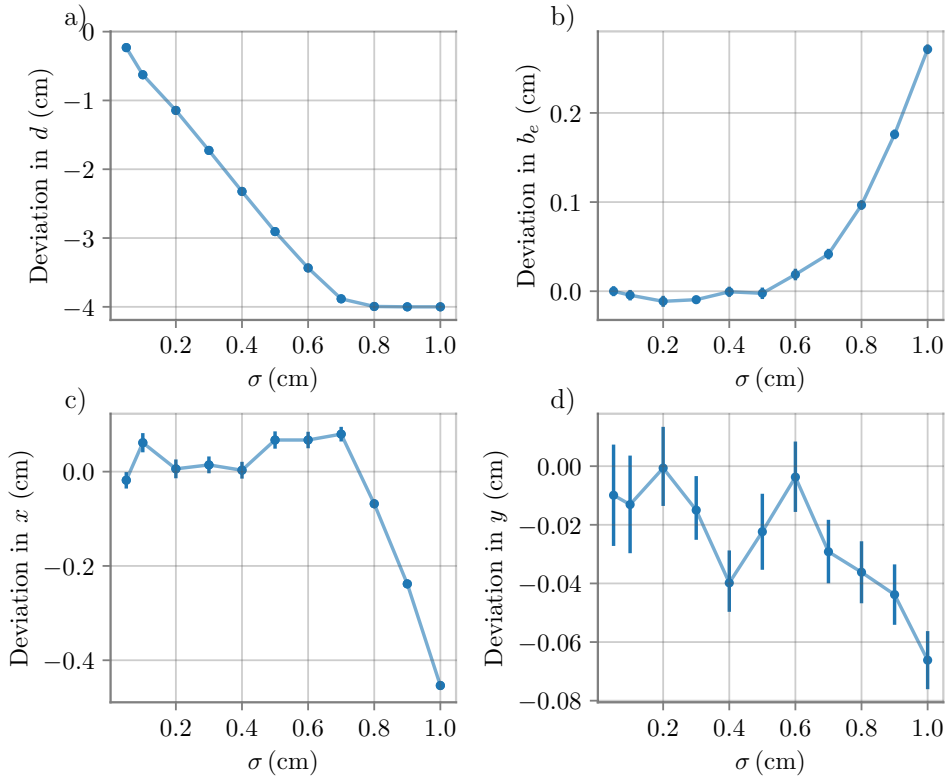


Figure 7.33: Deviations from the true value ($d = 16$ cm, $b_e = 3$ cm, $x = 0$ cm, $y = 0$ cm) of the reconstructed column parameters when a Gaussian-shaped transition region for the effective scattering length between the bubble column and the bulk ice is included and the 4-dimensional model with no transition region is used to reconstruct the parameters. σ stands for the standard deviation of the Gaussian transition region. Each subfigure shows the deviation when reconstructing: **a)** column diameter, **b)** effective scattering length of the column, **c)** column position (x), **d)** column position (y). Note that the deviations on the reconstructed values are limited by the difference between the true and the edges of the scanned parameter space ($d = [12$ cm, 20 cm], $b_e = [1.5$ cm, 4.5 cm], $x = [-2$ cm, 2 cm], $y = [-2$ cm, 2 cm]).

the concept of column diameter, using a diffuse column, is no longer valid. Thus, it can be expected that a smaller column diameter is being reconstructed in this case, linearly correlated with σ . Due to the large difference between the scattering lengths, the best fit is always obtained for a thinner column, which is indeed what the column has effectively become. Therefore, it cannot be stated that the size of the column is wrongly reconstructed. If the transition region is wider than $\Delta \approx 5$ cm ($\sigma \approx 0.5$ cm) deviations start to appear in the reconstruction of all parameters, showing that the model is no longer valid. However, such a large transition should not have gone unnoticed in IceCube studies; thus, this scenario is very unlikely. For a narrow transition region, the fact that the parameters (except for d) are well reconstructed indicates that the diffuseness of the column does not affect the validity of this method and that the simplification when modeling the column done in this chapter is sufficient.

Furthermore, once the detector is built, simulations similar to those performed in this section can also be made to determine how large, if any, the transition region is. Once the best fit is obtained for the bubble column parameters, this can be used as input data to the simulation. Then, a model can be produced with the layer structure as done here.

Later, this model can be used to check whether the log-likelihood returns a better fit with or without the transition model and the properties of these. The process can be done recursively to check whether, when using a model with transition in it, the remaining column parameters are reconstructed with the same values as before.

In Figure 7.34 the log-likelihood is obtained as a function of the transition width Δ . Both curves are obtained using the model with transition region. The figure on the left shows the LLH obtained when the standard simulation without transition region is reconstructed, whereas in the figure on the right, one of the simulations with the transition column was chosen as the reference data to reconstruct. The results on the left show that the LLH decreases with decreasing Δ , indicating that the data have a narrower or no transition region than the model and implying that the method would be sensitive to such a transition. This is proven in the figure on the right, where the LLH shows a deep minimum at the corresponding σ used for the data. Thus, it is possible to compare models similar to those with real measurements to determine whether there is a significant transition region between both ice bodies and, if so, the effective width of such transition. Different models can be compared with the real data to check which one fits the results better, not necessarily being a Gaussian-shaped transition as used here. One would ultimately need to calculate how the rest of systematic sources affect the resolution to these parameters.

In conclusion, if there is a transition region between the bubble column and the bulk ice, the method used in this chapter would obtain an effective value for the column diameter corresponding to what better resembles the model without transition, while the rest of the parameters would be unaffected if the transition region is not significantly wider than expected. However, once the detector is built, the models can include a transition region and use the same method to obtain the best model that fits the data. If the transition region is as narrow as expected, it could be that it has no impact on the final detector analyses, and there is no need to study it further; however, at this stage this can not be known. A similar discussion could be conducted about whether some of the systematics considered here can be reconstructed using the same method, where the bubble column would indeed be a source of systematic uncertainty in that study. These discussions go beyond what is intended in this chapter as an initial study of the feasibility of the method based solely on simulations, since this would require measurements to compare with models.

7.7.2 Combined systematics

Now that the impact of the previous systematic sources on the reconstruction of the column parameters has been individually studied, it is time to combine them into a single analysis to get the final sensitivity as close as possible to the real experiment. This can not be done by simply summing up the individual studies previously shown, since the contribution of different systematic sources might add up to the final result when they are simultaneously combined, the most trivial case being the orientation of the LEDs combined with the orientation of the modules. To this end, the LED flasher simulations are done with a column with the standard parameters defined before ($d = 16$ cm, $b_e = 3$ cm, $x = 0$ cm, $y = 0$ cm), but including all the systematic sources simultaneously, each following a given distribution. Then, $N = 1500$ simulations are performed. Based on the results and discussions about each systematic source previously done, the following are considered:

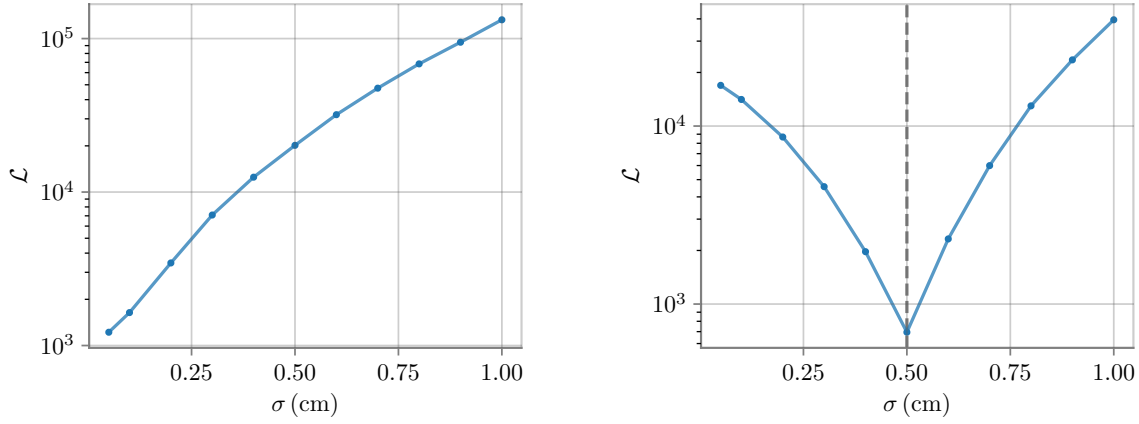


Figure 7.34: LLH curves from the simulations with a transition region between the bubble column and the bulk ice. In both curves, the simulated data is compared to the model with a transition region depending on σ **Left:** LLH space obtained for simulated data without transition. **Right:** LLH space obtained for simulated data with a transition region of $\sigma = 0.5$ cm.

- LED light profile: each simulation is done using a randomly selected sample from the measured LED light profiles. The wavelength of emitted photons is sampled from a Gaussian distribution centered on $\lambda = 405$ nm with $\sigma = 10$ nm.
- Relative position of the modules: the position in x and y of each module is sampled from a Gaussian distribution centered at 0 cm with $\sigma = 1$ cm. The distance between modules is also sampled from a Gaussian distribution centered on 3 m with $\sigma = 5$ cm.
- Relative orientation of modules: the orientation of each module is sampled from a Gaussian distribution centered on 0° with $\sigma = 0.5^\circ$ for both θ and ϕ . The rotation in θ is performed after the whole coordinate system was previously rotated randomly in ϕ within $[0, 2\pi)$, so that all orientations are considered.
- Bulk ice properties: the absorption and scattering lengths in the bulk ice are modified in each simulation by sampling a Gaussian distribution centered at 0% with $\sigma = 10\%$.
- LED orientation: the orientation of each LED with respect to the normal of the surface where they are mounted is also modified, sampling in θ' from a Gaussian distribution centered at $\theta' = 0^\circ$ with $\sigma = 2^\circ$. ϕ' is then sampled randomly within the $[0, 2\pi)$ range.
- Uncertainty in the PMT response: Each PMT for each simulation is assigned a value corresponding to its efficiency from a flat distribution. This is done by randomly sampling a value from 0.9 to 1.1, which multiplies the number of photons detected on this PMT for that simulation.

The values are chosen trying to be realistic, representing the uncertainty at which each variable might be known for ICU, without being too conservative or optimistic. Note that, as mentioned above, the final uncertainty of each variable is something that will be obtained once the actual detector is built, so some of the ranges chosen here for each variable could then change. Note that the transition region has not been included, as it was concluded that it would only affect the reconstruction of the column diameter, resulting in an *effective* column diameter instead.

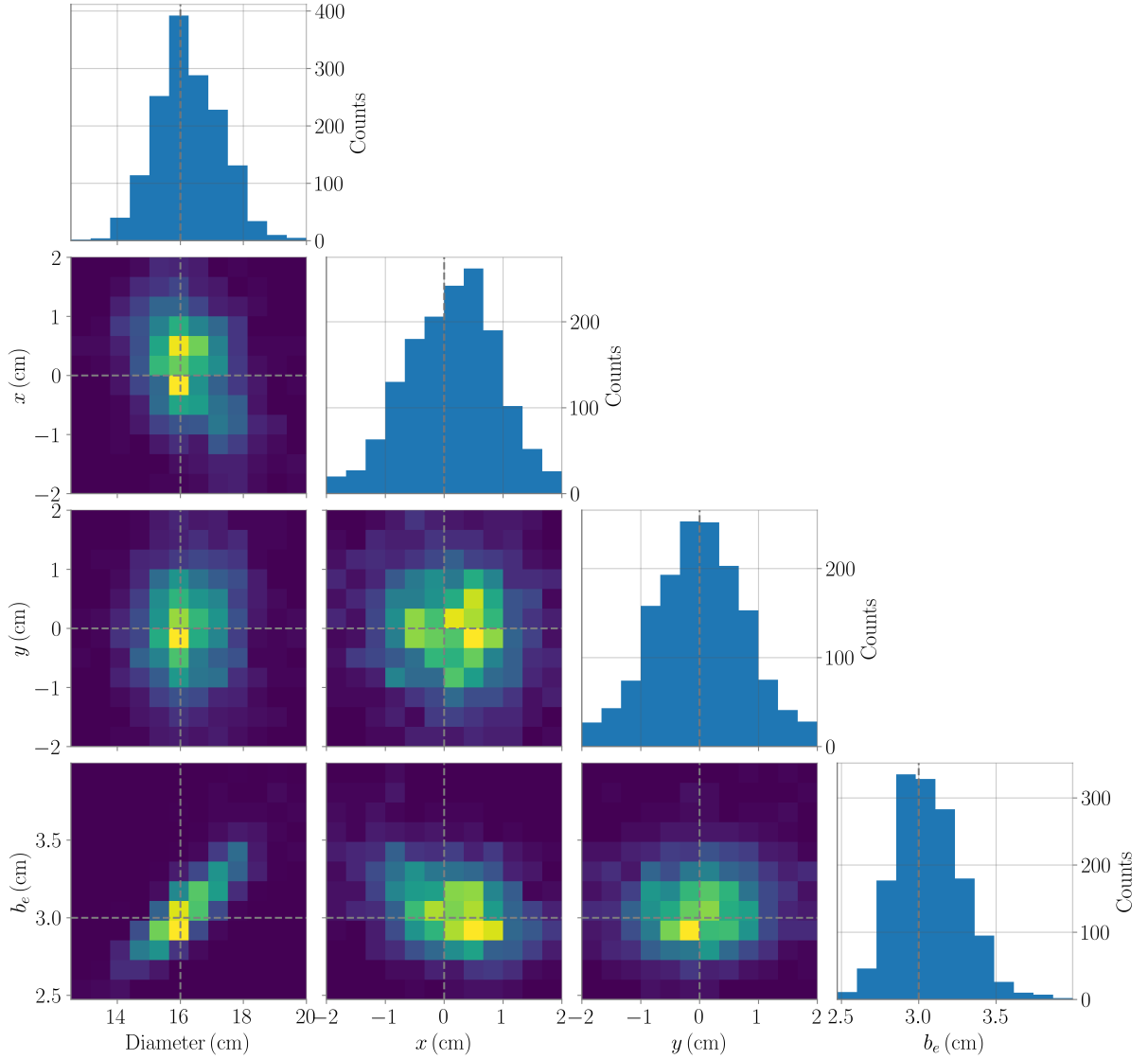


Figure 7.35: Histograms showing the minimums of the likelihood when reconstructing the bubble column parameters within the 4-dimensional space for $N = 1500$ simulations, in which all mentioned systematic sources of error are included simultaneously as described in the text, for reconstructing a bubble column with true values ($d = 16$ cm, $x = 0$, $y = 0$, $b_e = 3$ cm). Each figure is a marginalization of the 4-dimensional result in either one or two dimensions.

All systematic effects are sampled as described for each simulation. Then, the interpolated 4-dimensional model with no systematic included is used to reconstruct the bubble column parameters, similarly as done before. The best reconstructed value for each variable is then kept and shown in Figure 7.35 as histograms, marginalized in each dimension. This is done by summing up all entries in the nuisance parameters of each figure. Results are shown in a way similar to that done previously in Sections 7.5 and 7.6 so that it can be visualized in each 2-D and 1-D combination. The result for each variable is centered around the correct values, although it is only fully symmetric for y . This asymmetry could be expected from what has been shown before: for b_e and d , this is due to the lower values for the LLH curves at lower b_e or d , respectively. x and y were affected similarly by systematics, but the resolution in x was also shown to be asymmetric due to the position

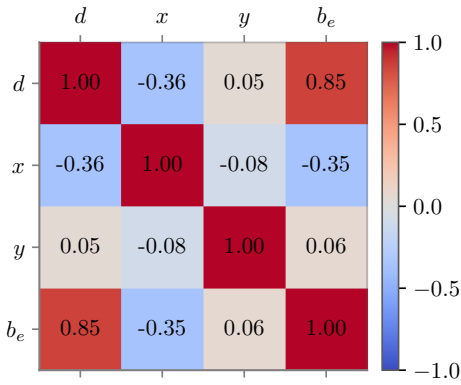


Figure 7.36: Correlation matrix between the bubble column parameters when these are simultaneously reconstructed using LED flashers in mDOMS, when all systematic sources considered in this section are included in the analysis.

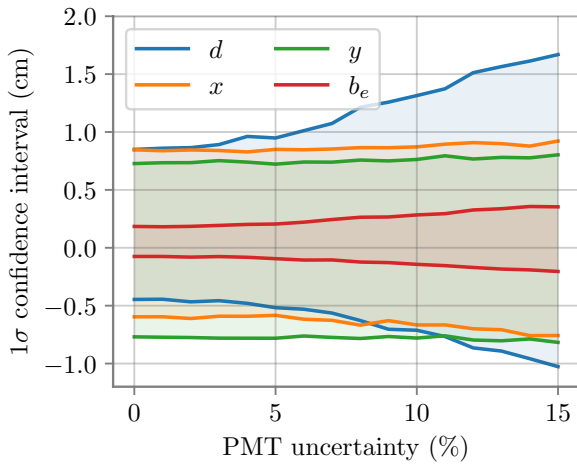


Figure 7.37: Width of the 1σ ($\pm 34.1\%$) confidence region when reconstructing all parameters of the bubble column simultaneously and considering all systematic sources as described in the text, as a function of the uncertainty in the efficiency of each PMT, for reconstructing a bubble column with true values ($d = 16$ cm, $x = 0$, $y = 0$, $b_e = 3$ cm).

of the centered LED. It might then appear counterintuitive to see that the reconstruction of x is worse in the direction where the LED is. When scanning different column positions, it is logical that the closer the LED is to the edge of the column, the more significant the change in the detected pattern will be. The extreme case being when the LED changes from being inside to being outside of the column, or vice versa, with only small changes in the bubble column position. Therefore, the reconstruction of x should be better in the opposite direction of the LED = 0, as is. It can also be observed that the reconstruction of the column position reaches the limits of the model in some cases for x and y , while d and b_e are fully contained within the scanned range.

It can also be observed how the determination of some column parameters is correlated. This was already visible before when systematics were not considered, especially for the case of d vs. b_e . To quantify the strength of each correlation, the correlation matrix has been calculated as $R_{ij} = C_{ij}/\sqrt{C_{ii}C_{jj}}$ [212], with C_{ij} being the element i, j of the covariance matrix and, as such, C_{ii} being σ_i , for i, j being each column variable. The result is shown in Figure 7.36. A correlation factor of 1 or -1 indicates a perfect direct linear dependency between the variables, increasing or decreasing, respectively, while 0 means that the reconstruction of the variables is completely uncorrelated. With a value of 0.85, a strong correlation between d and b_e is found, which was already visible when scanning the LLH space in Figure 7.19. The reason for such a correlation was discussed earlier when it was first observed in Section 7.5: the ratio of photons scattering back to the emitter module is higher for shorter scattering lengths and also for a wider bubble column, therefore, a detection pattern similar to what is obtained with the true parameters can also

Table 7.2: Resolution uncertainties on the reconstruction of the column parameters when the bubble column parameters are reconstructed simultaneously using LED flashers, taking into account the systematic sources of errors, for a bubble column with true values ($d = 16$ cm, $x = 0$, $y = 0$, $b_e = 3$ cm). The table shows each result assuming different uncertainties in the efficiency of each PMT. Each variable has been reconstructed for $N = 1500$ different simulations varying the parameters of each systematic source, and the table shows the median and the $\pm 34.1\%$ quantiles from reconstruction results, marginalizing each reconstructed variable distribution.

PMT efficiency uncertainty (%)	Median ($\pm\sigma$)			
	d (cm)	b_e (cm)	x (cm)	y (cm)
0	$16.0^{+0.9}_{-0.5}$	$3.03^{+0.18}_{-0.08}$	$0.2^{+0.8}_{-0.6}$	$0.0^{+0.7}_{-0.8}$
5	$16.1^{+0.9}_{-0.5}$	$3.03^{+0.20}_{-0.09}$	$0.2^{+0.9}_{-0.6}$	$0.0^{+0.7}_{-0.8}$
10	$16.1^{+1.3}_{-0.7}$	$3.05^{+0.28}_{-0.14}$	$0.2^{+0.9}_{-0.7}$	$0.0^{+0.8}_{-0.8}$
15	$16.1^{+1.7}_{-1.0}$	$3.03^{+0.35}_{-0.20}$	$0.2^{+0.9}_{-0.8}$	$0.0^{+0.8}_{-0.8}$

be obtained for larger b_e and larger d and vice-versa. To a lesser extent, a small correlation is also found between x , d and x , b_e , probably resulting again from the asymmetric position of the centered LED along the x axis.

It is interesting to see how the results behave when the uncertainty on the PMTs is changed. This can be done easily, since the PMT efficiency is only assigned to the simulation results afterward. Uncertainty intervals $\pm 1\sigma$ are calculated from the marginalized one-dimensional histograms using the corresponding quantiles after sampling the PMT efficiency with different values as done before. The results are shown in Figure 7.37. It is interesting to compare this figure with Figure 7.31, where the PMT uncertainty was the only systematic that was included. From a PMT uncertainty of approximately 10% onward, this is the major factor responsible for the overall uncertainty in b_e and d . The uncertainties in x and y are dominated by the other sources, as increasing the PMT uncertainty barely changes the resolution of these parameters. The final results on the resolution of the method for reconstructing each column variable simultaneously are presented in Table 7.2. The medians of the distributions of each reconstructed parameter are also given in the table, which can be used to conclude the final effect of the systematic on the reconstruction parameters, showing a small shift towards larger values for d and x , but well within the uncertainty range. Note that here the values have been reconstructed by assuming that the true column has parameters $d = 16$ cm, $b_e = 3$ cm and is centered within the string. The results would slightly vary if different values were assumed. Based on the likelihood curves shown throughout the chapter, it can be estimated that the accuracy in the parameter reconstruction is better for smaller d and b_e , and also if the column is displaced with respect to the modules in the positive x direction, being closer to the center LED¹. In comparison with the previous results obtained in Section 7.6, systematic errors clearly dominate over statistical errors when using the 1.6×10^9 photons per flash, being more than 1 order of magnitude superior.

¹However in this case, the position reconstruction should be slightly worse in x , as discussed before.

7.8 Summary and conclusions

In this chapter, the ability to reconstruct the bubble column parameters using LED flashers of two consecutive mDOMs has been studied. The bubble column consists of an accumulation of impurities and bubbles that occurs when the hole drilled in the ice refreezes after string deployment. Currently, it is one of the most important sources of systematic uncertainties in IceCube analysis, especially at low energies. If the column is also present in ICU, the reconstruction of its properties will be crucial to maximize the performance of the detector. The calibration of the column parameters will contribute not only to improve ICU analyses but also those with IceCube, since the information about the column obtained in ICU strings can be used to calibrate the models in IceCube analysis as well. Current knowledge about the column states that it is centered within the modules, with a diameter of about half DOM and a scattering length of just a few centimeters, although the exact values that would characterize the column remain uncertain [205].

The Geant4 simulation of the mDOM has been modified and adapted for this study. The light profile of the LEDs was measured by IceCube [210] and incorporated into the simulation here, with the necessary adjustments to match the output measured in the lab. The bubble column was characterized as a cylinder depending on four input parameters: its horizontal position with respect to the modules (x, y) , its diameter d , and its effective scattering length b_e . Once it was verified that the simulation worked correctly, it was run using two modules: emitter (EM) and receiver (RM) modules. Photons are generated from the bottom LEDs in the EM, which are facing the RM. The detection pattern in the PMTs of both modules was observed to vary depending on the bubble column parameters, information that can be used to reconstruct them. The simulation data was then used to build a model to reconstruct the column parameters by minimizing a LLH space. It was found that the LLH space is smooth and only contains a global minimum, independently if 1, 2 or all parameters of the bubble column are simultaneously scanned. The scans in 1 or 2 dimensions are interesting for assuming that some parameters of the column are reconstructed by another method. Although this will be the case in the real experiment, it is useful to study the same variables using different methods in order to reduce the impact of systematics on any of them. Therefore, the 4-dimensional case that assumes that there is no prior knowledge about the column is the most interesting and the one that was analyzed in detail later.

Subsequently, the statistical resolution was obtained by reconstructing the column parameters simultaneously. This is not strictly necessary for the real experiment in which the LEDs can be flashed as many times as desired, in contrast to the simulations used here that use a fixed and restricted number of photons per flash. However, it is important to check that the statistical errors in these simulations are small enough to be able to accurately study the effects of systematic errors. A continuous model was constructed by interpolating the expected value of photons detected in each PMT of each module for each LED flash in all dimensions (d, b_e, x, y) , which allowed us to obtain a continuous behavior of the LLH space and therefore to obtain the confidence level on each reconstructed parameter. Later, it was verified that this result was indeed below the systematic errors.

Next, the impact of different sources of systematic errors in the study was analyzed by independent simulations. It was checked how the reconstructed minimum deviated from the truth depending on several factors: the uncertainty in the position and orientation of

the modules, the differences between LEDs in light profile and light emission, the impact of their possible orientation with respect to their nominal axis, the uncertainty in the efficiency of the PMTs, the properties of the ice around the column, and the relative position of the data cable. Generally, the reconstruction of the column position is mostly affected by systematic uncertainties related to geometrical factors. The reconstruction of b_e is, on the other hand, mostly affected by systematic uncertainties in the PMT efficiencies, and is only significantly affected by geometrical uncertainties if these are very large. The reconstruction of the column diameter is in between the two previous cases, being more sensitive to geometrical uncertainties than b_e and also affected by hardware uncertainties, such as PMT efficiencies or LED light profiles. The possible errors resulting from the approximation done to simulate the bubble column were also studied, which verified that the model was usable when a possible transition region between the column and the bulk ice is narrow enough.

Finally, all sources of systematic errors were combined in the simulations at the same time. These were introduced based on current IceCube knowledge and initial studies of ICU components. The final results are represented in Table 7.2. It can be seen that the systematics sources of uncertainties introduce a small deviation in the best reconstructed value of x and, to a lesser extent, d and b_e . In the final results, a strong correlation between b_e and d , previously seen in the LLH spaces, was confirmed.

Within the IceCube Collaboration, studies have been done to determine the resolution that ICU will have to reconstruct different properties of the column. In particular, the most accurate method to study the column in ICU, in addition to the LEDs, is to use the cameras mounted on the modules. This method is especially sensitive to the size of the column, with an estimated resolution of < 5 mm [215], a higher precision than what was obtained here. This information can be used to further improve the reconstruction of b_e , due to the correlation between the parameters previously found. Depending on the case, cameras might also help to improve the reconstruction of the column position. In the analysis done in this chapter, the reconstruction of the bubble column position was largely affected by the uncertainties in the relative position of the modules as well as on the LED orientation. Improving the geometry calibration of the detector or individually calibrating the LED orientations will consequently improve the results obtained here. With respect to the scattering length within the column, this analysis resulted the determination of the effective scattering length parameter with a relative uncertainty of $\sim 7\%$ ¹ if a conservative value for the uncertainty on the PMT efficiency of 10% is assumed. If a less conservative value for the PMT uncertainty of 5% is chosen, the relative uncertainty on b_e is found to be $\sim 5\%$. To date, these results represent the most promising outcome for accurately reconstructing the optical properties of the bubble column in the ICU detector.

¹Assuming a true value of $b_e = 3$ cm and the standard deviation shown in Table 7.2.

Sensitivity of IceCube Upgrade to GeV neutrinos from compact binary mergers

In this chapter, the capabilities of IceCube Upgrade for detecting and identifying a transient GeV neutrino flux from compact binary mergers are studied. For that, a particle selection procedure is developed based on the current DeepCore event selection chain, with the goal of distinguishing events from the background in the detector. At the final level, the scope is to have a sample which can be used to search for an excess of the signal over the background within a certain time window.

Compact binary bodies rotating around a center of mass may move closer together as they lose energy through the emission of gravitational waves, ending with the eventual merger of the system [64]. Part of the energy of these merger events is emitted in the form of gravitational waves [69]. Furthermore, since a GRB has been detected associated with a compact binary merger GW event [216], it can be expected that these processes might also emit a flux of neutrinos [75, 217]. Depending on the energy range, such neutrinos could be detected with IceCube or with its low-energy extension, either the current DeepCore or the future ICU.

As introduced previously in Section 2.4, binary mergers have been detected through different messengers, but so far no neutrinos could be associated with these events. The most successful way of detecting them is through GWs, as has been proven by observations in the last few years of the LIGO-Virgo Collaboration [69]. IceCube has performed detailed offline analyses using GW catalogs in the high-energy region, which resulted in no significant neutrino emission found in correlation with any of the reported events [75, 76]. Furthermore, DeepCore performed the search targeting extreme low-energy neutrinos (*ElowEn*) from 0.5 to 5 GeV [217]. Whereas the analyses at high energies use the directional information of the GW detection to only select neutrinos correlated in direction with the signal, the *ElowEn* analysis only searches for an excess of low-energy neutrinos within a certain time window. This analysis did not find any significant signal excess in time coincidence with the reported mergers [217].

When comparing the potential of IceCube Upgrade with current DeepCore, an improvement can be expected on the detection of *ElowEn* events, due to the higher density of the new detector and the newer optical modules. However, this will apply to both the signal and background events. The newer modules will have higher background rates, and thus distinguishing neutrino events from other types of traces in the detector is crucial. In addition, the background from other neutrino sources, such as atmospheric neutrinos, will be higher in the new detector. These details are studied in this chapter, performing an event selection of low-energetic events using a machine learning technique. The final results will then be compared with those from DeepCore. Although the results here are applied to the case of a GeV neutrino flux coming from binary mergers, the selection chain is applicable to searches of any kind of transient event that would potentially emit a flux of neutrinos in the GeV energy range.

This chapter is organized as follows: first, a brief introduction is given to the neutrino flux that will be assumed for these sources and the expectation regarding the background. Then, the simulations used in this chapter are described. Later, the event selection is explained, in which the focus is to select neutrino events over the background composed of atmospheric muons and the background produced by the modules and PMTs. Later, the expected sensitivity to binary mergers is given as a 90% upper limit confidence level and the results are discussed.

8.1 Assumed signal and background

In recent years, LIGO and Virgo detectors have identified many mergers through GW events [69]. The detection of the gravitational wave event GW170817 [218] in coincidence with a GRB confirmed the hypothesis of binary mergers as progenitors of short GRBs [216]. Under this scenario, neutrinos can be produced from different processes depending on their energy range. TeV neutrinos are expected to be generated after internal shocks in the prompt emission phase of the GRBs, while GeV neutrinos could be produced after collisions of neutrinos and protons following their decoupling during the acceleration phase [217, 219]. The detection of these GeV neutrinos will not only provide evidence of the hadronic acceleration mechanism but will also allow a better constraint on the astrophysical object environment, acceleration processes, and progenitors of these events [217]. Astrophysical neutrino fluxes commonly follow a power-law decreasing with energy, thus more events are passing through the detector at lower energies, although these are often harder to identify. In this study, it will be assumed that the mergers emit a flux of neutrinos following a generic energy spectrum with E^{-2} , which helps to compare with the literature, within the energy range covered by ICU. The main challenge in this study is to be able to identify the neutrino events from the background, similar to what was done previously in Chapter 6 for the case of MeV CCSN neutrinos. However, considering a different energy range, it must be faced differently. Still, some of the approaches used there, such as the use of coincidences in mDOMs, can and will be utilized here as well.

The most important background for this study is composed of detector noise and atmospheric muons, together with the flux of atmospheric neutrinos. In this chapter, detector noise is defined as the combination of PMT dark rate with the detection of radioactive decays in the vessel glass, introduced previously for IceCube in Section 3.6. Regarding the background rate generated due to atmospheric muons, these are produced together with atmospheric neutrinos after the interaction of cosmic rays with the atmosphere (see Eqs. 2.12 and 2.13). These events generally leave signatures in the detector quite different from those produced by neutrinos: the noise would typically generate sparsely distributed hits in the detector, whereas a muon track going through the detector usually leaves an elongated signature of modules registering light. For the case of the atmospheric neutrinos, these are treated in this work as indistinguishable from the signal events, although later the influence of using the reconstructed incoming direction to exclude them will be discussed.

Distinguishing neutrinos from other event types becomes increasingly difficult as the energy range being examined decreases. For the case of noise-only produced background, the lower the energy of the signal events being searched, the higher the probability that the noise would produce a similar signature in the detector, since low-energetic events generally have fewer hits in the detector. For the case of muons, the smaller the muon energy, the shorter

the signature of the elongated detection pattern, up to being almost indistinguishable from point sources in some cases. However, muons that are generated outside the detector need to reach the ICU and DeepCore physics volumes to be detected as a possible signal event, possibly leaving a trace in the IceCube region. As stated in Section 3.3.1, IceCube uses veto regions and filters to determine whether the interaction occurred within the sensitive volume or whether it occurred outside and the light or the resulting particles traveled inside. The same idea is applied here, using the whole high-energy array and the DeepCore calibration region to form a veto region with which incoming particles can be identified.

Inevitably, a final background rate is present in any search. This work will first aim at distinguishing neutrinos from muons and noise. Later, the sensitivity to compact binary mergers will be given as an excess signal on top of the combined background of these two sources plus the atmospheric neutrino flux. With no detector built as of yet, the studies only rely on simulations for each event class, which are explained in the following section.

8.2 Events simulations

The analyses of this chapter are based on simulations made by the IceCube Upgrade Collaboration using the IceCube core software suite *IceTray* [197]. Based on C++ and Python, IceTray provides a uniform analysis framework for simulation, reconstruction, and analysis, including processing data and calibration studies. The framework is designed as a modular library, which means that, depending on the specific task, the user can select the modules to use or easily implement new ones. The data is represented as a collection of key-value pairs divided into different frames [197].

Although IceCube is constantly collecting data, not all of it may be useful for neutrino analyses, and due to bandwidth constraints, not all of it can be transmitted. Data is filtered on-site and in near real-time before being sent to the Collaboration for further analysis. This combines a chain of algorithms implemented within IceTray known as *Processing and Filtering* (PnF) that belong to the data acquisition (DAQ) software components. The filters are adapted and different between IceCube high-energy events and those low-energy events triggered in DeepCore. Particle interactions can be generated by different IceTray modules, and later photons are propagated through the ice using the *CLSim* module from IceTray. When the photons are about to reach the optical modules' positions, look-up tables are used to check whether the photon is detected or not based on the photon hit position and its direction. The simulated data is then run through the PnF system and ready to be used.

In all cases, the particle simulations are done following a set of generic steps:

1. Event generation: particles are generated within the chosen volume.
2. Photon propagation: photons resulting from the interaction of the injected particles are propagated to the modules using CLSim module in IceTray. A first cut is made if photons do not reach any optical module.
3. Detector simulation: the detection of the photons by the optical modules, PMTs readout, and triggers are simulated.

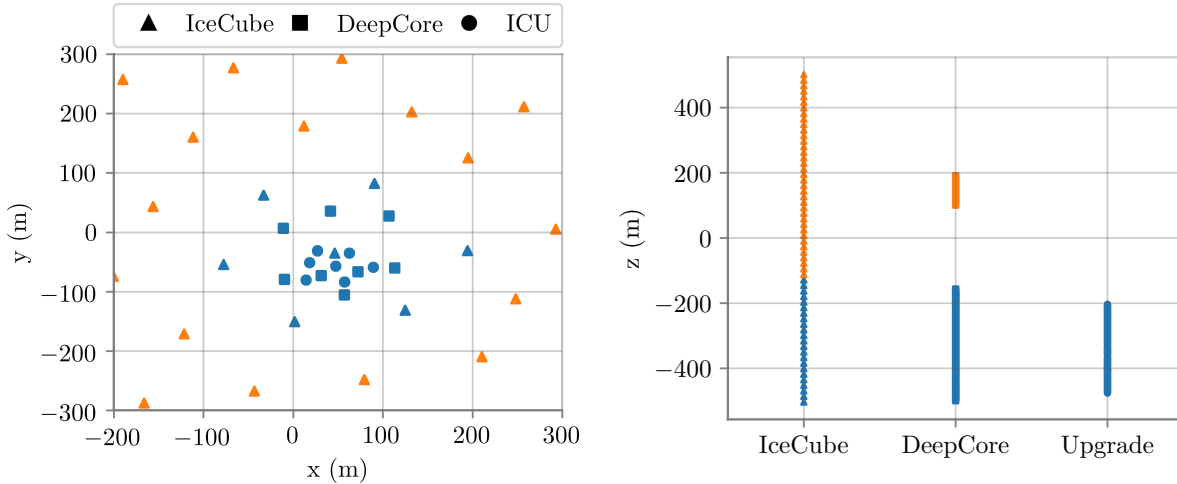


Figure 8.1: Representation of the geometry used in simulations in this chapter. Modules that form the fiducial volume are shown in blue, while modules considered to be the veto region are shown in orange. IceCube coordinates are used, where depths are relative to the center of IceCube (1948 m deep). **Left:** top-view, showing the area covered by the fiducial volume. **Right:** depths that are included in the fiducial volume for a string of each subarray. The IceCube string shown here is one of the strings within the fiducial area defined in the figure on the left.

After that, the filter algorithm can be run as a first step to reject background events. This algorithm is explained later in 8.3.1.

8.2.1 Geometry

The IceCube Upgrade geometry design has been modified several times during the realization of this thesis. This chapter is based on simulations performed using the geometry version named *v53 mixed*, which was the most up-to-date version of the geometry design when the study was started. The position of the ICU strings are shown in Figure 8.1. The geometry file contains IceCube, DeepCore and the modules in the physics region of ICU, equipped pDOMs, mDOMs and D-Eggs. Note that this geometry, currently outdated, does not include ICU modules in the *calibration* region. Current ICU design includes modules more sparsely distributed outside the physics region at depths similar to DeepCore, composed mostly of pDOMs¹, to perform calibration studies and to be used as a muon veto for ICU [23]. It is worth noting that the lack of optical modules in the calibration region may negatively impact the results of this chapter, as their inclusion is expected to enhance the muon rejection capability. The definition of the *fiducial* and *veto* regions considered in this chapter is also shown in Figure 8.1. The fiducial region is taken just as the DeepCore fiducial region but includes ICU modules. This distinction aims to identify neutrino events that interact within the most sensitive part of the detector for low-energy analysis from incoming muon events, and is later used in this chapter for event classification.

¹Also WOMs, LOMs and other modules will be included here to be tested for IceCube-Gen2. ICU might also include a second, smaller calibration region at deeper depths.

8.2.2 Simulation of neutrinos

The simulation of neutrino events has been done using *GENIE* [220], a module of IceTray. GENIE is a Monte Carlo generator of (anti)neutrinos from MeV to PeV. Since many different physical processes are relevant within this broad energy range, GENIE includes different physical models that cover nuclear cross sections and hadronization models and chooses the corresponding one depending on the energy. The interaction of neutrinos with nucleons in the few-GeV region, a regime that is used in this study and is also of highest interest for oscillation analyses, is a challenging region, since it is a *transition* region between different models. While neutrinos interact with a single quark inside a nucleon at $E_\nu > 10$ GeV, at lower energies the interaction can be approximated as the neutrino interacting with the whole nucleon (impulse approximation [221]) and it is more sensitive to the nuclear medium in which the nucleon resides [220]. Therefore, for neutrino energies above 10 GeV, the neutrino-nucleon data model is employed, while lower energy interactions also incorporate nuclear models that were developed for other probes, such as electron scattering [220].

The (anti)neutrinos have been generated in all flavors, coming from all directions and propagated through the simulated volume. The simulation was already done focusing on a sub-volume containing IceCube Upgrade, DeepCore and the closest strings of IceCube. Events for each flavor have been generated from 0.1 to 1000 GeV with a power law function $\propto E^{-\alpha}$ for a total number of events of $9 \times 10^7 \bar{\nu}_e^{(-)}$ with $\alpha = 2.0$, $2.25 \times 10^8 \bar{\nu}_\mu^{(-)}$ with $\alpha = 1.7$ and $1.8 \times 10^7 \bar{\nu}_\tau^{(-)}$ events with $\alpha = 1.5$, with a $\nu/\bar{\nu}$ ratio of 70/30 for each flavor. Then, weights have been stored according to an atmospheric neutrino flux calculated within IceTray from [222] assuming a normal hierarchy oscillation scenario.

Although atmospheric neutrinos are part of the background for this kind of study, this chapter will focus on selecting as many atmospheric neutrino events as possible while rejecting atmospheric muons or events solely produced by noise in the detector. This allows us to later weight the remaining neutrino events with any desirable flux and calculate the expected signal. Since the signal afterwards will be weighted with power laws similar to that of atmospheric neutrinos, optimizing the neutrino selection with the atmospheric flux is a valid approach.

8.2.3 Simulation of atmospheric muons

The atmospheric muon MC data set is generated using the *MuonGun* event generator within IceTray. While some popular tools such as *Corsika* [223] generates complete air showers, MuonGun directly generates single atmospheric muons. The events are generated using two cylindrical volumes centered in DeepCore. Events are generated from the outer volume, and those that do not reach the inner volume are directly eliminated in this step. The muons are produced following an energy distribution proportional to E^{-4} from 100 to 5000 GeV. Although these are much more energetic than the simulated ν sets, muons lose energy while propagating. Thus, muons are generated with a higher energetic spectrum, so that when these events reach the ICU volume, they have lower energies and leave signatures similar to those of low-energy neutrinos interacting in it. A sample of muon events 5×10^7 is generated, after which a corresponding weight [224] is calculated to transform the number of events into an atmospheric muon rate.

8.2.4 Noise generation

As previously mentioned, this chapter refers to the background generated internally by the detector modules as *noise* for simplicity in writing. This includes radioactive decays from the vessel glass and the PMT dark rate.

For the (anti)neutrino and muon MC data sets explained above, noise is simulated and added to the pulses. In addition, there is the possibility that the detector would produce a signal entirely from noise that would pass triggers and filters, and make its way into the final sample. This is especially true for low-energy studies, where noise might easily be confused with a signal. Consequently, simulations of noise-only events in the detector are done and are included in this analysis.

For both the simulation of detector noise-only and noise generation for neutrino and muon events, the *Vuvuzela* IceTray module is used. *Vuvuzela* includes both thermal and nonthermal noise that arises from decays in PMT and glass of modules, with its subsequent scintillation. It is important to note that the *Vuvuzela* code used for the simulations in this chapter does not include correlation between different PMTs, since each PMT noise rate is sampled separately from fit functions. The current implementation in *Vuvuzela* that is capable of handling correlations between different PMTs, accounting for the detection in several PMTs of, for example, radioactive decays in the vessel glass, is much slower and currently unable to generate a sample large enough for this study in a reasonable time. Thus, the older implementation of *Vuvuzela* is used to generate the background for the modules. This also does not include the higher PMT dark noise rate found in the delivered mDOM PMTs, since the simulation data set was produced prior to that.

After noise is simulated, the triggered events are maintained and undergo the same processes as the signal events. Including noise in the particle simulation is not computationally expensive, since it only needs to be calculated for a *livelime*¹ around the event trigger (generally up to a few microseconds for GeV events); however, to simulate noise-only events requires long detector livetime simulations and is computationally very costly. The data used here simulate one day of detector livetime, which is a compromise between computing resources and the statistical significance of the data. Ideally, a longer detector livetime could be simulated, so that less common events which might make its way to the final sample would have a higher probability to show up. Because this study is centered on ICU, only the noise produced in ICU, DeepCore, and their vicinity IceCube modules is simulated.

8.3 Selection of low energetic neutrino events in Upgrade

This section describes the steps undertaken to select neutrinos over other background events. As stated before, the atmospheric neutrinos sample is used to select this over the background from the module and over the atmospheric muons, although once the final signal is assumed, the atmospheric neutrinos is also part of the background for this study.

The selection of neutrinos and rejection of background follow a few common steps, in

¹Time of detector operation that has been considered or, in this case, simulated.

which a Gradient Boost Decision Tree (GBDT), a machine learning technique, is applied several times:

1. The filter, which will be described in 8.3.1, is applied to all events, eliminating those that do not pass it.
2. The first set of variables is calculated for all events that survived the filter. These are variables that are fast to compute for large datasets.
3. The sample after filter is used to train the GBDT to distinguish between neutrinos and noise, using variables calculated in the previous step. A threshold on the output of the GBDT is chosen and used to cut the event samples.
4. The remaining sample after the first GBDT selection is used to train the GBDT to distinguish between neutrinos and atmospheric muons from the variables calculated in the first step. Again, a cut from this GBDT output is made.
5. The second set of variables are calculated for all remaining events. These variables take slightly longer to compute than the variables in the first set, thus they are calculated at this step where the event rate is lower.
6. The remaining sample after the first two selections is used to train the GBDT, again to select neutrinos over atmospheric neutrinos. This training uses both the first and the second sets of variables. A cut using this GBDT is done, and the survival sample is the final rate.

Each time the GBDT is applied, always in a binary way, the events are classified according to a final score. Thus, a threshold on this score must be chosen to properly classify the events. This opens up a lot of possibilities. Because three GBDTs are applied, the performance of each consecutive one depends on the input sample, which varies depending on the threshold chosen in the previous step. However, the best combination of variables to use in each iteration can also change depending on the threshold decided in the previous step. Thus, fully optimizing the complete selection is a very complex problem that, due to the time needed for each training and the posterior checks, is not fully solved, since there is always room for little improvement.

After the event selection is made, an analysis searching for a signal using the survival events is performed. In this chapter, time windows of $\Delta t = 3$ s and $\Delta t = 1000$ s for signal detection will be assumed, following the same approach as in [217]. The shorter time window accounts for the search for a prompt signal between $[t, t + 3$ s] while the longer time window is based on the precursor and afterglow electromagnetic data of GRBs [225] as $[t - 500$ s, $t + 500$ s], with t being the absolute time of the merger reported from the gravitational wave detection. Because the searches in this chapter will be shown for two very different time windows, the threshold choice of each selection is not necessarily the same in both cases. Indeed, when considering the shorter time window, the last iteration of the GBDT is no longer necessary, and the final sample is obtained just after the fourth point enumerated above. For simplicity, the full selection process described above is explained considering the longer time window, named **Selection A**, while the selection focused on the shorter time window **Selection B** is shown only afterward. Both selections use the same combination of variables and only change in the chosen threshold values.

8.3.1 Triggers and filters

As mentioned above, IceCube calculates a set of trigger conditions to determine if there was an event detected, around which a time window is opened to encompass the detected light from such an event. Different triggers are assigned depending on the detection, and they are calculated directly online. Triggers require conditions based on modules detecting the signal within a certain time window, chosen depending on the detector geometry where the trigger occurred, or volumetric conditions. The only trigger required for the events in these simulations is the so-called SMT3, which stands for single multiplicity trigger of, at least, 3 HLC [89] (hard local coincidence) hits occurring in either DeepCore, ICU, or DeepCore + ICU. HLC pulses are those that satisfy the requirement that another pulse in a neighboring module (defined as two above or below) is detected within $1 \mu\text{s}$.

After being triggered, the events run through the filter algorithm, which cleans the signal from the most obvious muon events. To use the filter, a cleaning algorithm is first performed, which creates a new subset of pulses that are less likely to be related with noise produced by the modules themselves. In this way, the hits on the detector are classified into *clean* pulses (CP) or *unclean* pulses (UP), the unclean pulses being the complete pulse data saved after the trigger. The clean pulses are created by the *Seeded RT-cleaning* algorithm in IceTray, which selects the pulses according to the geometric and time correlation between them. The algorithm begins with the HLC pulses (the seed). Then, around each module with such pulse, a sphere of a certain radius R_t is drawn, in which pulses within a time window ΔT_t are selected. This process is repeated recursively, using the output of the previous iteration as the next seed, until no additional pulses are identified. R_t and ΔT_t depend on the sub-detector, and have been chosen as:

- IceCube pulses: $R_t = 150 \text{ m}$ and $\Delta T_t = 1000 \text{ ns}$.
- DeepCore pulses: $R_t = 80 \text{ m}$ and $\Delta T_t = 500 \text{ ns}$.
- ICU pulses: $R_t = 40 \text{ m}$ and $\Delta T_t = 250 \text{ ns}$.

Then, the DeepCore filter algorithm is used to reject atmospheric muon events. The filter works by separating the modules into fiducial and veto modules and then looking for causally connected pulses that occur outside the fiducial region (see Figure 8.1). The algorithm first calculates the mean average time of all fiducial hits. This is used to do a hit cleaning, removing all pulses outside one Gaussian standard deviation around the mean. From this pulse sub-sample, the center-of-gravity (CoG) is calculated, which is simply the average position of all cleaned pulses within the fiducial volume¹. With the central position and central time, the algorithm checks the hits in the veto region for causality. A hit i is considered causally connected to the triggered event if it satisfies the following criterion:

$$0.25 \text{ m/ns} \leq \frac{|\vec{r}_{\text{CoG}} - \vec{r}_i|}{t_{\text{CoG}} - t_i} \leq 0.4 \text{ m/ns}, \quad (8.1)$$

which identifies muons entering the fiducial volume after leaving a signature in the veto region based on assuming the particle travelling close to the speed of light ($c \approx 0.3 \text{ m/ns}$).

¹In this chapter, the CoG has been calculated without weighting by the charge and using only the first HLC hit in each module.

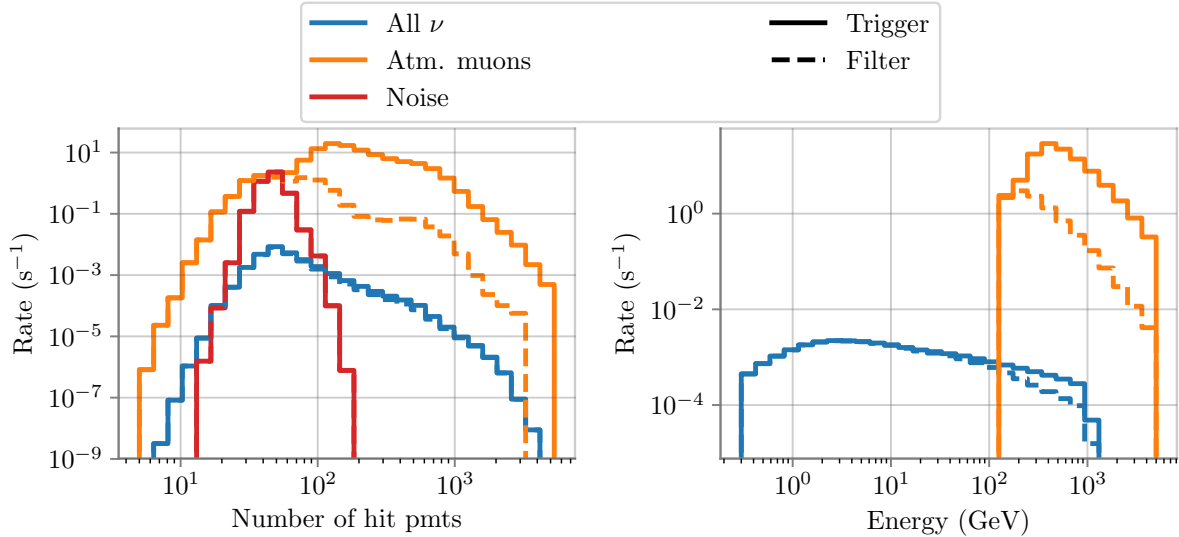


Figure 8.2: Rates of each sample after trigger (solid line) and filter (dashed line) levels, as a function of the number of PMTs that have detected light (**left**) and as a function of the MC true energy (**right**). Note that the lines for the trigger and filter levels for the noise-only simulation set mostly overlap.

Table 8.1: Rates of atmospheric muons, noise and atmospheric neutrinos after trigger and filter levels for each simulated sample.

Rates ($\times 10^{-3} \text{ s}^{-1}$)	Atm. muons	Noise	All ν	$\nu_e + \bar{\nu}_e$	$\nu_\mu + \bar{\nu}_\mu$	$\nu_\tau + \bar{\nu}_\tau$
Trigger level	1.05×10^5	4.10×10^4	29.06	8.62	19.51	0.94
Filter level	1.01×10^4	4.09×10^4	26.71	8.39	17.41	0.91

If one or more hits in the veto region are identified as causally related to the CoG, the event is rejected.

The sample after the simulated events have been triggered and passed through the filters, is shown in Figure 8.2 as a function of the number of PMTs that have detected light and of the Monte-Carlo energy of the particle. The first is chosen as a quantity that allows to visualize how large the detection pattern was and to include the noise sample in the figure, which is not possible when showing the energies. It can be observed that the filter rejects a large portion of the atmospheric muons, accounting for around 90% of all atmospheric muons passing the trigger, although it is less effective in the lowest energy region. The filter also wrongly rejects a portion of the neutrino events, mostly in the higher energetic region of the simulated sample, due to the higher probability of having hits within the veto region when the events emit more Cherenkov light: 91.9% of all triggered neutrinos pass the filter. Regarding noise simulations, about $\sim 99\%$ of the events pass through the filter, which is no surprise since the whole noise-only simulation already focused on the fiducial volume for generation.

In Table 8.1, the rates of each simulation sample after trigger and filter are shown, from which the variables to train the GBDTs will be calculated. Although the filter has substantially reduced the rate of atmospheric muons, the neutrino signal still lies several orders of magnitude below the background rate at this level.

8.3.2 Gradient boosting decision trees (GBDTs)

The general goal of any Machine Learning (ML) algorithm is to recognize patterns in the data and use them to give a score or probability that becomes a decision [226]. All these algorithms try to converge into minimizing a *loss function*, which describes the difference between the predicted values and the true values. In recent years, the use of such techniques has increased considerably due to improved algorithms and faster computers, resulting in significant advances in areas such as image recognition or automated software. Scientists of multiple disciplines have also become increasingly interested in ML, as it has the potential to yield impressive results for certain studies. From a scientific point of view, the problem of ML algorithms lies in the opaqueness of the models to our understanding, the reason these models are sometimes not yet fully accepted by a part of the community [226].

ML algorithms can be divided into supervised training, unsupervised training, and reinforcement training algorithms. In supervised learning, the algorithm is trained on a labeled dataset to predict outputs based on input features. In unsupervised learning, the algorithm would find the data structure to train on its own, which can result in the discovery of new useful hidden patterns in the data. Reinforcement learning is a case where a dynamic environment yields constant feedback to the algorithm to perform certain tasks [226]. For the study here, a decision tree is used, a type of supervised learning ML algorithm. Although unsupervised algorithms can potentially be more powerful for these kinds of tasks, they are also less transparent.

Decision trees are ML algorithms that take a set of input features or attributes and split the input data recursively based on those features. These are based on extending simple cut-based analysis into a multi-variable technique by continuing to analyze events after they fail a particular criterion; thus, they allow re-evaluation of otherwise rejected events [227]. In this chapter, where a binary case of separating signal from background will be conducted, this is useful for cases when events do not have all characteristics of either signal or background, which is the usual scenario. The name *tree* comes from the graphical representation of the decision scheme, where each decision divides the tree into different nodes or *leaves*. If the signal is more dominant in one leaf, then this becomes a signal leaf. The decision tree used here is *LightGBM* [228], a Gradient Boosted Decision Tree (GBDT) algorithm. GBDTs combine decision trees with a technique called boosting. This starts with a single tree where unweighted events¹ are classified. For each misclassified event, its weight is increased (boosted). A second tree is then built using the new weights, which are no longer equal, and the process is repeated. Hundreds or thousands of trees can be built this way. Then, each event is followed through each tree, and a score of 1 or -1 is assigned depending on it landing on a signal or background leaf. The renormalized weighted sum of all scores is the final score of the event, where high scores mean that the event is more likely to be signal and vice versa [227]. This process is depicted in Figure 8.3. While each tree on its own is a *weak* model, the final combination is a solid one. The term gradient comes from the way the loss function is minimized. This, often a complex problem, is simplified by minimizing the negative gradient between consecutive steps in these algorithms [229].

¹Or events with their nominal weights.

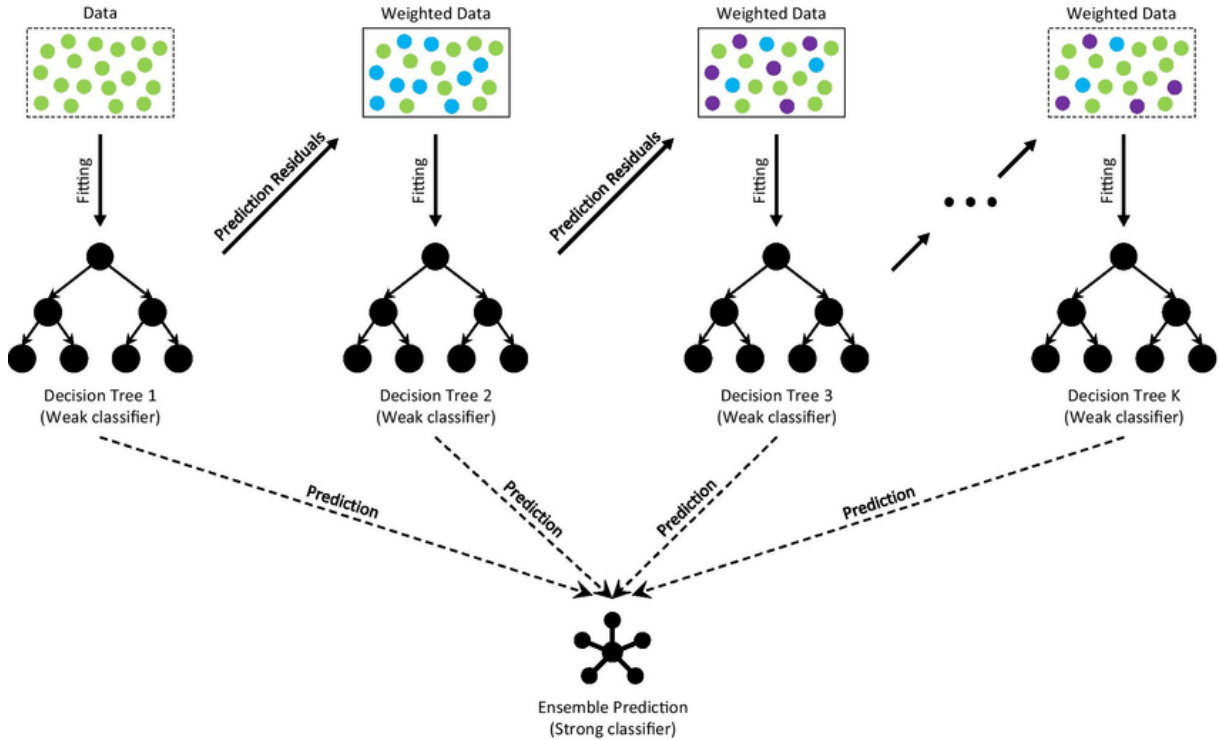


Figure 8.3: Sketch showing the architecture of gradient boosted decision trees. Note that, using LightGBM, trees may grow leaf-wise, thus splitting only some leaves (or a single one) in each level within the tree. Figure from [230].

8.3.3 GBDT configuration

Part of the work in this chapter consists of ensuring that the GBDT works as desired, for example, by avoiding *overfitting*. Overfitting is found when the model is too close to the particular set of training data from which it is derived. This means that the model cannot fit additional data or predict future observations reliably. The typical way to check if the model is overfitting is to randomly separate the data into *train* and *test* samples. The train sample is then the data that is used for training, while the test sample is used to verify the behavior of the train sample. When overfitting, the train sample would return better results than the test sample. The model can also be *underfitting*, which means that it is not complex enough to describe the data. This is easily noticeable because the model would either perform poorly in accurately selecting neutrinos or simply not converge.

After some tests, it was found that the algorithm performed well when using the following parameters, equal for each GBDT used in the chapter:

- The maximum depth of each tree is limited to $m_d = 6$. Higher values would make the algorithm slower, but potentially more effective. However, by limiting the depth of the tree, the tendency of simple decision trees to overtrain when they grow to a large depth is almost completely eliminated. This allows to increase the number of variables used without the risk of overfitting and reducing the impact of weak variables on the final selection [231, 232].
- Number of leaves = 25. This is the maximum number of nodes per tree and the main parameter that controls the complexity of the model; when it is set too large, it would

induce overfitting, which generally starts to appear when the number of leaves gets close to 2^{m_d} [228, 232].

- Max. number of bins set to 32. LightGBM bins the data into histograms and finds the optimal split point. A higher number of bins may induce overfitting, whereas a low number would result in underfitting [232].
- The minimum data in each leaf are set to 500, which should be sufficiently low for the number of events that each iteration contains and deals with variables with, for example, *NaN* values¹, and at the same time preventing overfitting. This would avoid using a feature on a leaf if the remaining data does not have at least 500 valid entries [228, 232].
- Feature fraction = 0.7. This is the subset of features that each tree node uses, which are selected at random [232].
- Minimum gain to perform a split = 2. Gain is defined as the reduction in training loss resulting from the addition of another split point. High values are used to speed up the training time, whereas low values in practice may not have a significant impact on the accuracy of the model [232].
- $\lambda_{l1} = 2$, $\lambda_{l2} = 1$. These are regularization parameters to avoid overfitting [232].

Some parameters are set to conservative numbers to speed up the convergence. These are useful when many parameter spaces are compared, meaning in our practical case training several times with different variables to compare the models and see which one performs better. This has been done many times during this work; thus, efficient hyperparameter optimization is important. However, it has also been tested that using a set of less restrictive parameters and making the algorithm slower does not significantly improve the final results. Regarding the parameters controlling overfitting, similar tests have been performed that verify that getting closer to the overfitting limits does not considerably improve the final selection power. The split of events between the train and test samples is of 0.5, since there are enough events in each state that it is not necessary to modify this value.

8.3.4 Selection of neutrinos over the noise of the modules

At this stage, the first set of variables to train the GBDTs is calculated for all events after the filter level. These are variables that are fast to compute and are based on simple positional and temporal relations. Most of these variables are currently used for event selection in DeepCore, with some small modifications to a few of them done here. Other new variables have also been added, which are mostly focused on the possibilities given by the new optical modules.

Furthermore, two new subsets of pulses are calculated based on local coincidences (LC), named *InterLC* and *IntraLC* pulses. *InterLC* searches for coincidences within the same string between different modules. The algorithm iterates over all pulses in the chosen pulse set and, for each pulse, saves the pulses within a certain time window in N modules above and below the current one. If no other pulses meet the criteria, the current pulse will not be saved. Here, it has been chosen $N = 2$ and a conservative time window of 100 ns. *IntraLC*

¹The algorithm can use variables that contains Not a Number (NaN) values. This occurs when a variable can not be calculated for all events. For example, later some variables will be calculated from pulses selected solely from mDOMs. If an event was not detected by any mDOM, it will have a NaN value here, but the variable is still usable for the other events.

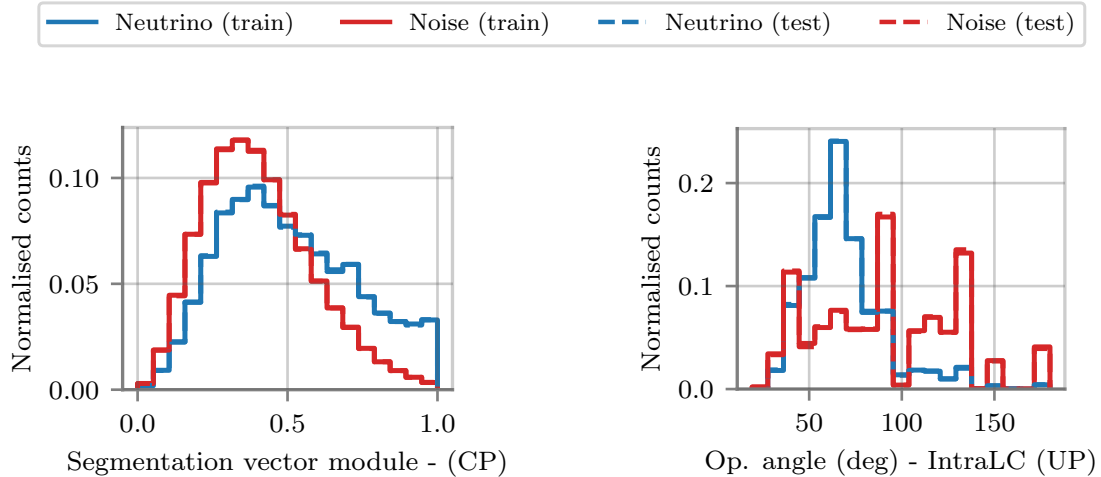


Figure 8.4: Two of the variables used in the GBDT trained to separate neutrinos from noise, considering noise all the background generated internally by the modules and the PMTs themselves. The train and test samples for each class (neutrino or noise) are displayed, although it is difficult to discern any differences as the lines mostly overlap. **Left:** module of a vector obtained by weighting the direction of each PMT in mDOMs with the detected charge from the clean pulse (CP) set. **Right:** mean opening angle of PMTs detecting light within each segmented sensor from the IntraLC pulse set, calculated from the unclean pulses (UP).

searches for coincidences between PMTs within the same module (IntraLC), similarly to what was done in Chapter 6. This is obviously only applied to mDOMs and dEggs, and the same time window of 20 ns than in Chapter 6 is used, which also proves to cover most of the light in this case.

Some variables that try to directly use the direction of the PMTs in mDOMs have also been calculated. Although many variables based on the modules segmentation were calculated, only a few ended up being powerful enough to separate neutrino events from atmospheric muons or noise. The reason is that only a type of module, the mDOM, has a considerable segmentation, thus the number of available hits to calculate these variables are lower than when more general variables are calculated. Still, some of these variables proved to be useful in the selection process, and will be showcased when they are used.

After calculating the variables, the GBDT is trained in order to separate signal events from the noise produced by the modules. The atmospheric muon sample is not included in the training at this step. The variables to train the model are chosen after testing the performance of the GBDT with different combinations, evaluating which variables has a higher impact on a correct event selection and discarding the weakest ones. In order to avoid an excessively large number of figures, only a few of these variables are shown at each stage of the selection process. These variables may be of particular interest or introduce new concepts related to the use of the new optical modules, for example. The remaining variables can be found in the corresponding appendix, which will be referenced at each stage of the selection process for those readers who wish to view them all. The variables are calculated with both the clean pulses and the unclean pulses sets. Sometimes variables are more efficient for selecting neutrino events when calculated using clean pulses, while sometimes unclean pulses perform better.

Two of the variables on which the GBDT is trained are shown in Figure 8.4. Although these are not the most powerful variables performance wise, they are shown because of directly using the modules segmentation. The variable shown on the left is the module of a vector calculated summing all PMT directions in the mDOMs that detected the events weighted by the charge, 0 meaning that the distribution of charge along the mDOM PMTs cancels and 1 meaning that the entire light was detected by the same PMT. This does not refer to a single PMT on a single mDOM, but the same PMT on all mDOMs that detected the event¹. The variable shown on the right-hand side of Figure 8.4 represents the mean opening angle of the PMTs that detect the event using the IntraLC pulse set. The opening angle is simply defined as the angle difference between the PMTs involved in the detection for each module, and the average for all modules detecting the event. Thus, this is the result of the sum of discrete values and as such the resulting distribution shown in the figure does not show a continuous pattern. Note that the variable on the left considers all detected hits from the clean pulse set to calculate the vector, while the variable on the right only uses the hits from the clean sample that met the intra-module condition to compute the opening angle. Both variables relate the events with the distribution of light detected in different PMTs, showing that the noise and signal events can be distinguished by the signature detected in segmented modules. However, their separation power is limited by the fact that this is only calculable for a subset of modules. The variables used for this GBDT are briefly described in the following:

- **Total charge:** total charge included in the pulse set.
- **Segmentation vector module:** Module of a vector created after summing all PMT directions in the mDOMs that detected the events, weighted by the charge.
- **Time spread:** spread of all detected times from the time of the CoG, calculated as $\sqrt{\sum (t_i - t_{\text{CoG}})^2 / (N - 1)}$, where N is the size of the sample and i each detected pulse.
- **Pos. vector sum:** length of the vector constructed with the positions of all modules detecting the event with respect to the center of the detector, chosen as the position of string 36 at the mean depth of the ICU physic region.
- **Depth spread:** spread of depths of modules detecting the event, calculated as $\sqrt{\sum (z_i - z_{\text{CoG}})^2 / (N - 1)}$, where N is the size of the sample and i each detected pulse.
- **Time $X\%$:** time needed to accumulated $X\%$ of all detected charge.
- **QR6:** ratio between the accumulated charge within the first 600 ns to all detected charge.
- **C2QR6:** same as QR6, but ignoring the first 2 hits, which are often related with noise. -1 if it can not be calculated.
- **Av. dist. from 36:** average distance of all modules detecting the event with respect to the center of DeepCore, chosen as the position of string 36 at the mean depth of the ICU physic region.
- **Av. dist. between hits:** average distance between modules detecting the event.
- **Fill ratio:** fraction of hits with positions inside a sphere with respect to the first HLC hit. A sphere of size $1.6\times$ the mean distance between each hit and the vertex is used.
- **Op. angle IntraLC:** mean opening angle of PMTs detecting light within each segmented sensor from the IntraLC pulse set.
- **Total depth:** difference between the deepest and the shallowest module detecting the event included in the corresponding pulse set.

¹Note that the geometry in the simulation assumes all mDOMs to be perfectly aligned.

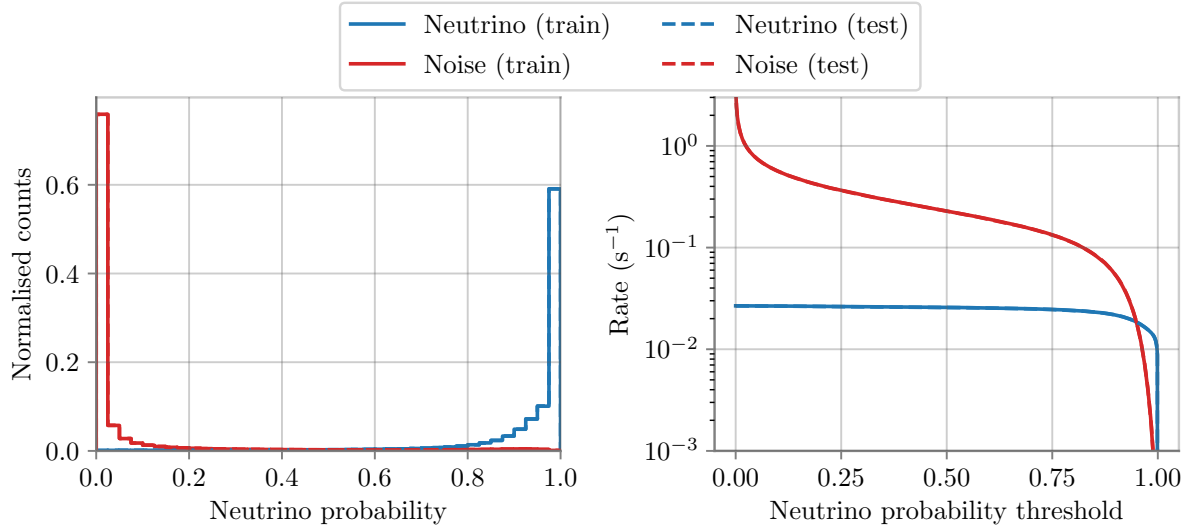


Figure 8.5: Results of the GBDT trained to separate neutrinos from noise, considering noise all the background generated internally by the modules and the PMTs themselves. The train and test samples for each class (neutrino or noise) are displayed, although it is difficult to discern any differences as the lines mostly overlap. **Left:** Histogram showing the neutrino probability score given by the GBDT for each set (train or test) of each class. **Right:** Rate of surviving events depending on the threshold choice for each set and class. Note that the rates have been normalized considering the split in test/train.

The corresponding figures for these variables can be found in the Appendix B, where it is indicated which pulse set is used in each case.

The performance of the GBDT with the chosen variables at this stage is shown in Figure 8.5. On the left side of the figure, the events of each class are binned as a function of the neutrino probability that was assigned by the GBDT. The neutrino probability is the output of the GBDT scaled between 0 and 1, where 0 means that the event is very likely to be noise and 1 to be neutrino. It can be seen that the neutrino data peaks at values close to 1, while the noise distribution peaks at 0, which means that the algorithm is successful in identifying each type of event. Although the train / test split for each class is 50%, the rates given in the figures take into account the number of events; thus, it shows the equivalent total rate. The similarity in behavior between the train and test samples of each class indicates that the algorithm is not overfitting. On the right-hand side of Figure 8.5, the curves show the rate of each sample depending on the threshold value chosen for the neutrino probability output of the GBDT. The rate of noise decreases much faster with increasing the threshold, but remains much higher than the neutrino rate up to very high thresholds.

To decide on the threshold level to apply the cut to the samples, different considerations can be made. A common way to decide on the threshold is to consider the behavior of the true positive rate (TPR) versus the false positive rate (FPR), the so-called ROC curve shown on the left-hand side of Figure 8.6. These quantities are calculated as

$$\text{TPR} = \frac{\text{TP}}{\text{TP} + \text{FN}}; \quad \text{FPR} = \frac{\text{FP}}{\text{FP} + \text{TN}}, \quad (8.2)$$

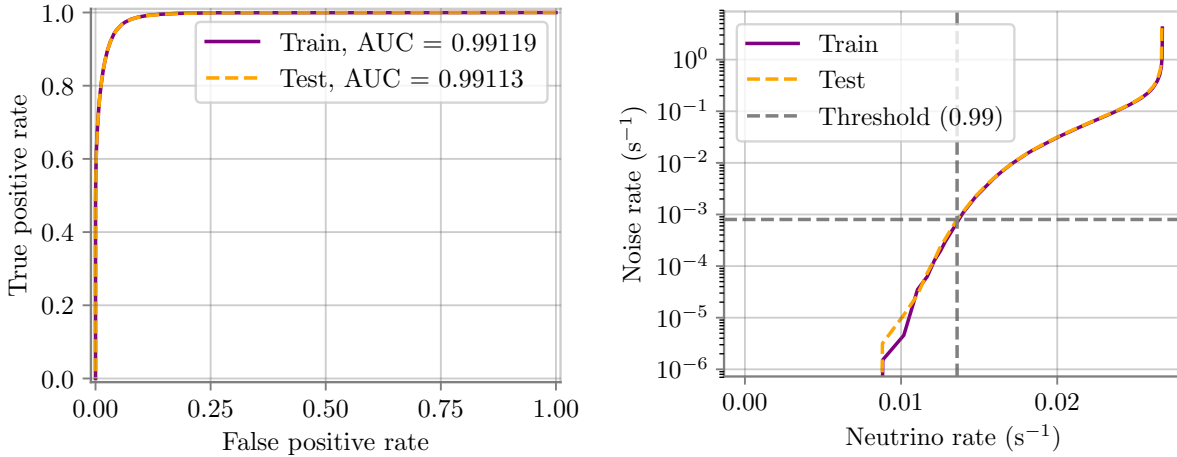


Figure 8.6: Results of the GBDT trained to separate neutrinos from noise, considering noise all the background generated internally by the modules and the PMTs themselves. **Left:** True Positive Rate (TRP) plotted against the False Positive Rate (FPR), with the Area Under the Curve (AUC) value shown in the legend for each set. **Right:** rate for each class type after applying a certain threshold, with the chosen value at a threshold of 0.99 marked by horizontal and vertical lines on the test sample.

with TP being the true positive, FN the false negative, FP the false positive and TN the true negative events. These are the events that are assigned correctly (True) or incorrectly (False) to the *positive* class (in this case, neutrino) or the *negative* class (in this case, noise). The Area Under the Curve (AUC) for the train and test samples is shown in the legend. The AUC value is a measure of the performance of the algorithm, a maximum value of 1 would indicate a perfect separation power. Looking at the AUC, the performance of train and test samples can be compared, showing that both samples behave very similar, which indicates that the algorithm is not overfitting nor underfitting. A typical way to choose the corresponding threshold is to maximize the TPR while minimizing the FPR as much as possible, which corresponds to getting as close to the upper left corner of Figure 8.6 (left figure). However, this is not a convenient approach in this case. One must consider that the only cut focused on noise events is done at this stage. Although the cuts on muon events that is applied in the next steps will surely also cut out some noise events, in principle it is not known how much of the noise sample will be rejected by them. Thus, it is decided that the noise rate should be $< 10^{-3} \text{ s}^{-1}$, which should be sufficiently low to be much lower than the neutrino rate at the final level. Thus, the threshold is placed at 0.99, resulting in a survival rate of $0.751 \times 10^{-3} \text{ s}^{-1}$ for noise events, while the survival rate of neutrino events is $13.59 \times 10^{-3} \text{ s}^{-1}$. The noise rate versus the neutrino rate is shown on the right-hand side of Figure 8.6, where the values of the chosen threshold are indicated.

One might think that this threshold could be placed at a less restrictive value and save some neutrino events that otherwise are lost, since the rate of neutrinos has been almost cut in half by this choice. However, note that the noise rate increases rapidly when the threshold is lowered. The neutrino events that are lost with this cut are highly noise dominated, so they are hardly useful in any analysis. This also comes with most of the events lost by this cut being in the lowest part of the simulated energy spectrum, which is inconvenient for an analysis focused on very low energetic events but expected at the same time, since the ratio of signal versus noise hits in these events is generally much lower. Although the new modules have better detection capabilities, they are also noisier,

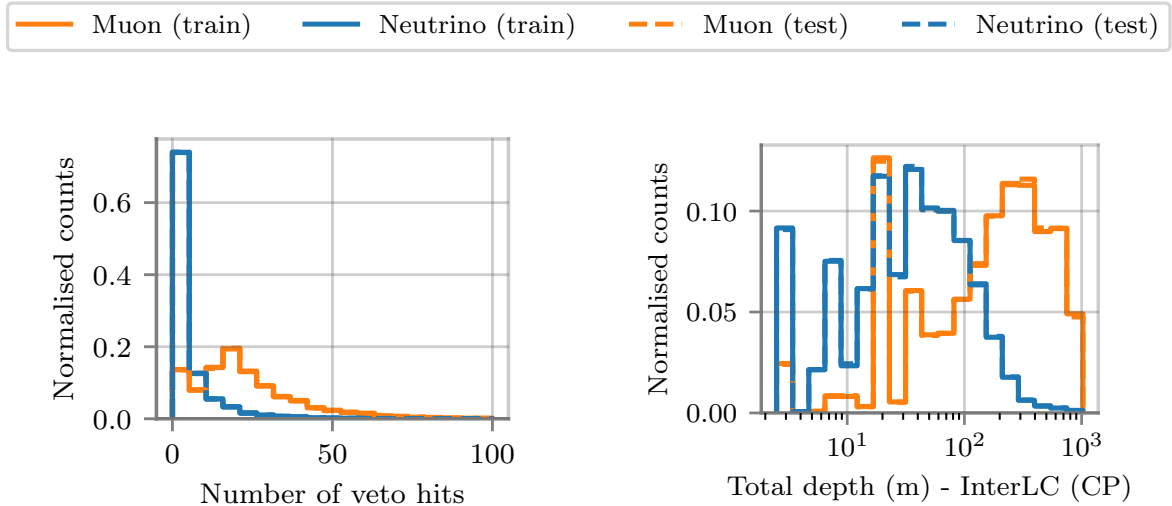


Figure 8.7: Variables from the GBDT trained for the first iteration to separate neutrinos from atmospheric muons. The train and test samples for each class (neutrino or muon) are displayed, although it is difficult to discern any differences as the lines mostly overlap. **Left:** number of hits in the veto region, defined in Figure 8.1. **Right:** total depth covered by the events from the InterLC pulse map. Note that the combination of the logarithmic scale in the x -axis, necessary to see the separation between the different event classes, and the discrete distance between modules, causes the discretization in the lower region of the x axis.

especially in the case of the mDOM.

8.3.5 First selection of neutrinos over atmospheric muons

Next, the first step for selecting the neutrino events over the atmospheric muon background is done. The previous cut reduces the atmospheric muon rate from 10.13 s^{-1} to 4.18 s^{-1} , still several orders of magnitude above the neutrino rate. For this iteration of the GBDT, the first set of calculated variables is now used, with a different choice of them to train the algorithm. The process is similar to that in the previous section, where different combinations of variables have been tested up to the final choice.

The most important variables in this step are those that focus on the positioning and spread of the modules detecting the events, in order to identify entering muons in the detector or to distinguish a track-like signature. Thus, many variables that use the previously described veto region (see Figure 8.1) are very powerful in this step, where the most obvious muon signatures are identified. As an example, on the left side of Figure 8.7, the number of hits in the veto region is shown. The atmospheric muons generally induce a lot of light in the veto volume, thus this variable is very efficient to distinguish the events. On the right side of Figure 8.7, the difference between the deepest and the shallowest hit registered in the InterLC pulse map is shown. A track-like event from atmospheric muons is often downgoing and, as such, deposits light at different depths. The whole set of variables chosen for this GBDT can be found in Appendix C. The variables used at this step of the selection are described below. Some variables used now were described in the previous step and are therefore not repeated here.

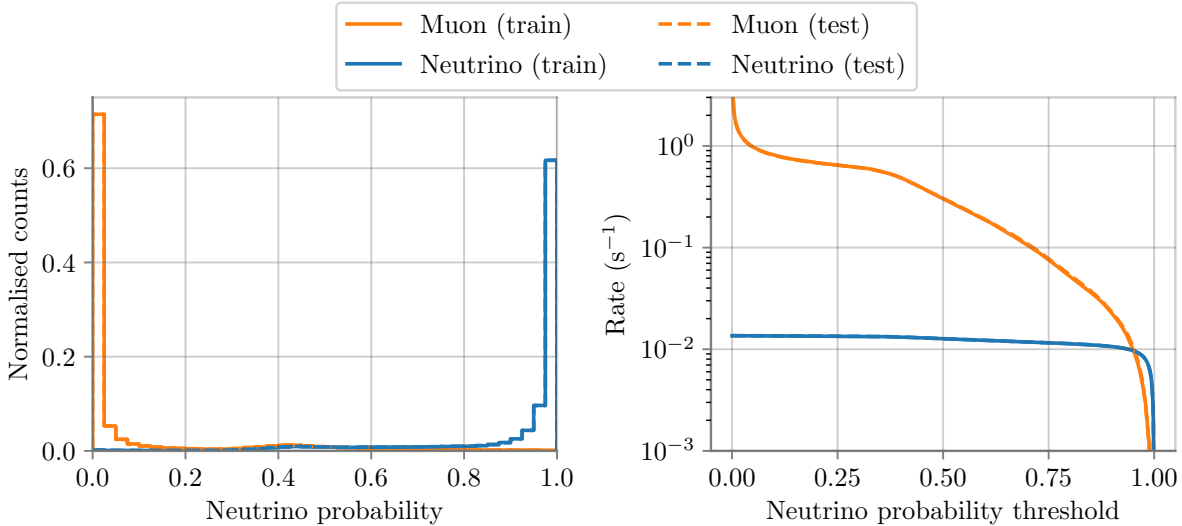


Figure 8.8: Results of the GBDT trained for the first iteration to separate neutrinos from atmospheric muons. The train and test samples for each class (neutrino or muon) are displayed, although it is difficult to discern any differences as the lines mostly overlap. **Left:** Histogram showing the neutrino probability score given by the GBDT for the two set (train or test) of each class (neutrino or atmospheric muon). **Right:** Rate of surviving events depending on the threshold choice for each event type. Note that the rates have been normalized considering the split in test/train.

- **Mean depth:** mean depth of all hits in the pulse set.
- **Depth variance:** variance of the depth distribution of all hits in the pulse set.
- **Accumulated time:** sum of time differences between the first and each other hit.
- **Number of veto hits:** number of hits in the veto region, shown in Figure 8.1.
- **Av. RMS dist. from 36:** average root mean square distance from string 36.
- **ρ first hit:** horizontal distance of the first hit from string 36.
- **First trigger boolean:** boolean variable evaluating whether the first trigger hit is either in DeepCore or ICU.
- **PMTs above -200 m:** PMTs hit above -200 m from the center of the detector.
- **PMTs above -200 m (tw=2 ns):** same, but within a time window of 2 ms
- **Charge above -200 m:** Charge accumulated above -200 m from the center of the detector.
- **RTVeto modules:** number of modules detecting events in the veto region.
- **ToI spherical ratio:** quantification of the sphericity of the tensor of inertia, calculated using all the pulses and the CoG. The closer to 1, the more spherical the signature of the event is.
- **Veto/Fiducial ratio:** ratio of veto and fiducial hits.
- **Veto causal hits:** hits in the veto region causally connected with the trigger in ICU, calculated from their spatial and temporal difference from the hit that opens the trigger in the ICU region.
- **Z travel:** vertical distance between the mean z position of the first quartile of hits and the average depth of all hits.

Although many variables are used in this step, and some of them are similar in nature and therefore correlated to some degree, it was observed that this did not induce overfitting

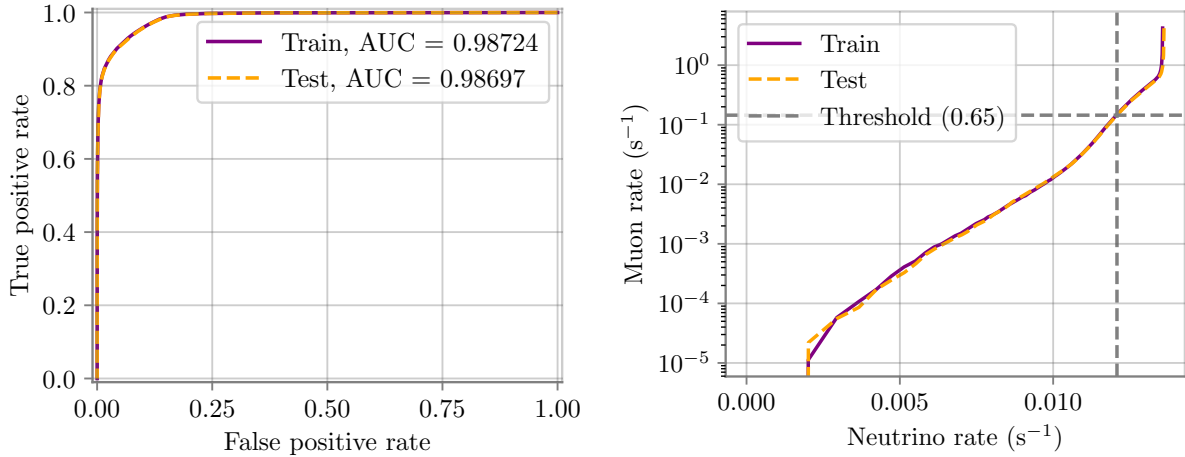


Figure 8.9: Results of the GBDT trained for the first iteration to separate neutrinos from atmospheric muons. **Left:** True Positive Rate (TRP) plotted against the False Positive Rate (FPR), with the Area Under the Curve (AUC) value shown in the legend for each set. **Right:** rate for each class type after applying a certain threshold, with the chosen value at a threshold of 0.65 marked by horizontal and vertical lines on the test sample.

due to the algorithm configuration described in Section 8.3.2. The veto is an essential element in this selection stage, as many variables rely on its information to reject muons at this stage. As a reminder, it is again stated that the geometry used in this stage does not include the new modules in the calibration region, and only the DeepCore and IceCube DOMs are used. The ICU calibration region would be included in the veto region defined above. It is safe to assume that, when simulations include these modules, the results at this stage will improve.

The performance of the GBDT for the chosen combination of variables is shown in Figure 8.8. As in the previous case, the curves for test and train in each sample mostly overlap. The algorithm shows a very good separation power, with the majority of neutrino events assigned a neutrino probability close to one, and the contrary for the muon events. On the right-hand side of Figure 8.8, it can be seen that the muon rate remains much higher than the neutrino rate for most values of the neutrino probability threshold.

The ROC curve is shown in Figure 8.9 (left). The AUC values are again very close to 1 for both samples, indicating that the algorithm can efficiently distinguish between both types of events. As in the previous case, both the train and test samples show very similar behavior, indicating that the algorithm is not overfitting. In this case, the threshold can be chosen more conservatively, since there will be another step to select neutrinos over muons later. The threshold is chosen at a value of 0.65, which is very close to the upper left corner of Figure 8.9 (left figure). On the right-hand figure, the surviving neutrino and muon rates are shown, with the values for the chosen threshold marked with gray lines. The neutrino rate after this cut is $12.06 \times 10^{-3} \text{ s}^{-1}$, while the atmospheric muon rate is $142.99 \times 10^{-3} \text{ s}^{-1}$, reduced by more than an order of magnitude. Still, the atmospheric muon rate is much higher than the neutrino rate at this stage.

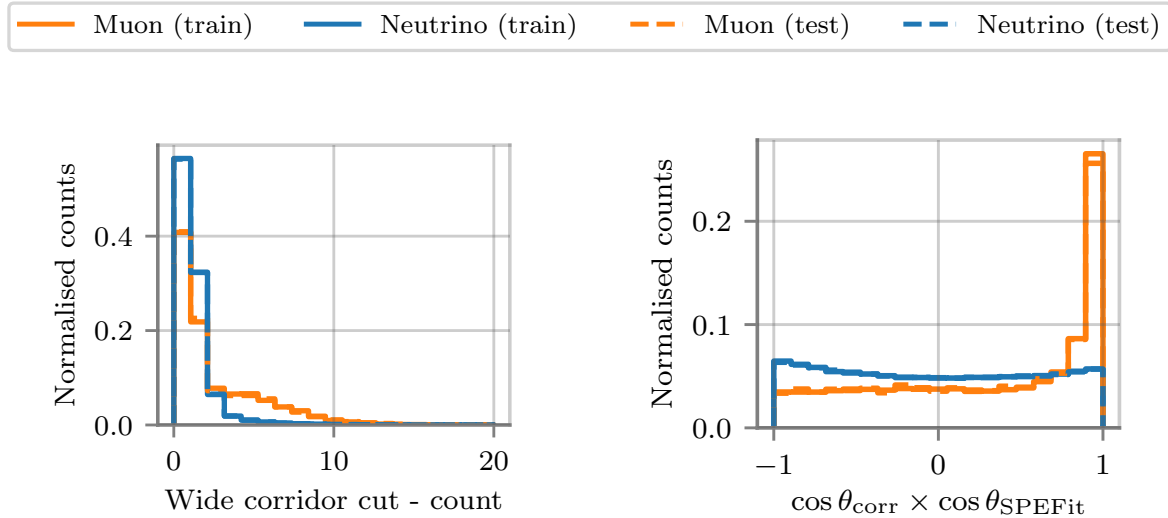


Figure 8.10: Variables from the GBDT trained for the second iteration to separate neutrinos from atmospheric muons. The train and test samples for each class (neutrino or muon) are displayed, although it is difficult to discern any differences as the lines mostly overlap. **Left:** number of hits matching the corridor track hypothesis. **Right:** product between the θ angle of the best corridor hypothesis with the SPE fit track.

8.3.6 Second selection of neutrinos over atmospheric muons

For the last GBDT training, new variables are calculated and added to the existing data, so they can all be combined and used at this step. The separation of the muon selection in two steps is done because these new variables are computationally costly to compute, therefore, it is convenient to calculate them after the event rate has been lowered. These variables focus on identifying muons entering through *empty corridors* in the detector. These corridors are simply the spaces between the strings: a muon entering the detector between strings and with the correct direction can potentially reach the fiducial detector volume without leaving a trace in the veto region. An algorithm developed for DeepCore aims at identifying these events by looping over each corridor hypothesis and selecting the most compatible one with the observed light in the detector. Thus, this is not a reconstruction even though a track hypothesis is the output of the algorithm. Different quantities of this outcome track hypothesis are used here to train the GBDT. In addition to the new variables, the process is identical to what was done before.

In Figure 8.10, two of the variables used in this GBDT are shown. On the left-hand side, the variable shows the number of hits that match the best corridor track hypothesis. It can be expected that muon events show more counts that match this hypothesis than neutrino events. On the right-hand side of Figure 8.10 shows the product of cosines of the θ angle for the best fit obtained with the corridor track and the θ angle of a track hypothesis. This track hypothesis is calculated with a relatively fast reconstruction algorithm that uses the first hit on each PMT in the clean pulses and using the so-called *Pandel function* [233]. If the track found by the corridor algorithm has a different direction than the SPE fit track, it is possible that the corridor hypothesis was made by noise rather than a muon passing through. This is observed in the figure, where the muon sample peaks at 1 more frequently than the neutrino sample. Thus, this variable is helpful to distinguish the events. The

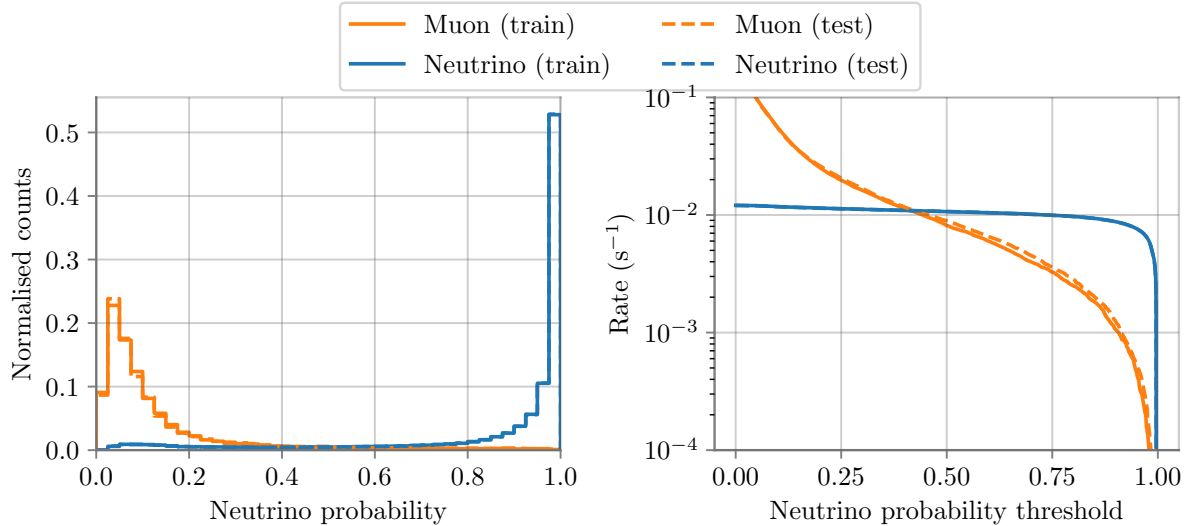


Figure 8.11: Results of the GBDT trained for the second iteration to separate neutrinos from atmospheric muons. Both subfigures show the data for both the train and the test datasets. **Left:** Histogram showing the neutrino probability score given by the GBDT for the two set (train or test) of each class (neutrino or atmospheric muon). **Right:** Rate of surviving events depending on the threshold choice for each event type. Note that the rates have been normalized considering the split in test/train.

whole set of variables chosen for this GBDT can be found in Appendix D. A brief summary of the new variables used at this selection step follows:

- **GBDT score, first muon rejection:** score from the previous step to select neutrinos over muons.
- **Wide corridor cut - count:** number of hits that match the chosen corridor track hypothesis.
- **Wide corridor cut - max. time:** time of the last hit matching the corridor muon track hypothesis.
- $\cos \theta_{\text{corr}} \times \cos \theta_{\text{SPEfit}}$: product between the θ angle of the best corridor hypothesis with the SPE fit track.

The results of the application of the GBDT at this stage are shown in Figure 8.11, similarly to the previous cases. On the left-hand side of the figure, the neutrino probability assigned to each class is visible. Two small differences can be noted comparing this case with those shown in the previous sections. Firstly, muon samples do not peak at 0 but at slightly higher values of the neutrino probability. Secondly, the lines for the test and train samples are slightly separated for the case of the muons. Both effects share the same origin: the number of atmospheric muon events left in the sample at this stage. Due to the previous cuts, the number of simulated events left for this GBDT training is of $\sim 5 \times 10^4$, while the remaining neutrino events are $\sim 1.87 \times 10^6$. Due to this large difference, the output of the GBDT is slightly biased towards the most abundant event type in the training sample. A train/test split that equalizes the number of events in the training set for each event type could mitigate this issue, but the large imbalance would still result in using nearly all atmospheric muons for training and only a minuscule fraction of neutrino events. However, this effect is not important since it is only an artificial bias, and thus it only slightly affects the threshold value that must be chosen afterward but not the performance itself.

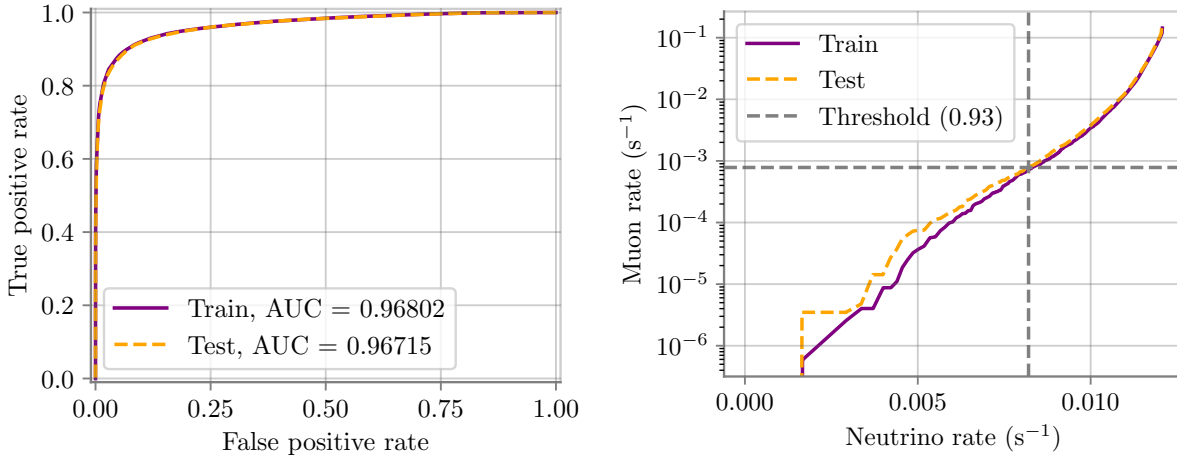


Figure 8.12: Results of the GBDT trained for the second iteration to separate neutrinos from atmospheric muons. **Left:** True Positive Rate (TRP) plotted against the False Positive Rate (FPR), with the Area Under the Curve (AUC) value shown in the legend for each set. **Right:** rate for each class type after applying a certain threshold, with the chosen value at a threshold of 0.93 marked by horizontal and vertical lines on the test sample.

Furthermore, because of the low number of muon events, the test and train samples already show small statistical differences depending on which events have been selected. The small difference between train and test here is therefore not caused by over- or under-training, since in that case the neutrino sample would also feature similar differences. It has been checked that the differences are small enough so that, by randomizing the seed to select the events in train and test sets, the GBDT performs similarly. In summary, the GBDT is working correctly; however, it would be advisable for future analyses to increase the number of simulated muon events, so that the algorithm will be more robust at this stage.

The figure on the right-hand side of Figure 8.11 shows the surviving rate of each class depending on the threshold value. The muon rate drops below the neutrino rate at probability values as low as ~ 0.45 . The discussion of which threshold to choose is again difficult to answer, and the best choice would depend on the application. A compromise must be searched, since harder criteria also mean fewer signal events. Here, a threshold value is sought that results in the atmospheric muon rate being at least 10 times lower than the neutrino rate, thus ensuring that in the subsequent physics case, where atmospheric neutrinos also constitute a background, the latter is dominated by neutrinos. However, another application might use the same selection used here and select a higher threshold value resulting in a cleaner final sample.

On the left side of Figure 8.12, the TPR versus FPR is shown again for this case, with the AUC values in the legend. Here, it can be seen that the AUC values are still very similar for both train and test samples. The AUC are slightly lower in this case than in the previous cases, indicating that these events are harder to distinguish than before. On the right side of Figure 8.12, the muon rate versus the neutrino rate is plotted for all threshold levels, indicating with lines the values for the chosen threshold at 0.93. The difference between the train and the test samples at the chosen threshold level is of $\sim 0.1\%$. This difference becomes larger for higher threshold values (thus, lower rates) due again to lower statistics. If another analysis uses this selection in order to obtain a cleaner sample and a

Table 8.2: Rates of atmospheric muons, noise and atmospheric neutrinos after each step of the event selection. Trigger and filter levels are equal for both selection approaches. Then, the selection is divided between **Selection A**, which focus on a longer time window of $[t - 500 \text{ s}, t + 500 \text{ s}]$ from the merger time, and **Selection B**, which will be used for a shorter time window of $[t, t + 3 \text{ s}]$.

Rates ($\times 10^{-3} \text{ s}^{-1}$)	Atm. muons	Noise	All ν	$\nu_e + \bar{\nu}_e$	$\nu_\mu + \bar{\nu}_\mu$	$\nu_\tau + \bar{\nu}_\tau$
Trigger level	1.05×10^5	4.10×10^4	29.06	8.62	19.51	0.94
Filter level	1.01×10^4	4.09×10^4	26.71	8.39	17.41	0.91
A - noise rejection	4.18×10^3	0.75	13.59	3.61	9.53	0.45
A - 1st muon rejection	1.43×10^2	0.48	12.06	3.19	8.47	0.40
A - 2nd muon rejection	0.72	0.02	8.17	2.32	5.54	0.31
B - noise rejection	7.12×10^3	35.33	20.37	6.04	13.64	0.69
B - muon rejection	1.48×10^2	5.29	12.90	3.52	8.94	0.44

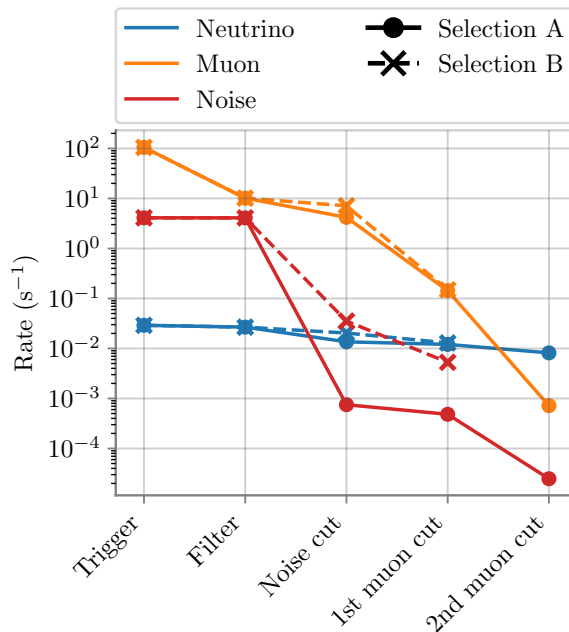


Figure 8.13: Rates after all the cuts explained in the text for each sample and each selection approach. Note that Selection B only has four levels (up to the 1st muon cut), while Selection A has five.

more strict threshold value, it would be necessary to increase the sample size. However, for the value chosen here, a $\sim 0.1\%$ discrepancy on the final rates depending on the split train / test can be accepted. After this cut, the remaining atmospheric muon rate is $0.72 \times 10^{-3} \text{ s}^{-1}$, while the atmospheric neutrino rate is of $8.17 \times 10^{-3} \text{ s}^{-1}$.

8.3.7 Background rates after the selections

The full selection stages described above are used for the **Selection A**, used for the search of signal events within a time window $[t - 500 \text{ s}, t + 500 \text{ s}]$ from the reported GW event time t . However, for the shorter time window of $[t, t + 3 \text{ s}]$, these cuts are unnecessarily strict. A much less restrictive selection is possible in this case, allowing for a higher background rate, and thus also cutting fewer signal events. For this case, named **Selection B**, the same variables are used for the GBDTs, but the thresholds are chosen at different values. The first GBDT threshold, regarding the selection of neutrinos over noise, is chosen at

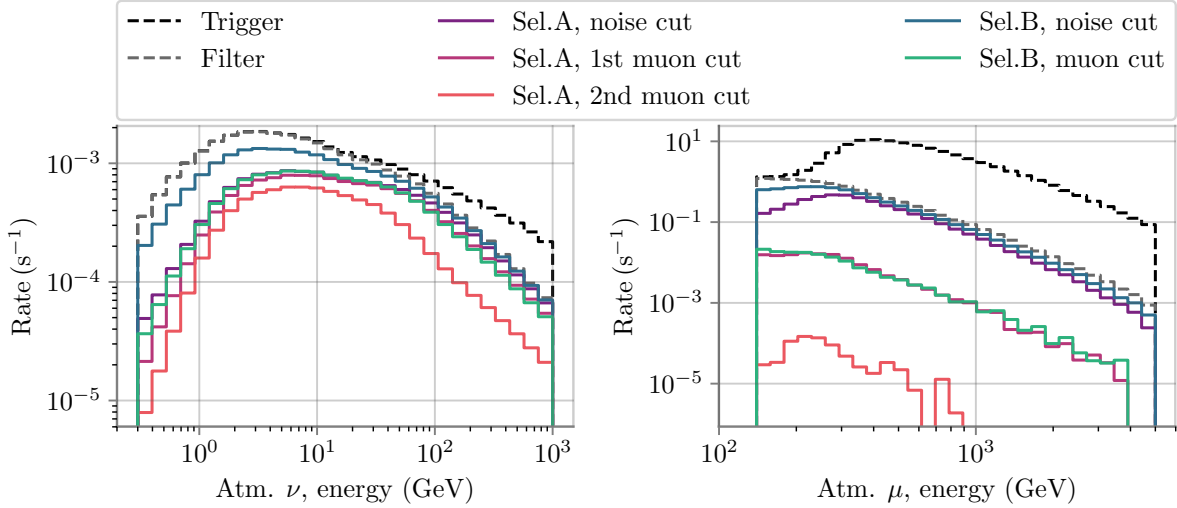


Figure 8.14: Rates after all selection steps explained in the text as a function of the MC true energy. Trigger and filter levels are common for both Selection approaches, after which Selection A or B applies. **Left:** for the atmospheric neutrino sample, combining all flavors. **Right:** for the atmospheric muons.

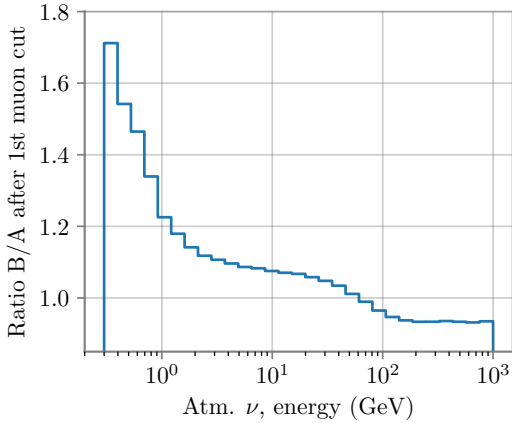


Figure 8.15: Ratio of the atmospheric neutrino rates after for each selection the first muon cut.

0.93. The second GBDT threshold, regarding the first selection of neutrinos over muons, is chosen at 0.78. The second selection of neutrinos over muons is not used here, since it is not necessary to further reduce the rate of muons or noise events in this case. Thus, the criterion for these threshold values is not to have a final background rate dominated by atmospheric neutrinos as in Selection A, since the final background expectation within 3 s is much lower and can easily be kept near 0 expected events. Thus, here it is chosen to have ~ 0.5 expected background events in the final analysis within the mentioned 3 s long time window, considering the sum of atmospheric muons and noise but also atmospheric neutrinos. This is obtained using the threshold values just mentioned to perform the cut after each GBDT.

The resulting rates after each step of each selection process are summarized in Table 8.2 and have been plotted in Figure 8.13. The rates after each step of each selection approach as a function of the energy of the events are shown in Figure 8.14 for the atmospheric neutrino sample (left) and the atmospheric muon sample (right).

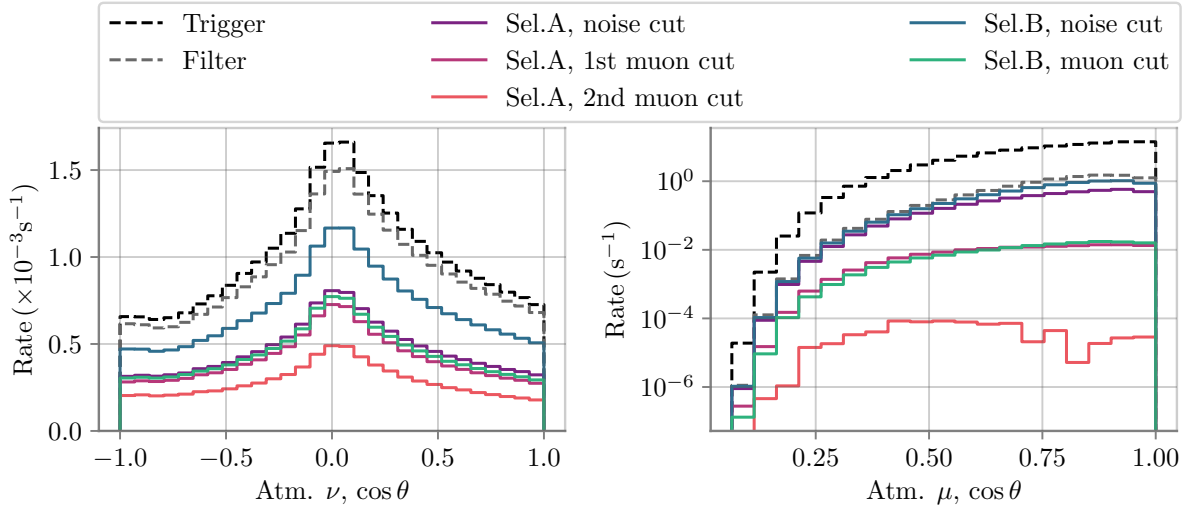


Figure 8.16: Rates after all selection steps explained in the text as a function of the cosine of the zenith angle, where $\cos\theta = 1$ stands for downgoing events. Trigger and filter levels are common for both Selection approaches, after which Selection A or B applies. **Left:** for the atmospheric neutrino sample, combining all flavors. **Right:** for the atmospheric muons.

At the final level of each selection, the event rates after Selection A are much smaller than those after Selection B, as expected from the more restrictive cuts. However, although Selection B has similar rates as Selection A after the 1st muon cut, the event distribution is slightly different. Selection B uses a softer noise cut threshold, which allows more events in the lower energy region of the spectrum to survive. This can be better seen in Figure 8.15, where the ratio between selection B and A is shown for the neutrino sample after the first muon cut (which is the only muon cut for selection B). In the case of the muon sample, it can be seen that the only events that are left after the last stage of Selection A are the lowest energetic ones, which are harder to distinguish from the neutrinos. In Figure 8.16, the direction of the particles is shown with respect to the zenith. The detected atmospheric neutrino flux is higher for $\cos\theta = 0$, which means events coming from the horizon. This is expected due to the longer path of the mesons generated in the atmosphere coming from the horizon. The longer path through the low-density atmosphere results in a higher decay ratio for mesons coming from these angles, leading to increased neutrino production [234]. On the other hand, the muon sample is only downgoing, peaking at $\cos\theta$ although flattening as more restrictive selections are applied.

8.4 Expected sensitivity to compact binary mergers

In this section, the events left after the selections explained above are used to calculate the sensitivity for detecting a transient neutrino flux generated by the merger of a compact binary system. For that, the neutrino events surviving the selection process are weighted with the assumed signal flux, and the combination of atmospheric neutrinos, atmospheric muons, and module's noise makes up for the background of the study.

8.4.1 Model flux and signal weights

The first step now is to calculate the signal flux from the surviving neutrino sample. In principle, if the merger of a compact binary system emits a flux of neutrinos, the spectrum of this flux is not known since it has not been detected yet. To compare the results obtained here with the literature, a generic power law energy spectrum with index -2 is assumed, which is a reasonable assumption considering Fermi acceleration [235]. The signal is calculated by reweighting the final neutrino sample as

$$w_i(E_i) = \phi(E_i) \frac{W_i}{4\pi N}, \quad (8.3)$$

with E_i being the energy of each neutrino. The factor N in Eq. 8.3 is a normalization factor that depends on the number of events that were simulated for each (anti)neutrino flavor. On the other hand, W_i is the original weight¹ stored in the simulation data to account for the propagation of the event through the detector and its interaction in the ice. This parameter, with units of GeVcm^2sr , is intended as a general weight that can be used to reweight the events for any desired flux. The 4π factor of Eq. 8.3 arises from the need to remove the diffuse nature of W_i , since our source is far enough to be considered a point source. The flux is assumed to follow the already mentioned power-law spectrum as

$$\phi(E) = \phi_0 \left(\frac{E}{E_0} \right)^{-\alpha} = CE^{-\alpha}, \quad (8.4)$$

with $\alpha = 2$ for the flux proposed in this chapter, with $E_0 = 1 \text{ GeV}$. ϕ_0 is then the flux at 1 GeV , with units $\text{GeV}^{-1}\text{cm}^{-2}\text{s}^{-1}$.

8.4.2 Statistical method

Now, it is necessary to calculate how many signal events must be detected in order to accept or reject the hypothesis of the detected events being associated with the merger. Thus, the flux must be scaled accordingly, so that the expected number of detected signal events is the required value. From the flux proposed in Eq. 8.4, the next step is therefore to calculate the necessary value for C , which is a constant parameter that scales the flux arriving at the detector. Here, the sensitivity will be given as the 90% confidence level upper limit (UL) that a measurement of n events was solely produced by background. The statistical analysis is done following [236] by using Poisson statistics. The probability of observing n events from an expected signal s and an expected background b is given by

$$P(n|s) = (s + b)^n e^{-(s+b)} / n!. \quad (8.5)$$

An example is useful to illustrate how the 90% UL is calculated. Consider that the expected signal for certain assumed flux within a time window of 1000 s is $s = 5.0$. The expected background within that time window is taken from the output of selection A,

¹Internally named *one weight* in IceTray simulation data.

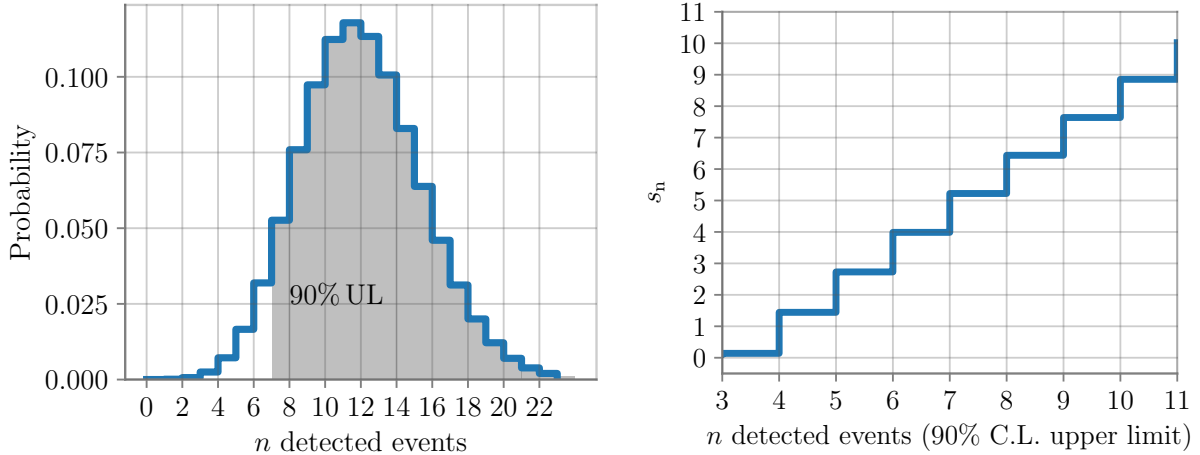


Figure 8.17: Left: example for the determination of the 90% confidence interval for the Poisson probability of detecting n events with $b = 6.54$ and $s = 5.0$. **Right:** value of maximum number of expected signal events, s_n , that would require detecting a total of n detected events to set the 90% upper limit confidence level, assuming $b = 6.54$.

which is $b = 6.54$ events combining atmospheric neutrinos, muons and noise. The PDF on how many total events n would be detected with such expectation of s and b as defined in Eq. 8.5 is shown on the left side of Figure 8.17. The dashed area shows the integral of the distribution that covers, at least, 90% of the PDF. This means that, given an expectation of $s = 5.0$ signal events and $b = 6.54$ background events, in at least 90% of cases the experiment will detect $n = 7$ or more events. However, due to the discretization of the Poisson distribution, this is not the only combination that returns that same value. Continuing with the example, there is a range of s values compatible with this 90% UL. This is shown on the right side of Figure 8.17. The y-axis shows s_n , being the highest s for the 90% UL. All s values in the range $s_{n-1} < s \leq s_n$ are valid hypotheses for having detected n events. To remain conservative, the standard procedure is to choose the highest s , that is s_n .

In an experiment, after measuring n events, it is assumed that all of these were produced by the background in order to give a limit on the signal flux that passed through the detector. For this work, based purely on simulations, n is assumed as the median of the background distribution, with the expectation b indicated above, and rounded to the next integer, for which s_n for the 90% UL is calculated.

At this stage, the results will consider two different energy ranges for the flux. Thus, this applies a restriction on the detected events, rejecting all signal neutrinos outside the energy range. The ranges $[0.1, 1000]$ GeV and $[0.5, 5]$ GeV are used. The first broader range covers the whole simulated spectrum, while the second range considers a spectrum constrained within those energies, as used in [217], so the results are comparable. Note that the energy limits are only applied to the signal flux, and the atmospheric neutrino background is kept entirely in all cases. Then, for each selection approach, each time window, and each energy limit, the minimum value for C that would result in the necessary number of signal events s_n can be calculated. This is done by scaling $s(\phi)$ until $s(\phi) = s_n$, with

Table 8.3: 90% confidence level upper limit on the time-integrated all-flavor neutrino flux detected Φ at Earth for each selection approach. DeepCore ElowEn results [217] are also included for comparison.

	Time window (s)	All-flavor neutrino flux (cm^{-2})	
		[0.5, 5] GeV	[0.1, 1000] GeV
Selection A	$[t - 500 \text{ s}, t + 500 \text{ s}]$	1.4×10^4	2.0×10^3
Selection B	$[t, t + 3 \text{ s}]$	3.3×10^3	3.2×10^2
DeepCore ElowEn	$[t - 500 \text{ s}, t + 500 \text{ s}]$	3.9×10^4	-
	$[t, t + 3 \text{ s}]$	1.2×10^4	-

$$s(\phi) = \Delta t \sum_i w(E_i) = \Delta t \sum_i \phi(E_i) \frac{W_i}{4\pi N}, \quad \text{for } [E_{\min} \leq E_i \leq E_{\max}], \quad (8.6)$$

the expected number of neutrino events for the assumed flux that accounts for each neutrino event i that survived selections A or B in each case.

8.4.3 Time-integrated all flavor fluxes

From the above, the time-integrated flux over all neutrino flavors after each selection approach is calculated as

$$\Phi = \Delta t \int_{E_{\min}}^{E_{\max}} \phi(E) dE, \quad (8.7)$$

for all cases mentioned above. This quantity represents the minimum flux necessary to go through the detector to set the 90% UL, determined by the value of C obtained after the minimization explained above for each selection and application of the different energy and time constraints.

The results are shown in Table 8.3, where the results for DeepCore are also included for each time window. Compared to them, a factor ~ 2.8 of improvement is found for the longer time window, while the result is ~ 3.6 better than the DeepCore result for the shorter time window of 3 s.

8.4.4 Isotropic energy limit on GW170817

Now, the 90% UL on the astrophysical quantity of interest, the isotropic equivalent energy, is calculated for the case of the source GW170817. The isotropic equivalent energy represents the total energy emitted in neutrinos within the considered time window and the assumed energy range, assuming a spherically symmetric emission. This can be calculated as [75]

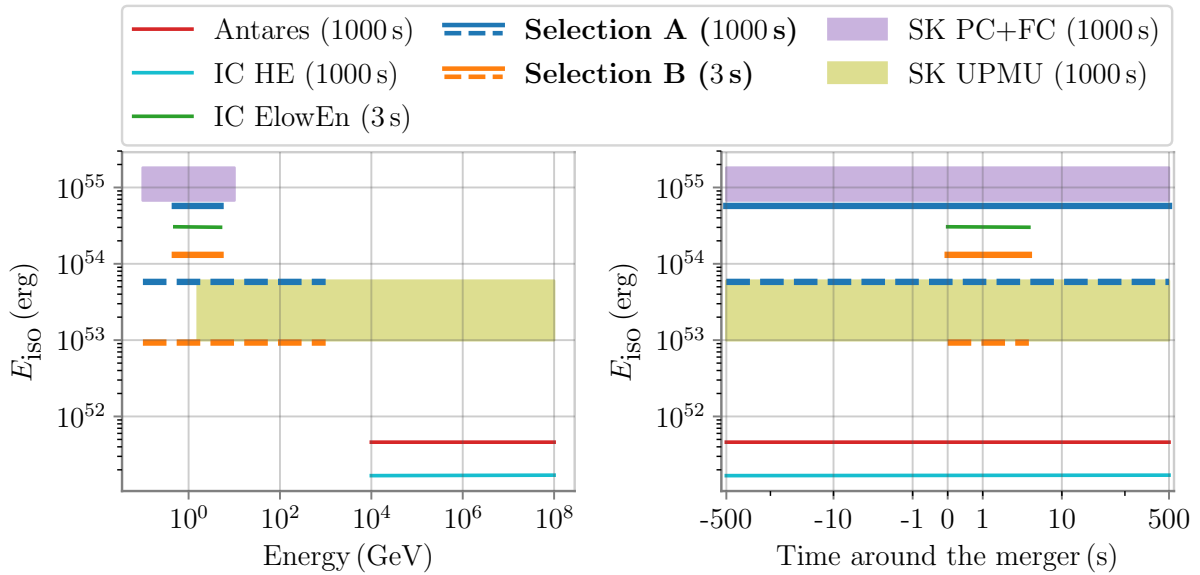


Figure 8.18: Comparison of 90% upper limit on E_{iso} obtained in this work applied to the merger event GW170817 with similar constrains from other studies. Results from this work are shown for each selection approach (**A** or **B**) in solid lines for the result assuming [0.1, 1000] GeV energy range and dashed lines for the result assuming [0.5, 5] GeV energy range. Other studies included in the figure are DeepCore ElowEn analysis [217], Antares [237] and IceCube (IC) [75] using high-energy neutrinos and results from SuperKamiokande (SK) [238] using all neutrino flavors (PC+FC, Partially/Fully Contained) and using only upward-going muonic neutrinos (UPMU). All studies assume a flux $\phi \propto E^{-2}$. SK results are given as a band to cover all cases of the flux assumption composed fully by neutrinos (lower range) to the flux composed fully by antineutrinos (higher range). **Left:** the x -axis shows the energy range considered for each study. Results from this work do not consider any cut based on the neutrino direction, as well as the ElowEn and the SK (PC+FC) results. **Right:** the x -axis shows the time window considered for each study.

$$E_{\text{iso}} = 4\pi d^2 \Delta t \int_{E_{\text{min}}}^{E_{\text{max}}} \phi(E) E dE = 4\pi d^2 \Delta t C \ln \left(\frac{E_{\text{max}}}{E_{\text{min}}} \right), \quad (8.8)$$

introducing the proposed flux with $\alpha = -2$ defined in Eq. 8.4, where d is the distance to the source.

The results obtained with each selection explained in this chapter are shown in Figure 8.18 for the source GW170817, together with some limits established by the literature and the results from the DeepCore study. In each subfigure, the x axis represents the energy or time range in which the limit was established for each study; thus, both figures show the same information and are complementary for understanding the considerations in flux energy and observation time taken in each analysis. Note that the results are only comparable when the same energy and time range have been used; otherwise, they represent supplementary information on the same source. In both subfigures, the upper limits on the isotropic energy obtained with IceCube, Antares, and SuperKamiokande are included.

On the left of Figure 8.18, the x axis shows the energy range assumed for the flux in each study. The result after Selection B for the energy range [0.5, 5] GeV are directly

comparable to those of the DeepCore ElowEn analysis, since the same energy range and time windows are used. The limit on the isotropic energy obtained in this work is a factor ~ 2.4 lower than the DeepCore analysis. Selection A, which considers that the neutrinos arrive within a much longer time window, naturally results in a higher E_{iso} limit within the flux duration, due to the higher noise. For both selections, the upper limit on E_{iso} is more than one order of magnitude lower if energies are not restricted and the whole sample within $[0.1, 1000]$ GeV is used, giving results competitive with SK UPMU sample even if the energy range of the SK search is much larger. In the figure on the right side of Figure 8.18, the x axis stands for the time window used in each analysis. All limits shown in the figure from other works consider the longer time window $[t - 500 \text{ s}, t + 500 \text{ s}]$, except for the ElowEn DeepCore analysis that considers $[t, t + 3 \text{ s}]$.

8.4.5 Discussion and limits at any distance

The results obtained in this chapter show an improvement over the ElowEn analysis of a factor 2.4. The greatest loss of neutrino events was found in the noise rejection stage, discussed in Section 8.3.4. In fact, most of the neutrino events lost by that cut are in the lowest energy region of the simulated spectrum, as shown in Figure 8.14. Although in this chapter, one single selection process has been detailed (using different thresholds to adapt to the different time windows), many different combinations were tested to try to get the best capability of the detector for this study. It has also been checked whether it is possible to further optimize the selection process for the $[0.5, 5]$ GeV energy range from the beginning. This was done first by performing cuts on the neutrino sample after filter level, and later training the GBDTs only using low-energy neutrinos. Considering the size of the simulated sample, this was chosen as training with all neutrinos with energies below 10 GeV, so enough events are available for each training. The event selection was then done similar to what is shown in the previous sections, but a different set of variables performed better in this case. When the whole selection process is done this way, a lower value for the 90% upper limit was obtained, however, the improvement is not significant enough to justify making an exclusive selection on these low-energy events. It also has the caveat that the GBDTs are less robust in this approach, probably caused by the low number of surviving neutrino events after each step. Therefore, it was decided that this should not be included in the results shown in this chapter, although the selection process and the results for this approach are summarized in the Appendix E.

The limit on the isotropic energy as obtained before is now calculated for any other source of known distance. Something that has not been considered yet is performing a cut based on the neutrino directions, using the position of the source in the sky to clean the final sample of background from atmospheric neutrino events. Applying a cut on the neutrino direction is interesting for the case of Selection A, where the background is dominated by atmospheric neutrinos. For selection B, dominated by atmospheric muons, the worst scenario is assumed in which these events are not differentiable from neutrinos, and no cut based on their direction is considered. For the case of energy limits $[0.5, 5]$ GeV, a counting-only analysis is a viable assumption, since these events are often hardly reconstructable. However, for the case that considers a larger energy range, the selection would benefit from directional reconstruction of the events. This benefit would depend on the position of the source in the sky, i.e. on the zenith angle, since the atmospheric

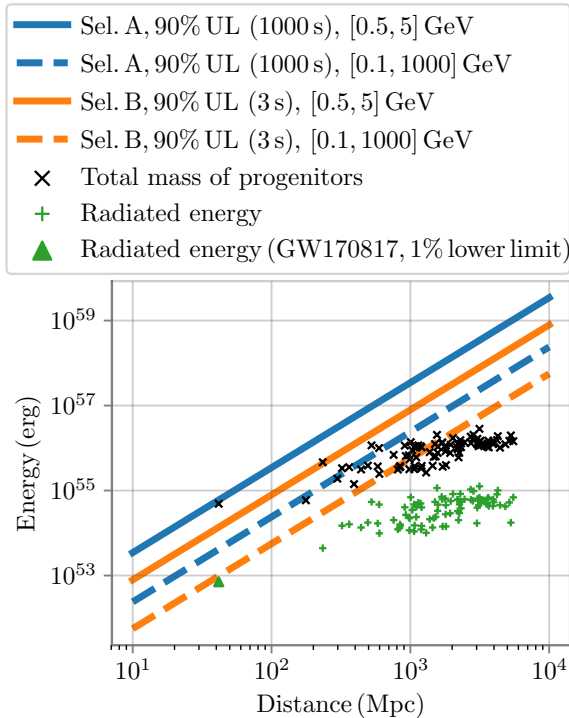


Figure 8.19: For each of the selections developed in this chapter, the 90% confidence level upper limit on the isotropic equivalent energy emitted in neutrinos within each considered energy range is shown as a function of the distance of the source. Related quantities on the energy of compact binary mergers detected in GW are obtained from [69], where error bars on the source distance and energies are not shown for clarity. For each source, $E_{\text{progenitor}}^{\text{tot}}$ is the sum of the total rest mass energy of the progenitors and E_{rad} is the total radiated energy, calculated as the difference between the total rest mass energy of the two progenitors and the final remnant mass. The radiated energy is calculated only for sources with a specified remnant mass in the catalog. For GW170817, the total radiated energy is given as the 1% confidence level lower limit [239]. Results for Selection A consider a neutrino flux in the energy range [0.1, 1000] GeV assumes a solid angle with a radius of 40 deg in the sky around the source where background neutrino events are allowed, in a general form where the background expectation has been averaged over the whole sky.

neutrinos in the final sample are equally distributed in azimuth¹ but not in zenith (see Figure 8.16). Considering a general scenario with no particular source, a solid angle is assumed equally along the sky with a radius of 40deg around the source position in which atmospheric neutrinos are allowed, considering the true direction of the MC sample for the calculation. The 40deg radius is chosen based on a conservative angular resolution expected for neutrinos in ICU [23]. This is only applied to the case of Selection A and when the energy range of [0.1, 1000] GeV is considered. This approximation reduces the 90% UL on E_{iso} at any given distance by a factor 1.5 on average, although the final improvement for a real analysis would depend on the direction of the source.

Finally, the results for the 90% UL on E_{iso} are generalized for any source as a function of distance (Figure 8.19), considering both selections focused on the different time windows and energy ranges used before. The figure includes data from the fourth GW Virgo-Ligo catalog [69]. The total radiated energy has been calculated as the difference between the total rest mass energy of the two progenitors and the final remnant mass. Note that these are just shown as a reference for the binary systems, since not all of the progenitor energy would be available for acceleration processes, and obviously not all the radiated energy would be in the form of neutrinos. Note also that, although error bars have not been included for clarity reasons, they are of considerable size, especially regarding the distance

¹The figure of the atmospheric neutrino sample in azimuth was shown since it does not provide any meaningful information. Note that IceCube is approximately symmetrical and that this work uses only simulated events, where the flux is normalized over time. This is why the distribution of these events in azimuth is symmetrical.

of each source. For GW170817, the radiated energy is shown as the 1% lower limit from [239].

In view of the results, it can be seen that although the selection here improves the results of the DeepCore analysis [217], the UL for E_{iso} for all the cases shown here are always above the total radiated energy of the binary system obtained from the GW detection. This would indicate that, despite the improvement, a long-distance compact binary merger would not be detected with sufficient statistical significance in low-energy neutrinos by ICU using the methods proposed here, considering that the GW catalog is a representative sample of the spectrum of compact binary mergers that can be expected in the next years. The method is still valid for proposing limits on the flux of neutrinos emitted by future binary mergers within the selected energy range. However, at the distances shown in Figure 8.19, the reason why the most powerful sources have not yet been detected closer to Earth should be only statistical. The existence of such sources is proven, as they have already been detected. Considering that they are equally distributed along the space, the probability of finding such a source decreases with d^2 . Thus, a detection of a similar source from a closer Galaxy could happen at any time, in which case the radiated energy might be above the upper limits obtained here for the isotropic energy in neutrinos.

The source GW170817, would, in principle, have had a chance of being detected in the form of low-energy neutrinos in the future detector, according to the results obtained here and considering the lower limit for the radiated energy given in [239], which is right below the upper limits obtained here. Being a NSNS merger, the energy radiated from the merger is lower than in cases when one or both objects are black holes, which are much more massive. It should not be forgotten that the radiated energy does not represent the energy emitted in the form of neutrinos. For example, the total energy detected in gamma rays from the source of the event GW170817 (GRB170817 [216]) by Fermi GBM is about 6 orders of magnitude below the lower limit of the radiated energy shown in the figure. To date, it is not known what part of the undetected energy of this event was emitted as neutrinos.

8.5 Summary and conclusions

In this chapter, the capability of IceCube Upgrade to identify transient signals of compact binary mergers by detecting a low energy neutrino flux has been studied, using simulations done in IceTray [197]. The background for this study is composed of the inner noise of the modules, including the dark rate of the PMTs together with the decays of radioactive impurities in the vessel glass, as well as the particles produced after the interaction of cosmic rays in the atmosphere: atmospheric neutrinos and muons. Thus, the work focused on differentiating the signal detected from an assumed low-energy flux neutrinos coming from the merger from these background events. To differentiate neutrinos from the other types of events, an event selection is made. Later, the neutrinos from the assumed signal flux are treated as indistinguishable from the atmospheric neutrino background, and, as such, an excess over the background rate is required to detect the merger within a certain time window around the reported merger time.

Events were generated with simulations in *IceTray* and consist of a neutrino flux between 0.1 and 1000 GeV, a muon flux consistent with atmospheric muons, and events generated

only from the module noise. The neutrino simulation is also used to calculate the signal flux by weighting the events accordingly after the event selection. All simulations were performed using the so-called v53 geometry, which did not include the new modules that will be located in the ICU calibration region.

All simulated events first pass through the event trigger and filter. The trigger determines whether events are detected, and the filter tries to reject the most obvious muon events that come from outside the detector. After these, the rate of atmospheric neutrinos is several orders of magnitude lower than that of atmospheric muons and noise. To detect the signal flux efficiently, the background must first be reduced, while trying to keep as many neutrino events as possible so that the signal flux can still be detected efficiently. This event selection was performed using a succession of gradient boost decision trees (GBDTs), a machine learning algorithm that is very efficient at separating two distinct classes of events based on specific input parameter distributions. In each step, the GBDT was configured using parameters that achieved good performance and at the same time did not introduce artifacts into the results, as might occur if, for example, the algorithm overfits. This was tested at each iteration of the GBDT.

The first GBDT is trained to separate neutrinos from noise events. The surviving events are passed on to the next GBDT, focused on selecting neutrinos over atmospheric muons. These first two iterations of the GBDT are performed by different combinations of a common set of variables that are fast to compute, so that they can be calculated efficiently over a large number of events, as is the case after filter level. These variables focus on the use of geometric and temporal correlation of hits in the detector to determine the type of event involved, making use of the veto volume to identify and reject muons. Then, for the surviving events, a new set of variables is calculated, which are slightly more computationally costly than the previous set, with which a GBDT is trained to select neutrinos over muons again. The new variables are focused on trying to identify the muons that have reached the inner part of the detector without leaving a trace in the veto volume, and therefore could not be rejected in the previous step.

In this chapter, two different time windows to search for the signal are considered. The first, of 3 seconds duration after the merger time reported by the GW detection, is based on the search of a prompt signal just after the GW detection. A longer time window of 500 seconds around the merger time searches for a neutrino flux based on the data obtained with the GRB detection, whose duration was estimated in [225]. Because these time windows are very different, the threshold for the GBDTs does not necessarily need to be the same. For the longer time window, tighter cut-offs make more sense, while with the shorter time window, softer threshold values can be chosen, allowing for a higher background rate but also more potential signal events. This way, the selection centered on the shorter time window does not require the last iteration of the GBDT trained to separate neutrinos from muons, since after the previous iterations the expected background level is already below a single event during the 3 seconds long time window. In the case of the longer time window, the thresholds were chosen such as the final level of atmospheric neutrinos is ~ 10 times higher than that of the other combined background sources.

Furthermore, the necessary flux from the source that must pass through the detector to establish a 90% upper limit confidence interval (90% UL) was calculated using Poisson statistics. To do this, a power law spectrum depending on the energy as $\propto E^{-2}$ was assumed. At this point, two hypotheses are considered; one in which the signal is emitted over the entire energy range considered in the simulation between 0.1 and 1000 GeV, and

another in which the signal is limited to a smaller energy range between 0.5 GeV and 5 GeV. The 90% UL for each is expressed as the total flux of all neutrinos passing through the detector and is shown in Table 8.3 under each time window and energy range condition.

Finally, the 90% UL on the quantity of interest, the isotropic energy of the merger, was calculated, first for the GW170817 source and then generalized to any source at any distance. The result for GW170817 is compared with the upper limit given by DeepCore, obtaining in this work an upper limit ~ 2.4 times lower than the DeepCore one when considering the same energy range and time window. The results at any distance were shown together with the total initial rest mass and the radiated energy of mergers detected by the Ligo-Virgo Collaboration [69]. The upper limits on the isotropic energy for all selection approaches done in this work were always above the total radiated energy of all sources, meaning that those sources would not have been detected by ICU. The only case from the catalog where the source could have been detected is for GW170817, which is much closer to Earth than all other events included in the catalog, even if it is less energetic. However, the detection would require that most of the energy emitted by GW170817 is in neutrinos. Nevertheless, the majority of the sources in the catalog have much higher values for the radiated energy than GW170817. If these more energetic events would occur closer to Earth, the radiated energy would be above the 90% UL obtained by this work, being therefore possible to detect them or to establish upper limits on the energy radiated in form of neutrinos by these events.

Regarding possible improvements to the method, the main negative impact to the final signal rate comes from the rejection of noise events, especially at low neutrino energies. During the course of this work, attempts were made to improve the selection of these events in several ways, using different variables or even focusing the entire event selection on low-energy neutrinos only. Focusing exclusively on low-energy neutrinos yields slightly better results when the smaller energy range is considered, but the GBDT loses robustness because of the low number of events being trained. The results obtained in this chapter might be enhanced if the selection of events over noise is improved, for example, by new cleaning algorithms that better consider the new optical modules. Furthermore, the simulations used in this work were based on a geometry that did not consider the modules that ICU will deploy in the calibration region, which potentially improves the rejection of atmospheric muons. Once the detector is built, newer simulations for the background can be made and tuned to match measured data. This is especially important for the case of noise simulations, since the current code has not yet been fully adapted to the new modules yet. Based on that, new noise cleaning algorithms can be evaluated and eventually improve the results obtained in this chapter.

The event selection done in this chapter was applied to the case of neutrino events coming from a binary merger, but it could be equally used for any other possible transient source of neutrinos within the energy range covered by ICU.

Summary and outlook

This thesis has presented studies based on simulations of future IceCube extensions on a variety of topics, demonstrating the capabilities of the new detectors using the features of the new segmented sensors. Special emphasis has been placed on the mDOM, the module with the greatest segmentation. The results of this thesis are obtained with simulations in Geant4 or IceTray and are divided into three different analyses.

First, the sensitivity of the future extensions to a MeV CCSN neutrino burst was studied in Chapter 6. The interaction of these events was separated from the background using multiplicity conditions in the PMTs of each single module. This considerably increases the capability of the detector to study CCSNe, exceeding the improvement that would be obtained simply by the extension of the effective volume of the detector. Considering an IceCube-Gen2 detector composed of 10000 mDOMs, CCSNe can be identified up to (246 kpc, 147 kpc) for a CCSNe with progenitor mass ($27.0 M_{\odot}$, $9.6 M_{\odot}$), with a false detection rate below one per century. If the arrival time of the neutrino burst is precisely known, the CCSNe can be identified over the background with a certainty of 5σ at (350 kpc, 232 kpc) for the ($27.0 M_{\odot}$, $9.6 M_{\odot}$) model, considering a conservative scenario of no oscillation. In comparison, if multiplicity conditions are not used, the 5σ horizon is found at ~ 60 kpc for the $27.0 M_{\odot}$ model when combining IceCube and IceCube-Gen2. Furthermore, IceCube-Gen2 with mDOMs was shown to be able to reconstruct the mean energy of the CCSN neutrino burst, as well as differentiating oscillation scenarios for galactic CCSNe. For IceCube Upgrade, considering only the 400 mDOMs in the detector, the results still exceed the detection range of IceCube even with a much smaller number of modules. Results were also obtained for the case of IceCube-Gen2 composed of 10000 LOM16s. In this scenario, the background at high multiplicities is significantly higher than in the case of the mDOM, resulting in a detection range of 220 kpc at 5σ for the $27.0 M_{\odot}$ when using the LOM16 construction design with the lowest radioactive contamination.

Secondly, studies were performed in Chapter 7 regarding the calibration of the bubble column in IceCube Upgrade. The bubble column is the central region of the refrozen ice of each string formed after building the detector. This region has much worse optical properties than the rest of the ice and is currently an important source of systematic uncertainty in IceCube. The study examined the use of two consecutive mDOMs, flashing the 5 LEDs of one mDOM hemisphere that points towards the other. It was shown that, by varying the properties of the bubble column (position in x, y , diameter d , and effective scattering length b_e), the detection pattern in each PMTs of both modules changes. Based on this, the bubble column parameters are reconstructed by minimizing a likelihood function. Various sources of systematic uncertainty were taken into account in this analysis, including the uncertainty in the relative position and orientation of the modules, the orientation and emission properties of the LEDs, the properties of the surrounding ice, the efficiencies of the PMTs, and the position of the data cable relative to the modules. It was found that the reconstruction of the bubble column position was most affected

by the systematic uncertainties related to the geometry (position, orientation). The reconstruction of the effective scattering length was most affected by uncertainties in the PMTs and LEDs. This is also true for reconstructing the size of the bubble column, but this measurement is also significantly impacted by uncertainties in the orientation of the LEDs. It was also shown that, if there is a significant transition region between the bubble column and the hole ice, the characteristics of this can also be fitted using this method. When all systematics effects are combined, the parameters of the a bubble column with true values ($d = 16$ cm, $b_e = 3$ cm, $x = 0$ cm, $y = 0$ cm) are simultaneously reconstructed as ($d = 16.1_{-0.7}^{+1.3}$ cm, $b_e = 3.05_{-0.14}^{+0.28}$ cm, $x = 0.2_{-0.7}^{+0.9}$ cm, $y = 0.0_{-0.8}^{+0.8}$ cm)¹.

Finally, the sensitivity of IceCube Upgrade to GeV fluxes from compact binary mergers was studied in Chapter 8. After the simulated events are triggered and pass the first filter designed to reject the most obvious muon tracks, an event selection was performed to identify neutrino events over the background. The event selection was divided into three steps, the first one aiming to select neutrinos over noise from the modules, and the last two aiming to identify neutrinos over atmospheric muons. These selections were made by training a gradient boost decision tree (GBDT) each time with different variables. Some variables that directly use the segmentation of the mDOMs proved to be effective when selecting neutrinos over the noise generated by the modules themselves. The event selection achieved an efficiency of 10 : 1 in selecting atmospheric neutrinos over background. The neutrino events were then weighted with a flux of neutrinos emitted from the binary merger source assuming a power law emission spectrum of $\propto E^{-2}$. The statistical analysis of the source flux over the combined background of atmospheric neutrinos, atmospheric muons and module noise was done to set the 90% confidence level upper limit (90% UL) on the time-integrated flux over all neutrino flavors and on the isotropic energy emitted by the source in the form of neutrinos, considering different energy ranges and time windows. Compared with a similar DeepCore result obtained for the source GW170817, the results obtained here show an improvement on the time-integrated all flavor flux by a factor 3.6, while the limit on the isotropic energy was improved by a factor 2.4. Despite the improvement, the best upper limit on the isotropic energy obtained in this study was still higher than the actual radiated energy of all sources from [69] except for GW170817. The latter, due to its proximity, is close to the upper limit obtained in this work. However, it is worth noting that the majority of sources in the catalog radiated significantly more energy than GW170817 but were detected at much greater distances. It is possible that these sources may also occur closer to Earth and therefore be within the sensitivity of IceCube Upgrade in the future.

It is important to continuously improve the code and models used in simulations by comparing the results obtained from the simulation with real data. Regarding the results obtained with the Geant4 simulations in this thesis, the code for the optical modules can be improved, since the entire PMT simulation has not yet been implemented for these results. In addition to that, Chapter 6 will be more comprehensive when simulations of atmospheric muons are performed with the full IceCube-Gen2 detector and dedicated trigger studies are carried out, so the impact of this background on the results can be evaluated. On the other hand, the analysis done in Chapter 7 shall be validated once the detector construction is complete. This is of special importance when considering the systematic sources, since some unexpected origin of systematic uncertainties might influence the results once the detector is finished. Then, it will be important to study the bubble column considering different models and determine the best fit, including the

¹ $X_{-\sigma}^{+\sigma}$, being X the median of the reconstructed value distribution and $\pm\sigma$ one standard deviation.

possibility of the transition region between the column and the bulk ice.

The results obtained with IceTray in Chapter 8 can be updated in the future with the latest ICU geometry, including modules in the calibration region, which will potentially improve the selection of neutrinos over muons. In addition, improvements in the noise simulation of segmented modules are still ongoing in the Collaboration. The event selection in this chapter was done using GBDTs, however, there are other approaches that also look promising in these types of studies, like the use of graph neural networks, for example. Different techniques could be employed, and their performances compared to later use the most convenient one in the real analyses.

While these details may affect the final results in each chapter, they are minor adjustments or improvements and are not expected to change the overall viability of the methods. The results presented in this thesis showcase the potential of the new IceCube extensions for two physics analyses and one calibration study, indicating a promising future for the detector.

Appendix A: detection patterns

for different bubble column parameters

This Appendix shows the detection pattern on the PMTs of both emitter and receiver modules (EM and RM) when varying the parameters of the bubble column, for a flash of 10^8 photons. Only the results from flashing the centered LED (LED=0) or one of the peripheral LEDs (LED=1, except for the last two figures) are shown.

- Figure A.1 (EM) and Figure A.2 (RM) show the detection pattern depending on b_e , fixing $d = 16$ cm, $x = 0$ cm, $y = 0$ cm, flashing LED=0 and LED=1.
- Figure A.3 (EM) and Figure A.4 (RM) show the detection pattern depending on b_e , fixing $d = 16$ cm, $x = 0$ cm, $y = -9$ cm, flashing LED=0 and LED=1.
- Figure A.5 (EM) and Figure A.6 (RM) show the detection pattern depending on d , fixing $b_e = 3$ cm, $x = 0$ cm, $y = -9$ cm, flashing LED=0 and LED=1.
- Figure A.7 (EM) and Figure A.8 (RM) show the detection pattern when varying the position of the column in x , fixing $b_e = 3$ cm, $d = 16$ cm, $y = 0$, flashing LED=0 and LED=2. LED=2 is more interesting in this case because it is located in the x axis, thus shows a higher dependency when varying x .

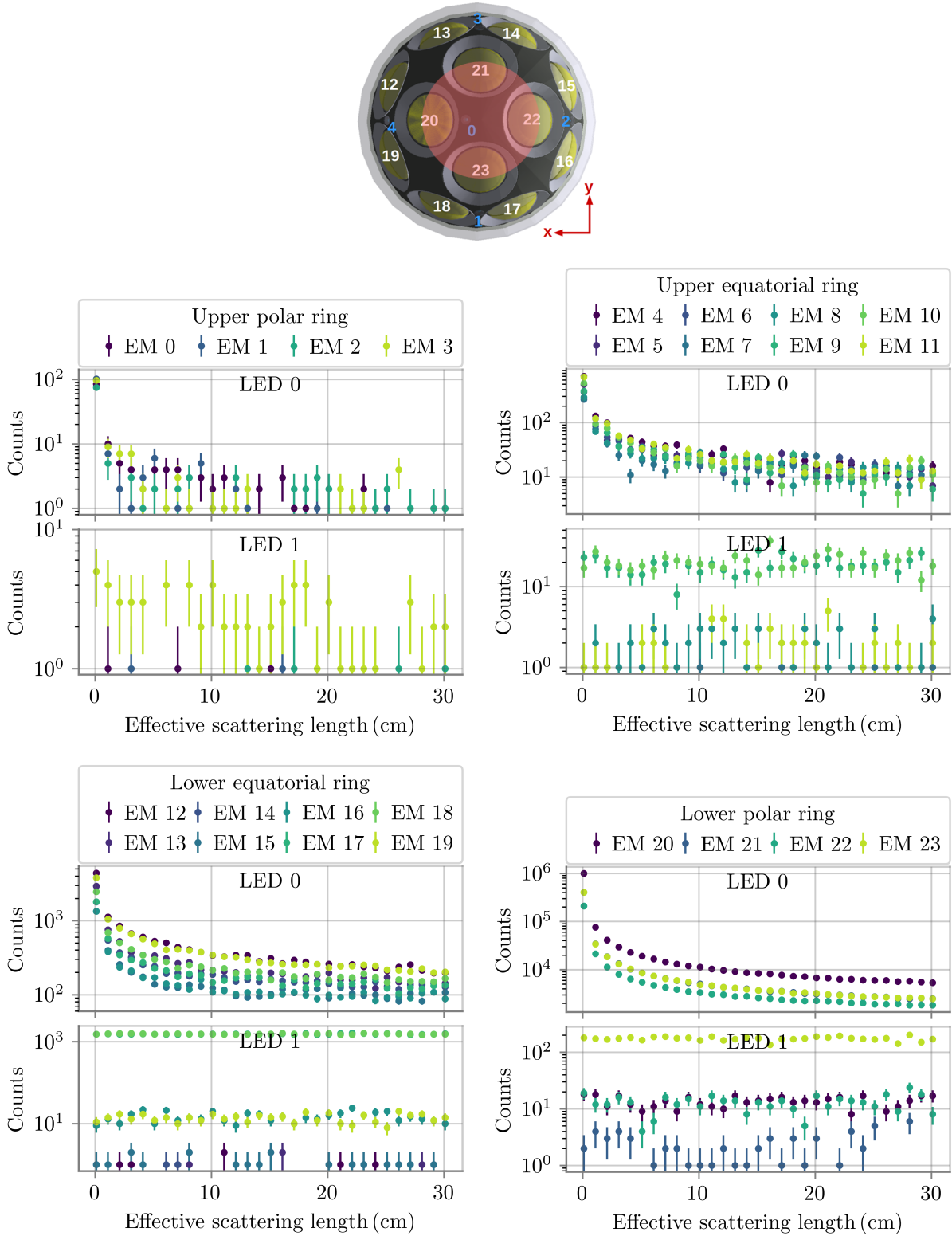


Figure A.1: Counts on different PMTs of the Emitter Module (EM) when flashing LEDs 0 and 1 varying the effective scattering length of the bubble column, with a column diameter of $d = 16$ cm centered in the modules ($x = 0, y = 0$). The sketch in the upper part of the figure shows the approximate location of the column (red circle) with respect to the emitter module.

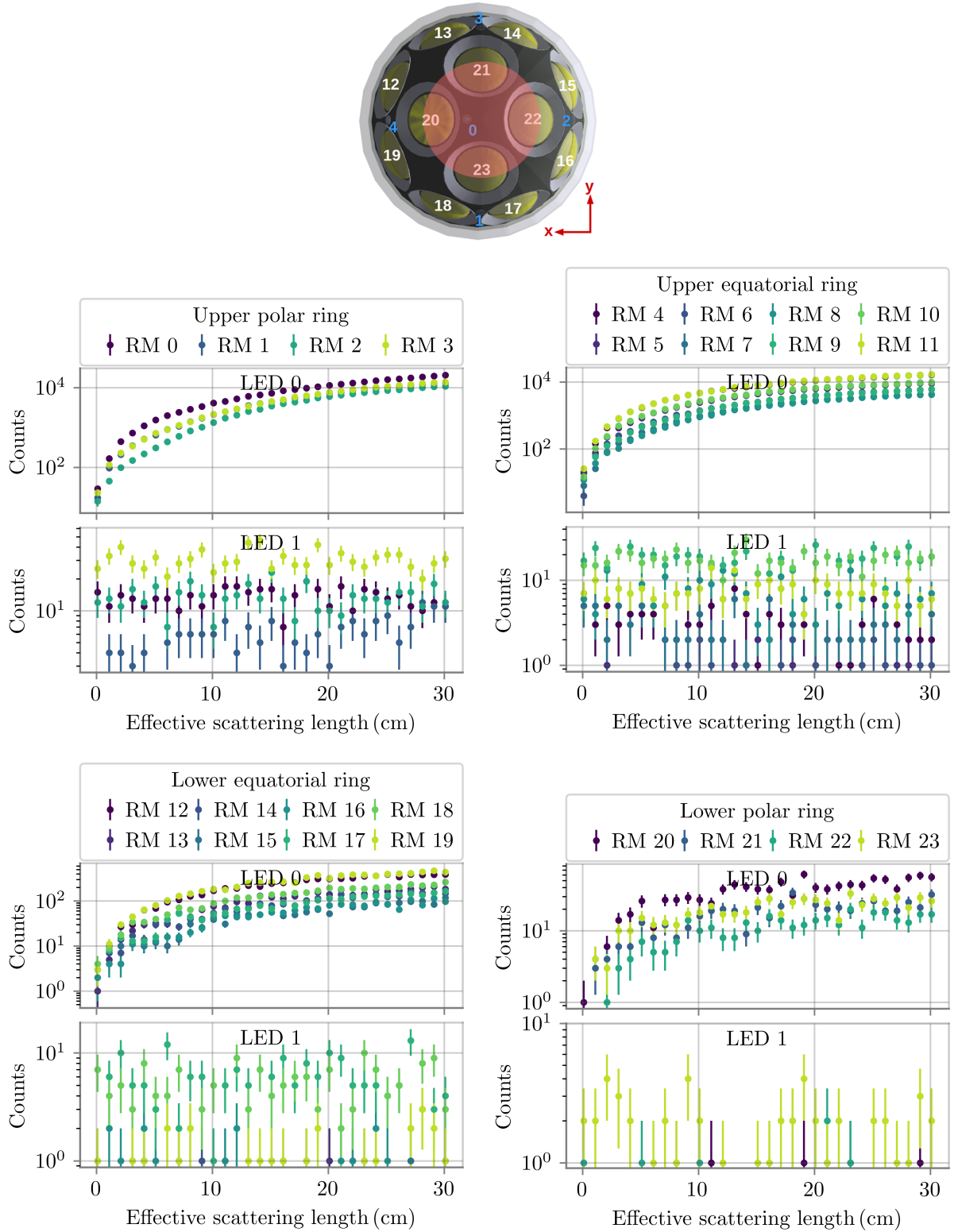


Figure A.2: Counts on different PMTs of the Receiver Module (RM) when flashing LEDs 0 and 1 varying the effective scattering length of the bubble column, with a column diameter of $d = 16$ cm centered in the modules ($x = 0, y = 0$). The sketch in the upper part of the figure shows the approximate location of the column (red circle) with respect to the emitter module.

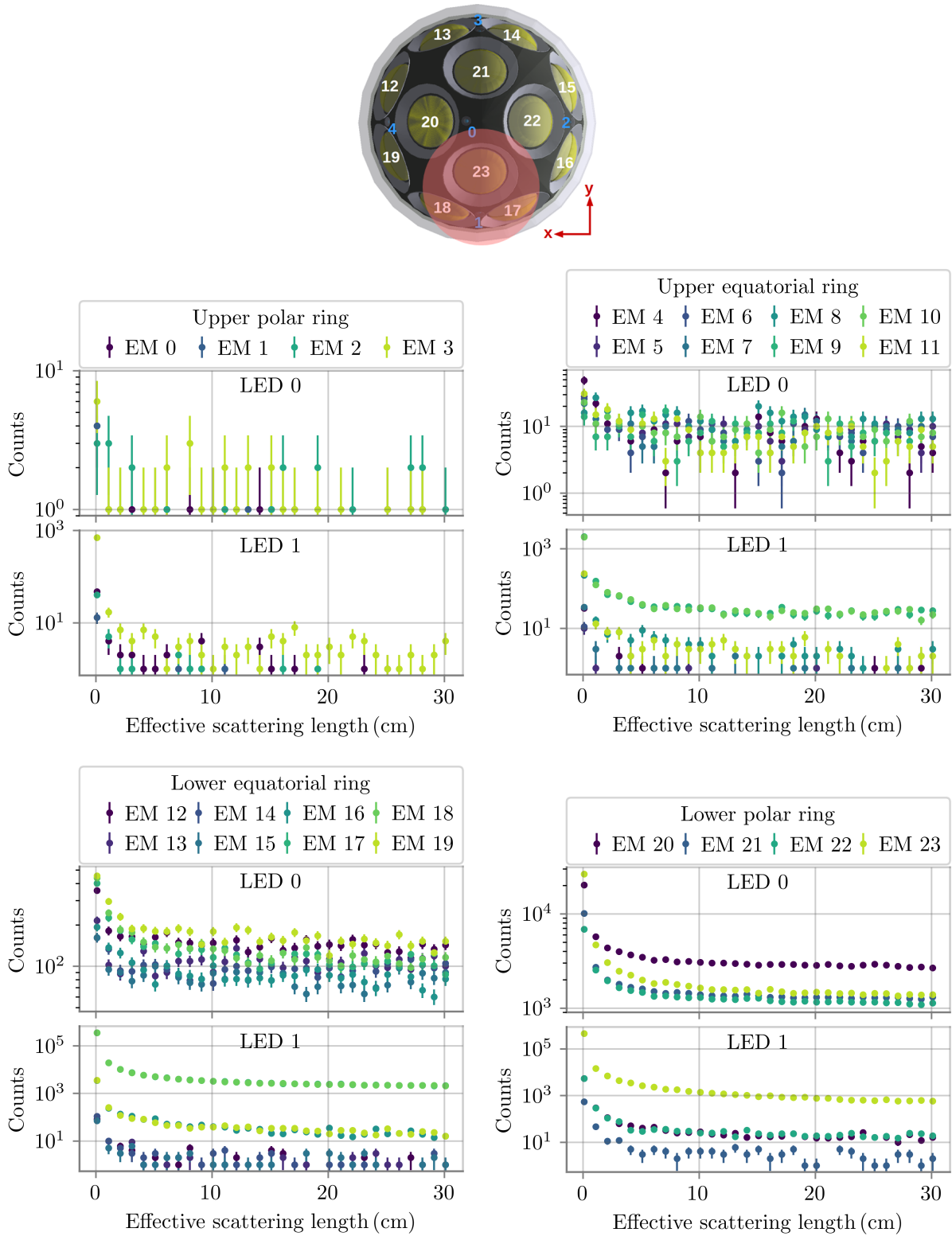


Figure A.3: Counts on different PMTs of the Emitter Module (EM) when flashing the LEDs 0 and 1 varying the effective scattering length of the bubble column, with a column diameter of $d = 16$ cm at $x = 0, y = -9$ cm. In this case, LED 1 is contained within the column, while LED 0 is not. The sketch in the upper part of the figure shows the approximate location of the column (red circle) with respect to the emitter module.

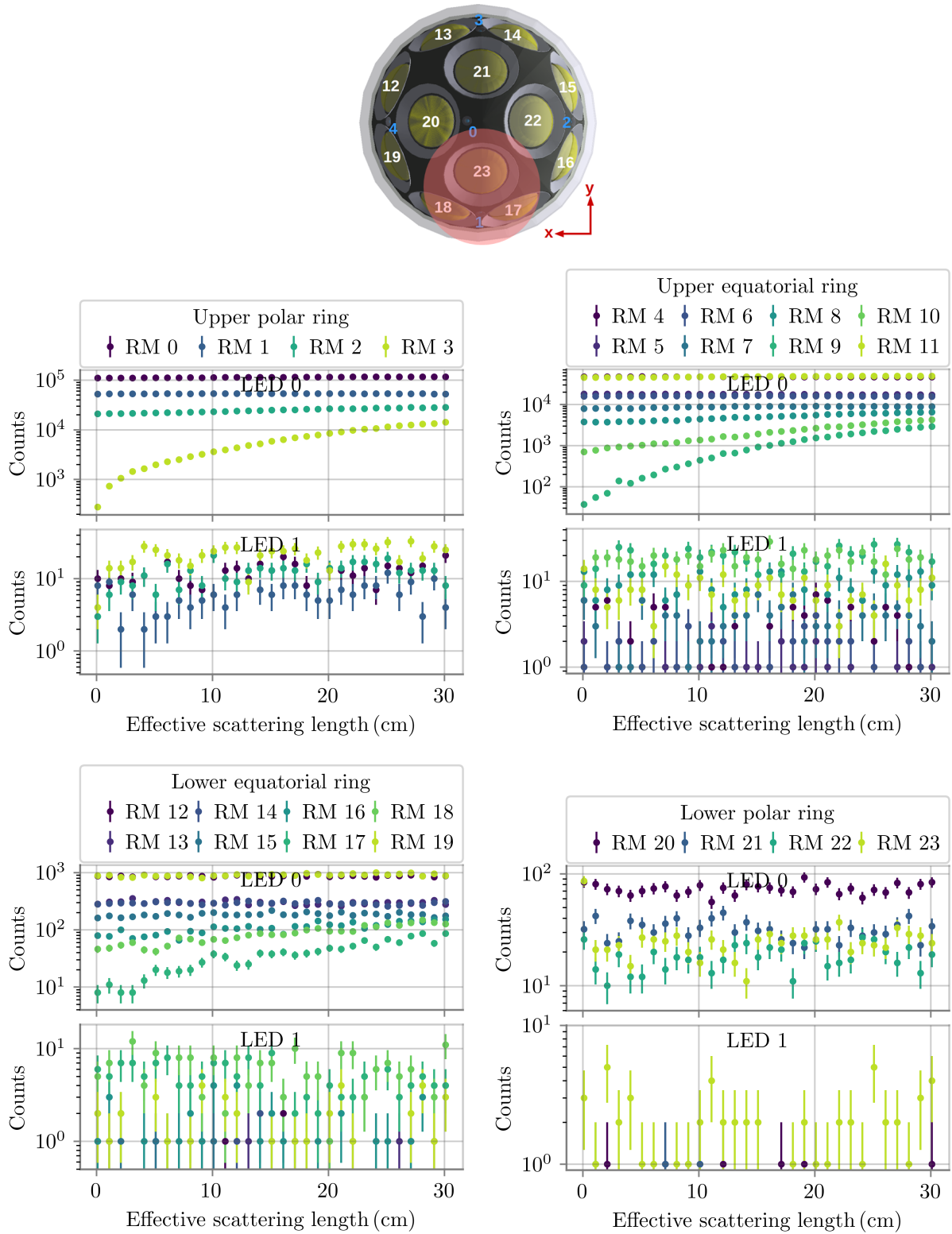


Figure A.4: Counts on different PMTs of the Receiver Module (RM) when flashing the LEDs 0 and 1 varying the effective scattering length of the bubble column, with a column diameter of $d = 16$ cm at $x = 0, y = -9$ cm. In this case, LED 1 is contained within the column, while LED 0 is not. The sketch in the upper part of the figure shows the approximate location of the column (red circle) with respect to the emitter module.

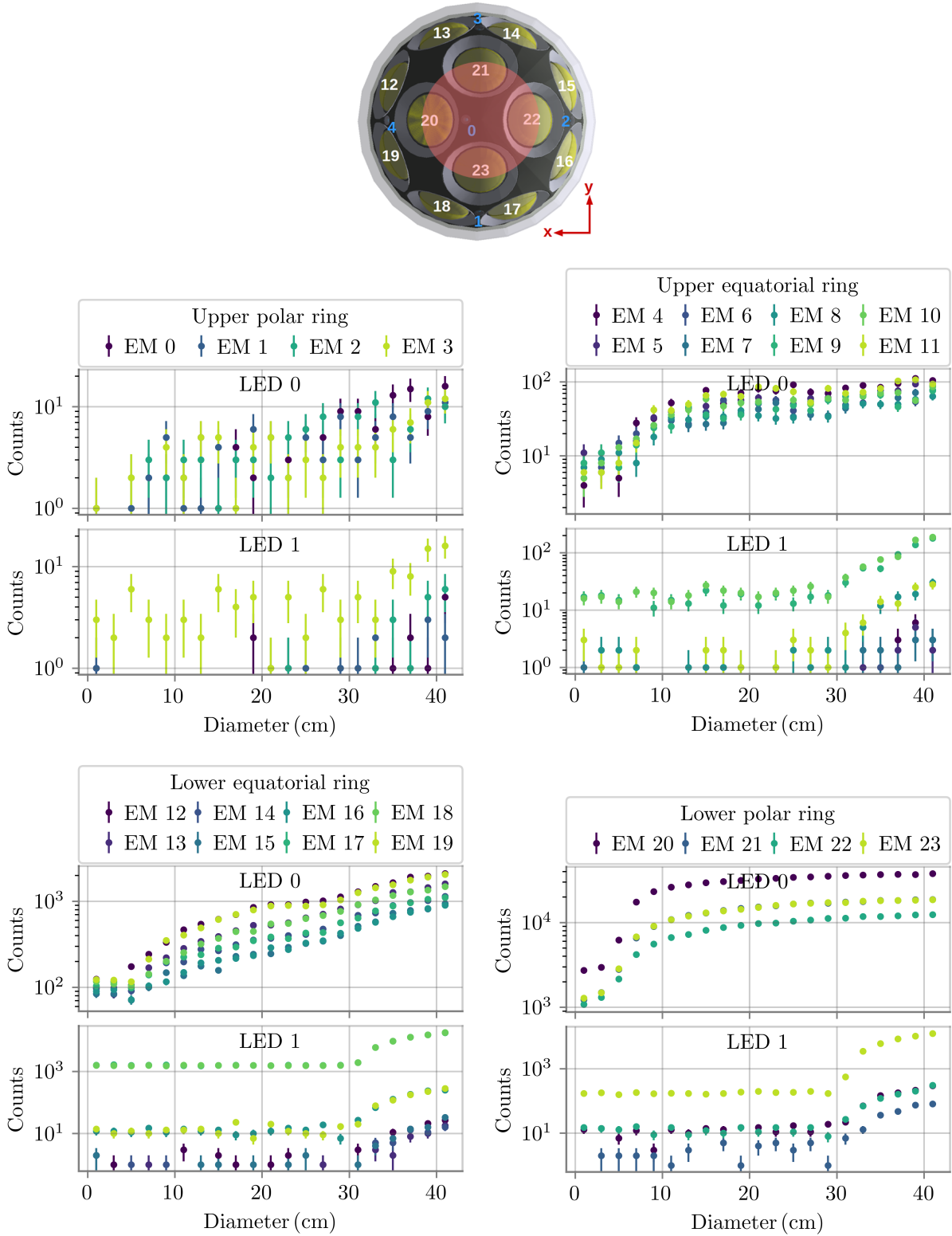


Figure A.5: Counts on different PMTs of the Emitter Module (EM) when flashing the LEDs 0 and 1 varying the diameter of the bubble column, with a effective scattering length of $b_e = 3$ cm centered in the modules ($x = 0, y = 0$). The sketch in the upper part of the figure shows the approximate location of the column (red circle) with respect to the emitter module.

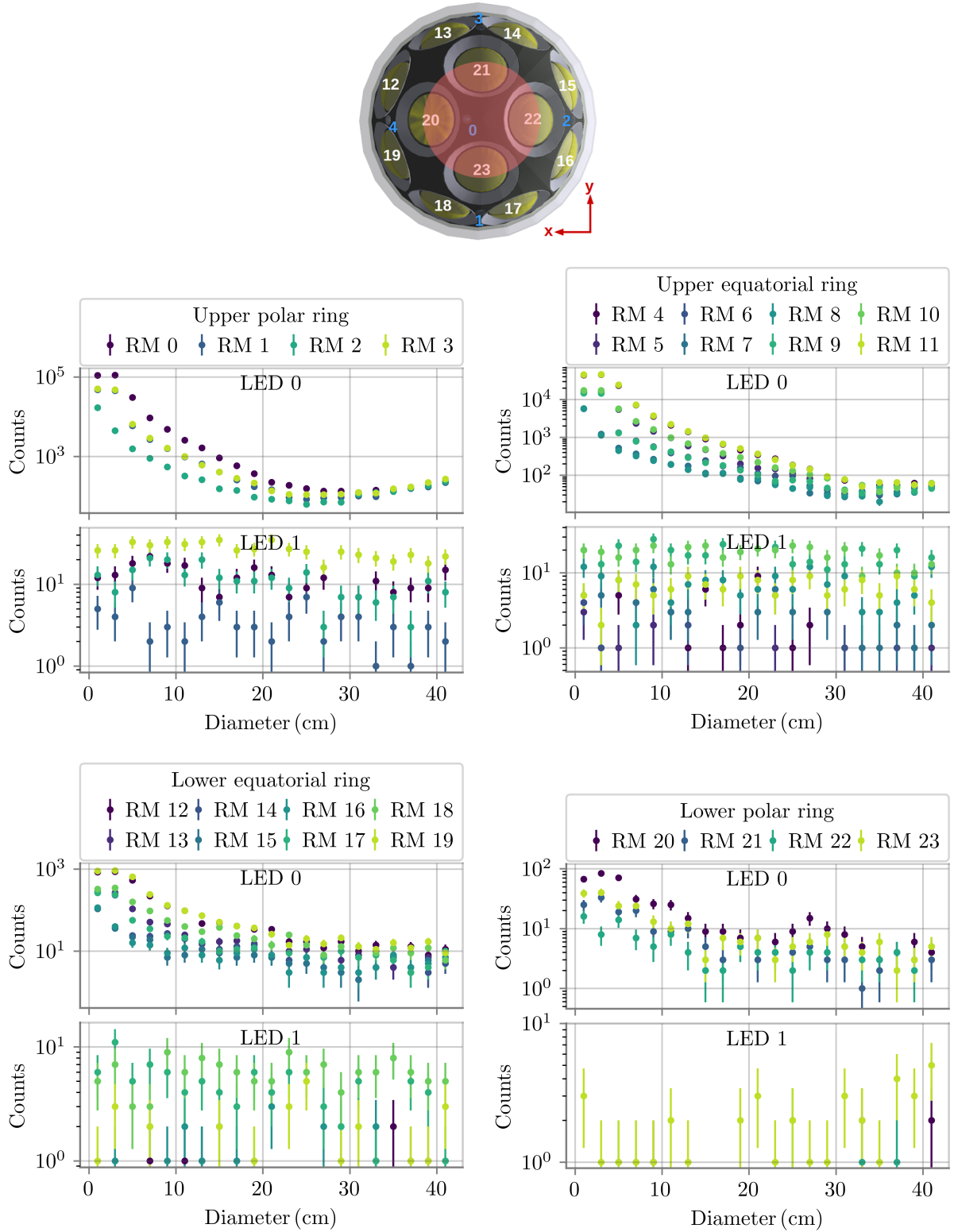


Figure A.6: Counts on different PMTs of the Receiver Module (RM) when flashing the LEDs 0 and 1 varying the diameter of the bubble column, with a effective scattering length of $b_e = 3$ cm centered in the modules ($x = 0, y = 0$). The sketch in the upper part of the figure shows the approximate location of the column (red circle) with respect to the emitter module.

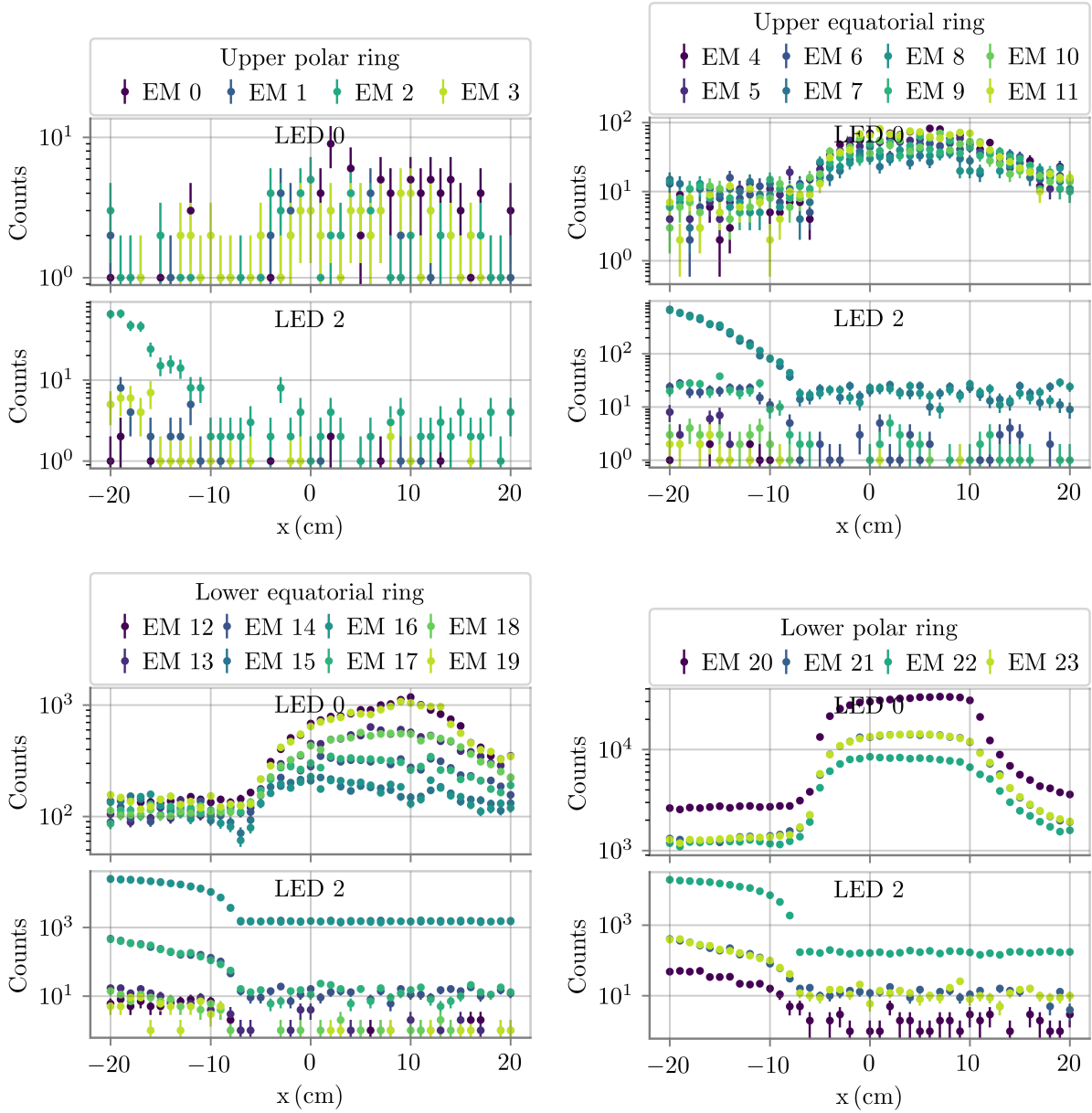


Figure A.7: Counts on different PMTs of the Emitter Module (EM) when flashing the LEDs 0 and 1 varying the position in x of the bubble column, with a effective scattering length of $b_e = 3$ cm, $d = 16$ cm and $y = 0$ cm.

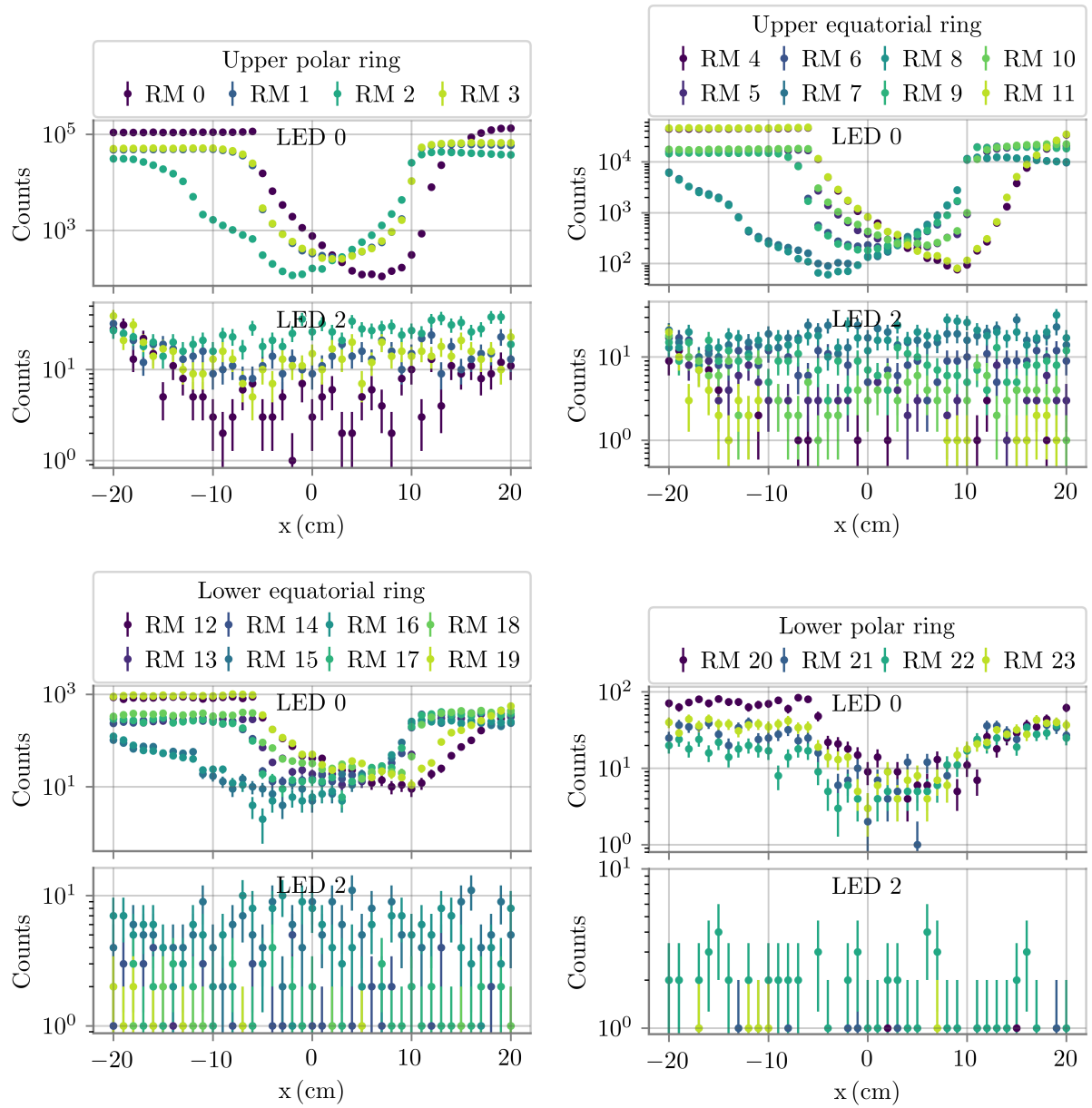


Figure A.8: Counts on different PMTs of the Receiver Module (RM) when flashing the LEDs 0 and 2 varying the position in x of the bubble column, with a effective scattering length of $b_e = 3$ cm, $d = 16$ cm and $y = 0$ cm.

B

Appendix B: variables used to train the GBDT to select neutrinos over noise

This Appendix shows the variables used to train the GBDT to select neutrinos over noise explained in Section 8.3.4, considering noise as the background internally generated by the modules themselves. Each variable has been calculated from the clean pulses (CP) or unclean pulses set (UP), indicated on the figure label.

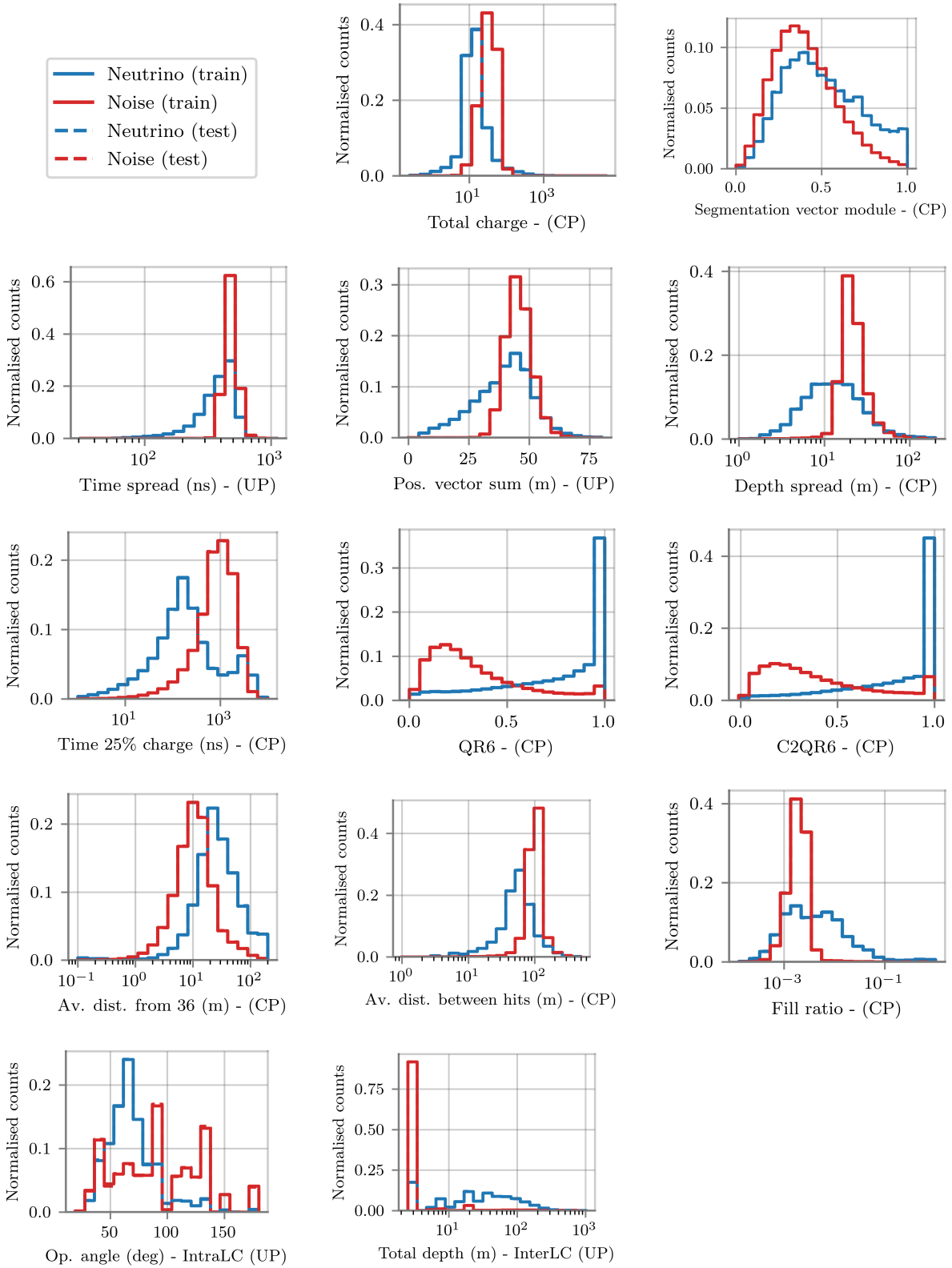


Figure B.1: Variables used for training the GBDT to separate neutrinos from noise, considering as noise all the background generated by the modules and the PMTs themselves. Lines show the bin data for the test and train samples, although they overlap in most cases.

*Appendix C: variables used to
train the GBDT to select neutrinos over muons - 1*

This Appendix shows the variables used to train the GBDT for the first iteration to select neutrinos over atmospheric muons explained in Section 8.3.5. Each variable has been calculated from the clean pulses (CP) or unclean pulses set (UP), indicated on the figure label.

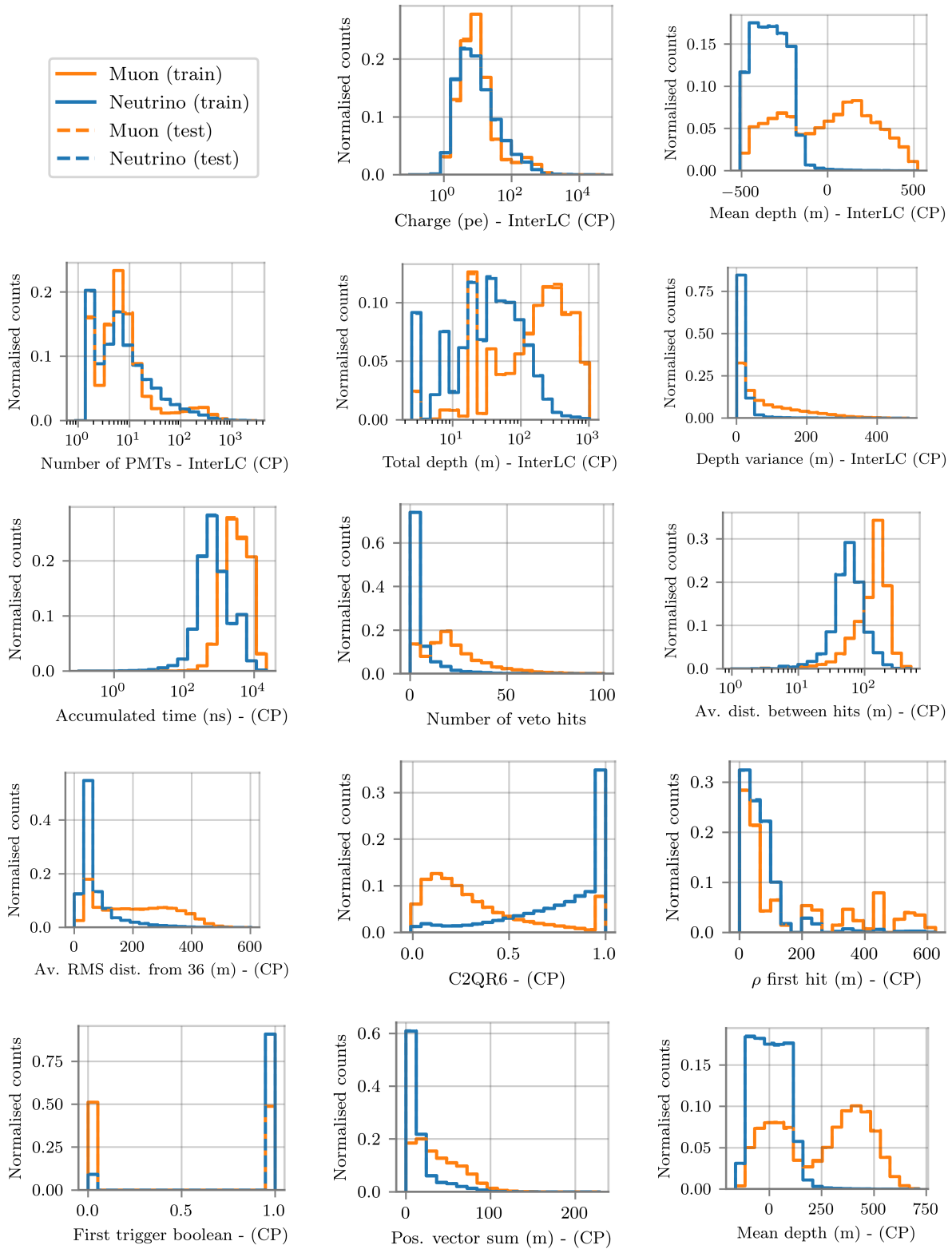


Figure C.1: Part 1 of variables used for training the GBDT for the first iteration to separate neutrinos from atmospheric muons. Lines show the bin data for the test and train samples, although they overlap in most cases.

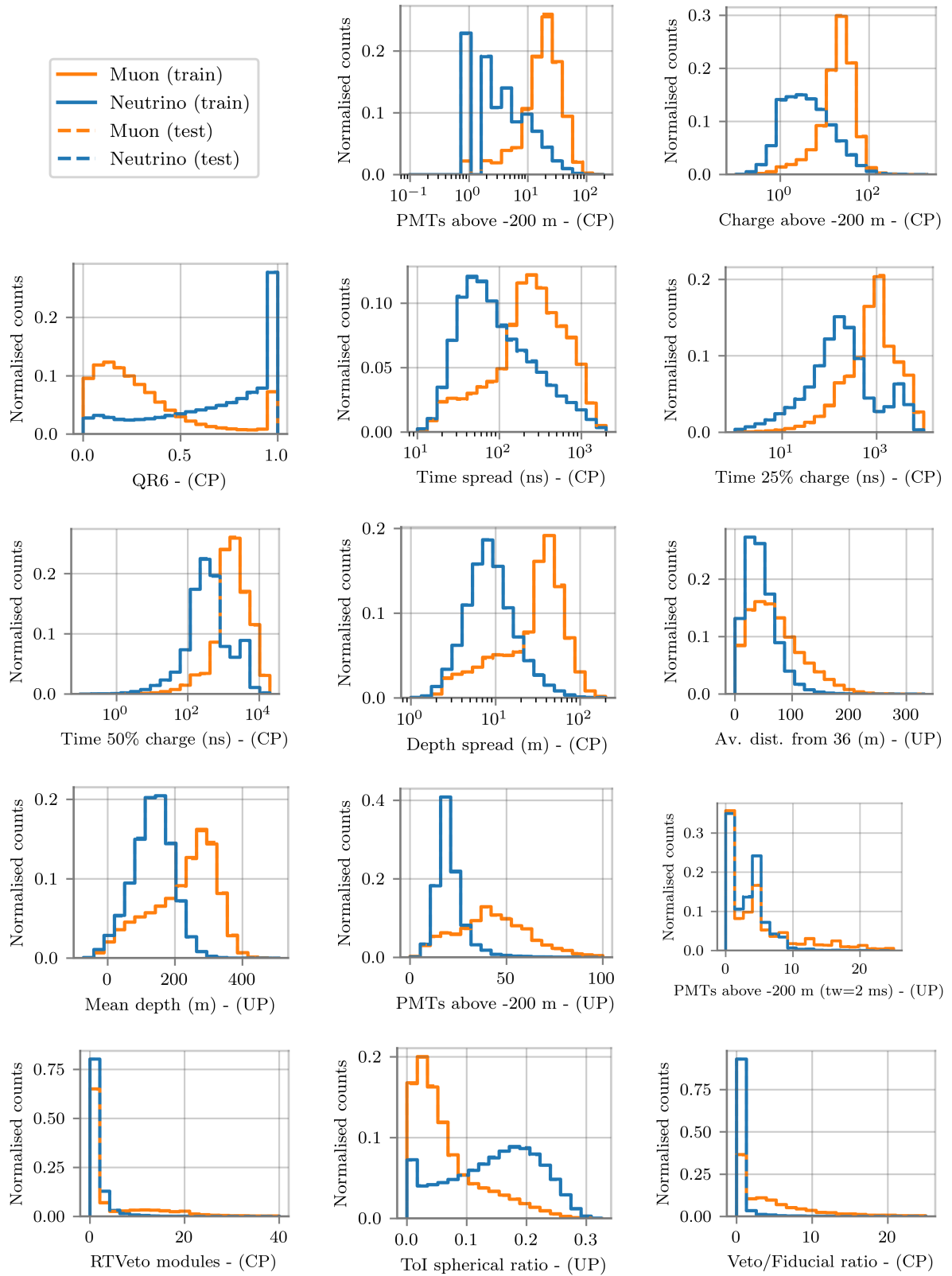


Figure C.2: Part 2 of variables used for training the GBDT for the first iteration to separate neutrinos from atmospheric muons. Lines show the bin data for the test and train samples, although they overlap in most cases.

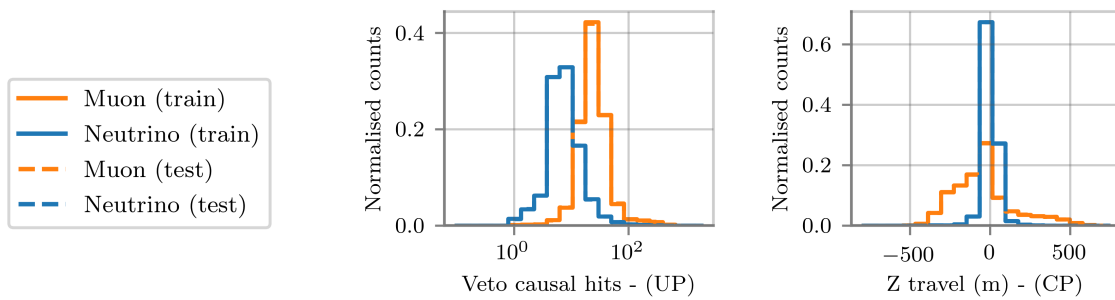


Figure C.3: Part 3 showcasing the variables used for training the GBDT for the first iteration to separate neutrinos from atmospheric muons. Lines show the bin data for the test and train samples, although they overlap in most cases.

D

Appendix D: variables used to train the GBDT to select neutrinos over muons - 2

This Appendix shows the variables used to train the GBDT for the second iteration to select neutrinos over atmospheric muons explained in Section 8.3.6. Each variable has been calculated from the clean pulses (CP) or the unclean pulses set (UP), indicated on the figure label.

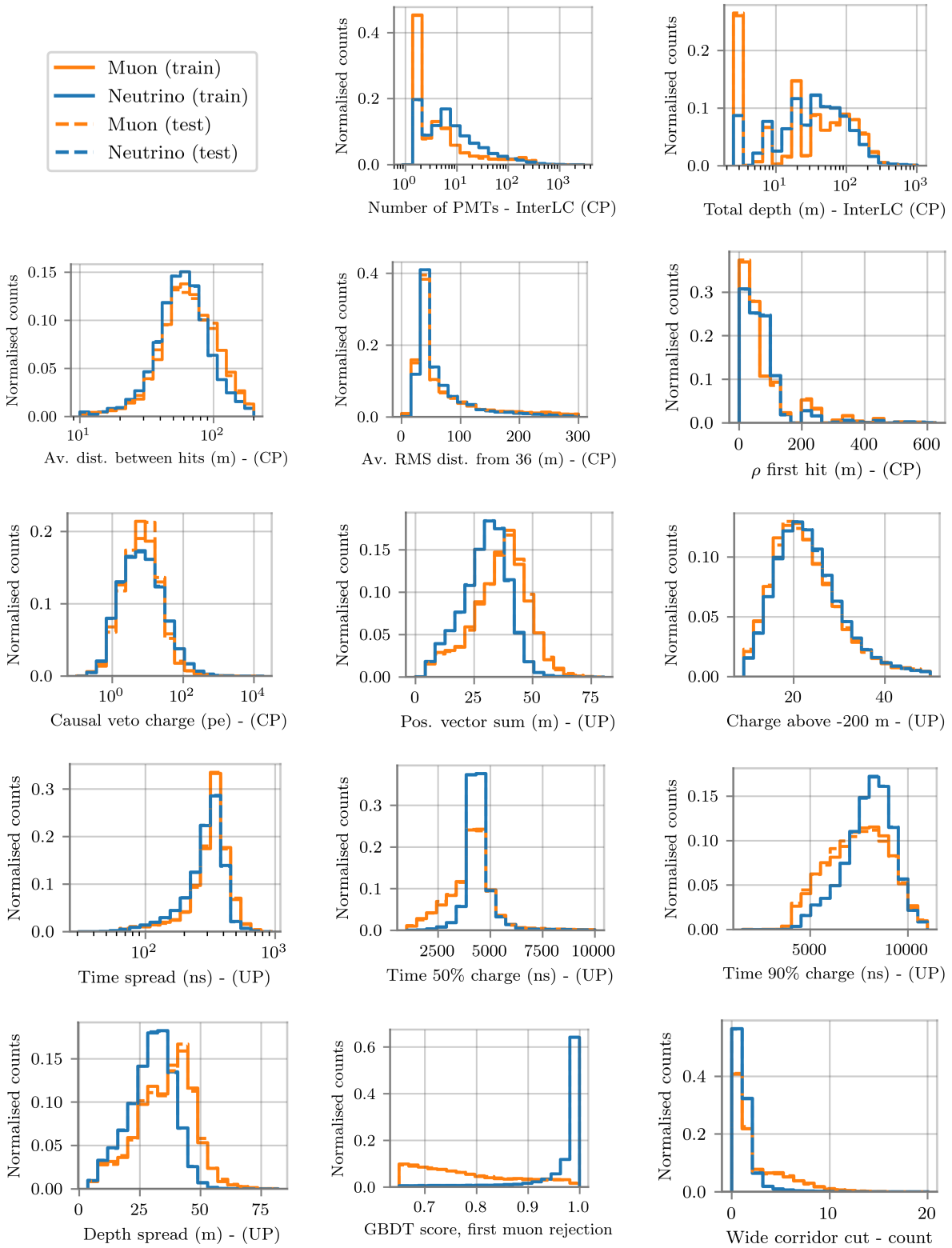


Figure D.1: Part 1 of variables used for training the GBDT for the second iteration to separate neutrinos from atmospheric muons. Lines show the bin data for the test and train samples, although they overlap in most cases.

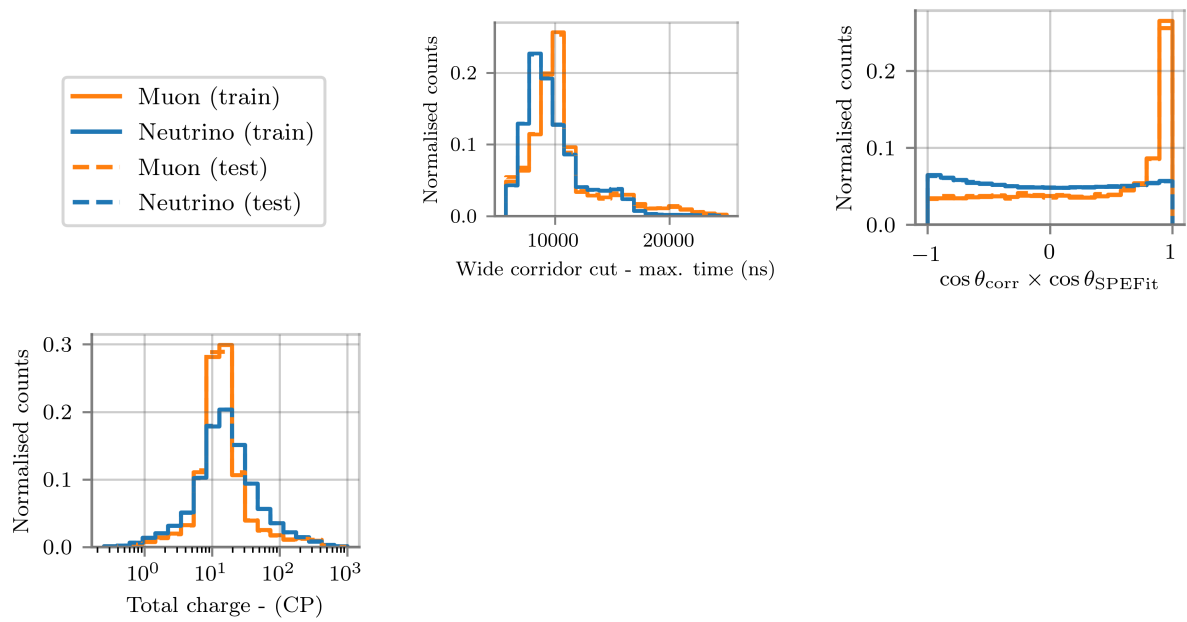


Figure D.2: Part 2 of variables used for training the GBDT for the second iteration to separate neutrinos from atmospheric muons. Lines show the bin data for the test and train samples, although they overlap in most cases.

Appendix E: Alternative selection focused on lower energetic events

This Appendix shows the results of performing the event selection of Chapter 8 focusing on low-energy neutrinos, with the goal of improving the results for the energy range [0.5, 5] GeV. The focus is set on keeping neutrinos below 10 GeV while rejecting higher energetic ones in order to decrease the background of atmospheric neutrinos in energies where no signal flux is assumed and increase the performance of the event selection at the lowest energies. 10 GeV is chosen instead of 5 GeV due to the sample size, being too small to train otherwise.

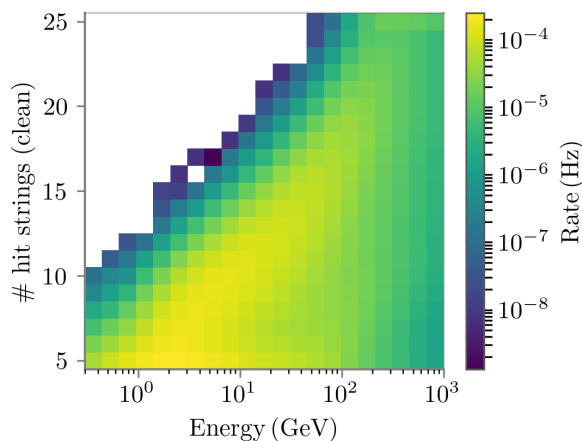


Figure E.1: Neutrino rate classified as a function of its energy and the number of strings that has detected the event in the cleaned pulses set.

After filter level, cuts to reject high-energy neutrinos are made. To perform these cuts, different combinations of simple variables have been analyzed, with the choice for the variables shown here. Each cut has been evaluated by observing the distribution of the variables in different energy bins for the neutrino sample. For example, this is shown in Figure E.1 for a variable that counts for the number of strings in which the event has been detected. Generally, higher energetic neutrinos will be detected in more strings, as can be seen in the figure. Using this feature to perform a cut on the neutrino sample, Figure E.2 is obtained. On the left, it is shown how the neutrino spectrum changes depending on the value of the cut. The ratio of events lost by each cut in comparison to the rate after the filter is shown on the right side of the figure. This is shown for all neutrino events and only for neutrinos with energies smaller than or greater than 10 GeV. Using this information, the cuts have been chosen at values where the ratio of rejected events at energies below 10 GeV is kept above 95%, while reducing the rate above 10 GeV as much as possible. These cuts are:

- Number of hits in IceCube ≤ 2 (clean pulses)
- Number of hit strings ≤ 12 (clean pulses)
- Number of hits in DeepCore fiducial region ≤ 14 (unclean pulses)

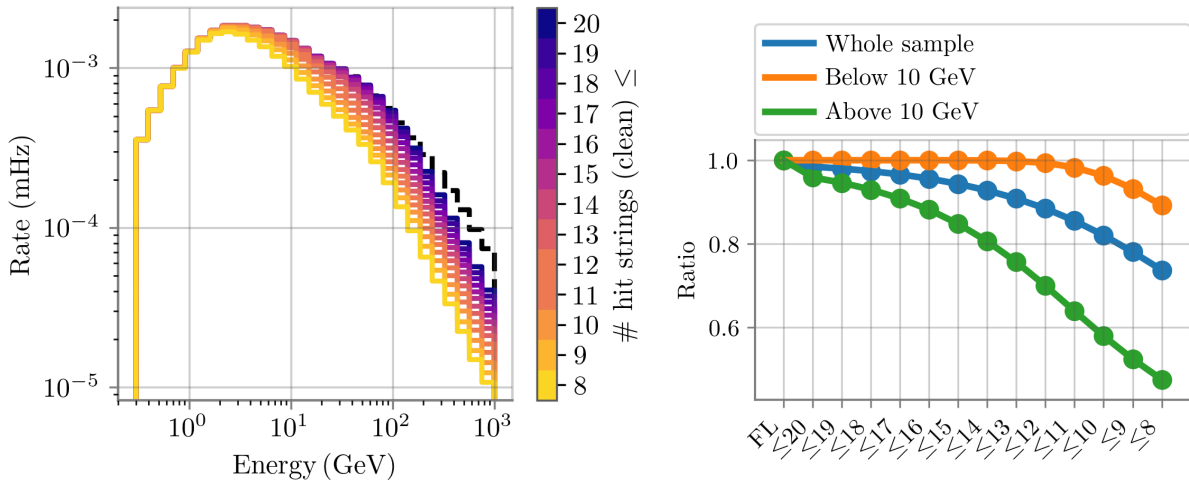


Figure E.2: **Left:** neutrino rate as a function of the energy when a cut on the number of strings detecting the event is made, using clean pulses. Black dashed line stands for the rate after filter. **Right:** ratio of remaining events after a cut depending on the number of strings detecting the event is made, with respect to the filter level (FL)

After these cuts, the rate of atmospheric neutrino events above 10 GeV is reduced by a factor ~ 3 , while $\sim 95\%$ of events below 10 GeV survive.

Then, the process is similar to what was shown in Chapter 8 for both selection approaches, in which a GBDT is first trained to select neutrinos over the module's noise and then two GBDTs (only one GBDT if the shorter time window of 3 s is considered) to select neutrinos over atmospheric muons. However, the importance difference is that only neutrino events below 10 GeV are used now for training.

The event selection uses a different combination of variables now that only events below 10 GeV are used for training. The whole selection is not shown in as much detail as it was done for the results in Chapter 8. The threshold after the first GBDT is set to a much smaller level than in Section 8.3.4, since this is responsible for losing most events at low energies. However, this has the consequence of keeping low energetic events with a significant ratio of hits due to noise, which affects the performance of the following selections over muons. This is shown in Figure E.4 for the last GBDT trained to separate neutrinos from muons, although a similar pattern is visible in the first iteration as well. The distribution of the output of the GBDT for muons peaks at 0, as expected. However, the neutrino distribution not only peaks at 1, but also accumulates misclassified neutrino events at 0. This also occurs in the previous step, when the GBDT is trained to select neutrinos over muons for the first time. Note that only neutrinos with energies ≤ 10 GeV are shown in the figure for both the train and the testing samples. This misclassification of events could not be avoided by any other of the many combinations of variables that were tested, nor by modifying the hyperparameters of the GBDTs. The train and test muon samples start to show discrepancies due to the low number of events left, since the cuts done prior to the training also reduce the muon rate and the events left at this stage are few¹.

However, the approach is indeed successful in having a final sample with more low-energy

¹The train/test split of each sample for the two GBDTs trained to separate neutrinos from muons also needed to be adjusted due to the differences between sample sizes.

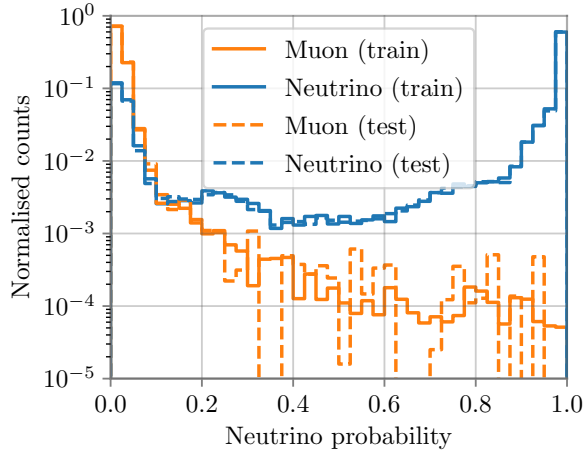


Figure E.3: Histogram showing the neutrino probability score given by the GBDT for the two set (train or test) of each class (neutrino or atmospheric muon) of the GBDT trained for the second iteration to separate neutrinos from atmospheric muons when a cut prior to the GBDT is done to reject high-energy neutrinos. Both train and test was done only with neutrinos of ≤ 10 GeV.

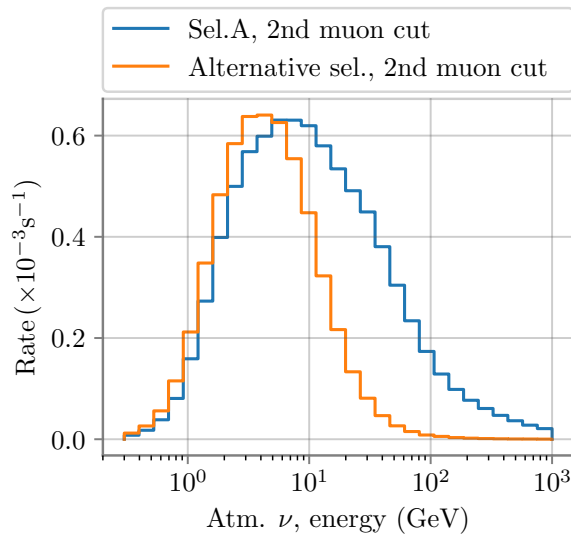


Figure E.4: Atmospheric neutrino sample after the event selection A explained in Chapter 8, and the alternative event selection explained here which focus on low energy neutrinos.

neutrinos, although the difference is not very large. This is visible when comparing the final rates of atmospheric neutrinos after the last GBDT (2nd selection over muons) of this selection approach with the selection performed in Section 8.3.7, which is shown Figure E.4. The results obtained with the selection approach done in this Appendix, named alternative selection, accumulate more neutrino events at low energies. However, despite the efforts, most neutrinos at low energy are still being lost.

When weighing the events with the signal flux and calculating the results shown in Section 8.4, there is an improvement when the smaller energy range of $[0.5, 5]$ GeV is used. Concretely, the 90% upper limit on the isotropic energy for the source GW170817 lowers by $\sim 10\%$ for both time windows considered in the analysis¹. This improvement is too small to consider using this selection in the final results, considering that the GBDTs are less robust due to the low number of events for training. Therefore, it was decided to leave this result out of Chapter 8, but it is still included in this Appendix, since these findings might be useful for someone considering doing a similar analysis. If this is the case, the analysis shall first aim to improve the existing cleaning algorithm, so that those noise-dominated events can be better cleaned up. Otherwise, it is difficult to achieve a significant improvement in the selection of the lowest events, and they will be lost at one

¹Note that, for the shorter time window, the last step of the GBDT is not done.

or another stage of the selection process.

Bibliography

- [1] U.F. Katz and C. Spiering, *High-Energy Neutrino Astrophysics: Status and Perspectives*, *Prog. Part. Nucl. Phys.* **67** (2012) 651 [arXiv: 1111.0507].
- [2] S.M. Bilenky, *Neutrino. History of a unique particle*, *Eur. Phys. J. H* **38** (2013) 345 [arXiv: 1210.3065].
- [3] PARTICLE DATA GROUP collaboration, *Review of Particle Physics*, *PTEP* **2020** (2020) 083C01.
- [4] P.F. De Salas, S. Gariazzo, O. Mena, C.A. Ternes and M. Tórtola, *Neutrino Mass Ordering from Oscillations and Beyond: 2018 Status and Future Prospects*, *Front. Astron. Space Sci.* **5** (2018) 36 [arXiv: 1806.11051].
- [5] W. Pauli, *Über den zusammenhang des abschlusses der elektronengruppen im atom mit der komplexstruktur der spektren*, *Zeitschrift für Physik* **31** (1925) 765.
- [6] Wikipedia, “Standard Model — Wikipedia, the free encyclopedia.”
<http://en.wikipedia.org/w/index.php?title=Standard%20Model&oldid=1083767944>, accessed 03-May-2022, 2022.
- [7] SNO+ collaboration, *Status and Prospects of the SNO+ Experiment*, *PoS PANIC2021* (2022) 274.
- [8] SUPER-KAMIOKANDE collaboration, *Evidence for oscillation of atmospheric neutrinos*, *Phys. Rev. Lett.* **81** (1998) 1562 [arXiv: hep-ex/9807003].
- [9] SNO collaboration, *Measurement of the rate of $\nu_e + d \rightarrow p + p + e^-$ interactions produced by 8B solar neutrinos at the Sudbury Neutrino Observatory*, *Phys. Rev. Lett.* **87** (2001) 071301 [arXiv: nucl-ex/0106015].
- [10] KATRIN collaboration, *KATRIN: status and prospects for the neutrino mass and beyond*, *J. Phys. G* **49** (2022) 100501 [arXiv: 2203.08059].
- [11] B. Pontecorvo, *Mesonium and anti-mesonium*, *Sov. Phys. JETP* **6** (1957) 429.
- [12] B. Pontecorvo, *Neutrino Experiments and the Problem of Conservation of Leptonic Charge*, *Soviet Journal of Experimental and Theoretical Physics* **26** (1968) 984.
- [13] R. Davis, D.S. Harmer and K.C. Hoffman, *Search for neutrinos from the sun*, *Phys. Rev. Lett.* **20** (1968) 1205.
- [14] T.-K. Kuo and J.T. Pantaleone, *The Solar Neutrino Problem and Three Neutrino Oscillations*, *Phys. Rev. Lett.* **57** (1986) 1805.
- [15] E. Kearns, *Experimental measurements of atmospheric neutrinos*, *Nucl. Phys. B Proc. Suppl.* **70** (1999) 315 [arXiv: hep-ex/9803007].
- [16] SUPER-KAMIOKANDE collaboration, *Evidence for oscillation of atmospheric neutrinos*, *Phys. Rev. Lett.* **81** (1998) 1562 [arXiv: hep-ex/9807003].
- [17] KATRIN collaboration, *The KATRIN Neutrino Mass Experiment*, *Nucl. Instrum. Meth. A* **623** (2010) 442 [arXiv: 0810.3281].
- [18] I. Esteban, M.C. Gonzalez-Garcia, M. Maltoni, T. Schwetz and A. Zhou, *The fate of hints: updated global analysis of three-flavor neutrino oscillations*, *JHEP* **09** (2020) 178 [arXiv: 2007.14792].

- [19] ν FIT, *v5.1: Three-neutrino fit based on data available in October 2021*, <http://www.nu-fit.org>, accessed 09-Jan-2023.
- [20] SNO collaboration, *Direct evidence for neutrino flavor transformation from neutral current interactions in the Sudbury Neutrino Observatory*, *Phys. Rev. Lett.* **89** (2002) 011301 [arXiv: [nucl-ex/0204008](https://arxiv.org/abs/nuc1-ex/0204008)].
- [21] JUNO collaboration, *Neutrino Physics with JUNO*, *J. Phys. G* **43** (2016) 030401 [arXiv: [1507.05613](https://arxiv.org/abs/1507.05613)].
- [22] KM3NET collaboration, *KM3NeT - ORCA: Measuring neutrino oscillations and the mass hierarchy in the Mediterranean Sea*, *PoS ICRC2015* (2016) 1140.
- [23] ICECUBE collaboration, *The IceCube Upgrade - Design and Science Goals*, *PoS ICRC2019* (2021) 1031 [arXiv: [1908.09441](https://arxiv.org/abs/1908.09441)].
- [24] T.K. Gaisser, R. Engel and E. Resconi, *Cosmic rays*, in *Cosmic Rays and Particle Physics*, Cambridge University Press (2016), doi: [10.1017/CBO9781139192194.003](https://doi.org/10.1017/CBO9781139192194.003).
- [25] C. Ding, N. Globus and G.R. Farrar, *The Imprint of Large Scale Structure on the Ultra-High-Energy Cosmic Ray Sky*, *Astrophys. J. Lett.* **913** (2021) L13 [arXiv: [2101.04564](https://arxiv.org/abs/2101.04564)].
- [26] L.A. Anchordoqui, *Ultra-High-Energy Cosmic Rays*, *Phys. Rept.* **801** (2019) 1 [arXiv: [1807.09645](https://arxiv.org/abs/1807.09645)].
- [27] K.-H. Kampert and P. Tinyakov, *Cosmic rays from the ankle to the cutoff*, *Comptes Rendus Physique* **15** (2014) 318 [arXiv: [1405.0575](https://arxiv.org/abs/1405.0575)].
- [28] K. Greisen, *End to the cosmic-ray spectrum?*, *Phys. Rev. Lett.* **16** (1966) 748.
- [29] G.T. Zatsepin and V.A. Kuz'min, *Upper Limit of the Spectrum of Cosmic Rays*, *Soviet Journal of Experimental and Theoretical Physics Letters* **4** (1966) 78.
- [30] PIERRE AUGER collaboration, *The ultra-high-energy cosmic-ray sky above 32 EeV viewed from the Pierre Auger Observatory*, *PoS ICRC2021* (2021) 307.
- [31] PIERRE AUGER collaboration, *Features of the Energy Spectrum of Cosmic Rays above 2.5×10^{18} eV Using the Pierre Auger Observatory*, *Phys. Rev. Lett.* **125** (2020) 121106 [arXiv: [2008.06488](https://arxiv.org/abs/2008.06488)].
- [32] H.P. Dembinski, R. Engel, A. Fedynitch, T. Gaisser, F. Riehn and T. Stanev, *Data-driven model of the cosmic-ray flux and mass composition from 10 GeV to 10^{11} GeV*, *PoS ICRC2017* (2018) 533 [arXiv: [1711.11432](https://arxiv.org/abs/1711.11432)].
- [33] V.S. Berezhinsky and G.T. Zatsepin, *Cosmic neutrinos of superhigh energy*, *Yad. Fiz.* **11** (1970) 200.
- [34] E. Fermi, *On the origin of the cosmic radiation*, *Phys. Rev.* **75** (1949) 1169.
- [35] PIERRE AUGER collaboration, *The Pierre Auger Cosmic Ray Observatory*, *Nucl. Instrum. Meth. A* **798** (2015) 172 [arXiv: [1502.01323](https://arxiv.org/abs/1502.01323)].
- [36] M. Sajjad Athar et al., *Status and perspectives of neutrino physics*, *Prog. Part. Nucl. Phys.* **124** (2022) 103947 [arXiv: [2111.07586](https://arxiv.org/abs/2111.07586)].
- [37] G.D.O. Gann, K. Zuber, D. Bemmerer and A. Serenelli, *The Future of Solar Neutrinos*, *Ann. Rev. Nucl. Part. Sci.* **71** (2021) 491 [arXiv: [2107.08613](https://arxiv.org/abs/2107.08613)].
- [38] N. Vinyoles, A.M. Serenelli, F.L. Villante, S. Basu, J. Bergström, M.C. Gonzalez-Garcia et al., *A new Generation of Standard Solar Models*, *Astrophys. J.* **835** (2017) 202 [arXiv: [1611.09867](https://arxiv.org/abs/1611.09867)].

- [39] J. Billard, L. Strigari and E. Figueroa-Feliciano, *Implication of neutrino backgrounds on the reach of next generation dark matter direct detection experiments*, *Phys. Rev.* **D89** (2014) 023524 [arXiv: 1307.5458].
- [40] ICECUBE collaboration, *The Design and Performance of IceCube DeepCore*, *Astropart. Phys.* **35** (2012) 615 [arXiv: 1109.6096].
- [41] O. Pisanti, *Astrophysical neutrinos: theory*, *J. Phys. Conf. Ser.* **1263** (2019) 012004 [arXiv: 1906.12258].
- [42] Y. Farzan and A.Y. Smirnov, *Coherence and oscillations of cosmic neutrinos*, *Nucl. Phys. B* **805** (2008) 356 [arXiv: 0803.0495].
- [43] A. Franceschini, G. Rodighiero and M. Vaccari, *The extragalactic optical-infrared background radiations, their time evolution and the cosmic photon-photon opacity*, *Astron. Astrophys.* **487** (2008) 837 [arXiv: 0805.1841].
- [44] ICECUBE collaboration, *Evidence for High-Energy Extraterrestrial Neutrinos at the IceCube Detector*, *Science* **342** (2013) 1242856 [arXiv: 1311.5238].
- [45] D.J. Croton, V. Springel, S.D.M. White, G. De Lucia, C.S. Frenk, L. Gao et al., *The Many lives of AGN: Cooling flows, black holes and the luminosities and colours of galaxies*, *Mon. Not. Roy. Astron. Soc.* **365** (2006) 11 [arXiv: astro-ph/0602065].
- [46] J.K. Becker, *High-energy neutrinos in the context of multimessenger physics*, *Phys. Rept.* **458** (2008) 173 [arXiv: 0710.1557].
- [47] ICECUBE, FERMI-LAT, MAGIC, AGILE, ASAS-SN, HAWC, H.E.S.S., INTEGRAL, KANATA, KISO, KAPTEYN, LIVERPOOL TELESCOPE, SUBARU, SWIFT NUSTAR, VERITAS, VLA/17B-403 collaboration, *Multimessenger observations of a flaring blazar coincident with high-energy neutrino IceCube-170922A*, *Science* **361** (2018) eaat1378 [arXiv: 1807.08816].
- [48] ICECUBE collaboration, *Evidence for neutrino emission from the nearby active galaxy NGC 1068*, *Science* **378** (2022) 538 [arXiv: 2211.09972].
- [49] A. Bell, K. Schure, B. Reville and G. Giacinti, *Cosmic ray acceleration and escape from supernova remnants*, *Mon. Not. Roy. Astron. Soc.* **431** (2013) 415 [arXiv: 1301.7264].
- [50] ICECUBE collaboration, *Search for High-energy Neutrino Emission from Galactic X-Ray Binaries with IceCube*, *Astrophys. J. Lett.* **930** (2022) L24 [arXiv: 2202.11722].
- [51] G.J. Fishman and C.A. Meegan, *Gamma-ray bursts*, *Ann. Rev. Astron. Astrophys.* **33** (1995) 415.
- [52] S. Woosley and T. Janka, *The physics of core-collapse supernovae*, *Nature Phys.* **1** (2005) 147 [arXiv: astro-ph/0601261].
- [53] H.A. Bethe, *Supernova mechanisms*, *Rev. Mod. Phys.* **62** (1990) 801.
- [54] KAMIOKANDE-II collaboration, *Observation of a Neutrino Burst from the Supernova SN 1987a*, *Phys. Rev. Lett.* **58** (1987) 1490.
- [55] R.M. Bionta et al., *Observation of a Neutrino Burst in Coincidence with Supernova SN 1987a in the Large Magellanic Cloud*, *Phys. Rev. Lett.* **58** (1987) 1494.
- [56] E.N. Alekseev, L.N. Alekseeva, I.V. Krivosheina and V.I. Volchenko, *Detection of the Neutrino Signal From SN1987A in the LMC Using the Inr Baksan Underground Scintillation Telescope*, *Phys. Lett. B* **205** (1988) 209.

- [57] K. Rozwadowska, F. Vissani and E. Cappellaro, *On the rate of core collapse supernovae in the Milky Way*, *New Astron.* **83** (2021) 101498 [arXiv: 2009.03438].
- [58] C. Chiosi, *Hydrostatic Evolution of Stars and Chemical Evolution of Galaxies*, in *Saas-Fee Advanced Course 16: Nucleosynthesis and Chemical Evolution*, J. Audouze, C. Chiosi and S.E. Woosley, eds., p. 199 (1986).
- [59] M.P. Fewell, *The atomic nuclide with the highest mean binding energy*, *Am. J. Phys.* **63** (1995) 653.
- [60] H. Suzuki, *Physics and Astrophysics of Neutrinos*, Springer (2014).
- [61] A. Mirizzi, I. Tamborra, H.-T. Janka, N. Saviano, K. Scholberg, R. Bollig et al., *Supernova Neutrinos: Production, Oscillations and Detection*, *Riv. Nuovo Cim.* **39** (2016) 1 [arXiv: 1508.00785].
- [62] M. Herant, S.A. Colgate, W. Benz and C. Fryer, *Neutrinos and supernovae*, *Los Alamos Sci.* **25** (1997) 164.
- [63] H.-T. Janka et al., *Theory of Core-Collapse Supernovae*, *Phys. Rept.* **442** (2007) 38 [arXiv: astro-ph/0612072].
- [64] T.M. Tauris et al., *Formation of Double Neutron Star Systems*, *Astrophys. J.* **846** (2017) 170 [arXiv: 1706.09438].
- [65] A. Abramovici et al., *LIGO: The Laser interferometer gravitational wave observatory*, *Science* **256** (1992) 325.
- [66] VIRGO collaboration, *Advanced Virgo: a second-generation interferometric gravitational wave detector*, *Class. Quant. Grav.* **32** (2015) 024001 [arXiv: 1408.3978].
- [67] KAGRA collaboration, *Overview of KAGRA: Detector design and construction history*, *PTEP* **2021** (2021) 05A101 [arXiv: 2005.05574].
- [68] LIGO, VIRGO collaboration, *Observation of Gravitational Waves from a Binary Black Hole Merger*, in *Centennial of General Relativity: A Celebration*, C.A.Z. Vasconcellos, ed., pp. 291–311 (2017), doi: 10.1142/9789814699662_0011.
- [69] A.H. Nitz, S. Kumar, Y.-F. Wang, S. Kastha, S. Wu, M. Schäfer et al., *4-OGC: Catalog of gravitational waves from compact-binary mergers*, 12, 2021, [arXiv: 2112.06878].
- [70] M. Maggiore et al., *Science Case for the Einstein Telescope*, *JCAP* **03** (2020) 050 [arXiv: 1912.02622].
- [71] M. Ruiz, S.L. Shapiro and A. Tsokaros, *Multimessenger Binary Mergers Containing Neutron Stars: Gravitational Waves, Jets, and γ -Ray Bursts*, *Front. Astron. Space Sci.* **8** (2021) 39 [arXiv: 2102.03366].
- [72] LIGO SCIENTIFIC, VIRGO, KAGRA collaboration, *GWTC-3: Compact Binary Coalescences Observed by LIGO and Virgo During the Second Part of the Third Observing Run*, 11, 2021, [arXiv: 2111.03606].
- [73] LIGO SCIENTIFIC, VIRGO, FERMI GBM, INTEGRAL, ICECUBE, ASTRO SAT CADMIUM ZINC TELLURIDE IMAGER TEAM, IPN, INSIGHT-HXMT, ANTARES, SWIFT, AGILE TEAM, 1M2H TEAM, DARK ENERGY CAMERA GW-EM, DES, DLT40, GRAWITA, FERMI-LAT, ATCA, ASKAP, LAS CUMBRES OBSERVATORY GROUP, OZGRAV, DWF (DEEPER WIDER FASTER PROGRAM), AST3, CAASTRO, VINROUGE, MASTER, J-GEM, GROWTH, JAGWAR, CALTECHNRAO, TTU-NRAO, NUSTAR, PAN-STARRS, MAXI TEAM, TZAC

- CONSORTIUM, KU, NORDIC OPTICAL TELESCOPE, EPESSTO, GROND, TEXAS TECH UNIVERSITY, SALT GROUP, TOROS, BOOTES, MWA, CALET, IKI-GW FOLLOW-UP, H.E.S.S., LOFAR, LWA, HAWC, PIERRE AUGER, ALMA, EURO VLBI TEAM, PI OF SKY, CHANDRA TEAM AT MCGILL UNIVERSITY, DFN, ATLAS TELESCOPES, HIGH TIME RESOLUTION UNIVERSE SURVEY, RIMAS, RATIR, SKA SOUTH AFRICA/MEERKAT collaboration, *Multi-messenger Observations of a Binary Neutron Star Merger*, *Astrophys. J. Lett.* **848** (2017) L12 [arXiv: 1710.05833].
- [74] P. Mészáros, D.B. Fox, C. Hanna and K. Murase, *Multi-Messenger Astrophysics*, *Nature Rev. Phys.* **1** (2019) 585 [arXiv: 1906.10212].
- [75] ICECUBE collaboration, *IceCube Search for Neutrinos Coincident with Compact Binary Mergers from LIGO-Virgo's First Gravitational-wave Transient Catalog*, *Astrophys. J. Lett.* **898** (2020) L10 [arXiv: 2004.02910].
- [76] R. Abbasi et al., *IceCube search for neutrinos coincident with gravitational wave events from LIGO/Virgo run O3*, 8, 2022, [arXiv: 2208.09532].
- [77] J.A. Formaggio and G.P. Zeller, *From eV to EeV: Neutrino Cross Sections Across Energy Scales*, *Rev. Mod. Phys.* **84** (2012) 1307 [arXiv: 1305.7513].
- [78] L. Classen, *The mDOM - a multi-PMT digital optical module for the IceCube-Gen2 neutrino telescope*, Friedrich Alexander-Universität Erlangen-Nürnberg, *Ph.D. thesis*, 2017.
- [79] MINOS collaboration, *The MINOS detectors*, in *29th International Cosmic Ray Conference*, 7, 2005 [arXiv: hep-ex/0507018].
- [80] NOvA collaboration, *NOvA: Proposal to Build a 30 Kiloton Off-Axis Detector to Study $\nu_\mu \rightarrow \nu_e$ Oscillations in the NuMI Beamline*, 3, 2004, [arXiv: hep-ex/0503053].
- [81] T. Kirsten, *Retrospect of GALLEX/GNO*, *J. Phys. Conf. Ser.* **120** (2008) 052013.
- [82] J.V. Jelley, *Cerenkov radiation and its applications*, *British Journal of Applied Physics* **6** (1955) 227.
- [83] J.D. Jackson, *Classical electrodynamics*, Wiley, New York, NY, 3rd ed. ed. (1999).
- [84] M. A. Unland Elorrieta, *Studies on dark rates induced by radioactive decays of the multi-PMT digital optical module for future IceCube extensions*, Westfälische Wilhelms-Universität Münster, *Master thesis*, 2017.
- [85] I.M. Frank and I.E. Tamm, *Coherent visible radiation of fast electrons passing through matter*, *Compt. Rend. Acad. Sci. URSS* **14** (1937) 109.
- [86] SUPER-KAMIOKANDE collaboration, *The Super-Kamiokande detector*, *Nucl. Instrum. Meth. A* **501** (2003) 418.
- [87] “Super-kamiokande website, visited at 11.10.2021.” <http://www-sk.icrr.u-tokyo.ac.jp/sk/index-e.html>.
- [88] K. Abe et al., *Letter of Intent: The Hyper-Kamiokande Experiment — Detector Design and Physics Potential* —, 9, 2011, [arXiv: 1109.3262].
- [89] ICECUBE collaboration, *The IceCube Neutrino Observatory: Instrumentation and Online Systems*, *JINST* **12** (2017) P03012 [arXiv: 1612.05093].
- [90] E. Andres et al., *The AMANDA neutrino telescope: Principle of operation and first results*, *Astropart. Phys.* **13** (2000) 1 [arXiv: astro-ph/9906203].
- [91] ICECUBE collaboration, *IceCube: Status and Results*, 8, 2011, [arXiv: 1108.1838].

- [92] J.P. Yañez and A. Kouchner, *Measurement of atmospheric neutrino oscillations with very large volume neutrino telescopes*, *Adv. High Energy Phys.* **2015** (2015) 271968 [arXiv: [1509.08404](#)].
- [93] ICECUBE collaboration, *IceTop: The surface component of IceCube*, *Nucl. Instrum. Meth. A* **700** (2013) 188 [arXiv: [1207.6326](#)].
- [94] ICECUBE collaboration, *Measurement of the cosmic ray energy spectrum with IceTop-73*, *Phys. Rev. D* **88** (2013) 042004 [arXiv: [1307.3795](#)].
- [95] ICECUBE collaboration, *Study of High pT Muons in IceCube*, 9, 2009, [arXiv: [0909.0055](#)].
- [96] <https://www.hamamatsu.com/eu/en/product/type/R7081/index.html>, visited on 18.10.2021).
- [97] ICECUBE collaboration, *Design and production of the IceCube digital optical module*, *Nucl. Instrum. Meth. A* **567** (2006) 214.
- [98] C. Spiering, *Neutrino Detectors Under Water and Ice*, in *Particle Physics Reference Library: Volume 2: Detectors for Particles and Radiation*, C.W. Fabjan and H. Schopper, eds., pp. 785–822 (2020), doi: [10.1007/978-3-030-35318-6_17](#).
- [99] A.G. Wright, *The Photomultiplier Handbook*, Oxford University Press (aug, 2017), [10.1093/oso/9780199565092.001.0001](#).
- [100] Hamamatsu Photonics K. K., *Photomultiplier Tubes: Basics and Applications*, 3a ed. (2007).
- [101] ICECUBE collaboration, *Calibration and Characterization of the IceCube Photomultiplier Tube*, *Nucl. Instrum. Meth. A* **618** (2010) 139 [arXiv: [1002.2442](#)].
- [102] ICECUBE collaboration, *Measurement of South Pole ice transparency with the IceCube LED calibration system*, *Nucl. Instrum. Meth. A* **711** (2013) 73 [arXiv: [1301.5361](#)].
- [103] M. Rongen, *Kalibration des IceCube Neutrino-Observatoriums*, RWTH Aachen University, **Ph.D thesis**, 2019.
- [104] ICECUBE collaboration, *South Pole glacial climate reconstruction from multi-borehole laser particulate stratigraphy*, *J. Glaciol.* **59** (2013) 1117.
- [105] ICECUBE collaboration, *IceCube performance with artificial light sources: The road to cascade analyses*, in *30th International Cosmic Ray Conference*, vol. 3, pp. 1233–1236, 7, 2007.
- [106] S.-O. Flyckt and C. Marmonier, *Photomultiplier tubes - principles and applications*, Photonis (2002).
- [107] K. Helbing et al., *Light emission in Amanda pressure spheres*, AMANDA-internal report, 2003.
- [108] ICECUBE collaboration, *An improved muon track reconstruction for IceCube*, *PoS ICRC2019* (2021) 846 [arXiv: [1908.07961](#)].
- [109] D. Chirkin and W. Rhode, *Propagating leptons through matter with Muon Monte Carlo (MMC)*, 2016, [arXiv: [hep-ph/0407075](#)].
- [110] ICECUBE collaboration, *An improved method for measuring muon energy using the truncated mean of dE/dx* , *Nucl. Instrum. Meth. A* **703** (2013) 190 [arXiv: [1208.3430](#)].

- [111] ICECUBE collaboration, *Energy Reconstruction Methods in the IceCube Neutrino Telescope*, *JINST* **9** (2014) P03009 [arXiv: 1311.4767].
- [112] J.H. Koehne, K. Frantzen, M. Schmitz, T. Fuchs, W. Rhode, D. Chirkin et al., *PROPOSAL: A tool for propagation of charged leptons*, *Comput. Phys. Commun.* **184** (2013) 2070.
- [113] ICECUBE collaboration, *First observation of PeV-energy neutrinos with IceCube*, *Phys. Rev. Lett.* **111** (2013) 021103 [arXiv: 1304.5356].
- [114] M. Meier, *Search for astrophysical tau neutrinos using 7.5 years of IceCube data*, Tech. U., Dortmund (main), Ph.D. thesis, 2019.
- [115] ICECUBE collaboration, *Tau neutrinos in IceCube*, *J. Phys. Conf. Ser.* **60** (2007) 227.
- [116] ICECUBE collaboration, *Determining neutrino oscillation parameters from atmospheric muon neutrino disappearance with three years of IceCube DeepCore data*, *Phys. Rev. D* **91** (2015) 072004 [arXiv: 1410.7227].
- [117] ICECUBE collaboration, *Measurement of Atmospheric Neutrino Oscillations at 6–56 GeV with IceCube DeepCore*, *Phys. Rev. Lett.* **120** (2018) 071801 [arXiv: 1707.07081].
- [118] ICECUBE collaboration, *Measurement of Atmospheric Tau Neutrino Appearance with IceCube DeepCore*, *Phys. Rev. D* **99** (2019) 032007 [arXiv: 1901.05366].
- [119] ICECUBE collaboration, *Search for Nonstandard Neutrino Interactions with IceCube DeepCore*, *Phys. Rev. D* **97** (2018) 072009 [arXiv: 1709.07079].
- [120] ICECUBE collaboration, *All-flavor constraints on nonstandard neutrino interactions and generalized matter potential with three years of IceCube DeepCore data*, *Phys. Rev. D* **104** (2021) 072006 [arXiv: 2106.07755].
- [121] ICECUBE collaboration, *Search for sterile neutrino mixing using three years of IceCube DeepCore data*, *Phys. Rev. D* **95** (2017) 112002 [arXiv: 1702.05160].
- [122] ICECUBE collaboration, *Search for Neutrinos from Dark Matter Self-Annihilations in the center of the Milky Way with 3 years of IceCube/DeepCore*, *Eur. Phys. J. C* **77** (2017) 627 [arXiv: 1705.08103].
- [123] ICECUBE collaboration, *Evidence for High-Energy Extraterrestrial Neutrinos at the IceCube Detector*, *Science* **342** (2013) 1242856 [arXiv: 1311.5238].
- [124] ICECUBE collaboration, *Observation of High-Energy Astrophysical Neutrinos in Three Years of IceCube Data*, *Phys. Rev. Lett.* **113** (2014) 101101 [arXiv: 1405.5303].
- [125] ICECUBE collaboration, *Measurement of the Diffuse Astrophysical Muon-Neutrino Spectrum with Ten Years of IceCube Data*, *PoS ICRC2019* (2020) 1017 [arXiv: 1908.09551].
- [126] ICECUBE collaboration, *A combined maximum-likelihood analysis of the high-energy astrophysical neutrino flux measured with IceCube*, *Astrophys. J.* **809** (2015) 98 [arXiv: 1507.03991].
- [127] ICECUBE collaboration, *Observation and Characterization of a Cosmic Muon Neutrino Flux from the Northern Hemisphere using six years of IceCube data*, *Astrophys. J.* **833** (2016) 3 [arXiv: 1607.08006].
- [128] ICECUBE collaboration, *Time-Integrated Neutrino Source Searches with 10 Years of IceCube Data*, *Phys. Rev. Lett.* **124** (2020) 051103 [arXiv: 1910.08488].

- [129] ICECUBE collaboration, *The IceCube Realtime Alert System*, *Astropart. Phys.* **92** (2017) 30 [arXiv: 1612.06028].
- [130] ICECUBE collaboration, *Characteristics of the diffuse astrophysical electron and tau neutrino flux with six years of IceCube high energy cascade data*, *Phys. Rev. Lett.* **125** (2020) 121104 [arXiv: 2001.09520].
- [131] P. Padovani, P. Giommi, E. Resconi, T. Glauch, B. Arsioli, N. Sahakyan et al., *Dissecting the region around IceCube-170922A: the blazar TXS 0506+056 as the first cosmic neutrino source*, *Mon. Not. Roy. Astron. Soc.* **480** (2018) 192 [arXiv: 1807.04461].
- [132] ICECUBE collaboration, *Neutrino emission from the direction of the blazar TXS 0506+056 prior to the IceCube-170922A alert*, *Science* **361** (2018) 147 [arXiv: 1807.08794].
- [133] C.S. Kochanek, *Tidal disruption event demographics*, *Mon. Not. Roy. Astron. Soc.* **461** (2016) 371 [arXiv: 1601.06787].
- [134] R. Stein et al., *A tidal disruption event coincident with a high-energy neutrino*, *Nature Astron.* **5** (2021) 510 [arXiv: 2005.05340].
- [135] D.W. Weedman, *Seyfert galaxies*, *Ann. Rev. Astron. Astrophys.* **15** (1977) 69.
- [136] ICECUBE collaboration, *Detection of astrophysical tau neutrino candidates in IceCube*, *Eur. Phys. J. C* **82** (2022) 1031 [arXiv: 2011.03561].
- [137] ICECUBE collaboration, *Detection of a particle shower at the Glashow resonance with IceCube*, *Nature* **591** (2021) 220 [arXiv: 2110.15051].
- [138] S.L. Glashow, *Resonant scattering of antineutrinos*, *Phys. Rev.* **118** (1960) 316.
- [139] ICECUBE-GEN2 collaboration, *IceCube-Gen2: the window to the extreme Universe*, *J. Phys. G* **48** (2021) 060501 [arXiv: 2008.04323].
- [140] ICECUBE collaboration, *D-Egg: new optical sensors for the IceCube Upgrade and Gen2*, *J. Phys. Conf. Ser.* **1468** (2020) 012166.
- [141] ICECUBE collaboration, *A multi-PMT Optical Module for the IceCube Upgrade*, *PoS ICRC2019* (2020) 855 [arXiv: 1908.10802].
- [142] M.A. Unland Elorrieta, R.S. Busse, L. Classen and A. Kappes, *Homogeneity of the photocathode in the Hamamatsu Photomultiplier Tube*, *JINST* **16** (2021) P11038 [arXiv: 2109.13868].
- [143] C.J. Lozano Mariscal, L. Classen, M.A. Unland Elorrieta and A. Kappes, *Sensitivity of multi-PMT optical modules in Antarctic ice to supernova neutrinos of MeV energy*, *Eur. Phys. J. C* **81** (2021) 1058 [arXiv: 2106.14199].
- [144] ICECUBE collaboration, *Performance of the D-Egg optical sensor for the IceCube-Upgrade*, *PoS ICRC2021* (2021) 1042.
- [145] ICECUBE-GEN2 collaboration, *Overview and performance of the D-Egg optical sensor for IceCube-Gen2*, *PoS ICRC2017* (2018) 1051.
- [146] ICECUBE-PINGU collaboration, *Letter of Intent: The Precision IceCube Next Generation Upgrade (PINGU)*, 1, 2014, [arXiv: 1401.2046].
- [147] ICECUBE collaboration, *Electronics Development for the New Photo-Detectors (PDOM and D-Egg) for IceCube-Upgrade*, *PoS ICRC2019* (2020) 966 [arXiv: 1908.11564].

- [148] ICECUBE collaboration, *The Wavelength-shifting Optical Module (WOM) for the IceCube Upgrade*, *PoS ICRC2021* (2021) 1038 [arXiv: 2107.10194].
- [149] ICECUBE-GEN2 collaboration, *Performance studies for a next-generation optical sensor for IceCube-Gen2*, *PoS ICRC2021* (2021) 1041 [arXiv: 2108.05548].
- [150] ICECUBE collaboration, *Camera Calibration for the IceCube Upgrade and Gen2*, *PoS ICRC2021* (2021) 1064 [arXiv: 2107.12186].
- [151] ICECUBE collaboration, *POCAM in the IceCube Upgrade*, *PoS ICRC2021* (2021) 1049 [arXiv: 2108.05298].
- [152] ICECUBE collaboration, *Advances in IceCube ice modelling & what to expect from the Upgrade*, *JINST* **16** (2021) C09014 [arXiv: 2108.03291].
- [153] ICECUBE collaboration, *The Acoustic Module for the IceCube Upgrade*, *PoS ICRC2021* (2021) 1059 [arXiv: 2108.05631].
- [154] ICECUBE collaboration, *Searches for Dark Matter with the IceCube neutrino telescope*, in *International Conference on Neutrinos and Dark Matter*, 2020, doi: 10.31526/ACP.NDM-2020.4.
- [155] ICECUBE-GEN2 collaboration, *The Surface Array planned for IceCube-Gen2*, *PoS ICRC2021* (2021) 407 [arXiv: 2108.00364].
- [156] G.A. Askar'yan, *Excess negative charge of an electron-photon shower and its coherent radio emission*, *Zh. Eksp. Teor. Fiz.* **41** (1961) 616.
- [157] GEANT4 collaboration, *GEANT4—a simulation toolkit*, *Nucl. Instrum. Meth. A* **506** (2003) 250.
- [158] B. Herold, *Simulation and Measurement of Optical Background in the Deep Sea Using a Multi-PMT Optical Module*, Friedrich Alexander-Universität Erlangen-Nürnberg, *Ph.D. thesis*, 2017.
- [159] C. J. Lozano Mariscal, *Studies on the sensitivity of multi-PMT optical modules to supernova neutrinos in the South Pole ice*, Westfälische Wilhelms-Universität Münster, *Master thesis*, 2017.
- [160] L. Evans, *The LHC machine*, *PoS EPS-HEP2009* (2009) 004.
- [161] M.G. Pia, T. Basaglia, Z.W. Bell and P.V. Dressendorfer, *Geant4 in Scientific Literature*, in *NSS/MIC 2009*, pp. 189–194, 2009, doi: 10.1109/NSSMIC.2009.5401810 [arXiv: 0912.0360].
- [162] M. Dittmer, *Characterisation of scintillation light induced by radioactive excitation in the mDOM glass pressure vessel*, Westfälische Wilhelms-Universität Münster, *Master thesis*, 2020.
- [163] J. Schneider, personal communication.
- [164] M. Ackermann et al., *Optical properties of deep glacial ice at the South Pole*, *J. Geophys. Res.* **111** (2006) D13203.
- [165] G. Mie, *Beiträge zur optik trüber medien, speziell kolloidaler metallösungen*, *Annalen der Physik* **330** (1908) 377.
- [166] E. Andres et al., *The AMANDA neutrino telescope: Principle of operation and first results*, *Astropart. Phys.* **13** (2000) 1 [arXiv: astro-ph/9906203].
- [167] K. Woschnagg and P.B. Price, *Temperature dependence of absorption in ice at 532 nm*, *Appl. Opt.* **40** (2001) 2496.

- [168] ICECUBE collaboration, *IceCube Sensitivity for Low-Energy Neutrinos from Nearby Supernovae*, *Astron. Astrophys.* **535** (2011) A109 [arXiv: [1108.0171](#)].
- [169] S. Böser, M. Kowalski, L. Schulte, N.L. Strotjohann and M. Voge, *Detecting extra-galactic supernova neutrinos in the Antarctic ice*, *Astropart. Phys.* **62** (2015) 54 [arXiv: [1304.2553](#)].
- [170] P. Vogel and J.F. Beacom, *Angular distribution of neutron inverse beta decay, $\bar{\nu}_e + p \rightarrow e^+ + n$* , *Phys. Rev.* **D60** (1999) 053003 [arXiv: [hep-ph/9903554](#)].
- [171] T. Totani, K. Sato, H.E. Dalhed and J.R. Wilson, *Future detection of supernova neutrino burst and explosion mechanism*, *Astrophys. J.* **496** (1998) 216 [arXiv: [astro-ph/9710203](#)].
- [172] C. Giunti and C.W. Kim, *Fundamentals of Neutrino Physics and Astrophysics*, Oxford University Press (2007).
- [173] M. Buchkremer. *Electroweak Interactions: Neutral currents in neutrino-lepton elastic scattering experiments*, Université Catholique de Louvain / CP³, 2011.
- [174] P. Antonioli et al., *SNEWS: The Supernova Early Warning System*, *New J. Phys.* **6** (2004) 114 [arXiv: [astro-ph/0406214](#)].
- [175] SNEWS collaboration, *SNEWS 2.0: a next-generation supernova early warning system for multi-messenger astronomy*, *New J. Phys.* **23** (2021) 031201 [arXiv: [2011.00035](#)].
- [176] ICECUBE collaboration, *Supernova Neutrino Detection with IceCube*, *J. Phys. Conf. Ser.* **309** (2011) 012029 [arXiv: [1106.6225](#)].
- [177] T. Totani, K. Sato, H.E. Dalhed and J.R. Wilson, *Future detection of supernova neutrino burst and explosion mechanism*, *The Astrophysical Journal* **496** (1998) 216–225.
- [178] R. Bruijn, *Supernova Detection in IceCube: Status and Future*, *Nucl. Phys. B Proc. Suppl.* **237-238** (2013) 94 [arXiv: [1302.2040](#)].
- [179] T. Sukhbold, T. Ertl, S.E. Woosley, J.M. Brown and H.T. Janka, *Core-Collapse Supernovae from 9 to 120 Solar Masses Based on Neutrino-powered Explosions*, *Astrophys. J.* **821** (2016) 38 [arXiv: [1510.04643](#)].
- [180] J.M. Lattimer and F.D. Swesty, *A Generalized equation of state for hot, dense matter*, *Nucl. Phys. A* **535** (1991) 331.
- [181] I. Tamborra et al., *High-resolution supernova neutrino spectra represented by a simple fit*, *Phys. Rev.* **D86** (2012) 125031 [arXiv: [1211.3920](#)].
- [182] M.T. Keil, G.G. Raffelt and H.-T. Janka, *Monte Carlo study of supernova neutrino spectra formation*, *Astrophys. J.* **590** (2003) 971 [arXiv: [astro-ph/0208035](#)].
- [183] *Inverse transform method*, in *Encyclopedia of Operations Research and Management Science*, S.I. Gass and M.C. Fu, eds., (Boston, MA), pp. 815–815, Springer US (2013), doi: [10.1007/978-1-4419-1153-7_200343](#).
- [184] M.A. Unland Elorrieta, L. Classen, J. Reubelt, S. Schmiemann, J. Schneider and A. Kappes, *Characterisation of the Hamamatsu R12199-01 HA MOD photomultiplier tube for low temperature applications*, *JINST* **14** (2019) P03015 [arXiv: [1902.01714](#)].
- [185] M. A. Unland Elorrieta, *Development, simulation, and characterization of a novel multi-PMT optical module for IceCube Upgrade with emphasis on detailed*

- understanding of photomultiplier performance parameters*, Westfälische Wilhelms-Universität Münster, Ph.D. thesis, in preparation.
- [186] J.N. Bahcall et al., *Standard neutrino spectrum from B-8 decay*, *Phys. Rev.* **C54** (1996) 411 [arXiv: [nucl-th/9601044](#)].
- [187] W.C. Haxton and R.G.H. Robertson, *Solar neutrino interactions with O-18 in Super-Kamiokande*, *Phys. Rev.* **C59** (1999) 515 [arXiv: [nucl-th/9806081](#)].
- [188] M. Salathe, M. Ribordy and L. Demirors, *Novel technique for supernova detection with IceCube*, *Astropart. Phys.* **35** (2012) 485 [arXiv: [1106.1937](#)].
- [189] D.F. Cowen, A. Franckowiak and M. Kowalski, *Estimating the Explosion Time of Core-Collapse Supernovae from Their Optical Light Curves*, *Astropart. Phys.* **33** (2010) 19 [arXiv: [0901.4877](#)].
- [190] G. Cowan, K. Cranmer, E. Gross and O. Vitells, *Asymptotic formulae for likelihood-based tests of new physics*, *Eur. Phys. J. C* **71** (2011) 1554 [arXiv: [1007.1727](#)].
- [191] L. Köpke, private communication.
- [192] S. Bityukov, N. Krasnikov, A. Nikitenko and V. Smirnova, *Two approaches to combining significances*, *PoS ACAT08* (2008) 118.
- [193] M. A. Unland Elorrieta, private communication.
- [194] F. Sprenger, *Studies on the Sensitivity of Multi-PMT Optical Modules to the Energy Spectrum of MeV Supernova Neutrinos for Future IceCube Extensions*, Westfälische Wilhelms-Universität Münster, *Master thesis*, 2019.
- [195] D. Su'arez Garc'ia, *Modeling of a multi-PMT optical sensor for IceCube-Gen2 in Geant4 and Monte Carlo studies to optimize its sensitivity*, Westfälische Wilhelms-Universität Münster, *Master thesis*, 2021.
- [196] F. J. Vara Carbonell, *Gel pad sensitivity studies and muon reconstruction in a water basin in Geant4 for IceCube multi-PMT optical modules*, Westfälische Wilhelms-Universität Münster, *Master thesis*, 2022.
- [197] T. DeYoung, *IceTray: A software framework for IceCube*, in *14th International Conference on Computing in High-Energy and Nuclear Physics*, pp. 463–466, 2005.
- [198] KM3NET collaboration, *The KM3NeT potential for the next core-collapse supernova observation with neutrinos*, *Eur. Phys. J. C* **81** (2021) 445 [arXiv: [2102.05977](#)].
- [199] KM3NET collaboration, *Dependence of atmospheric muon flux on seawater depth measured with the first KM3NeT detection units: The KM3NeT Collaboration*, *Eur. Phys. J. C* **80** (2020) 99 [arXiv: [1906.02704](#)].
- [200] Y. Becherini, A. Margiotta, M. Sioli and M. Spurio, *A Parameterisation of single and multiple muons in the deep water or ice*, *Astropart. Phys.* **25** (2006) 1 [arXiv: [hep-ph/0507228](#)].
- [201] ANTARES collaboration, *Transmission of light in deep sea water at the site of the ANTARES Neutrino Telescope*, *Astropart. Phys.* **23** (2005) 131 [arXiv: [astro-ph/0412126](#)].
- [202] E. Kolbe, K. Langanke and P. Vogel, *Estimates of weak and electromagnetic nuclear decay signatures for neutrino reactions in Super-Kamiokande*, *Phys. Rev. D* **66** (2002) 013007.

- [203] KM3NET collaboration, *Letter of intent for KM3NeT 2.0*, *J. Phys. G* **43** (2016) 084001 [arXiv: 1601.07459].
- [204] D. Chirkin, preliminary results presented in internal calls, from 2019 to 2021.
- [205] ICECUBE collaboration, *A calibration study of local ice and optical sensor properties in IceCube*, *PoS ICRC2021* (2021) 1023 [arXiv: 2107.10435].
- [206] Internal IceCube calibration site, visited during 2019 to 2021.
- [207] ICECUBE collaboration, *Calibration LEDs in the IceCube Upgrade D-Egg modules*, *PoS ICRC2019* (2020) 923 [arXiv: 1908.10780].
- [208] Internal communication with members of the calibration group in IceCube.
- [209] A. Tenbruck, *Implementation von LEDs in eine Geant4-Simulation des mDOM-Sensors für das IceCube Upgrade und Simulationsstudien zu deren Emissionsprofil*, Westfälische Wilhelms-Universität Münster, *Bachelor thesis*, 2022.
- [210] J. Nuckles, private communication.
- [211] T. Eder, Studies on an in-situ calibration method for the IceCube multi-PMT optical module using radioactive decays, Westfälische Wilhelms-Universität Münster, *Master thesis*, 2019.
- [212] R.J. Barlow, *Statistics. A guide to the Use of Statistical Methods in the Physical Sciences*, John Wiley & Sons. Chichester (England) (1989).
- [213] F. James and M. Roos, *Minuit: A System for Function Minimization and Analysis of the Parameter Errors and Correlations*, *Comput. Phys. Commun.* **10** (1975) 343.
- [214] H. Dembinski and P.O. et al., *scikit-hep/iminuit*, *Zenodo* (2020) .
- [215] C. Toennis, preliminary results presented in internal calls, 2021.
- [216] LIGO SCIENTIFIC, VIRGO, FERMI-GBM, INTEGRAL collaboration, *Gravitational Waves and Gamma-rays from a Binary Neutron Star Merger: GW170817 and GRB 170817A*, *Astrophys. J. Lett.* **848** (2017) L13 [arXiv: 1710.05834].
- [217] ICECUBE collaboration, *Probing neutrino emission at GeV energies from compact binary mergers with the IceCube Neutrino Observatory*, 5, 2021, [arXiv: 2105.13160].
- [218] LIGO SCIENTIFIC, VIRGO collaboration, *GW170817: Observation of Gravitational Waves from a Binary Neutron Star Inspiral*, *Phys. Rev. Lett.* **119** (2017) 161101 [arXiv: 1710.05832].
- [219] N. Gehrels and S. Razzaque, *Gamma Ray Bursts in the Swift-Fermi Era*, *Front. Phys. (Beijing)* **8** (2013) 661 [arXiv: 1301.0840].
- [220] C. Andreopoulos et al., *The GENIE Neutrino Monte Carlo Generator*, *Nucl. Instrum. Meth. A* **614** (2010) 87 [arXiv: 0905.2517].
- [221] T. De Forest, *Off-Shell electron Nucleon Cross-Sections. The Impulse Approximation*, *Nucl. Phys. A* **392** (1983) 232.
- [222] M. Honda, M. Sajjad Athar, T. Kajita, K. Kasahara and S. Midorikawa, *Atmospheric neutrino flux calculation using the NRLMSISE-00 atmospheric model*, *Phys. Rev. D* **92** (2015) 023004 [arXiv: 1502.03916].
- [223] D. Heck, J. Knapp, J.N. Capdevielle, G. Schatz and T. Thouw, *CORSIKA: a Monte Carlo code to simulate extensive air showers*, *KIT documentation* (1998).

- [224] T.K. Gaisser, *Spectrum of cosmic-ray nucleons, kaon production, and the atmospheric muon charge ratio*, *Astropart. Phys.* **35** (2012) 801 [arXiv: 1111.6675].
- [225] B. Baret et al., *Bounding the Time Delay between High-energy Neutrinos and Gravitational-wave Transients from Gamma-ray Bursts*, *Astropart. Phys.* **35** (2011) 1 [arXiv: 1101.4669].
- [226] G. Carleo, I. Cirac, K. Cranmer, L. Daudet, M. Schuld, N. Tishby et al., *Machine learning and the physical sciences*, *Rev. Mod. Phys.* **91** (2019) 045002 [arXiv: 1903.10563].
- [227] Y. Coadou, *Boosted Decision Trees and Applications*, *EPJ Web Conf.* **55** (2013) 02004.
- [228] G. Ke, Q. Meng, T. Finley, T. Wang, W. Chen, W. Ma et al., *Lightgbm: A highly efficient gradient boosting decision tree*, in *Advances in Neural Information Processing Systems*, vol. 30, Curran Associates, Inc., 2017.
- [229] J.H. Friedman, *Greedy function approximation: A gradient boosting machine.*, *Annals Statist.* **29** (2001) 1189.
- [230] H. Deng, Y. Zhou, L. Wang and C. Zhang, *Ensemble learning for the early prediction of neonatal jaundice with genetic features*, *BMC Medical Informatics and Decision Making* **21** (2021) .
- [231] P. Speckmayer, A. Hocker, J. Stelzer and H. Voss, *The toolkit for multivariate data analysis, TMVA 4*, *J. Phys. Conf. Ser.* **219** (2010) 032057.
- [232] LightGBM documentation website, <https://lightgbm.readthedocs.io/en/latest/index.html>, accessed 10-Oct-2022.
- [233] N. van Eijndhoven, O. Fadiran and G. Japaridze, *Implementation of a Gauss convoluted Pandel PDF for track reconstruction in Neutrino Telescopes*, *Astropart. Phys.* **28** (2007) 456 [arXiv: 0704.1706].
- [234] T.K. Gaisser and M. Honda, *Flux of atmospheric neutrinos*, *Ann. Rev. Nucl. Part. Sci.* **52** (2002) 153 [arXiv: hep-ph/0203272].
- [235] F.M. Rieger, V. Bosch-Ramon and P. Duffy, *Fermi acceleration in astrophysical jets*, *Astrophys. Space Sci.* **309** (2007) 119 [arXiv: astro-ph/0610141].
- [236] G.J. Feldman and R.D. Cousins, *A Unified approach to the classical statistical analysis of small signals*, *Phys. Rev. D* **57** (1998) 3873 [arXiv: physics/9711021].
- [237] ANTARES, ICECUBE, PIERRE AUGER, LIGO SCIENTIFIC, VIRGO collaboration, *Search for High-energy Neutrinos from Binary Neutron Star Merger GW170817 with ANTARES, IceCube, and the Pierre Auger Observatory*, *Astrophys. J. Lett.* **850** (2017) L35 [arXiv: 1710.05839].
- [238] SUPER-KAMIOKANDE collaboration, *Search for Neutrinos in Super-Kamiokande Associated with the GW170817 Neutron-star Merger*, *Astrophys. J. Lett.* **857** (2018) L4 [arXiv: 1802.04379].
- [239] LIGO SCIENTIFIC, VIRGO collaboration, *GWTC-1: A Gravitational-Wave Transient Catalog of Compact Binary Mergers Observed by LIGO and Virgo during the First and Second Observing Runs*, *Phys. Rev. X* **9** (2019) 031040 [arXiv: 1811.12907].

Acknowledgements

I would like to express my gratitude to Prof. Dr. Alexander Kappes for giving me the opportunity to grow as a scientist in his group over the past years. I am very grateful for his helpful advice, personal support, patience, and the great atmosphere he fosters in our group. I also thank Prof. Dr. Christian Weinheimer for being my second supervisor, and Prof. Dr. Jochen Heitger for evaluating this thesis.

I would like to thank many members of the IceCube Collaboration that have greatly assisted me, including Prof. Dr. Lutz Köpke for his assistance with Supernova studies, Dr. Tom Stuttard and Dr. Michael Larson for their detailed answers to my many questions and guidance with the event selection, Dr. Martin Rongen for his help with calibration studies, and Dr. Thomas Kittler for helping with my never-ending struggles at the beginning of my Ph.D.

I am also very grateful for the time I spent with my colleagues in the AG Kappes working group, where the atmosphere was always great and with whom I shared many memorable moments. Special thanks to Martin Unland for forming a symbiotic relationship with me, without whom I am convinced that I would not have made it this far, to Dr. Raffi Busse for helping me keep my nose, and to Dr. Lew Classen for being a big brother for me. I give a big thank you to Daniel Guderian, Markus Dittmer, Berit Schlüter, Javi Vara, Guillermo Achtermann, and Dr. Ben Eberhardt for proofreading different parts of this thesis.

I am particularly grateful to Mayara Ferreira for her compassionate care when I needed it most, to Agu Procikieviez for his persistent efforts to take me out and make plans with me, to Juan Bernal for sharing less amusing jokes than mine, and to Laura Gallardo for withstanding us all. And thanks to all the friends who made my years in Münster unforgettable: Mehrnoush, Ale, Vicky, Andrea, Aurora, Alicia, Julien...

Lastly, I would like to thank my family for their understanding and support throughout my studies. I have missed you greatly, and I will forever be grateful for your love.

Resume and publications

Publications

- C.J.Lozano Mariscal, L. Classen, M.A. Unland Elorrieta and A. Kappes, *Sensitivity of multi-PMT optical modules in Antarctic ice to supernova neutrinos of MeV energy*, *Eur. Phys. J. C* 81 (2021) 1058 [arXiv: 2106.14199].

Resume

NAME	Cristian Jesús Lozano Mariscal
ADRESSE	Kolde-Ring 39, 48151 Münster
E-MAIL	crilozmar@gmail.com
GEBURTSDATUM	24.07.1991
GEBURTSORT	San Roque, Cádiz (Spanien)
ELTERN	Guillermo Lozano López Juana María Mariscal Agüera
Schule	
09/1995 - 06/2005	CEIP San Bernardo (Estación de San Roque, Cádiz)
09/2005 - 06/2007	IES Mar del sur (Taraguilla, Cádiz)
09/2007 - 06/2009	IES Carlos Castilla del Pino (San Roque, Cádiz)
06/2009	Allgemeine Hochschulreife (Selectividad), Note: 7.78/10
Studium	
10/2009 - 06/2015	Grado en Física (240 ECTs), Note: 6.7/10 - Universidad de Sevilla (Spanien)
10/2015 - 01/2017	Internationaler Doppelabschluss: Master of Science in Physics & Interuniversity Master in Nuclear Physics , Note: 1.6 (im deutschen Notensystem) - Deutschland: WWU Münster - Spanien: US, UAM, UB, UGR, USAL y UCM
9/2017 - 01/2023	Physik Promotion - Institut für Kernphysik (AG Kappes), WWU Münster
Berufstätigkeit	
01/2017 - 08/2017	Wissenschaftliche Mitarbeiter - Institut für Kernphysik (AG Kappes), WWU Münster